

# THÈSE

Présentée devant

L'ÉCOLE CENTRALE DE LYON

Pour obtenir

Le titre de DOCTEUR  
SPECIALITÉ ACOUSTIQUE

Par

**Mikhail AVERIYANOV**

**Propagation des ondes acoustiques à travers un milieu turbulent : études théorique et expérimentale des effets de diffraction et des effets non linéaires**

Nonlinear-diffraction effects in propagation of sound waves through turbulent atmosphere: experimental and theoretical studies

Soutenue le 9 octobre 2008 devant la Commission d'Examen

## JURY

Président : M. Daniel JUVÉ  
Examineurs : M. Philippe BLANC-BENON (Co-Directeur de Thèse)  
Mme. Vera KHOKHLOVA (Co-Directeur de Thèse)  
M. Robin CLEVELAND (Rapporteur)  
M. Vladimir PREOBRAZHENSKY (Rapporteur)  
M. Oleg SAPOZHNIKOV

Laboratoire de Mécanique des Fluides et d'Acoustique, UMR CNRS 5509  
Ecole Centrale de Lyon

et

Département d'Acoustique, Faculté de Physique, Université d'État de Moscou



# TABLE OF CONTENTS

Nomenclature of main used notations .....	5
Introduction .....	11
<b>Chapter 1</b> <b>NONLINEAR SOUND WAVES IN INHOMOGENEOUS MOVING MEDIA (REVIEW)</b> .....	<b>19</b>
<b>§ 1.1</b> <b><i>Sonic boom in turbulent atmosphere</i></b> .....	<b>19</b>
1.1.1    Ecological aspects of the problem .....	19
1.1.2    Outdoor and laboratory experiments .....	21
<b>§ 1.2</b> <b><i>Mathematical models for nonlinear sound waves propagating in inhomogeneous moving media</i></b> .....	<b>24</b>
1.2.1    Wave equations in acoustics of inhomogeneous moving media .....	24
1.2.2    Parabolic approximation for nonlinear sound waves in media with scalar inhomogeneities.....	28
1.2.3    Equations of nonlinear geometrical acoustics .....	33
<b>§ 1.3</b> <b><i>Theoretical modelling of turbulent media</i></b> .....	<b>36</b>
<b>§ 1.4</b> <b><i>Conclusion</i></b> .....	<b>41</b>
<b>Chapter 2</b> <b>PROPAGATION OF NONLINEAR N-WAVES IN A TURBULENT VELOCITY FIELD (laboratory-scaled experiment)</b> .....	<b>43</b>
<b>§ 2.1</b> <b><i>Generation and measurement of fully developed turbulent field</i></b> .....	<b>45</b>
2.1.1    Experimental setup .....	45
2.1.2    Measurement of the turbulent field parameters .....	46
<b>§ 2.2</b> <b><i>Acoustic measurements</i></b> .....	<b>53</b>
2.2.1    Experimental setup .....	53
2.2.2    Characteristics of <i>N</i> -waves measured without turbulence.....	55
<b>§ 2.3</b> <b><i>Analysis of the effects of turbulence on N-waves</i></b> .....	<b>58</b>
2.3.1    Typical measured waveforms. Estimation of the focusing zone width .....	58
2.3.2    Effect of the turbulence intensity on the <i>N</i> -wave statistics, average and peak characteristics.....	60
2.3.3    Effect of propagation distance through turbulent medium on the statistics, average and peak characteristics of the acoustic <i>N</i> -wave .....	64
<b>§ 2.4</b> <b><i>Characteristic scales: atmosphere and laboratory experiment</i></b> .....	<b>67</b>
<b>§ 2.5</b> <b><i>Conclusion</i></b> .....	<b>68</b>
<b>Chapter 3</b> <b>MEASUREMENT AND MODELLING OF SPHERICALLY DIVERGING SHOCK PULSES IN RELAXING AIR. CALIBRATION OF THE MICROPHONE.</b> .....	<b>71</b>
<b>§ 3.1</b> <b><i>Acoustic measurements. Mean and peak characteristics of the N-wave parameters</i></b> .....	<b>73</b>
<b>§ 3.2</b> <b><i>Theoretical model</i></b> .....	<b>74</b>
3.2.1    Modified Burgers equation for divergent waves in relaxing medium .....	74
3.2.2    Numerical algorithm.....	76
3.2.3    Effects of nonlinearity, thermoviscous absorption and relaxation on the acoustic wave propagation.....	78
<b>§ 3.3</b> <b><i>Calibration of measuring system based on nonlinear effects</i></b> .....	<b>81</b>
<b>§ 3.4</b> <b><i>Amplitude and phase frequency characteristics of measuring system</i></b> .....	<b>82</b>
<b>§ 3.5</b> <b><i>N-wave characteristic parameters. Comparison of experimental data with the results of numerical modelling</i></b> .....	<b>85</b>
<b>§ 3.6</b> <b><i>Conclusion</i></b> .....	<b>86</b>

<i>Chapter 4</i>	NONLINEAR EVOLUTION EQUATION OF KHOKHLOV- ZABOLOTSKAYA TYPE FOR THE DESCRIPTION OF ACOUSTIC WAVE PROPAGATION IN INHOMOGENEOUS MOVING MEDIA .....	89
§ 4.1	<b><i>Theoretical model. Parabolic equation for nonlinear sound waves in inhomogeneous moving media.</i></b> .....	<b>90</b>
§ 4.2	<b><i>Self similarity property of the KZK type equation</i></b> .....	<b>95</b>
§ 4.3	<b><i>Numerical algorithms</i></b> .....	<b>96</b>
4.3.1	Frequency domain approach to model periodic waves with shocks.....	96
4.3.2	Time domain approach to model propagation of single shock pulses .....	98
§ 4.4	<b><i>Benchmark solutions and validation of the model</i></b> .....	<b>106</b>
§ 4.5	<b><i>Conclusion</i></b> .....	<b>108</b>
<i>Chapter 5</i>	NONLINEAR AND DIFFRACTION EFFECTS DURING THE PROPAGATION OF ACOUSTIC SIGNALS IN RANDOMLY INHOMOGENEOUS MOVING MEDIUM (Numerical modelling).....	111
§ 5.1	<b><i>Periodic waves</i></b> .....	<b>111</b>
5.1.1	Nonlinear <i>versus</i> linear effects of random focusing in an inhomogeneous moving medium .....	111
5.1.2	Effect of the transverse component of turbulent velocity field: vector <i>versus</i> scalar contributions of inhomogeneities .....	115
5.1.3	Diffraction effects: ray tracing and acoustic field patterns obtained with the KZK equation .....	116
5.1.4	Effect of spatial correlation lengths and intensity of the turbulence on acoustic field characteristics .....	117
§ 5.2	<b><i>Acoustic pulses. N-waves</i></b> .....	<b>120</b>
5.2.1	Parameters of simulations, 2D patterns of randomly inhomogeneous velocity field .....	120
5.2.2	Diffraction effects: ray tracing and acoustic field patterns obtained with the KZK equation .....	121
5.2.3	Nonlinear <i>versus</i> linear effects on random focusing in an inhomogeneous medium .....	124
5.2.4	Influence of randomly inhomogeneous medium on statistics, average and peak characteristics of the acoustic <i>N</i> -wave.....	127
5.2.5	Effect of the transverse component of turbulent velocity: vector <i>versus</i> scalar contributions of inhomogeneities .....	132
5.2.6	Effect of spatial correlation lengths and turbulent kinetic energy distribution law on acoustic field characteristics .....	134
§ 5.3	<b><i>Comparison of numerical model results with experimental data</i></b> .....	<b>136</b>
§ 5.4	<b><i>Conclusion</i></b> .....	<b>146</b>
	CONCLUSION .....	149
	Appendix A : GEOMETRICAL ACOUSTICS APPROACH .....	153
	Appendix B : NUMERICAL GRID STEPS.....	157
	Appendix C : SYNTHÈSE DES RÉSULTATS (en français) .....	163
	LIST OF FIGURES.....	187
	LIST OF REFERENCES.....	195

## Remerciement

*Ce travail de thèse en co-tutelle s'est déroulé au département d'acoustique de la Faculté de Physique de l'Université d'Etat de Moscou et au Département de Mécanique des Fluides et d'Acoustique de l'École Centrale de Lyon.*

*Je remercie d'abord le Professeur Oleg Rudenko, Directeur du département d'acoustique de la Faculté de Physique de l'Université d'Etat de Moscou, et le Professeur Michel Lance, Directeur du Laboratoire de Mécanique des Fluides et d'Acoustique de l'École Centrale de Lyon, de m'avoir accueilli au sein de leurs équipes.*

*J'adresse également mes plus sincères remerciements à l'Ambassade de France en Russie qui m'a permis d'obtenir une bourse du Gouvernement Français pour l'accomplissement de cette thèse en co-tutelle, et qui m'a permis de connaître la France.*

*J'exprime ma plus profonde gratitude au Professeur Daniel Juvé, Directeur du Centre Acoustique, qui m'a accueilli au sein de son équipe de recherche et qui m'a fait l'honneur de présider ce jury.*

*Ma gratitude s'adresse également aux Professeurs Vladimir Preobrazhensky et Robin Cleveland qui ont accepté d'être rapporteurs de ce travail et me font l'honneur d'être membres de mon jury.*

*J'adresse toutes mes plus vives reconnaissances à mes directeurs de thèse en co-tutelle Vera Khokhlova (Université d'État de Moscou) et Philippe Blanc-Benon (École Centrale de Lyon). Ils ont beaucoup contribué à cette thèse par leurs conseils, par leurs commentaires et par leurs soutiens. Ils étaient toujours disponibles pour la discussion et ils m'ont toujours aidé à trouver une solution aux questions tant scientifiques que de la vie quotidienne. Et si ma thèse est lisible c'est en partie grâce à leurs lectures attentives.*

*Toute ma gratitude va de même au Professeur Oleg Sapozhnikov. Ses conseils et ses discussions sur mes résultats expérimentaux et théoriques ont beaucoup contribué à la*

*réalisation de mon travail de thèse. Je remercie tous les autres professeurs de l'équipe acoustique de l'Université d'Etat de Moscou qui m'ont fait découvrir au travers des cours d'acoustique, la théorie des ondes dans ses divers aspects.*

*Je remercie également Sébastien Ollivier, qui a été mon troisième « chef de science » en ce qui concerne les expériences faites à l'École Centrale de Lyon. J'aimerais bien dire un grand merci à Emmanuel Jondeau et Jean-Michel Perrin pour leur aide dans la réalisation pratique des expériences. Je remercie de même tous les autres membres de l'équipe acoustique pour m'avoir accueilli au centre acoustique.*

*Je joins à ces remerciements ceux que j'adresse à Petr Yuldashev, un doctorant, qui va continuer mon expérience de thèse en co-tutelle avec Vera et Philippe. Il a contribué en partie au Chapitre 3 de cette thèse.*

*Je remercie aussi tous les étudiants et doctorants avec qui j'ai travaillé pendant l'écriture de ma thèse pour l'ambiance positive et optimiste qu'ils ont créée.*

*J'exprime ma grande reconnaissance à Anne Zucco pour sa contribution à la collaboration entre MSU et ECL, et en particulier son travail administratif pour l'organisation de cette collaboration. Elle a également pris part à l'organisation de mon séjour en France.*

*Enfin, je remercie ma famille pour sa confiance et son soutien, lequel m'a toujours permis de choisir les bonnes solutions et m'a donné de l'enthousiasme pendant mon travail de thèse.*

## Abstract

Propagation of nonlinear acoustic signals in randomly inhomogeneous moving media is one of the most important problems in many modern applications of theoretical and experimental acoustics. For example, a detailed knowledge of the acoustic field structure is necessary in order to predict peak positive pressure levels caused by supersonic flights near the ground surface. Up to date, distortions of the acoustic wave in media with turbulent flows have been studied only in the linear parabolic approximation or in the approximation of nonlinear geometrical acoustics. In this context, investigation of nonlinear acoustic fields taking into account wave diffraction effect and influence of both longitudinal and transverse components of medium motion is of great importance.

In this work, propagation of nonlinear acoustic signals in randomly inhomogeneous moving media is studied numerically and experimentally. The nonlinear evolution equation of Khokhlov-Zabolotskaya-Kuznetsov type, which accounts for both longitudinal and transverse to the wave propagation direction components of the inhomogeneous velocity field, is derived. An effective numerical algorithm is developed to simulate the propagation of acoustic shock waves with narrow fronts in inhomogeneous media. Advantages of the derived parabolic equation compared to the geometrical acoustics approximation are shown based on numerical modeling. It is shown that the characteristic structure of the acoustic field in turbulent media is mainly determined by the longitudinal component of the velocity field. However, under certain conditions, the transverse velocity fluctuations lead to essential distortions of the acoustic field. The influence of nonlinear effects on acoustic wave random focusing in turbulent medium is also studied.

The laboratory scale experimental setup is designed to investigate the multiple focusing effects on the intense  $N$ -wave propagation in turbulent flow. Statistical distributions of acoustic wave parameters are measured up to distances longer than the distance of first caustic occurrence, determined by the outer turbulence scale. In order to interpret correctly the distortion introduced by the measuring system, a method of wide band high frequency microphone calibration based on nonlinear lengthening of the acoustic pulse in absorptive media is developed. It is shown that in turbulent medium, acoustic wave mean peak positive pressure decreases and mean rise time increases faster than in homogeneous air. However, in turbulent medium acoustic pressure amplitudes, 3-4 times higher than that measured in homogeneous air, are observed. Results of numerical modeling appear to be in a good agreement with the experimental data that confirms the validity of the developed theoretical model.



## Nomenclature of main used notations

### *Romanic letters*

$A$	dimensionless parameter of absorption
$b$	coefficient of viscosity
$C_n$	complex amplitude of the $n^{\text{th}}$ harmonic
$c$	local sound speed
$c_0$	ambient sound speed
$c_\infty^v$	frozen sound speed for $v^{\text{th}}$ relaxation process
$c_e$	effective sound speed
$d_v$	relaxation parameter of $v^{\text{th}}$ process
$D_v$	dimensionless relaxation parameter of $v^{\text{th}}$ process
$E$	kinetic energy spectrum of the turbulent field
$f_v$	relaxation frequency of $v^{\text{th}}$ process
$f$	longitudinal two-point correlation function
$g$	transverse two-point correlation function
$h_\theta, h_\sigma, h_\rho$	temporal and spatial grid steps
$\mathbf{k}$	acoustic wave vector
$\mathbf{K}$	wave vector of the turbulent field
$L, l$	characteristic scale of inhomogeneity
$L_f, L_g$	longitudinal and transverse integral length scales of turbulent inhomogeneity
$l_0, L_0$	inner and outer scales of turbulent inhomogeneity
$M$	hydrodynamic Mach number
$\mathbf{n}$	unit vector, showing the direction of wave propagation and transverse to its front
$n$	refraction index of the medium
$N$	dimensionless nonlinear parameter
$p$	acoustic pressure
$p_0$	atmospheric pressure level
$p_+$	peak positive pressure of the wave
$p_+^0$	peak positive pressure of the wave, propagating in motionless medium
$r$	radial propagation coordinate
$r_0$	reference distance
$\mathbf{R}, \mathbf{Q}$	geodesic elements
$t$	time coordinate
$t_{0.1-0.9}$	rise time of the acoustic wave shock front
$T$	half duration of the acoustic wave
$T_0$	initial half duration of the acoustic wave

$\mathbf{u}, (u_x, \mathbf{u}_\perp)$	medium velocity
$u_{rms}$	standard deviation of medium velocity fluctuations
$U_{jet}$	flow velocity at the exit of the jet
$U_{mean}$	local mean velocity of the turbulent flow
$U_{\parallel}, U_{\perp}$	normalized longitudinal and transverse flow components
$V$	dimensionless acoustic pressure
$\mathbf{w}$	vibrational velocity of medium particles
$w_{gr}$	sound wave local group velocity
$x$	longitudinal coordinate
$x_i$	components of a position vector $\mathbf{r} = (x, y, z)$ , ( $i = 1, 2, 3$ )
$x_s$	shock formation distance (harmonic plane wave), characteristic nonlinear distance
$y$	transverse coordinate

### ***Greek letters***

$\beta$	acoustic nonlinearity coefficient
$\Gamma$	Goldberg number
$\delta_{ij}$	Dirichlet function
$\varepsilon$	small parameter
$\lambda$	wavelength or length of the acoustic pulse
$\lambda_f, \lambda_g$	longitudinal and transverse Taylor scales of random inhomogeneity
$\rho$	dimensionless transverse coordinate
$\rho_0$	ambient medium density
$\sigma$	dimensionless propagation coordinate
$\tau$	retarded time
$\tau_v$	relaxation time of $v^{\text{th}}$ process
$\theta$	dimensionless retarded time
$\Delta\theta$	arrival time shift
$\theta_{0.1-0.9}$	dimensionless rise time of the acoustic wave shock front
$\theta_0$	dimensionless initial half durations of the acoustic wave
$\theta_j$	angle between $i^{\text{th}}$ random Fourier mode and $x$ axis
$\phi_j$	phase of the $i^{\text{th}}$ random Fourier mode
$\psi$	eikonal
$\omega$	characteristic frequency of the acoustic wave

## Introduction

Propagation of intense acoustic waves in inhomogeneous moving media is one of the most important problems in many modern applications of theoretical and experimental acoustics, such as propagation of intense ultrasound in inhomogeneous biological tissues with blood vessels [1], propagation of nonlinear acoustic pulses in atmospheric turbulent layers near the ground [2 - 8], propagation of shock waves and waves from explosive sources in fluctuating ocean [9]. In aeroacoustics, a great interest to this problem is caused mainly by the development of the supersonic civil transport aviation, which is inseparably related to the sonic boom propagation in the atmosphere. Sonic boom pulses or *N*-waves, formed during supersonic jet flights, propagate in the atmosphere in the direction of the ground surface and under the influence of atmospheric inhomogeneities form an acoustic field with a very complex structure. This structure is strongly dependent on the presence in the atmosphere of various types of inhomogeneities including constant winds and flows, random temperature and velocity turbulent fields, and also gradients of density and temperature [10, 11].

For the applications already mentioned, a detailed knowledge of the acoustic field structure is necessary. For example, it allows estimation of the acoustic pressure level near the ground surface or estimation of the ultrasonically induced biological effects in tissue. At the same time, it is desirable to predict peak and average values of acoustic pressure and rise time of the shock front in order to evaluate possible damages. For this purpose a theoretical model, which takes into account the effects introduced by the inhomogeneities of the medium, diffraction, acoustic nonlinearity, thermoviscous dissipation and relaxation processes, should be developed.

Despite a diversity of the previously mentioned examples of sound wave propagation in inhomogeneous media, theoretical models to govern the acoustic field, are very similar to each other, and the problems to solve can be classified into two types depending on the nature of the inhomogeneities. The inhomogeneities can be of scalar nature, i.e. spatial fluctuations of the

sound speed and density, for example, due to variations in temperature or salt concentration in the ocean or variations in tissue type; and of vector nature, i.e. spatial fluctuations of the background particle velocity, for example, due to the presence of vortices, wind, or flow in the medium. A complete theoretical model, derived from the fundamental equations of the fluid mechanics and that incorporates the vector type inhomogeneities, is very complicated for analysis. A common approach is to replace the real moving medium with a hypothetical motionless medium with an effective sound speed, which takes into account only the velocity component along the direction of propagation, that is, the moving medium is modelled as having scalar type inhomogeneities. A detailed analysis of this approach can be found in Refs. [4, 12, 24]. However, in many problems, refracted sound waves and those scattered by inhomogeneities propagate in directions, which may significantly differ from the initial one. Furthermore if the transverse component of the velocity field has a non-zero mean component this may result in the shift and distortion of the caustics, and therefore may have a strong effect on propagation of the acoustic wave.

Theoretical investigation of intense sound wave propagation in inhomogeneous moving atmosphere is a very difficult problem. In case of a medium including vector-type inhomogeneities only simplified models, generally under the assumption of nonlinear geometrical acoustics (NGA) [13 - 17], can be found in recent literature. The propagation both in media with scalar and vector inhomogeneities has been considered in NGA approximation [18, 19]. Nevertheless, analytical solutions have been obtained only for stratified media [20, 21, 22]. The main limitation of the geometrical acoustics approach is that it does not account for the diffraction effects. Only recently, due to the growing computational power and the development of efficient numerical methods for solving differential equations, the nonlinear-diffraction problems had started to be considered. Parabolic equations have been derived for linear sound propagation in inhomogeneous moving media [23 - 29] which do maintain the vector properties of the velocity of the medium. Nonlinear propagation in media with scalar inhomogeneities has been also considered in parabolic approximation [30-33]. It is worth to note, that vector inhomogeneities like vortices of various scales and winds or flows, which do contain the transverse component of medium velocity, in nonlinear parabolic approximation have been not considered. The combined effect of acoustic nonlinearity and different type inhomogeneities has been investigated for only several specific problems [34 - 39]. In general, to the best of our knowledge, nonlinear propagation of diffracting sound beams in random inhomogeneous moving media has not been previously studied.

Experimental studies of acoustic signal propagation in turbulent atmosphere are complicated because field experiments are not well controlled and not all the varying parameters of atmosphere could be measured. Moreover, field experiment is very expensive. That is why experimental efforts of the acoustical community in investigation of sonic boom problem are pointed on the conduction of laboratory scaled experiments that have been shown to be a good alternative to the field measurements. The results of such experiments are published in the papers of different authors, who used for generation of high amplitude shock  $N$ -waves either spark sources [7, 40 - 45], or lasers [46]. In laboratory scaled experiments the acoustic sources are well controlled, that gives an opportunity to conduct measurements that are more accurate. The results of such experiments will allow to not only qualitatively describe the general features of acoustic pulse propagation in inhomogeneous moving media, but also, by comparison with the numerical simulations, to verify the validity of the derived nonlinear parabolic equation and built numerical algorithm. In future, it will also allow quantitative estimations of the statistics, peak and average values of the main parameters of the acoustic field that is formed during the propagation of high amplitude acoustic pulses (sonic booms) in the turbulent atmosphere.

### **Aims of the dissertation**

The general aim of the dissertation is to develop experimental and theoretical methods and, based on these methods, to investigate nonlinear acoustic wave propagation in inhomogeneous moving media. According to this aim, the following tasks can be outlined:

- 1 Development of the laboratory scale experimental setup and investigation of high amplitude acoustic  $N$ -pulse propagation in turbulent airflow.
- 2 Development of the theoretical model for the description of nonlinear acoustic signals propagation in inhomogeneous moving media taking also into account the combined effects of diffraction, thermoviscous absorption and relaxation processes.
- 3 Development of the numerical algorithm that allows modelling the problems of nonlinear propagation of periodic and pulsed signals with a steep front in inhomogeneous moving media.
- 4 Determination of the relative influence of nonlinear, thermoviscous, and relaxation processes on the  $N$ -wave propagation in homogeneous air under laboratory experiment conditions with the aim to develop calibration method of the measuring system.
- 5 Experimental and theoretical investigation of both nonlinear-diffraction and random focusing effects in inhomogeneous turbulent medium on the statistics, peak, and average values of the acoustic field parameters.

**Dissertation scientific novelty**

- 1 A new term that accounts for the component of the medium velocity fluctuations transverse to the direction of the wave propagation was introduced into the Khokhlov-Zabolotskaia-Kuznetsov type equation.
- 2 A new numerical algorithm to solve the derived nonlinear parabolic equation for the periodic and pulsed signals with steep fronts was developed.
- 3 Propagation of high amplitude acoustic signals in inhomogeneous moving media was investigated in details: with account for nonlinear and diffraction effects, thermoviscous absorption and relaxation processes, and effects related to the presence of transverse and longitudinal components of inhomogeneous medium velocity field fluctuations.
- 4 It was shown that transverse fluctuations of randomly inhomogeneous velocity field might lead to the sufficient changes in acoustic field structure both in longitudinal and transverse directions.
- 5 A new experimental method of calibrating the broadband measuring system based on the nonlinear  $N$ -pulse lengthening in homogeneous absorptive air and using the determination of the pulse duration by the positions of nulls in its spectrum, was proposed and validated.

**Reliability** of the results presented in dissertation is verified by the benchmark numerical and physical experiments, and by the agreement of the results of these experiments to *a priori* known information, to the theoretical data, and numerical simulations, obtained in the papers of other authors.

**Dissertation scientific and practical amount**

- 1 A new theoretical model and a set of numerical algorithms developed to govern nonlinear acoustic propagation in inhomogeneous moving media allow to compute simultaneously the statistical distributions, peak and average characteristics of the acoustic field.
- 2 The optimisation of the numerical algorithm allows modelling of shock wave fields with minimal computational time.
- 3 The experimental setup built in this work allows conducting laboratory scale investigations of high amplitude acoustic pulse propagation in turbulent atmosphere and studying the formation of the random foci of the first and higher orders.

- 4 Numerical modelling of physical processes during the propagation of  $N$ -waves in inhomogeneous moving media allows predicting the characteristic values of acoustic pressure amplitude and shock rise time fluctuations. This may help to avoid possible negative influence of intense ultrasound on biological tissue during ultrasound surgery and negative influence of sonic booms on human being and environment at the ground surface.
- 5 Developed experimental method of broadband microphone calibration - based on the analysis of measured  $N$ -pulse lengthening with propagation distance in homogeneous air compared to theoretical prediction of acoustic pulse nonlinear lengthening with account for the relaxation effects - allows obtaining in the laboratory environment the frequency response of the measuring system. This allows on-place calibration, which is necessary due to possible changes in the system components, or system geometry, or due to changes in characteristics of the system with time.

### **Presentations and conferences**

The results included into the dissertation have been presented at the XII Scientific School «Nonlinear waves 2004» (Nizhniy Novgorod, Russia 2004); at the International Symposium CFA/DAGA'04, (Strasbourg, France 2004); at the Young Scientist Conference «Lomonosov 2004» (Moscow, Russia 2004); at the Conference «Wave phenomena in inhomogeneous media» (Zvenigorod, Russia 2004); at the International Conference IEEE UFFC (Montreal, Canada 2004); at the 2<sup>nd</sup> International Conference "Frontiers of Nonlinear Physics" (Nizhniy Novgorod, Saint-Petersburg, Russia 2004); at the International Conference Forum Acusticum (Budapest, Hungary 2005); at the Russian French seminar RAS/SFA (Moscow, Russia 2005); at the Session of the French Acoustical Society "CFA06" (Tour, France 2006); at the XVIII Session of the Russian Acoustical Society (Taganrog, Russia 2006); at the Conference «Waves 2006» (Zvenigorod, Russia 2006); at the international school-seminar "Waves 2006" (Coarse, France 2006); at the International Conference AIAA/CEAS (Rome, Italy 2007); at the XIX Session of Russian Acoustical Society (Nizhniy Novgorod, Russia 2007). All the results obtained have been also discussed at the scientific seminars of the Department of Acoustics of the Moscow State University and at the seminar of the Acoustical Institute (Moscow).

This work was partially supported in by the grant of the president of the Russian Federation RF № IIII-4449.2006.2, by the grant RFBR №06-02-16860, by the grant INTAS №05-100008-7841, by the international student award of the Acoustical Society of America. and by special stipend of the French Government for the preparation of the dissertation under the

co-supervision in the frame of the agreement between Ecole Centrale de Lyon, France and Physics Faculty of the Moscow State University, Russia.

### **Publications**

Main results of the dissertation are published in 20 papers, 3 of which are pre-reviewed articles in journals, 13 articles in conference proceedings and 4 abstracts of conferences.

### **Author's personal contribution**

The author took part in all the steps of the investigation, presented in the dissertation. Investigation consisted of the development of the theoretical and numerical models, design of the experimental setup, and conduction of the experiment itself. The author in collaboration with the team of LMFA, Ecole Centrale de Lyon (Sébastien Ollivier, Emmanuel Jondeau, Jean Michel Perrin), obtains all experimental data, presented in the dissertation personally.

### **Structure and volume of the dissertation**

The dissertation consists of the introduction and five chapters, the first of which is the literature review, and others are original. Each chapter contains a short introduction and conclusion. The references list contains 136 articles; the total volume of the dissertation is 201 pages, including 80 figures and 6 tables.

Figures and formulas in the dissertation are referred as (4.3) where the first number is the chapter number and the second number is the number of the formula or figure in this chapter.

### **Dissertation content**

In the first chapter of the dissertation the published literature review, concerning experimental (§1.1) and theoretical (§1.2) investigation of the sonic boom propagation in turbulent atmosphere is presented. The review of theoretical investigations (§1.2) is dedicated to the description of the main mathematical models of acoustic signal propagation in inhomogeneous moving media. It follows from the review that the comprehensive quantitative description of the shock wave acoustic fields in inhomogeneous moving media has not yet been provided. In §1.3 the short review of existing models of randomly inhomogeneous and turbulent media is presented. The main part of the paragraph is devoted to the description of the model of randomly oriented Fourier modes, where random velocity field of the medium is modelled as a set of spatial Fourier modes with given Gaussian or von Karman energy spectrum, random direction and random phase of the wave vector.

Second Chapter of the dissertation is devoted to the design of the experimental setup and laboratory scale measurements of the statistical distributions, peak and average values of the acoustic wave parameters after passing the inhomogeneous turbulent layer. The experimental setup designed at Ecole Centrale de Lyon allows generating fully developed turbulent velocity fields (§2.1) and acoustic pulses of short duration ( $30 \mu\text{s}$ ) and very high amplitude (1000 Pa) (§2.2). To generate the fully developed turbulence the intense air flow (0 - 50 m/s), forced by the turbine, outgoing from the plane jet of 160 mm width and 1400 mm length is used. To generate acoustic pulses, electric sparks are produced by applying a high voltage (15kV) between two tungsten electrodes. *N*-waves are recorded by the wideband high frequency 1/8" *Brüel & Kjaer* microphones (up to 140 kHz). In §2.4 the characteristic scales of the turbulent velocity and sonic boom acoustic fields in real atmosphere and laboratory scaled experiment are compared.

Third chapter of the dissertation is devoted to the development of a method to calibrate the acoustic measuring system (§3.3) and to determine its spectral characteristics (§3.4). This task is necessary for accurate interpretation of the experimental data for the rise time and peak pressure of the *N*-wave in the laboratory scale experiment conducted in inhomogeneous air (§3.1). Numerical analysis based on extended Burgers equation is provided (§3.2) for the spherically divergent *N*-wave propagating in homogeneous air with thermoviscous absorption and relaxation.

Fourth chapter of the dissertation is devoted to the derivation of the Khokhlov-Zabolotskaya-Kuznetsov type nonlinear parabolic evolution equation, which governs the propagation of acoustic signals in inhomogeneous moving media with account for component of the medium velocity fluctuations transverse to the direction of the wave propagation (§4.1). The similarity properties of the derived nonlinear evolution equation are considered in §4.2, and a numerical algorithm is developed (§4.3), which allows describing the propagation of periodic and pulsed acoustic signals with narrow fronts in inhomogeneous media with high accuracy and minimal CPU time consumption. Good accuracy of the built numerical algorithm and evolution model is also confirmed by the benchmark simulations for the simple single Gaussian inhomogeneities and by comparison with the known linear results, obtained on the basis of wide angle parabolic equation (§4.4).

Fifth chapter of the dissertation is devoted to the numerical simulations and investigation of nonlinear acoustic propagation in inhomogeneous moving media. The propagation of both periodic waves (§5.1) and acoustic pulses in the form of *N*-waves (§5.2) is considered. Numerical results are obtained for the peak and average characteristics and statistical distributions of acoustic wave parameters. The influence of nonlinear and diffraction effects on

the formation of the acoustic field structure and formation of the random caustics is investigated. Randomly inhomogeneous velocity fields with both Gaussian and modified von Karman energy spectrum are considered. The effects of the turbulent field intensity and characteristic length scales, as well as the effect of the transverse component of the medium velocity on the acoustic field is studied. Finally, in §5.3, experimentally obtained data are compared to the results of simulations under the conditions of the laboratory scale experiment.

.

## Chapter 1

# NONLINEAR SOUND WAVES IN INHOMOGENEOUS MOVING MEDIA (REVIEW)

### § 1.1 Sonic boom in turbulent atmosphere

#### *1.1.1 Ecological aspects of the problem*

In 2003 when the Concorde flights were cancelled the interest of the acoustical community to the problem of sonic boom propagation in turbulent atmosphere was significantly diminished. However, nowadays, following the development of the small civil supersonic jets of new generation, the investigations in this area arose with the new force. The problem itself is due to the fact, that during the supersonic flight of the airplane, intense acoustics waves are generated by different parts of the fuselage. The resulting shape of that disturbance has a complex structure with multiple high amplitude fronts that, due to the strong nonlinear phenomenon, coalesce during propagation to a single shock front. The waveform thus is finally transformed into a classical *N*-wave [47,48]. Propagating further to the ground surface through the turbulent atmosphere, the *N*-wave continues to be distorted by numerous physical effects. This distortion is determined by the combined influence of nonlinear effects, diffraction, and scattering of the wave on the atmosphere inhomogeneities, and dissipative processes: thermoviscous absorption and relaxation phenomena [11, 49- 51]. That is why during supersonic flight tests, various waveforms with distorted shapes which are far from the classical *N*-wave are observed [52 - 55]. For example, in the areas of focusing, which are also often named caustics, the waveform transforms to the classical *U*-wave with a peak positive pressure, which can be several times higher than the amplitude of the wave, propagating in the turbulence-free medium. The *N*-wave amplitude near the ground surface can vary from 10 Pa to 300 Pa (up to 145 dB, ref  $2 \cdot 10^{-5}$  Pa) depending on the speed of the airplane, its aerodynamic shape, the altitude of the

flight, and the atmospheric conditions [55]. However, sometimes at the distance of several hundreds meters from the airplane the pressure amplitude of the acoustic wave can reach 750 – 800 Pa (up to 152 dB) [53, 54]. The pain barrier of the human ear is about 100 – 200 Pa or 130-140 dB depending on the sound frequency. It is obvious that levels of acoustic pressure in the  $N$ -wave may exceed the pain barrier. Negative influence of sonic booms on the human health is amplified due to the narrow width of the shock front, i.e. small rise time of the  $N$ -wave. The rise time of the shock front is determined as the time needed for the pressure to increase from 10% level to 90% level of the shock amplitude. The rise time can strongly vary depending on the flight conditions. The typical values are 0.5 – 10 ms. The duration of the sonic boom pulse is usually about 90 – 300 ms and depends mainly on the airplane length. As it was shown in experiments with human participation, the subjective loudness and annoyance intensity level increases with the decrease of the rise time [56-58]. For example, when the  $N$ -wave amplitude is equal to 50 Pa, the decrease of the rise time from 4 ms to 1 ms leads to the twofold increase in subjective loudness; if the sonic boom amplitude is 115 Pa, the same decrease in rise time result in 1.3 times decrease in subjective loudness [58]. The low frequencies of the sonic boom noise are also of great importance. They lead to the vibration of window glasses and furniture inside buildings, and affect the general level of perception of the sonic boom. In the Table 1.1 are shown the characteristic values of the sonic boom peak pressure and the possible influence of this wave on the environment and human being [59]. Thus, to clarify the possibility of the supersonic flights above the ground populated areas it is necessary to investigate possible pressure levels in the field of the acoustic shock wave, the rise time of the shock front, and the spatial structure of the acoustic field. This information can be further used in the aero dynamical design of the airplane fuselage to diminish the intensity of the generated by the airplane shock wave [60, 61].

**Table 1.1** Shock noise phenomena [59].

$p$ , Pa	$p$ , dB	Resulting physiological reaction	Associated physical phenomena
5 - 15	108-118	Not objectionable	Barely audible explosion
15 - 50	118-128	Tolerable	Distant explosion or thunder
50 - 150	128-138	Objectionable	Close-range thunder, some window damage
200	140	Ear pain barrier	
200 - 500	140-148		Damage to large plate glass windows
500 – 1500	158-158		Definitive damage to small barracks-type windows

### 1.1.2 Outdoor and laboratory experiments

Supersonic flights of aircrafts through the atmosphere create shock waves called “sonic booms”. At a sufficient distance from the plane, this waveform is an  $N$ -wave. Nevertheless, sonic boom measurements show that waveforms measured at low altitude are randomly distorted and differ from the ideal  $N$ -wave shape (see the measurements of Lee and Downing [54]). The variability of waveforms is a consequence of temperature and velocity random inhomogeneities due to the atmospheric turbulence near the ground [10]. Some authors compared theoretical predictions of sonic boom distortion to sonic booms recordings, but such analysis is limited because the parameters of turbulence cannot be measured enough accurately to allow detailed quantitative comparisons. Consequently, experimental investigation of sonic boom propagation in real atmosphere is very difficult due to impossibility to have a full description of the atmospheric conditions during the flight of a supersonic airplane, and due to the high cost of these field experiments.

From this point of view, laboratory-scale experiments are a very good alternative to the field experiments. Lipkens *et al.* [7, 40-42], Ollivier *et al.* [44] showed that laboratory-scale experiments using  $N$ -waves produced by electrical sparks and downscaled turbulent medium offer an attractive alternative to field measurements since both the acoustic source and the turbulence can be controlled. The experiments of Lipkens are based on the propagation of spark produced  $N$ -waves through kinematic turbulence produced by a plane jet of variable speed and variable width, between 0.05 m and 0.3 m. Propagation of both plane and spherical waves was studied. In order to outline more specifically the effect of occurrence of random caustics, Ollivier *et al.* [44] investigated longer propagation distances than Lipkens and two types of inhomogeneities: temperature and velocity fluctuations. A plane free jet was used to generate a field of velocity random fluctuations, and a heated grid was used to generate a field of random fluctuations of temperature. In the case of thermal turbulence, the random variable is scalar, while in the case of kinematic turbulence it is vectorial. This difference induces different probability distributions for the occurrence of caustics. The thermal turbulence set-up was used mainly to investigate long-range propagation (0.6 m to 4.4 m) for a fixed level of turbulence. The kinematic turbulence set-up was used to investigate the effect of turbulence intensity. Note that these experiments [44] were limited to the spherically divergent waves.

The characteristic spatial and temporal scales of the real atmosphere sonic boom problem and those of the laboratory scale experiments from the series of publications [7, 40-42, 44] are compared in the table 1.2.

**Table 1.2** Comparison of spatial and temporal parameters of the sonic boom problem in real atmosphere [52] and in laboratory-scale experiments [40, 44]

	Atmosphere	Laboratory
Distance of propagation through turbulence	1-2 km	0.05 – 4.4 m
Turbulence outer scale	100-200 m	0.01-0.12 m
Turbulence inner scale	0.01 – 0.1 m	0.01 – 0.1 mm
Acoustic pulse length	30 – 100 m	3.5- 15 mm
Peak positive pressure level $p_{\max}$	10-800 Pa	100-600 Pa
Duration of the $N$ -wave	90-300 ms	10-45 $\mu\text{s}$
Rise time	0.5-10 ms	0.4 – 10 $\mu\text{s}$

We note that the scaling factor for the duration of the wave, the outer scale of turbulence, and the propagation distance in the laboratory and outdoor experiments is of the order of 1/10000, while for the rise time of the wave it is approximately 1/1000. As thermoviscous dissipation increases significantly with frequency (i.e. decreases with the wavelength), the dissipation parameter is not scaled properly in model experiments in air. For example, the plane wave attenuation coefficient at 50 Hz is of the order of  $10^{-5}$  and  $10^{-1}$  at 50 kHz [62]. Main contribution to the energy spectrum of the sonic booms are at the frequencies lower than 10 Hz. In the laboratory scale experiment, the duration of the  $N$ -wave is around 30  $\mu\text{s}$  and main contribution to the energy spectrum is in the interval 5 kHz – 50 kHz. One consequence is that the overpressure cannot be scaled with the same factor as the turbulence lengths since the pressure in the laboratory experiments then must be too high to get the same nonlinear effects. Another consequence of the increase of thermoviscous dissipation with the frequency is that the shock rise time in the model experiments for a homogeneous atmosphere is mostly governed by the thermoviscous dissipation, while in the case of a sonic boom the dominant mechanism is the molecular relaxation. In fact, for sonic booms the rise time is mainly determined by relaxation effects [63], as soon as the relaxation times of  $O_2$  and  $N_2$  molecules are much shorter than the duration of the pulse. For example, in the air with 34% humidity and 20° C temperature relaxation times are equal to 236  $\mu\text{s}$  and 21 ms respectively for  $O_2$  and  $N_2$  molecules.

In model experiments [7, 40-42,44], the distorted waveforms of the same shape as for the sonic booms in atmosphere were observed. It was shown that turbulence leads to decrease of the mean peak positive pressure (15-20% depending on the turbulence intensity and propagation distance), to significant widening of the mean rise time (2-3 times), and to significant dispersion of these parameters (the standard deviation of the rise time is comparable with its mean value). In [44, 64] the authors show that sound reinforcement can be attributed to the propagation through random caustics. Their experiments also outline the occurrence of multi-peaked waveforms, which are caused by multiple paths, and summation of waves with slightly different

arrival times after propagation through caustics. These multi-peaked waveforms can have much longer rise times than the mean rise time. These observations are consistent both with the analysis of Pierce [65] who claims that long rise times are due to the summation of folded wave fronts, and with the numerical simulations of Blanc-Benon *et al.* [31].

In addition to the experimental investigation of spherically divergent wave propagation in turbulent medium, there was also an effort to generate a plane shock acoustic wave. In this purpose, the spark source was placed in the focus of the parabolic reflector [Lipkens *et al.*, 7, 40-42]. It was supposed that such experiment would allow more accurate comparison of the experimental data with the results of numerical modelling, which were mainly obtained in 2D geometry due to high time consumption of the full 3D computation. However, the measurements showed that the wave remains plane in still air at the distances from the source (about 40 cm), shorter than the distance where random caustics formed behind the outer scale random inhomogeneities in case of the presence of the turbulent flow. This distance therefore was not sufficient for accurate investigation of nonlinear-diffraction effects and the effects of inhomogeneous media in the case of the presence of caustics.

Laboratory scale experiments on focusing of high amplitude acoustic signal due to a single inhomogeneity are also presented in the paper by Thomas *et al.* [66]. The scaled propagation of the periodic acoustic wave through the inhomogeneous liquid medium was studied. To model a regular scalar inhomogeneity the cylinders made of materials with different densities were placed into the liquid. It was shown experimentally that the presence of inhomogeneities in the propagation medium leads to the formation of focusing areas and, in average, to the widening of the shock front.

Propagation of intense acoustic waves in the inhomogeneous atmospheric boundary layer was also in the field experiments [67-71]. Explosive sources of different type have been used to generate an acoustic wave. In these papers various effects were studied: the effects of nonlinear propagation [67], and effects of scattering of low frequency sound pulses on atmosphere inhomogeneities [70]. The experimental data obtained for the arrivals of acoustic pulses at different microphones have been further used to check the validity of some mathematical models of sound wave propagation at long distances [71]. Some statistical parameters of atmospheric inhomogeneities have been also obtained from the experimental data (velocity of horizontal wind fluctuation and its scale) [69].

## § 1.2 Mathematical models for nonlinear sound waves propagating in inhomogeneous moving media

### 1.2.1 Wave equations in acoustics of inhomogeneous moving media

The rigorous way to derive the equations of acoustics of moving inhomogeneous media is to begin with the hydrodynamic system of equations. For the moving inhomogeneous medium in the case of linear acoustic wave propagation, the system of equations of hydrodynamics can be rewritten in the following form [3, 4, 72]:

$$\frac{d\mathbf{w}}{dt} + (\mathbf{w} \cdot \nabla)\mathbf{u} + \rho^{-1}\nabla p = \mathbf{F} \quad (1.1)$$

$$\frac{1}{\rho c^2} \frac{dp}{dt} + \nabla \cdot \mathbf{w} = Q \quad (1.2)$$

where  $\mathbf{w}$  – is the vibrational velocity of medium particles,  $\mathbf{u}$  – the medium velocity,  $\rho = \sum \rho_i$  – total density of the medium,  $p$  – the acoustic pressure,  $c$  – the sound speed,  $\mathbf{F}$  – the external forces affecting the medium,  $Q$  – the sound sources,  $d/dt = \partial/\partial t + \mathbf{u} \cdot \nabla$ .

This system of equations describes the propagation of linear acoustic wave in moving medium with velocity  $\mathbf{u}$ , under the following assumptions. First, it is assumed that the gravitational acceleration  $\mathbf{g} = 0$ . Second, the terms of the order and smaller than  $\varepsilon^2 = \max(u^2/c^2, \Omega \cdot u/\omega c)$  are neglected, where  $\Omega$  – is the characteristic frequency of variations of the medium properties (movement)  $\partial u/\partial t \sim \Omega \cdot u$  and  $\omega$  – is the characteristic frequency of the acoustic wave. Third, it is assumed that the medium velocity field  $\mathbf{u}$  is solenoidal, i.e.  $\nabla \cdot \mathbf{u} = 0$ , and therefore, from the continuity equation, it follows that the considered medium is incompressible:  $d\rho/dt = 0$ .

Following the transformations made by Ostashev *et al.* [4] and one more time neglecting the terms of the order or smaller than  $\varepsilon^2$  ( $\varepsilon \ll 1$ ), the system of equations (1.1) and (1.2) can be rewritten in the form of a stand alone equation for the acoustic pressure in inhomogeneous moving medium:

$$\frac{d}{dt} \frac{\partial}{\partial t} \left( \frac{1}{\rho c^2} \frac{dp}{dt} \right) - \nabla \cdot \frac{\partial}{\partial t} \left( \frac{\nabla p}{\rho} \right) + 2 \frac{\partial u_i}{\partial x_j} \frac{\partial}{\partial x_i} \left( \frac{1}{\rho} \frac{\partial p}{\partial x_j} \right) = \frac{d}{dt} \frac{\partial Q}{\partial t} - \nabla \cdot \frac{\partial \mathbf{F}}{\partial t} + 2 \frac{\partial u_i}{\partial x_j} \frac{\partial F_j}{\partial x_i} \quad (1.3)$$

Neglected terms are usually very small in the ocean acoustics as soon as  $u/c \sim 10^{-3} - 10^{-4}$ . These terms are also neglected when the effects of medium velocity fluctuations on acoustic wave

propagation in turbulent atmosphere are studied. The small parameter in atmosphere is usually about  $u/c \sim 3 \cdot 10^{-2}$  [Ostashev *et al.*, 4] for outdoors sound propagation.

From the other side, the system of equations (1.1) and (1.2) is used for precise description of the propagation of low amplitude sound waves in uniformly moving medium, when spatial derivatives of the medium motion are equal to zero,  $\partial u_i / \partial x_j = 0$  [Ostashev *et al.*, 4]. Particularly for this type of the medium motion the system of equations (1.1, 1.2) accounts for all orders of smallness of the hydrodynamic Mach number  $M=u/c$  and it is possible to derive an exact wave equation:

$$\left(\frac{\partial}{\partial t} + \mathbf{u} \cdot \nabla\right)^2 p - c^2 \nabla^2 p = 0 \quad (1.4)$$

Note, that the first term in Eq. (1.4) contains the temporal derivative of  $\mathbf{u}$ , which should be neglected due to the uniformity of the described medium.

Moreover, it can be shown, that in acoustics of inhomogeneous moving media, Eq. (1.4) approximates the high frequency acoustic field [4]. The spatial derivatives of the parameters, characterized by the evolution of the acoustic field (acoustic pressure, vibrational velocity *etc.*), are proportional to  $1/\lambda$ , where  $\lambda$  is the acoustic wavelength, and the derivatives of medium parameters (for example, hydrostatic pressure, medium motion velocity *etc.*) are proportional to  $1/l$ , where  $l$  is the characteristic scale of inhomogeneity. Thus, the last derivatives can be neglected assuming that the acoustic wavelength is much smaller than the scale of inhomogeneity  $\lambda \ll l$ . With this approximation, the Eq. (1.4) can be easily derived directly from the linearized system of the hydrodynamics equations. Note, that the Eq. (1.4) also follows from the Eq. (1.3) if it is assumed that there are no external forces and acoustic sources in the uniformly moving homogeneous medium.

A simplified equation was derived in [4] for the stratified moving medium. It is assumed that the vertical component of medium velocity is equal to zero, i.e. the velocity is given by the relation:  $\mathbf{u} = (\mathbf{u}_{\parallel}, 0)$ , where  $\mathbf{u}_{\parallel}$  is the horizontal component of the medium velocity, which depends on the vertical coordinate  $z$ . In this case, it is convenient to represent the acoustic pressure  $p$  and the vibrational velocity  $\mathbf{w}$  in terms of Fourier integrals, for example for the pressure :

$$p(\mathbf{r}, z, t) = \iint d\mathbf{k} \cdot d\omega \cdot \exp(i\mathbf{k}\mathbf{r} - i\omega \cdot t) \tilde{p}(\mathbf{k}, z, \omega) \quad (1.5)$$

Here  $\mathbf{r} = (x, y)$  is the horizontal radius vector,  $\mathbf{k}$  is the horizontal component of the wave vector,  $\omega$  is the acoustic wave frequency,  $\tilde{p}$  is the spectral density of the acoustic pressure field. From

the system of equations (1.1, 1.2), taking into account the representation (1.5), an equation for the spectral density of the acoustic pressure field  $\tilde{p}$  in stratified medium can be obtained:

$$\frac{\partial^2 \tilde{p}}{\partial z^2} + \left( \frac{2\mathbf{k} \cdot d\mathbf{u}_{\parallel} / dz}{\omega - \mathbf{k}\mathbf{u}_{\parallel}} - \frac{1}{\rho} \frac{d\rho}{dz} \right) \frac{\partial \tilde{p}}{\partial z} + \left( \frac{(\omega - \mathbf{k}\mathbf{u}_{\parallel})^2}{c^2} - k^2 \right) \tilde{p} = 0 \quad (1.6)$$

Equation (1.6) for the acoustic wave propagation in the stratified moving medium exactly follows from the linearized system of the hydrodynamics equations and therefore precisely describes the effects at all orders of the hydrodynamic Mach number  $M = u/c$ .

In 1986, O.A. Godin [28] derived a wave equation for the sound propagating in 3D inhomogeneous moving medium with slow currents:

$$\frac{\partial}{\partial t} \left( \frac{1}{\rho c^2} \frac{\partial^2 p}{\partial t^2} - \text{div} \frac{\nabla p}{\rho} \right) + \frac{2\mathbf{u}\nabla}{\rho c^2} \frac{\partial^2 p}{\partial t^2} + 2\text{div} \left[ \left( \frac{\nabla p \nabla}{\rho} \right) \mathbf{u} \right] = 0. \quad (1.7)$$

In fact, this equation does not contain the second order spatial derivatives of the medium velocity  $\mathbf{u}$  as soon as by use of the incompressibility equation the last term in (1.7) can be rewritten as  $2(\partial u_i / \partial x_j) \partial(\rho^{-1} \partial p / \partial x_j) / \partial x_i$ . In this form, the Eq. (1.7) coincides with the Eq. (1.3) written for the medium without external forces and acoustic sources.

Equation (1.7) was derived under the following assumptions: first, the derivation is done for the non layered medium in the absence of gravity waves  $g = 0$  m/s<sup>2</sup>; second, the flow is supposed to be incompressible and medium parameters do not change along the medium trajectories in undisturbed flow:  $\nabla \mathbf{u} = 0$ ,  $dp_0 / dt = 0$ ,  $d\rho / dt = 0$ ,  $dc / dt = 0$ ; third, the Eq. (1.7) contains only linear component in terms of hydrodynamic Mach number  $M = u/c$ .

Let us assume that the propagation medium is the ideal gas for which the equation of state is  $p_0 + p = RT(\rho + \rho')$ ,  $R = \text{const}$ . Medium deviations from the equilibrium state with  $p_0 = \text{const}$ ,  $T_0 = \text{const}$  are small and governed by the fluctuations of temperature  $T_1$ . Then for the monochromatic sound wave, retaining only linear on  $T_1$  terms in Eq. (1.7), the following equation can be derived [27]:

$$\Delta p + \frac{\omega^2}{c_0^2} p = - \frac{\partial}{\partial x_j} \left( \frac{T_1}{T_0} \frac{\partial p}{\partial x_j} \right) + \frac{2i}{\omega} \frac{\partial^2}{\partial x_j \partial x_k} \left( u_j \frac{\partial p}{\partial x_k} \right) \quad (1.8)$$

where  $c_0$  is the sound speed at the ambient temperature  $T = T_0$ .

Equation (1.8) coincides with the equation of A.S. Monin [2, 73] used in the theory of sound wave scattering by the atmospheric turbulence. The effects of sound scattering on atmosphere inhomogeneities have been also studied in the papers of Kraichnan [74], Lighthill

[75], Batchelor [76] and Neubert *et al.* [77] based on analysis of linearized system of hydrodynamics equations.

In atmospheric acoustics the equation of A.M. Obukhov [27] is also often used

$$\frac{d^2}{dt^2} \left( \frac{\partial \varphi}{\partial t} \right) = c^2 \Delta \left( \frac{\partial \varphi}{\partial t} \right) + \frac{\nabla p_0}{\rho} \nabla \frac{\partial \varphi}{\partial t} + c^2 \Delta \mathbf{u} \nabla \varphi = 0 \quad p = -\rho \frac{\partial \varphi}{\partial t} \quad (1.9)$$

This equation is valid for smooth inhomogeneities of sound speed and density of the medium ( $kl \gg 1$ ), and for small hydrodynamic Mach number under the condition of entropy conservation. In the case of ocean acoustics, the last assumption is not valid.

In recent papers, the concept of Rayleigh has been also widely used. This concept was introduced in view of the 2D problem investigation of sound refraction by the wind. According to this concept, the real moving medium is replaced by a still medium with the effective values of medium density and sound speed. For sound wave propagation in such a medium, the following wave equation was obtained [Godin *et al.*, 12]:

$$\nabla \frac{\nabla p}{\rho_e} + \frac{\omega^2}{\rho_e c_e^2} p = 0 \quad (1.10)$$

where  $\rho_e$  and  $c_e$  are the effective medium density and effective sound speed, respectively. Effective parameters of the medium in Eq. (1.10) are dependent on the direction of the sound wave propagation:

$$c_e = c + \mathbf{u} \cdot \mathbf{n}, \quad \rho_e = \rho c^2 / c_e^2 \quad (1.11)$$

where  $\mathbf{n}$  is the vector, which determines the direction of the wave propagation in each point of the wave front (it is assumed that  $\nabla p = ik\mathbf{n}p + O(\varepsilon + M)$ ,  $0 < \varepsilon \ll 1$ , i.e. the acoustic wave is a locally plane wave associated to the wave vector  $k\mathbf{n}$ ).

Equation (1.10) describes the propagation of the sound wave in moving medium if the following assumptions are valid:

$$\frac{(\mathbf{n} \cdot \nabla) \mathbf{n}}{k} = O(\varepsilon), \quad \frac{(\mathbf{n} \cdot \nabla) \mathbf{u}}{\omega} = O(\varepsilon M), \quad \frac{\mathbf{n} \cdot \nabla c}{\omega} = O(\varepsilon) \quad (1.12)$$

These assumptions have been derived based on comparison of the Eq. (1.10) with the Eq. (1.7) [12]. Therefore, the wave Eq. (1.10) describes the effects of medium motion on the acoustic wave propagation with the accuracy of the order of  $O(\varepsilon + M)$ . To solve equations of the type (1.10) the high frequency asymptotic methods are used [Babich *et al.*, 13].

In [Wochner *et al.*, 78] the propagation of nonlinear acoustic waves in air is modelled numerically using the system of hydrodynamics equations, which includes the continuity equation, Navier-Stokes equations, general equation of the heat transfer and Van-der-Waals equation of state to describe the relaxation processes of oxygen and nitrogen. With the numerical algorithm developed in [78], authors obtained a good accuracy (less than 1% error) in the benchmark comparison of the solution to the system of equations with the existing analytical solutions for nonlinear wave propagation, for example with the Fubini-Bessel's series [47]. The agreement between the numerical and analytical solutions for the thermoviscous absorption and dispersion caused by relaxation effects are also shown with the same accuracy (1%) [Pierce *et al.*, 63]. However, such approach is not convenient due to the high computational costs of numerical modelling.

Theoretical approaches, accounting for the statistical properties of the turbulent medium have been also developed. For example, in [Pierce, 79] a dispersion relation was derived, and then on its basis the wave equation for sound wave propagation in the turbulent atmosphere with the scale of inhomogeneities smaller than acoustic wavelength was built. The derived equation accounts for the medium velocity fluctuations in the direction of the acoustic wave propagation and also for the statistical properties of randomly inhomogeneous turbulent medium. In case of linear sound wave propagation in the media without dissipation the derived equation takes the form of the Korteweg-de-Vries equation, in which the third spatial derivative of the field describes the effect of small-scale inhomogeneities on the acoustic wave propagation in turbulent media.

Nonlinear propagation of one dimensional random waves, but in regular medium, was studied in details [80, 81]. Statistics of waves was considered based on the Burgers equation introducing random initial conditions in the form of the wideband noise [Gurbatov, 80]. Nonlinear transformation of waveforms and spectrum of random signals was investigated. Statistics of nonlinear waves reflected from stratified randomly inhomogeneous media is also of interest. In particular, based on the analysis of Eq. (1.4) in Born approximation, the optimal duration of acoustic broadband signal for sounding of ocean microstructure was obtained.

### 1.2.2 *Parabolic approximation for nonlinear sound waves in media with scalar inhomogeneities*

Despite of the existence of various different types of wave equations for sound propagation in inhomogeneous moving medium, derivation of the quantitative results is very difficult. Solving these equations analytically is impossible in most of cases. As for the

numerical modelling, existing algorithms require huge memory capacities, that leads to the long calculation time and makes these numerical full wave equations solvers not effective for our problem. For this reason, it becomes more interesting to consider the application of evolution equations obtained in the parabolic approximation of diffraction theory. These equations are simpler for numerical analysis, and at the same time account for maximal possible variety of different physical effects, related to the sound propagation in inhomogeneous moving medium. Due to the numerical efficiency and to sufficient precision in description of the diffraction effects, the parabolic approximation has been successfully used in modelling of acoustic fields in inhomogeneous media. In particular, it is widely employed in ocean and atmospheric acoustics.

The classical evolution equation in nonlinear acoustics is the following equation of Khokhlov-Zabolotskaya-Kuznetsov type [Pelinovsky *et al.*, 30]:

$$\frac{\partial}{\partial \tau} \left[ \frac{\partial p}{\partial x} - \frac{\beta}{\rho c^3} p \frac{\partial p}{\partial \tau} - \frac{b}{2c^3 \rho} \frac{\partial^2 p}{\partial \tau^2} - p \frac{\partial}{\partial x} \ln(\sqrt{\rho c}) + \frac{1}{2c} (n^2 - 1) \frac{\partial p}{\partial \tau} \right] = \frac{c}{2} \Delta_{\perp} p \quad (1.13)$$

Equation (1.13) describes diffraction of nonlinear sound beams in smoothly inhomogeneous medium. Here  $p$  is the acoustic pressure,  $c(x, r_{\perp})$  and  $\rho(x, r_{\perp})$  are the sound speed and density of the medium respectively,  $x$  is the longitudinal coordinate and  $r_{\perp}$  is the transverse coordinate,  $\beta$  is the nonlinearity and  $b$  is the thermoviscous absorption coefficients,  $\tau = t - x/c$  is the retarded time,  $n$  is the refraction index of the medium. When refraction distorts acoustic rays in inhomogeneous medium, the distance  $x$  is counted along the central ray (beam axis).

Nonlinear evolution Eq. (1.13) describes the combined effect of different physical phenomena like nonlinearity (second term on left hand side of equation), thermoviscous absorption (third term on the left hand side), diffraction (right hand side), and accounts for the influence of scalar inhomogeneities on the sound wave propagation in smoothly inhomogeneous medium (fourth and fifth terms on the left hand side). Equation (1.13) appears to be sufficiently effective in terms of numerical modelling. However, when using the parabolic approximation it is necessary to have in mind that it is valid only for small angles of diffraction.

Equation (1.13) has no analytical solutions. However, in some particular cases it can be simplified to take the form of parabolic equation for homogeneous media. For example, in the problem of random sound speed inhomogeneities influence on parametric generation of low frequency radiation, Gurbatov came to the homogeneous problem [80]. In this purpose he rewrote the initial equation of type (1.13) in the local coordinates system related with the acoustic ray. Based on these equations he found the directional diagrams and on-axis intensity distributions for parametric array.

Parabolic equation of the KZK type (1.13) accounts for scalar inhomogeneities and inhomogeneities, which can be reduced to scalar ones (local fluctuations of sound speed due to the medium motion in the direction of the wave propagation). However, as it was already mentioned in the introduction, taking into account the vector inhomogeneities, in particular of their transverse components is of great interest for atmospheric acoustics. Consider now the KZK-type evolution equation, which accounts for the motion of the medium. For example, in [Godin, 28] starting from the Eq. (1.7), a 2D linear parabolic equation for sound propagating in ocean with slow currents was derived in cylindrical coordinates for a fixed angle  $\varphi$ :

$$2ik_0 \frac{\partial}{\partial r} B + \frac{\partial^2}{\partial z^2} B + (k^2 - k_0^2) B - [ik_0 B \frac{\partial}{\partial r} (\ln \rho) + \frac{\partial}{\partial r} (\ln \rho) \cdot \frac{\partial}{\partial z} B] - 2k^2 k_0 u_r / \omega \cdot B + 2k_0 \left( \frac{\partial}{\partial z} u_r / \omega \right) \frac{\partial}{\partial z} B = 0 \quad (1.14)$$

where  $k_0 = \text{const}$ ,  $k = \omega/c$ ,  $r^2 = x^2 + y^2$ ,  $u_r$  is the projection of  $\mathbf{u}$  on the direction of wave propagation. The quantity  $B = p\sqrt{r} \exp(-ik_0 r)$  is assumed to be a slow varying function of  $r$ :  $|B_r| = k_0 |B|$ . To obtain Eq. (1.14), in addition to the usual approximations introduced in the derivation of the parabolic equation, the author also neglected the terms of the order of  $M^2$  and ignored the horizontal refraction. Note, that for the motionless medium, Eq. (1.14) takes the form of the classical linearized parabolic KZK type Eq. (1.13). The only remained difference is due to the retaining of different orders of smallness of medium scalar inhomogeneities (variations of sound speed are not taken into account in Eq. (1.14), but the second term in square brackets is not neglected).

Now let us consider that the sound source is centred near the point  $(0,0,z_0)$  and that we are investigating the acoustic field at the distances from the source that are long in comparison with the acoustic wavelength. For this particular problem in [Godin, 27] starting from the wave equation analogous to Eq. (1.3), and assuming that  $(k_0 r)^{-1}$  is a small parameter, a more precise (terms of order higher than  $O(M)$  are retained) than (1.14) linear parabolic equation was derived:

$$2ik_0 \frac{\partial}{\partial r} B + (k^2 \beta^2 - k_0^2 - ik_0 \frac{\partial}{\partial r} (\beta^2 \ln \rho)) B - \frac{\partial}{\partial z} B \cdot \frac{\partial}{\partial z} (\beta^2 \ln \rho) - \frac{i u_\varphi}{\omega \beta} (k_0^2 - 3k^2 \beta^2) r^{-1} \frac{\partial}{\partial \varphi} B + r^{-2} \frac{\partial^2}{\partial \varphi^2} B + \frac{\partial^2}{\partial z^2} B = 0 \quad (1.15)$$

Here  $\tan \varphi = y/x$ ,  $\beta = 1 - k_0 u_r / \omega$  are the local Doppler factor,  $u_\varphi$  and  $u_r$  are the components of  $\mathbf{u}$  in a cylindrical coordinates system. The component of the velocity field in transverse direction  $u_z$  is small due to the continuity equation and, therefore, it was not included into the Eq. (1.15). The

terms of smallness order higher than  $(k_0 r)^{-1}$  were also neglected. Thus, all neglected terms can be assessed with  $O\left(\left(u_\varphi/c\right)^3 + \left(u_\varphi/c\right)\varepsilon + \varepsilon^2\right)$ , where  $\varepsilon$  is the small angle parameter,  $m = u_\varphi/c \leq M = u_r/c$ .

If in Eq. (1.15) the terms containing  $\varphi$  derivatives are neglected, and if  $Ox$  axis is pointed from the source to receiver, then the parabolic equation will be transformed into a 2.5D equation: for each azimuthal direction, the 2D parabolic equation should be solved. If the terms of the order of  $O(M^2)$  are neglected this equation coincides with the Eq. (1.14).

Starting from the same Eq. (1.3) V.E Ostashev [4] derived a linear parabolic equation for the complex amplitude  $C$ :  $p = C \exp(ik_0 r)$   $k_0 = \omega/c_0$

$$2ik_0 \frac{\partial C}{\partial x} + \Delta_\perp C + k_0^2 \varepsilon_c C - 2k_0^2 \frac{u_x}{c_0} C + 2ik_0 \frac{\mathbf{u}_\perp \cdot \nabla_\perp C}{c_0} = 0 \quad (1.16)$$

where  $\varepsilon_c = c_0^2/c^2 - 1 = n^2 - 1$  is the parameter which characterizes variations in the speed of sound.

Parabolic Eq. (1.16) is valid for sound waves, propagating in inhomogeneous moving media, and is derived using the following assumptions: the backscattering from the medium inhomogeneities is neglected and:

$$\theta \ll 1, \quad (k_0 l)^{-1} \ll 1, \quad (\theta_m > (k_0 l)^{-1}) \quad |\varepsilon_c| \ll 1, \quad M \ll 1, \quad x \ll k_0^3 l^4 \quad (1.17)$$

where  $\theta$  is the angle of acoustic ray deviation from the  $x$  axis,  $l$  is the characteristic scale of inhomogeneity,  $M = u/c_0$ .

The first inequality tells about small angle approximation of the parabolic equation, i.e. it is valid only for small angles of deviation of acoustic rays from the axis. Second inequality limits the size of inhomogeneities for which (1.16) is valid; the scale of inhomogeneity should be sufficiently large in comparison with the wavelength. Next inequality is always correct for the parabolic approximation (due to multiple scattering). Fourth and fifth assumptions limit the variation of sound speed in the medium and therefore the medium velocity. Sixth assumption was used to approximate the Green's function by the Fresnel's function  $G_{Fr} = -\exp\left[ik_0\left(|x| + r^2/2|x|\right)/(4\pi|x|)\right]$ . For  $\mathbf{u} = 0$ , Eq. (1.16) takes the form of the well-known parabolic equation for the acoustic wave propagating in motionless medium [47, 48]. It is also worth to note, that vector inhomogeneities, acting only in the direction of acoustic wave propagation are mathematically described in the parabolic equation with the term similar to that, describing the contribution of scalar inhomogeneities in sound speed.

In spite of existence of a variety of well-developed theoretical models of sound wave propagation in inhomogeneous moving media, their analytical solutions have been not yet found and numerical modelling is still very difficult to realize. First results of numerical modelling for the parabolic equation have been only recently obtained for simplified models. For example in [Blanc-Benon *et al.*, 31] numerical modelling of sound propagation in the field of scalar inhomogeneities has been done using the modified evolution equation of the KZK type. The term accounting for the effects of scalar inhomogeneous field, like medium temperature or density fluctuations, was introduced into the KZK equation. The inhomogeneity itself is included into the local sound speed  $c(x,y)$ , for example, using well-known expression for gas between sound speed and medium temperature. Thus,  $c(x,y)=c_0+ c'(x,y)$ .

$$\frac{\partial p}{\partial x} = \frac{c_0}{2} \int_{-\infty}^{\tau} \nabla_{\perp}^2 p d\tau + \frac{b}{2\rho_0 c_0^3} \frac{\partial^2 p}{\partial \tau^2} + \frac{\beta p}{\rho_0 c_0^3} \frac{\partial p}{\partial \tau} + \frac{c'}{c_0^2} \frac{\partial p}{\partial \tau} \quad (1.18)$$

where  $\beta$  and  $b$  are the coefficients of nonlinearity and absorption respectively,  $\tau$  is the retarded time.

The first term on the right hand side of the Eq. (1.18) accounts for the effects of diffraction, the second term accounts for the thermoviscous absorption, and the third term accounts for the nonlinear effects. The fourth term on the right hand side is implemented to account for the effects of scalar inhomogeneities. Note that for numerical modelling the 2D formulation of the equation was used.

Numerical results were also obtained for wide-angle linear parabolic equations. A number of papers is devoted to the investigations of sound wave propagation through scalar and vector inhomogeneities [23-26, 29]. A typical wide-angle parabolic equation written for complex amplitude  $C$  ( $p = C \exp(ik_0 r)$ ,  $k_0 = \omega/c_0$ ) takes the following form [Dallois *et al.*, 24]:

$$\left[ 1 + \frac{1}{4} \left( -\frac{u_x}{c_0} + \frac{1}{k_0^2} \frac{\partial}{\partial z^2} \right) \right] \frac{\partial C}{\partial x} = \frac{ik_0}{2} \left( -\frac{u_x}{c_0} + \frac{1}{k_0^2} \frac{\partial}{\partial z^2} \right) C \quad (1.19)$$

The acoustic wave propagates here along  $x$  axis,  $u_x$  is the projection of the medium velocity on the direction of the wave propagation. This equation is valid up to the angles of refraction equal to  $80^\circ$  from the axis. If one neglects the second term in square brackets in Eq. (1.19), it will take the form of the parabolic Eq. (1.16) for the homogeneous moving medium with longitudinal flows,  $\mathbf{u}_{\perp} = 0$ .

In addition to the typical wide-angle parabolic equation the linear WAPE were derived for sound wave propagation in homogeneous media with currents or flows and in

inhomogeneous moving media without flows [23, 24, 29]. First type of WAPE equations is used to investigate the effect of wind in all directions on the propagation of sound waves in atmosphere. The second one is used for the investigation of the effects of inhomogeneous atmospheric turbulence on the sound wave propagation. A linear wide-angle parabolic equation for sound in inhomogeneous moving media was also derived in [Godin, 26]. In this work, the variety of linear WAPE wave equations was considered. Equations of this type are more accurate than the “usual small angle” parabolic equation and provide the accomplishment of the energy conservation law and theorem of flow reversal in parabolic approximation. However, these equations are linear and do not allow investigating the evolution of nonlinear-diffraction acoustic fields.

### 1.2.3 Equations of nonlinear geometrical acoustics

As we already mentioned, it is very difficult to find the solutions to the previously referred wave equations and simpler parabolic equations even using numerical methods: only recently, due to the development of new powerful computing systems, it became possible to find numerical solutions in acceptable computational time. That is why in previous studies [16-22] the propagation of sound waves through different type inhomogeneities (scalar and vector ones) were considered in the high frequency approximation of geometrical acoustics. These studies were mainly devoted to the development of analytical solutions in the case of stratified inhomogeneous media. The main advantage of the geometrical acoustics approach is that the obtained results are relatively simple and easy to interpret visually, and their physical interpretation is clear. The main disadvantage is that it does not account for the diffraction effects.

In [Rudenko *et al.*, 16] the equations of nonlinear geometrical acoustics in inhomogeneous media were derived starting from the classical evolution parabolic Eq. (1.13) of KZK type for the inhomogeneous medium. With the following change of variables  $\theta = \tau - \psi(x, \mathbf{r})/c$ , where function  $\psi(x, \mathbf{r})$  is the eikonal, and in the limit of short wavelength, a system of equations in the approximation of geometrical acoustics was derived:

$$\frac{\partial \psi}{\partial x} + \frac{1}{2}(\nabla_{\perp} \psi)^2 + \frac{1}{2}(n^2 - 1) = 0 \quad (1.20)$$

$$\frac{\partial p}{\partial x} - \frac{\beta}{\rho c^3} p \frac{\partial p}{\partial \theta} - \frac{b}{2c^3 \rho} \frac{\partial^2 p}{\partial \theta^2} - p \frac{\partial}{\partial x} \ln(\sqrt{\rho c}) + \nabla_{\perp} \psi \cdot \Delta_{\perp} p + \frac{1}{2} \nabla_{\perp} \psi \cdot p = 0 \quad (1.21)$$

Equation (1.20) describes the eikonal spatial evolution, i.e. the bending of acoustic rays in the medium with scalar inhomogeneities. Equation (1.21) appears to be a generalized Burgers equation and describes the distortion of the waveform. In comparison with the classical Burgers equation, it contains three additional terms: the first one is proportional to  $p$  and is responsible for waveform evolution due to changes in medium impedance, the two other terms describe the waveform behaviour according to the distortion of the wave front and narrowing or widening of the ray tube. Note that the system of equations (1.20, 1.21) was obtained in the limit of short waves that means that the wave amplitude, components of the wave vector, and medium index of refraction vary slowly at distances, comparable to the wavelength. Such wave appears to be locally plane.

It turns out, that Eq. (1.21) can be simplified by eliminating the  $\theta$  variable using the representation of plane waves for the acoustic pressure  $p$ . It is straightforward to do the transformation in the very important case of sawtooth wave propagation. For this type of waves, the function  $C(x, \mathbf{r})$  is no more the complex amplitude of the pressure, but the peak pressure value in the sawtooth waveform. Following this approach the modified transport equation, comprehensively accounting for nonlinear effects, was derived as:

$$\frac{\partial C}{\partial x} + \frac{\beta \omega}{\pi \rho c^3} C^2 - C \frac{\partial}{\partial x} \ln(\sqrt{\rho c}) + \nabla_{\perp} \psi \cdot \Delta_{\perp} C + \frac{1}{2} \nabla_{\perp} \psi \cdot C = 0 \quad (1.22)$$

However, the rigorous way to derive the equations of geometrical acoustics is to start with the full wave equation. For example, in [Rudenko *et al.*, 22] as the starting equation the nonlinear wave equation for acoustic pressure  $p$  was used:

$$\Delta p - \frac{1}{c^2} \frac{\partial^2 p}{\partial t^2} = \nabla \ln \rho \cdot \nabla p - \frac{\beta}{c^4 \rho} \frac{\partial^2 p^2}{\partial t^2} \quad (1.23)$$

As it was already denoted, here  $c(\mathbf{r}), \rho(\mathbf{r}), \beta(\mathbf{r})$  are the sound speed, the density of the medium and nonlinearity coefficient at an arbitrary spatial point  $K$ . At a fixed point of space  $K_0$  these parameters have the following values  $c_0, \rho_0, \beta_0$ . The solution is represented in the form  $p = p(\tau = t - \psi(\mathbf{r})/c_0, \mathbf{r})$ . After substituting this formulation of the pressure  $p$  in (1.23), and after transformations it is possible to derive a system of geometrical acoustics equations for sound propagation in media with inhomogeneous sound speed and density fields:

$$(\nabla \psi)^2 = \frac{c_0^2}{c^2} = n^2 \quad (1.24)$$

$$\nabla \psi \cdot \nabla p + \frac{1}{2} p \Delta \psi - \frac{1}{2} p \nabla \ln \rho \cdot \nabla \psi - \frac{\beta n}{c^3 \rho} p \frac{\partial p}{\partial \tau} = 0 \quad (1.25)$$

During the derivation of Eqs. (1.24) and (1.25) the high frequency approximation and approximations of nonlinear acoustics were used. According to the high frequency approximation, the derivative  $\partial/\partial\tau$  is proportional to the large number  $\varepsilon^{-1}$  ( $\varepsilon \ll 1$ ). Moreover if we assume that  $\varepsilon$  and  $M$  are of the same order of smallness  $\varepsilon \sim M$ , then the equations (1.24) and (1.25) follow from the Eq. (1.23) after the division on terms of the same order of smallness. According to the nonlinear acoustics, the acoustic Mach number is assumed to be a small parameter  $M = p / \rho c^2 \ll 1$ . Note also, that the eikonal Eq. (1.24) coincides with the eikonal equation for linear acoustics [Vinogradova *et al.*, 47].

Solving geometrical acoustics equations leads to certain difficulties, due to the *a priori* determination of the eikonal  $\psi$ . Description, based on the Eq. (1.24) permits intersection of the acoustic rays, and therefore the eikonal function is determined ambiguously in these points. Thus, the approach (1.24, 1.25) still allows solving the problem of sound wave propagation with arbitrary angle of ray divergence, but due to the ambiguity, only up to the first intersection of rays.

Previous equations of nonlinear geometrical acoustics (1.24, 1.25) were derived for motionless medium. However, for more accurate description of sound wave propagation in the media like inhomogeneous moving atmosphere or fluctuating ocean it is also necessary to account for medium motion. In the recent work [Rudenko *et al.*, 21] starting from the system of hydrodynamics equations a system of geometrical acoustics equations for sound propagation in the field of stationary winds was derived. The equations of nonlinear geometrical acoustics for sound propagation in inhomogeneous moving media are then:

$$(\nabla \psi)^2 = n^2 \left(1 - \frac{\mathbf{u}}{c_0} \nabla \psi\right)^2 \quad (1.26)$$

$$2w_{gr} \nabla p + p \nabla w_{gr} - p w_{gr} \nabla \ln \left[ \frac{\rho c (1 - 2\mathbf{u}/c_0 \nabla \psi)}{|\nabla \psi|} \right] - \frac{2\beta |\nabla \psi|}{c_0 c \rho} p \frac{\partial p}{\partial \tau} = 0 \quad (1.27)$$

$$w_{gr} = \mathbf{u} + c \frac{\nabla \psi}{|\nabla \psi|} \quad (1.28)$$

Here  $w_{gr}$  is the vector of sound wave local group velocity. Equation (1.26) was derived by Blokhintsev in 1944 and has been then widely used for determining of rays trajectories in media with different type of inhomogeneities [3]. The transport Eq. (1.27) and eikonal Eq. (1.26) will

take the form of geometrical acoustics equations for motionless media (1.24, 1.25) if it is assumed that  $\mathbf{u}=0$ .

In spite of relative simplicity of geometrical acoustics equations it is very difficult to find their analytical solutions in the general case of moving inhomogeneous medium. Even in the case of stratified medium (this assumption sufficiently simplifies the equations) the solutions are found mainly for the eikonal equation [17, 20]. In recent work [Rudenko *et al.*, 20], the general solution of the transport equation has been also derived for the stratified medium. However, for more general case of sound wave propagation the numerical methods are necessary.

To account for the diffraction effects during propagation of acoustic waves in inhomogeneous moving media, a modified method based on the numerical solutions to the nonlinear geometrical acoustics equations up to the distances of caustics formation combined with the solution to the nonlinear diffraction evolution equation around caustics is developed in [82-85]. To estimate the diffraction effects on the cusp caustic [Kravtsov *et al.*, 15] the nonlinear Tricomi equation is solved [Coulouvrat, 84]. Diffraction effects around more complex fold caustics are described using nonlinear parabolic equation of the KZ type [Marchiano *et al.*, 85]. The solutions in different spatial areas are matched at a distance from the caustics where diffraction effects can be neglected. Such approach, in contrast to pure geometrical acoustics, allows predicting the value of the acoustic pressure in the caustic. However, it is convenient only for the description of nonlinear diffraction effects on single standing alone caustics. When the acoustic wave propagates in randomly inhomogeneous medium multiple caustics occurred along the ray paths, and that makes this approach not very efficient.

Another interesting approach is to calculate the diffraction pattern of the acoustic field in inhomogeneous turbulent medium along the ray trajectories [Coulouvrat *et al.*, 86]. For this purpose, the parabolic equation should be rewritten in the ray coordinates. This gives an opportunity to calculate the acoustic field with account for the diffraction effects along rays propagating at arbitrary angles to the initial direction of the wave propagation. However, finding the solution of such equation is quite difficult and appropriate numerical methods are not yet developed.

### § 1.3 Theoretical modelling of turbulent media

In the recent literature, we found several methods used to generate a random inhomogeneous velocity field in order to model the propagation of acoustic signals in turbulent atmosphere. If it is assumed that the atmospheric turbulent layer is sufficiently thin and it is only

a small fraction of the wave propagation distance then the model of infinitely thin phase screen is used [87 - 92]. If the width of the turbulent layer is comparable with the distance of the acoustic wave propagation then the model of continuous random medium is used [18, 19]. In this work, the second method is further described and implemented.

When the random velocity field is modelled, it is assumed that the propagation time of acoustic wave through turbulent layer is short in comparison with characteristic time scale of the evolution of the medium parameters, i.e. turbulent field is assumed to be “frozen” (it does not depend on time). The medium with vector inhomogeneities is further modelled as the set of  $J_{max}$  randomly oriented spatial Fourier modes [18, 93]:

$$\mathbf{u}(\mathbf{r}) = \sum_{j=1}^{J_{max}} \tilde{\mathbf{U}}(\mathbf{K}_j) \cos(\mathbf{K}_j \cdot \mathbf{r} + \phi_j) , \quad (1.29)$$

$$\tilde{\mathbf{U}}(\mathbf{K}_j) \cdot \mathbf{K}_j = 0 . \quad (1.30)$$

Here  $\mathbf{K}_j$  is the wave vector,  $\phi_j$  is the phase of  $j^{\text{th}}$  Fourier mode. The angle  $\theta_j$  between  $\mathbf{K}_j$  and  $x$  axis, and the phase values  $\phi_j$  for each mode are taken from the independent random number sequences with uniform distributions within the interval  $[0, 2\pi]$ . Equation (1.30) is the consequence of velocity field incompressibility. The velocity amplitude of each mode  $|\tilde{\mathbf{U}}(\mathbf{K}_j)|$  in Eq. (1.29) is determined by kinetic energy spectrum  $E(K)$  of considered type of medium turbulence:  $|\tilde{\mathbf{U}}(\mathbf{K}_j)| \sim \sqrt{E(K)}$ ,  $K = |\mathbf{K}|$ . In this work, two different formulations for the turbulence energy spectrum are considered. The first one is derived for a single-scale medium with a Gaussian longitudinal correlation function:  $f(r) = \exp(-r^2 / L^2)$ , and the second one is derived for a multiple-scales medium with the modified von Karman energy spectrum, which is closer to the spectrum of realistic turbulent atmosphere [94-96]. For 2D turbulence, the Gaussian energy spectrum takes the form:

$$E(K) = \frac{1}{8} u_{rms}^2 K^3 \cdot L^4 \exp\left(-\frac{K^2 \cdot L^2}{4}\right), \quad (1.31)$$

where  $u_{rms}^2$  is the medium velocity fluctuations variance,  $L$  is the characteristic scale of the inhomogeneity, which is connected to the longitudinal integral length scale  $L_f$  by the relation  $L = \sqrt{\pi} L_f / 2$ . In the other words, the energy of turbulent fluctuations is mainly concentrated in disturbances of scale  $L$ . This idealized energy spectrum is further used for generation of “simple” randomly inhomogeneous fields. Gaussian spectrum decreases rapidly at high wave numbers (Fig. 1.2h). In practice, the spectrum of real atmosphere has sufficiently wide inertial zone and

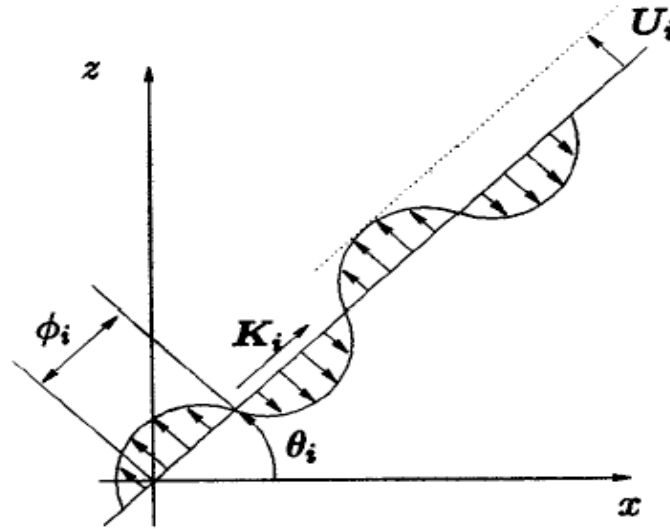


Fig. 1.1 Fourier modes orientation in space

such decrease is observed at much higher wave numbers. However, the results, obtained using Gaussian approximation of the real atmosphere spectrum, and the conclusions made will not be limited to the Gaussian formalism only.

Distribution of turbulent ripples energy in the interval from outer scale  $L_0$  and inner scale  $l_0$  is well described by a modified von Karman energy spectrum (Fig. 1.2h):

$$E(K) = 8u_{rms}^2 L_0^{-2/3} K^3 \left( K^2 + \frac{1}{L_0^2} \right)^{-14/6} \exp\left(-\frac{K^2}{K_m^2}\right), \quad (1.32)$$

where  $K_m = 5.92/l_0$ . The inertial zone, described by a modified von Karman spectrum appears to be in a very good agreement with the “five third” Kolmogorov’s law:  $E(K) \sim K^{-5/3}$

If a sufficiently high number of modes is considered in Eq. (1.29), and each of them is randomly chosen with uniform probability distribution of  $\theta_j$  and  $\phi_j$ , then the resulting velocity field  $\mathbf{u}(\mathbf{r})$  will be statistically homogeneous and isotropic and will have *a priori* defined energy spectrum [Karweit *et al.*, 19]. In this work random velocity field with Gaussian spectrum is modelled using 300 Fourier modes, uniformly distributed between  $0.01/L$  and  $9.0/L$ . In the case of the modified von Karman spectrum the medium velocity field is modelled with 600 Fourier modes (for a better discretization of the inertial zone), logarithmically distributed between  $K_{min}=0.1$  and  $K_{max}=35$ . The outer scale of the inhomogeneity  $L_0$  for the modified von Karman spectrum is chosen to be equal to the scale of the field with Gaussian energy spectrum  $L_0=L=4\lambda$ , where  $\lambda$  is the acoustic wave length in the medium of propagation. The inner scale  $l_0$  is equal to  $l_0=2.4\lambda$ . The root mean square value of velocity fluctuations for both spectra is equal to  $u_{rms} = 3$  m/s, that results in the velocity fluctuations amplitude about 15 m/s.

Thus, each realization of randomly inhomogeneous medium is characterized by the shape of its energy spectrum, the root mean square velocity of the fluctuations and by the set of random modes. Such method of inhomogeneous field generation allows to simulate the propagation of acoustic waves under different conditions through the same realization of inhomogeneous field as soon as we use the same sequence of random numbers.

Shown in Fig. 1.2 are typical random velocity field realizations obtained for both the Gaussian (left column, a - c) and modified von Karman (right column, e - g) formulations of the random medium energy spectra. The realizations are represented as field patterns for the longitudinal  $U_{\parallel}$  (a, e) and transverse  $U_{\perp}$  (b, f) velocity components, and the absolute value (d, g). In the distribution patterns of longitudinal and transverse components of the medium velocity, blue colours correspond to the negative velocity directions. In the distributions of the absolute value of the medium velocity, blue colours correspond to less intense fluctuations. As it was previously mentioned, the velocity fluctuations with Gaussian energy spectrum have one characteristic scale, and therefore have smoother structure without small-scale inclusions. Contrary to that, inhomogeneity with modified von Karman energy spectrum contains many different scales that result in jagged fine structure of the field.

It should be emphasized here, that the randomly inhomogeneous medium velocity fields shown here are statistically homogeneous and isotropic. The two-point correlation function of homogeneous and isotropic turbulent medium depends only on two scalar correlation functions (Karman-Howarth relation [2, 73, 97]), longitudinal  $f$  and transverse  $g$  (Fig. 1.2d):

$$R_{ij}(\mathbf{r}) = \frac{\overline{u_i(\mathbf{x}) \cdot u_j(\mathbf{x} + \mathbf{r})}}{\sqrt{\overline{u_i(\mathbf{x})^2}} \sqrt{\overline{u_i(\mathbf{x} + \mathbf{r})^2}}} = (f - g) \frac{r_i r_j}{r^2} + g \delta_{ij}, \quad (1.33)$$

where  $r$  is the radius vector and  $\delta_{ij}$  is the Dirichlet function. Longitudinal and transverse correlation functions have different characteristic scales (correlation lengths), which are determined by the following relations:  $L_f = \int_0^{\infty} f dr$  and  $L_g = \int_0^{\infty} g dr$ . The Taylor scales of correlation functions can be also determined as:  $\lambda_f = -f''(0)/2$ ,  $\lambda_g = -g''(0)/2$ . For incompressible flows, it is possible to obtain the exact relation between the correlation lengths using the following formula:  $\frac{\partial f}{\partial r} + \frac{f - g}{r}(N - 1) = 0$ , where  $N$  is the dimension of space. Thus, in 3D Cartesian geometry one may obtain, that the longitudinal correlation length is two times longer than the transverse one:  $L_f = 2L_g$ , and for Taylor scales it can be found that:  $\lambda_f = \sqrt{2}\lambda_g$ . In 2D Cartesian geometry, the integration of the relation  $g = f + r \cdot f'$  gives  $L_g = 0$ ; which means

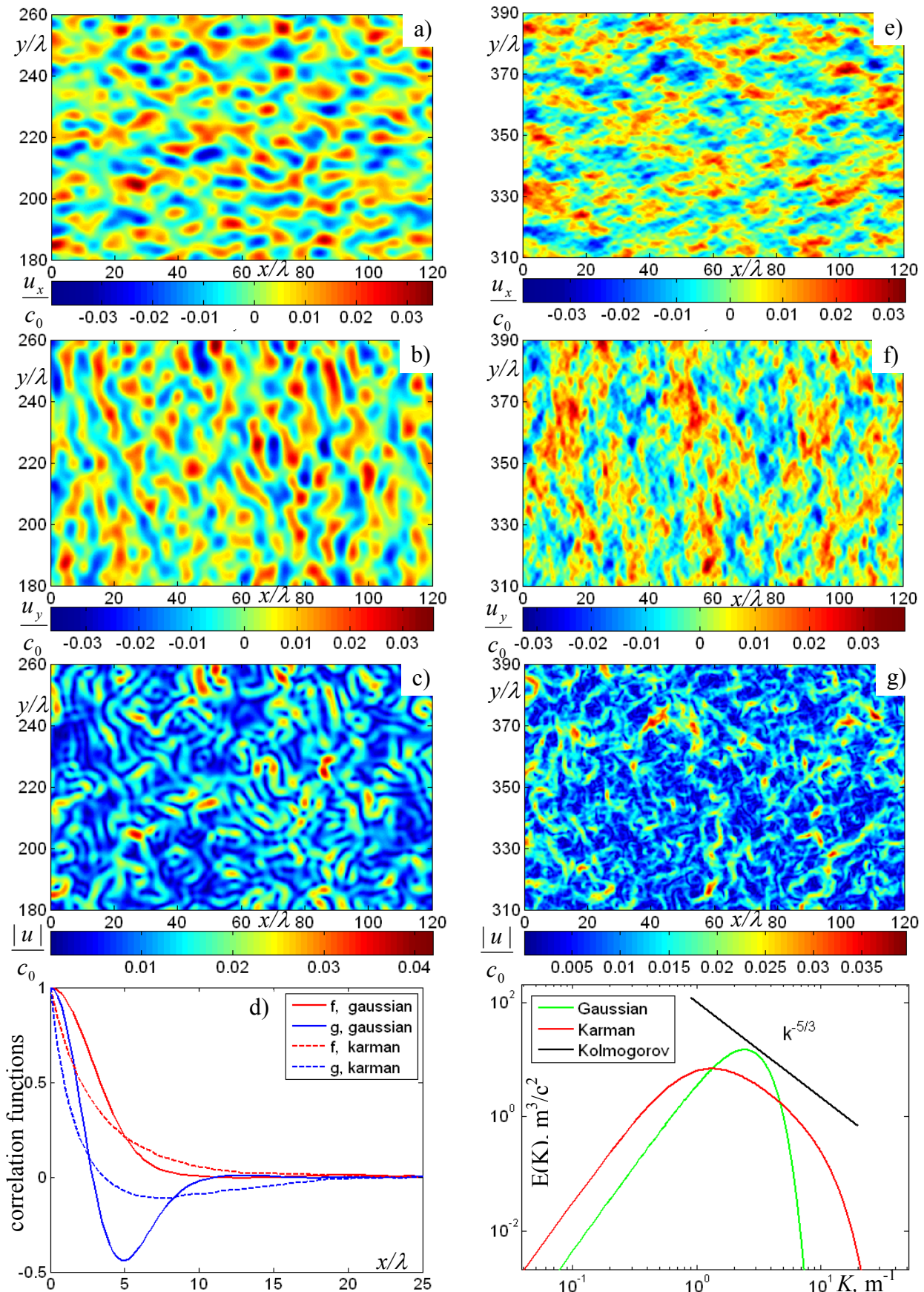


**Fig. 1.2** Comparison of random velocity field distributions with Gaussian (a-c) and von Karman (e-g) energy spectra. a) and e) – longitudinal components of medium velocity fluctuations, b) and f) transverse components, c) and g) – absolute value of velocity fluctuations, d) – longitudinal and transverse correlation functions, h) – comparison of Gaussian and von Karman spectra with the Kolmogorov's law.

that the negative part of the correlation function is more pronounced than in the 3D case. However one can obtain the relation between Taylor scales  $\lambda_f = \sqrt{3}\lambda_g$ . It means that in longitudinal (i.e. parallel to the chosen component of the velocity) direction the characteristic scale of inhomogeneity is longer than in the transverse direction. That is,  $x$  component of the random velocity field appears to be elongated along the  $x$  axis, and  $y$  component – along the  $y$  direction. In other words, medium particles move easier in the direction of local disturbance than in transverse one.

## § 1.4 Conclusion

Starting from early 40<sup>th</sup> a strong breakthrough in understanding of sound wave propagation in inhomogeneous moving medium was made. Many experimental and theoretical studies have been done in application of sonic boom propagation in the turbulent atmosphere. Formed near the ground surface overpressures were shown to be dangerous for human being. Theoretical studies based mainly on geometrical acoustics approach and parabolic approximation showed a strong influence of turbulent fluctuations on acoustic field structure, peak and mean wave parameters near the ground surface. However, these studies do not give the full understanding of the investigated phenomenon. To predict more accurately the peak and mean characteristics of the acoustic field, a more complete theoretical model should be developed. The combined effect of nonlinearity, frequency dependent thermoviscous absorption and relaxation, diffraction effects and effects, related to the presence of inhomogeneous moving medium should be simultaneously taken into account. Moreover, numerical methods, which should be used to find a solution to this model, became efficient only nowadays with developing of powerful computational facilities. In addition, in experimental investigations the effect of random caustics and the effect of multiple focusing on statistics of acoustic wave parameters have not been completely studied and is still of interest. Thus, the problem of nonlinear acoustic signals propagation in turbulent atmosphere appears to be relevant for the scientific community.



## Chapter 2

### **PROPAGATION OF NONLINEAR $N$ -WAVES IN A TURBULENT VELOCITY FIELD (laboratory-scaled experiment)**

As we already discussed in the §1.1.2, experimental investigation of sonic boom propagation in real atmosphere is very difficult due to impossibility of to have a full description of the atmospheric conditions during the flight of a supersonic airplane, and also due to the high costs of these field experiments. Lipkens *et al.* [7, 40-42] and Ollivier *et al.* [44] showed that laboratory-scale experiments using  $N$ -waves produced by electrical sparks and a downscaled turbulent medium offer an attractive alternative to field measurements since both the acoustic source and the turbulence can be well controlled.

Moreover, the laboratory experiment is much easier and repeatable under given environmental condition that makes it indispensable for the investigation of high amplitude acoustic pulse propagation in inhomogeneous moving media. Well-designed and conducted laboratory experiment will allow to validate both the developed theoretical model and numerical algorithm by comparison of the results of simulations with the experimental data.

Such experiments have been previously conducted in [7, 40-42], but due to the small width of the generated turbulent layer, which was the propagation path for the pulse, it was not possible to investigate the influence of random caustics on the statistics of acoustic field parameters. The width of the turbulent layer in considered experiments was of the order of the characteristic distance of first caustics formation, determined by the large-scale inhomogeneities. In particular, these inhomogeneities lead to more considerable augmentation of the acoustic wave focusing coefficient. Moreover, short length of the generated acoustic wave lead to strong thermoviscous and relaxation-induced absorption of acoustic energy, which was tens of times stronger than for sonic booms propagating in real atmosphere.

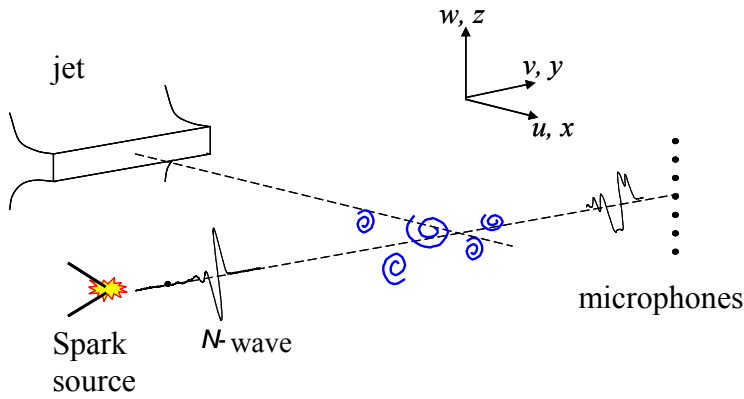


**Fig. 2.1** Geometry of the experimental setup

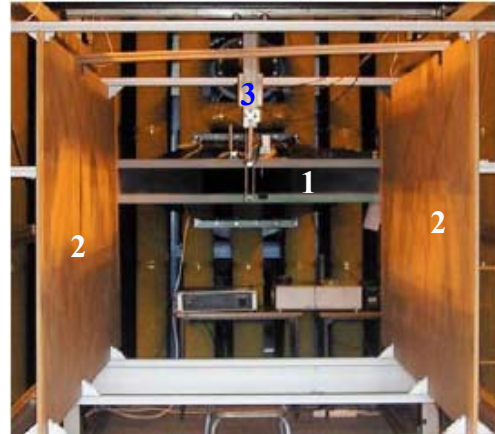


**Fig. 2.2** Experimental setup to generate turbulent fields. 1- jet, 2- wooden baffles, 3- positioning system.

An experimental setup has been built in Ecole Centrale de Lyon to create random caustics of different orders and at different distances of acoustic wave propagation. Thus, depending on the intensity of turbulent fluctuations it is possible to measure caustic of high order, caustics of first order only, or no caustics at all. For this purpose, a 2D-jet larger than used in Refs. [7, 40-42] has been designed. Consequently, the characteristic scales of turbulence and the propagation distance are larger than in previous experiments. This decreases the relative effect of the thermoviscous absorption and relaxation phenomena, compared to the effect of the presence of inhomogeneities. Thus, the experimental setup allows investigating the effect of random caustics on the statistics of acoustic field in turbulent medium under conditions, which better correspond to real atmosphere than in the previous studies [7, 40-42].

This new arrangement of the ECL facilities allows generating fully developed turbulent fields and high amplitude acoustic pulses, which propagate through the turbulent layer perpendicular to the mean flow (Fig. 2.1). The experimental setup for the turbulent field generation is discussed in §2.1 together with the results of the turbulent flow measurements. Main goal of this paragraph is to set the vertical plane where the turbulent field is fully developed, i.e. its properties are well described using the Kolmogorov's model. In this plane, the acoustic part of experiment is then conducted. Corresponding experimental setup for generation of  $N$ -pulses is presented in §2.2 together with the results of acoustic field measurements (§2.3).

## § 2.1 Generation and measurement of fully developed turbulent field

### 2.1.1 Experimental setup

The experimental setup, designed to create fully developed turbulent velocity fields (Fig. 2.2) consists of a jet [1] installed between two wooden baffles [2], and air turbine (not presented in the picture), which was used to create strong airflow. The height of the jet is  $L = 160$  mm and its width is 1400 mm, therefore it can be considered as a plane one [Gutmark *et al.*, 98]. The airflow, accelerated by the turbine, passes through the jet and further propagates between the wooden baffles of 2000 mm x 3100 mm (height x length) dimension. The length of the baffles was chosen in such way that the turbulent flow coming out from the bounded region was fully developed. These baffles are necessary elements of the experimental setup, intended to avoid the decrease in turbulent intensity due to the widening of the flow in free space. The absence of baffles would result in small and insufficiently intense turbulent fluctuations at the distances where the flow is fully shuffled and the turbulence becomes developed.

The velocity of the flow at the exit of the jet during measurements varied from 0 to 50 m/s. Mean characteristics of the velocity field were measured using a Pitot tube and fluctuations were measured using the method of simple hot wire probes (DANTEC 55P11), and cross wire probes (DANTEC 55P51). The tungsten wires of the cross wire anemometer (Fig. 2.3) were tightened perpendicularly to each other. The length of the wire was 3 mm, including the sensitive part of 1.25 mm length. The distance between the wires was 1 mm, while the diameter of each wire was about  $5 \mu\text{m}$ . Such construction allows simultaneous measurement of two airflow velocity components. To measure the flow velocity the wire of the simple anemometer was placed perpendicularly to the flow direction. To reach maximal efficiency of the cross wire anemometer its wires were placed at the  $45^\circ$  angle to the flow direction.

Calibration of anemometers was done in the potential cone near the exit of the jet (Fig. 2.4a), where the flow was assumed to be nearly laminar [97, 98, 99]. Absolute flow velocity measurements done by the Pitot tube were used as a reference to calibrate the anemometer. Using the heat transfer law, the anemometer output voltage  $E$  was correlated with the flow velocity by the following polynomial expression of the 4<sup>th</sup> order:

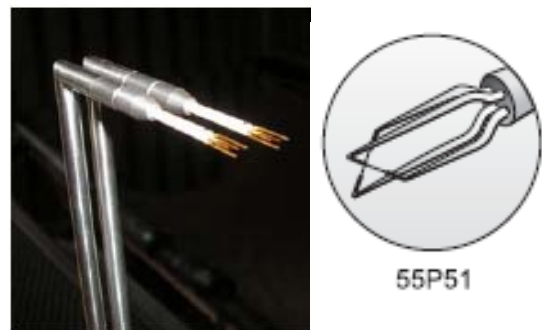


**Fig. 2.3.** Photo and sketch view of the cross wire thermo anemometer

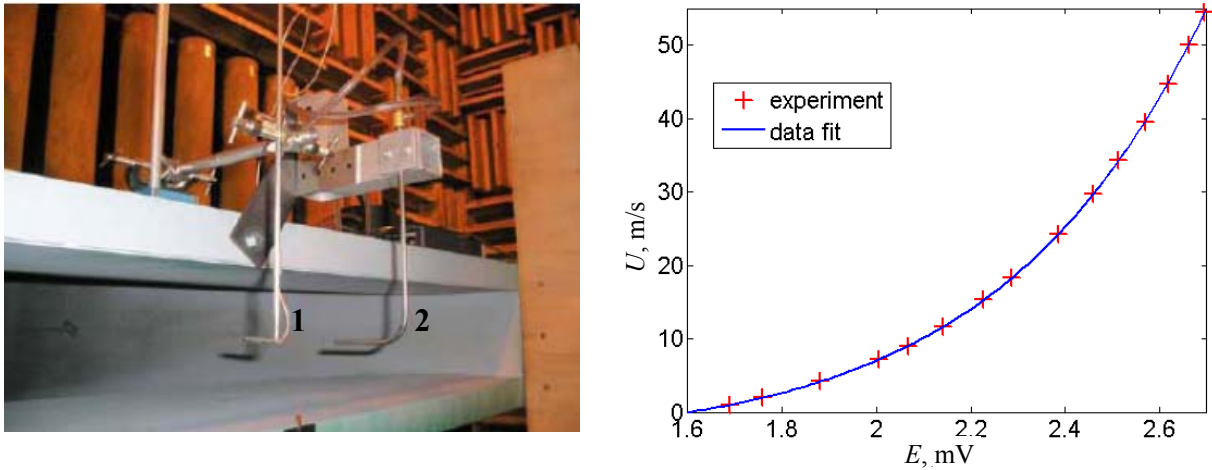


**Fig. 2.4** a) View of a Pitot tube (2) and anemometer (1) positioning in the potential cone during the calibration; b) calibration curve. Experimental data are well described by the 4<sup>th</sup> order polynomial law.

$U_{jet} = C_0 + C_1E + C_2E^2 + C_3E^3 + C_4E^4$ , where  $U_{jet}$  is the flow absolute velocity at the exit of the jet measured with the Pitot tube,  $E$  is the anemometer output voltage,  $C_i$  are real coefficients, chosen so that the polynomial fits experimental data with a very good accuracy (Fig. 2.4.b). The calibration of the anemometer was repeated twice one day before each series of measurements.

### 2.1.2 Measurement of the turbulent field parameters

Mean velocity of the turbulent flow was measured both in the area between wooden baffles and outside this area using of a Pitot tube and a simple hot wire. The results of measurements between baffles are presented in Fig. 2.5 as two-dimensional patterns of mean

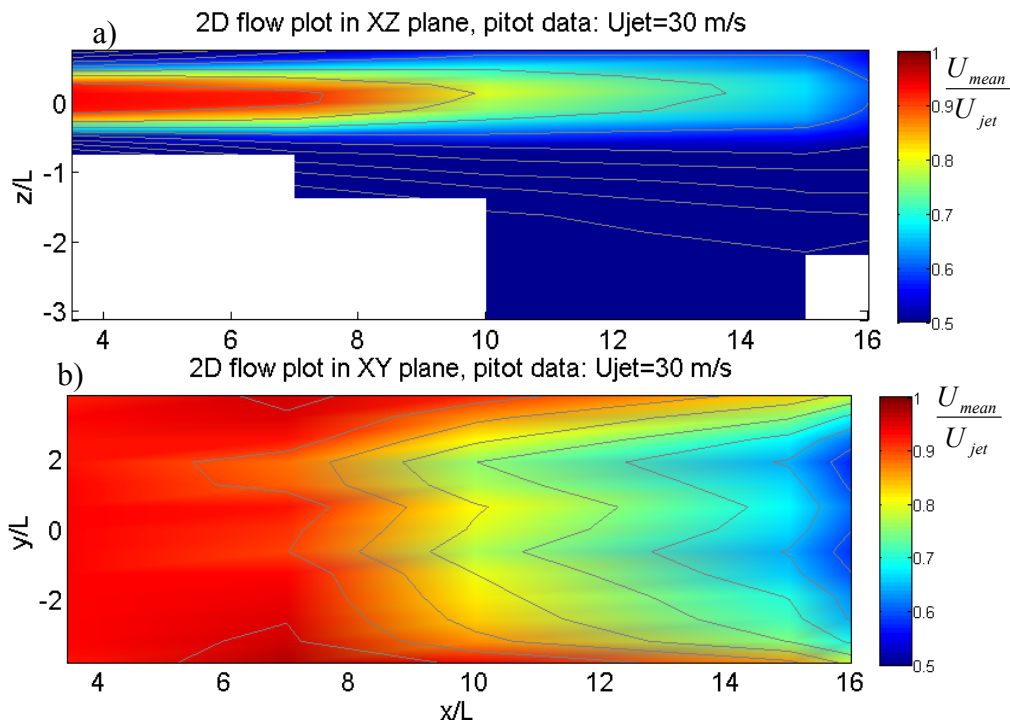


**Fig. 2.5** 2D distribution of mean flow velocity a) in vertical XZ plane and b) in horizontal XY plane.

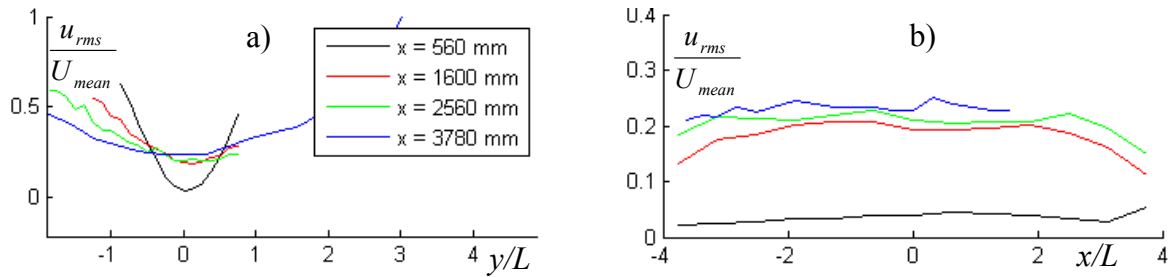


**Fig. 2.6** The level of turbulent interfusion in the flow a) in OZ axis and b) in OX axis.

flow velocity distribution in the XY horizontal plane and in the XZ vertical plane. Measurements showed that at the end of the bounded by baffles area the mean flow becomes about two times slower than at the exit of the jet independently from the turbine power. Note also, that the axis of the flow is slightly inclined in the positive direction of Z axis and maximum of the mean velocity is reached at the vicinity of baffles and then drops to zero.

In contrast to the mean flow velocity, the root mean square velocity of turbulent fluctuations increases gradually with the distance from the jet (Fig. 2.6). The rate of turbulent interfusion of the medium  $u_{rms} / U_{mean}$  at the distance of 560 mm from the jet is sufficiently small and is about 2%, for all investigated flow velocities at the exit of the jet. At the distance 1600 mm from the jet the turbulence level increases up to 17 - 20%, depending on the initial flow velocity. The level of turbulent interfusion of the air equal to  $u_{rms} / U_{mean} = 20\%$ , at which the turbulence can be assumed as fully developed [Gutmark *et al.*, 98], is reached at the distance  $X = 2560$  mm from the jet and further slightly increases with the distance. These turbulent levels indicate that the turbulence itself became fully developed [Gutmark *et al.*, 98]. At the distance  $X = 3780$  mm from the jet, generated turbulent field also appears to be fully developed and, moreover, mean and root mean square medium velocities remain intact almost everywhere inside the flow, that represents the necessary condition for the selection of the plane of acoustic pulse propagation.

In addition to the selection of the distance, at which the acoustic measurements should be done, it was necessary to determine the turbulent velocity field parameters, i.e. the characteristic fluctuation scale and its intensity should be measured. It is possible to determine the turbulence scale by measuring the turbulence energy spectrum. Sufficiently long measured time profile of the turbulence was measured and the energy spectrum of the medium velocity was calculated from this measurement. The experiments was done using low discretization frequency (5 kHz) and sufficiently long time profile (2 - 3 min) to describe low frequency part of the energy spectrum and high discretization frequency (100 kHz) in order to register its high frequency part according to the Nyquist theorem. When the frequency spectrum of the registered realization was found, it was transformed to the spatial spectrum using the Taylor hypothesis about the

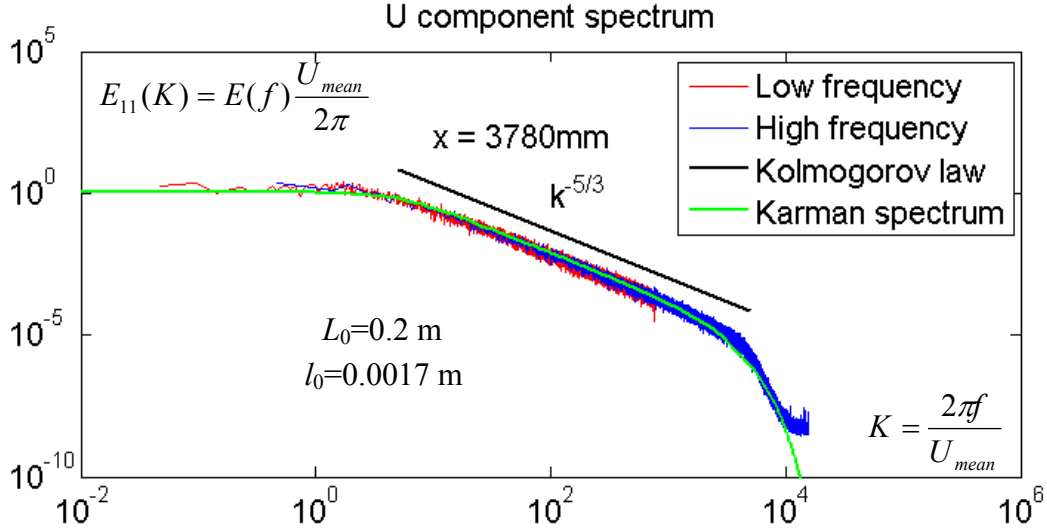


**Fig. 2.7.** Comparison of the measured energy spectrum of turbulent fluctuations (low and high frequency parts) with the theoretical formulation of von Karman spectrum and with the «-5/3» Kolmogorov's law for the inertial interval. Measurements were done at the distance  $X = 3780$  mm from the jet at the axis of the turbulent flow.

turbulent structures transfer by the mean flow [Monin *et al.*, 73]:  $E_{11}(K) = E(f)U_{mean} / (2\pi)$  where  $K = 2\pi f / U_{mean}$  (Fig. 2.7). According to the Kolmogorov's hypothesis, the energy spectrum of fully developed turbulence has overextended inertial interval of energy distribution and this inertial interval is given by the «-5/3» power law (Fig. 2.7). The limits of the inertial interval are determined by the given for each turbulent medium outer and inner scales. Moreover, experimentally obtained energy spectrum is well described by the theoretical formulation of one dimensional modified von Karman spectrum  $E_{11}(K)$  (Fig. 2.7) [97], that also confirms the statistical isotropy and homogeneity of the turbulent field at chosen distance from the jet (i.e. turbulent field is fully developed here). One-dimensional modified von Karman spectrum can be obtained from the 3D formulation by means of the integration on the wave numbers:

$$E_{11}(K) = \frac{1}{2} \int_k^\infty E_{3D}(x) \frac{1}{x} \left(1 - \left(\frac{K}{x}\right)^2\right) dx \quad \text{where} \quad (2.1)$$

$$E_{3D}(K) = 3 \frac{\Gamma(17/6)}{\Gamma(5/2) \Gamma(-2/3)} (u_{rms})^2 L_0^{-2/3} \frac{K^4}{(K^2 + L_0^{-2})^{17/6}} \exp\left(-\left(\frac{K}{K_m}\right)^2\right) \quad (2.2)$$

Here  $u_{rms}$  is the root mean square velocity of the turbulent flow,  $L_0$  is the outer scale of the turbulence,  $K_m = 5.92/l_0$ , where  $l_0$  is the inner scale of the inhomogeneous turbulent medium,  $\Gamma$  is the Gamma function. The best fit of experimental data with the modified von Karman spectrum is achieved for the following values of outer and inner scales  $L_0 \in [200, 220]$  mm,  $l_0 \in [1.25, 1.7]$  mm. Note here, that the value of the inner scale may be not accurately measured as the sensitivity of measurements is limited with the length of the hot wire sensitive part  $l = 1.25$  mm.

Another characteristic scale of the turbulent field – integral length scale – can be estimated by the theoretical relation between its value and the outer scale:  $L_f = 0.747L_0 \in [150, 164]$  mm. The integral length scale of the turbulent flow can be also estimated by the starting point of the energy spectrum, that for different measured spectra gives:

$$L_f = L_{11}^{(1)} = \pi \frac{E_{11}(K=0)}{(u_{rms})^2} \in [150, 170] \text{ mm}$$

Variation in integral length scale value is due to the measurements in different points of turbulent flow at the same distance from the jet and due to the interpolation of low wave numbers energy spectrum to zero axis. However estimated integral length scale value seems to be correct as soon as it is in a very good agreement with the main characteristic scale of the experimental setup – the width of the jet, which is equal to  $L = 160$  mm. Thus, selection of the plane for the acoustic experiment at the distance  $X = 3780$  mm is well justified. In this area, the turbulent fluctuations can be assumed as fully developed, and, in particular, homogeneous and isotropic. It worth to note, that at this distance the wooden baffles – bounds are not present and turbulent fluctuations are developed in free space.

Characteristic properties of the turbulent flow are further investigated in the plane of acoustic measurements ( $X = 3780$  mm) using the method of cross wire anemometry. This allows measuring two fluctuating components of the turbulent field. Shown in Fig. 2.8 are the distributions of flow velocity mean values  $U_{mean}/U_{jet}$  (Fig. 2.8a), and root mean square velocities of two horizontal component of medium

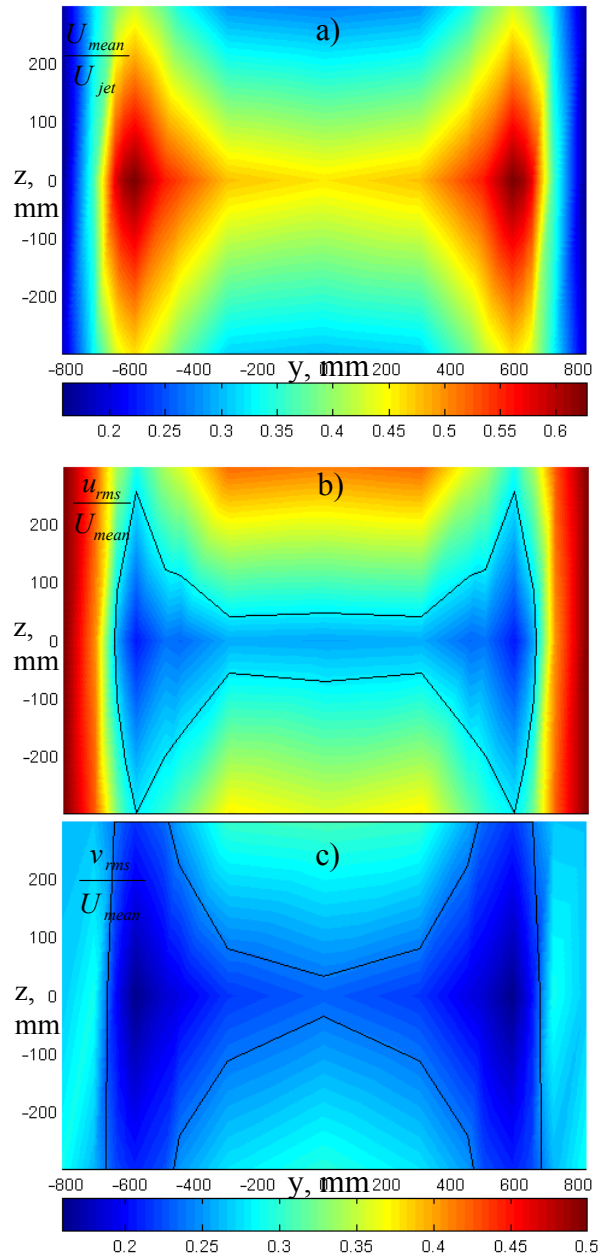


**Fig. 2.8** Distributions of mean flow velocity  $U_{mean}/U_{jet}$  a); root mean square values of turbulent fluctuations  $u_{rms}/U_{mean}$  b); and  $v_{rms}/U_{mean}$  c) in the plane of acoustic measurements at  $X = 3780$  mm from the jet at  $U_{jet} = 40\text{M}/\text{c}$ . Contour lines show the areas of fully developed turbulence (levels of interfusion are  $u_{rms}/U_{mean} < 0.28$  and  $v_{rms}/U_{mean} < 0.24$ ).

motion  $u_{rms}/U_{mean}$  (Fig. 2.8b) and  $v_{rms}/U_{mean}$  (Fig. 2.8c). It is seen that the mean flow velocity is about two and more times lower than at the exit of the jet  $U_{jet}$ , and it is nonuniformly distributed in the YZ plane. Mean flow velocity decreases in the vertical direction while moving away from the axis of the jet. In horizontal direction the slight increase of velocity is observed with increasing the distance from the Z axis, and its maximum is reached in the vicinity of baffle projections ( $Y = \pm 700$  mm) on the plane of interest. Then the fast drop of the mean flow velocity is observed. As for the mean  $W_{mean}$  and  $V_{mean}$  components – they are almost equal to zero, like it should be, as soon as there is no mean flow in transverse direction (these components are not presented in the figure). Root mean square values of medium velocity components are also changed nonuniformly while moving away from the axis of the jet. Therefore, the turbulence appears to be fully developed only in the limited area. Contour lines in Fig. 2.8b,c show the level of turbulent interfusion equal to  $u_{rms}/U_{mean} = 0.28$  and  $v_{rms}/U_{mean} = 0.24$ . As for the fluctuations along Z axis, their root mean square velocity  $w_{rms}$  behaves like  $v_{rms}$ . In areas confined with the described contour lines, the turbulence can be assumed as fully developed, i.e. homogeneous and isotropic. Thus, the area of interest is limited in vertical direction with  $Z = [-50, 50]$  mm and in horizontal direction with  $Y = [-650, 650]$  mm. It can be shown, that the acoustic wave almost always propagates in this area of fully developed turbulence on its way to the receiver (maximum displacement of the acoustic wave due to the most intense steady flow in the narrowest place of the marked region is equal to  $L_p U_{mean} / c_0 = 700 \text{ mm} \cdot 20 \text{ m/s} / 340 \text{ m/s} = 41 \text{ mm}$ , where  $L_p$  is the distance of propagation up to the narrowest zone).

Note that distributions of mean and root mean square velocities presented in Fig. 2.8 correspond to the flow velocity at the exit of the jet equal to  $U_{jet} = 40$  m/s. However, for other values of flow velocity at the exit of the jet the shape of velocity distributions are similar due to the same geometry of the experimental setup. Shown in Fig. 2.9 is an example of root mean square velocity and mean flow velocity dependence (measured at the axis of the system in the plane of acoustic measurements) on the flow velocity at the exit of the jet. Obtained dependencies are linear

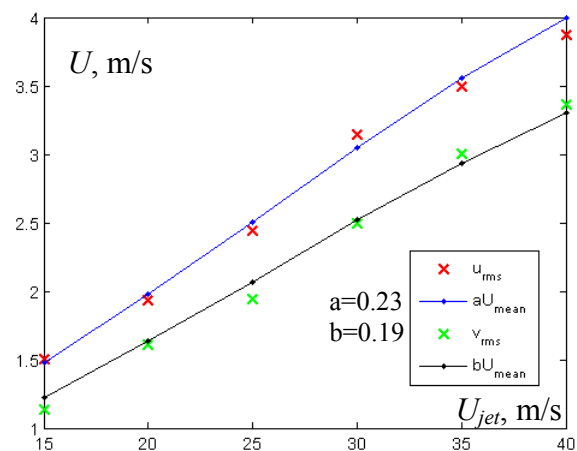


**Fig. 2.9.** Dependence of the root mean square and mean medium velocities on flow velocity at the exit of the jet

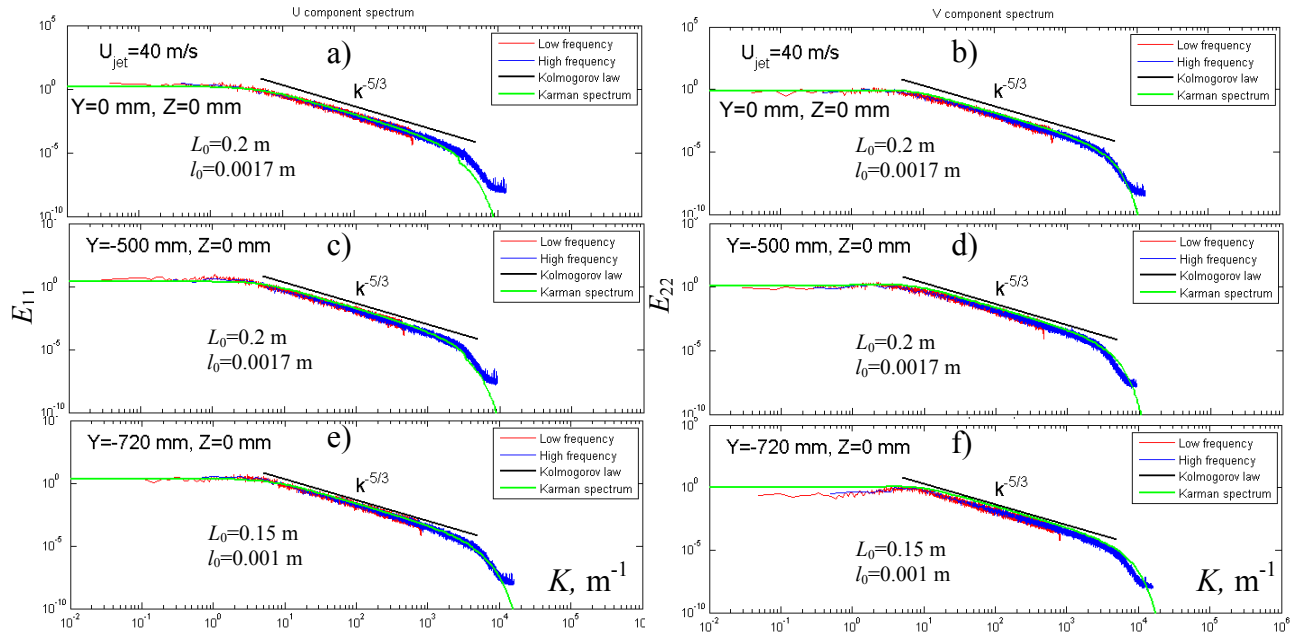


**Fig. 2.10** Spatial spectra of  $u$  (left) and  $v$  (right) components of medium velocity fluctuations in different points of the acoustic measurement plane.

and tell about invariability of turbulent interdiffusion coefficient at the axis of the jet while varying the flow velocity at the exit of the jet:  $u_{rms} / U_{mean} = 0.23$  and  $v_{rms} / U_{mean} = 0.19$ , that corresponds to the fully developed turbulence in all cases.

In Fig. 2.10 are presented the spectra of the  $x$  and  $y$  components of turbulent velocity field, measured at different points of the  $YZ$  plane at the distance  $X = 3780$  mm from the jet. Measurements were done for the flow velocities  $U_{jet} = 20, 30, 40$  m/s at the exit of the jet and are presented here for  $U_{jet} = 40$  m/s. All experimentally obtained spectra are in a good agreement with those calculated analytically using the modified von Karman formulation (2.2) for the turbulent field spectrum. Note that the outer and inner scales were chosen specifically for each figure to make the best fit to the experimental data by the modified von Karman spectrum. Therefore, in the earlier defined area of isotropic turbulence one may obtain that inner and outer scales remain constant and are about  $L_0 = 200$  mm,  $l_0 = 1.7$  mm (Fig. 2.10a-d). Outside the area of developed turbulence (Fig. 2.10e-f) the characteristic scales vary from point to point: in point  $Z = 0, Y = 720$  mm the outer and inner scales are approximated to be  $L_0 = 150$  mm and  $l_0 = 1.0$  mm (in general, model (2.2) is not valid in this region, as soon as turbulence here is not isotropic and is not stationary).

Previously, to determine the integral length scale of the turbulence fluctuations the theoretical model was fitted to the measured energy spectrum, and it was shown that  $L_f \in [150, 170]$  mm. Another method to determine the integral length scale is based on the direct



**Fig. 2.11** View of the experimental setup for measuring the correlation function. 1 and 2 are the positioning systems, 3 are the mounted cross-wire probes.

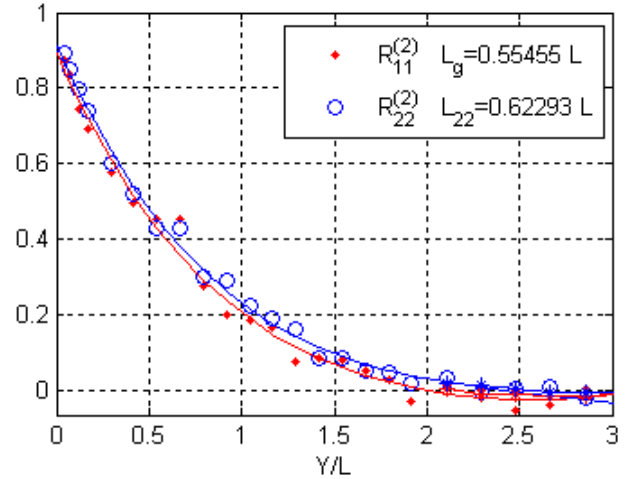


**Fig. 2.12** Correlation functions of the turbulent velocity field.

computation of integral scale using its definition *via* integration of the corresponding correlation function:

$$L_f = 2L_g = 2L_{11}^{(2)} = 2 \int_0^{\infty} R_{ij}^{(2)}(0, r, 0) dr, \quad (2.3)$$

where  $L_f$  and  $L_g$  are the longitudinal and transverse correlation functions, respectively. This method of integral length scale definition is preferable as soon as no theoretical approximation is used for the energy spectrum shape. Moreover, its measurement will allow validation of the modified von Karman model by comparison with the obtained results.

Thus to determine the integral length scales of turbulent fluctuations it is necessary to measure their correlation functions. To measure the correlation functions the special experimental setup was used. Two cross wire anemometers were mounted on two branches of the positioning system 2 (Fig. 2.11). Positioning system 1 was used to change the reference point in the turbulent field. Positioning system 2 changed the distance between the two cross-wire probes. It was necessary to keep both probes in the developed turbulence area during measurements. If one of the probes during the measurement procedure goes out from the area of interest, the two-points correlation rapidly goes to zero, and gives incorrect estimation of the developed turbulence integral length scale. The duration of one correlation function measurement takes about one hour. Therefore, measured correlation functions vary in shape due to changes in atmospheric conditions during the experiment. Typical measured correlation functions are presented in Fig. 2.12. They are transverse correlation functions  $R_{11}^{(2)} = \langle u(r)u(r + dy) \rangle = g$  (displacement in  $y$  axis direction) and  $R_{22}^{(2)} = \langle v(r)v(r + dy) \rangle$ . According to different measurements and to the integration (2.3) the value of the integral length

scale is estimated to be around  $L_f=2L_g \in [166, 182]$  mm. This value is in a good agreement with the integral length scale obtained by interpolating the measured spectrum of turbulent fluctuations to the axis  $K = 0$  ( $L_f \in [150, 170]$  mm). In particular, this allows us to conclude that the modified von Karman model describes very well the turbulence energy spectrum in our experiment and can be used in our numerical simulations

## § 2.2 Acoustic measurements

### 2.2.1 Experimental setup

The sketch of the experimental setup for acoustic measurements is given in Fig. 2.13. It shows the electrical spark source to generate short spherically divergent acoustic  $N$ -pulses, the microphones to measure the pulse waveform at different distances from the source, the amplifier, the oscilloscope, and the acquisition card to record the signal. The source and the microphones were mounted on a positioning system to have a possibility of changing the distance between them. An additional reference microphone (not shown in the sketch) fixed at the distance of 37 cm above the source was used to control the stability of the shape and peak characteristics of the propagating shock wave. Acoustic measurements of shock pulses were performed in air, in an anechoic chamber, at the distances from 15 cm to 2 m from the spark source.

To produce an electric spark, a high voltage (15 kV) was applied to two tungsten electrodes with a 6 mm gap between them. The electric discharge creates a sudden local heating of the gas between the electrodes, which generates a short duration but high amplitude pressure

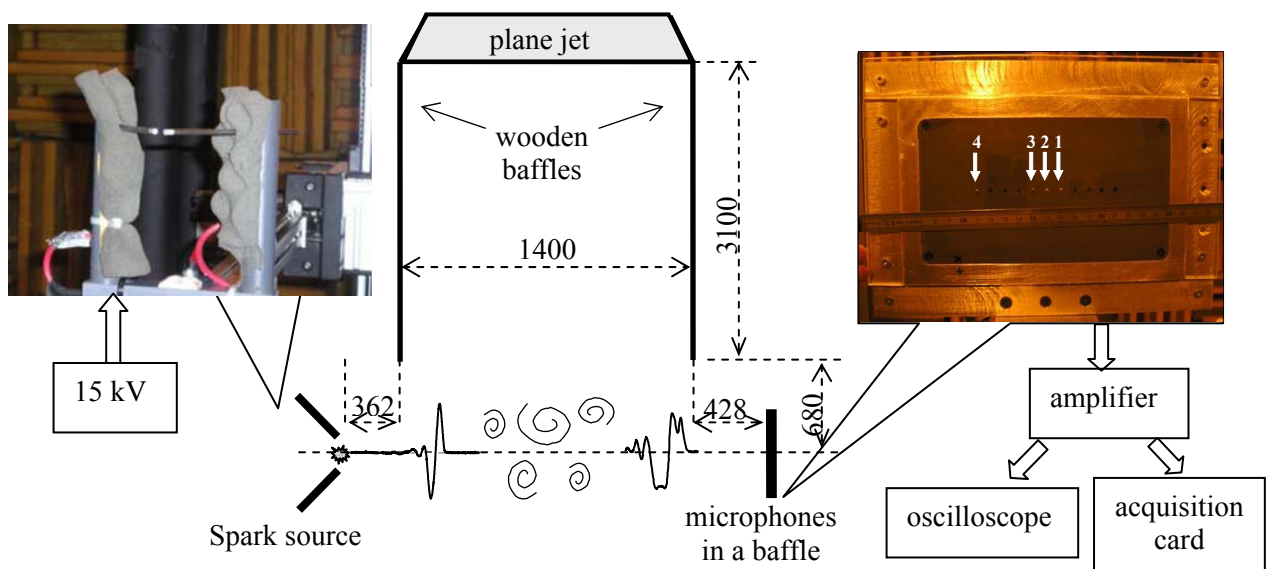


Fig. 2.13 Sketch of the experimental setup. Top view. All distances are given in millimeters.

perturbation. This perturbation has a complex shape that varies from one spark to another. However, as the pressure amplitude of the pulse is very high ( $> 1000$  Pa), the initial waveform transforms into an  $N$ -wave due to nonlinear effects along the first centimetres of propagation. Conducted experiments showed a good reproducibility of the generated  $N$ -wave parameters: the peak positive pressure measured by the reference microphone was  $290 \pm 10$  Pa, the pulse half duration was  $13.16 \pm 0.23 \mu\text{s}$ , and standard deviation of arrival time was  $1.7 \mu\text{s}$ . At the distance of one meter from the source the typical maximum pressure amplitude  $P_{max}$  was 85 Pa, the half duration  $T$  was  $14.55 \mu\text{s}$ , and the shock rise time  $t_{0.1-0.9}$ , defined as an interval between the peak pressure increase from 10% to 90% of  $P_{max}$ , was about  $3 \mu\text{s}$ .

Wide band high frequency 1/8 inch diameter *Brüel & Kjaer* 4138 microphones were used in experiments. The size of the microphones' membrane is of the same order of magnitude as the wavelengths of the acoustic signal. Therefore, in order to postpone the diffracted waves, four microphones were mounted, without their grids, in a baffle (Fig. 2.13) [7, 44]. The microphones' electric outputs were amplified by *Brüel & Kjaer* Nexus amplifier, which was modified to extend its bandwidth up to 200 kHz. The amplifier output voltages were digitally recorded at a sampling frequency of 5 MHz by two National Instrument data acquisition cards driven by Labview.

To measure correctly the propagation time between the spark generation and the detection of the acoustic shock wave on the membrane of the microphone, the synchronization of the acquisition card with the acoustic spark source was done by means of electric signal from an antenna, used to detect a high amplitude electromagnetic pulse generated during the spark discharge. After being triggered by this electromagnetic pulse, an oscilloscope produced a TTL signal, which was used to synchronize the acquisition cards. The reference trigger level from the antenna was chosen to be 12 V. The same electromagnetic pulse was also detected by the microphone but gave only 0.5-1 V at the output of the amplifier. Necessary delay between the spark discharge and the detection of the acoustic wave depends on the distance of acoustic wave propagation and is introduced by means of PC governing the acquisition.

In Fig. 2.14a the electromagnetic wave (red) and following acoustic wave (blue) measured in homogeneous medium are presented. The time delay between the spark discharge and arrival of the acoustic wave on the microphone is about 3.7 ms. This corresponds to 1.26 m distance of propagation. High amplitude of the electromagnetic pulse (6-15V) allows its reliable detection against a background of various breakthroughs given by working in neighbour rooms electrical devices. The acoustic signal measured by microphone gives only the level of 3-4 V, depending on chosen tuning of the gain of the amplifier.

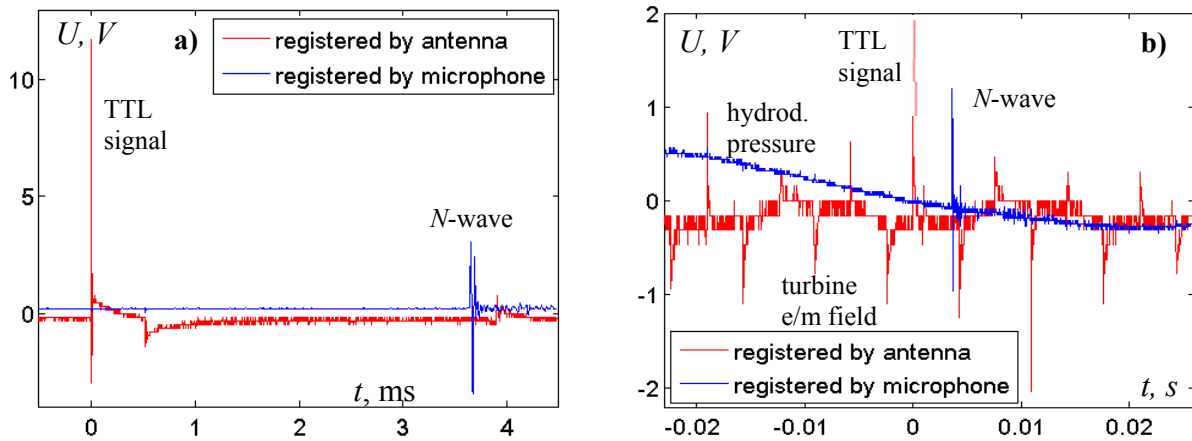


**Fig. 2.14** Signals, measured by microphones and by antenna in homogeneous air (a) and when the air turbine was switched on (b).

When the air turbine used for generation of turbulent fields was switched on, detection of the effective electromagnetic wave by the antenna was complicated due to the parasitic breakthrough coming from the working engine (Fig. 2.14b). Fortunately, the level of this additional electromagnetic noise was not as high as the electromagnetic pulse produced by the spark source and therefore we could still synchronize the acquisition device by properly setting the trigger level.

Another problem for acoustic wave measurement lies in the turbulent field itself because fluctuating hydrodynamic pressure results in low frequency pressure perturbations on the membrane of the microphones. Microphones are also sensitive to this pressure perturbation, which results in the change of their dynamical range. In Fig. 2.14b it can be seen, that the acoustic wave (random sample) is measured on the slope of low frequency perturbation that changes its shape. This poses problems for the treatment of the recorded signal. To diminish the influence of the turbulence on the acoustic field measurements, the microphones were placed at about 43 cm from the projection of a wooden baffle on the measuring plane (Fig. 2.13).

### 2.2.2 Characteristics of *N*-waves measured without turbulence

Shown in Fig. 2.15 are a typical waveform (a) and corresponding spectrum (b) measured at the distance 210 mm from the spark source. The waveform has the shape of an *N*-wave with a very thin shock front, but it is not an ideal *N*-wave. It is a bit asymmetric: the absolute value of the peak positive pressure  $p_+ = 517$  Pa is higher than that of the peak negative pressure  $p_- = 400$  Pa. The slope of the acoustic pulse is not a linear function as it would be for the ideal *N*-wave, and has some low amplitude oscillations on it. The rise time of the shock front is defined here as time, needed for pressure to change from  $0.1p_+$  to  $0.9p_+$  on the front (Fig. 2.15a). The half duration of the wave is defined as time from the middle of the shock front till the

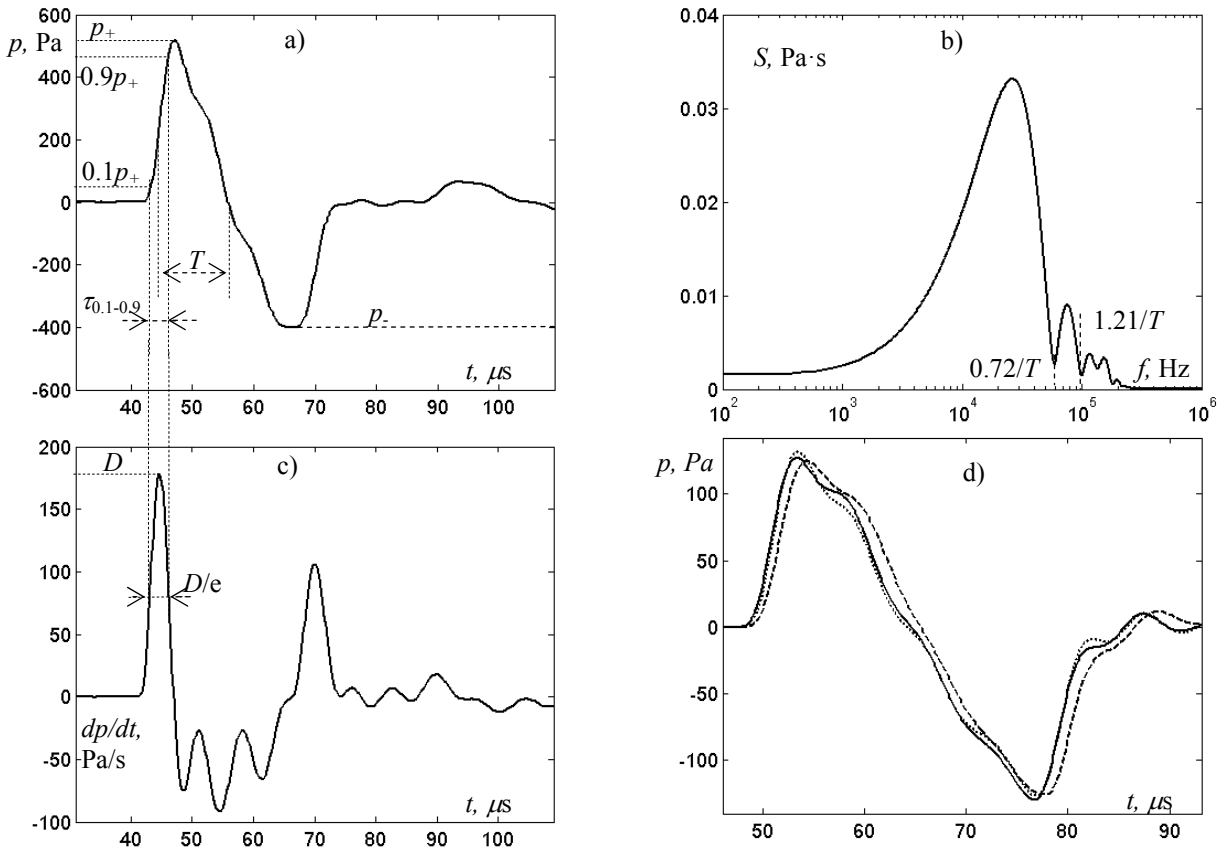


**Fig. 2.15** Typical waveform a) and its spectrum b) measured at the distance 210 mm from the spark source in homogeneous air; the derivative of the time profile c); waveforms, measured with different microphones for the same spark at the distance 690 mm from the source d).

intersection of the zero value pressure by the slope.

Note, that these definitions for the rise time and half duration are not always effective. For example, the rise time definition is not effective for defining the shock front width of the pulse with several pikes (in turbulent medium). The alternative definition for the rise time is based on the derivative of the pulse time profile. The rise time of the shock front is equal to the width of the derivative highest peak at the level  $D/e$ , where  $D$  is the maximum derivative value (Fig. 2.15c). For waves, propagating in homogeneous air these two definitions are equivalent. This is due to the fact that the shock front is always steeper than the back front of the wave, in particular, because of diffraction effects. In heterogeneous medium the second definition is preferable, as soon as the steepest fronts are of the interest, and it is not always the first one. Usually these fronts have the highest amplitude, according to the effects of nonlinear wave propagation.

As for the duration of the wave, it is difficult to define it using time domain formulation even for waves propagating in homogeneous air. It is not always obvious how to define middle point of the shock. Moreover, due to the asymmetry of the pulse its duration defined using the positive part differs from the duration defined using the negative part (up to 25% difference). To

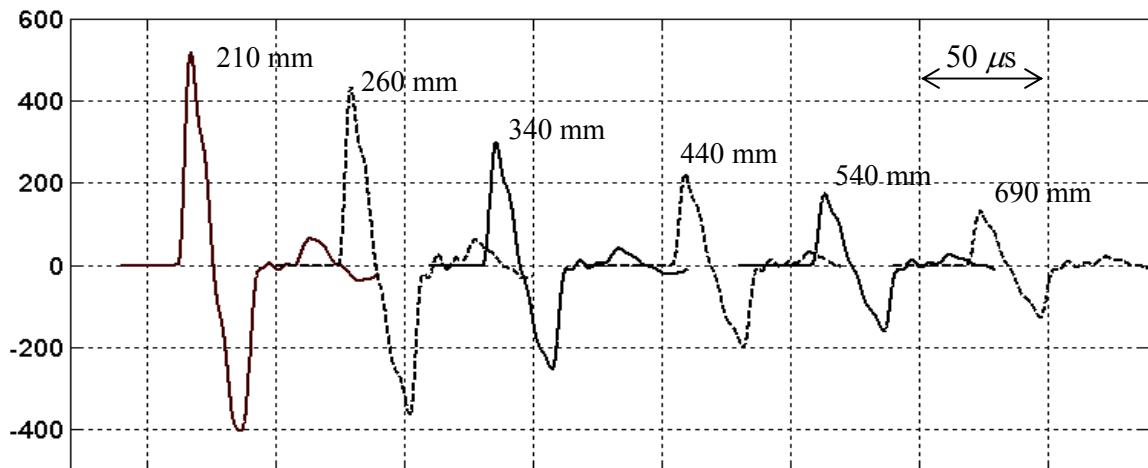


**Fig. 2.16** Typical waveforms measured at different distances from the source in homogeneous air.

define the pulse duration more accurately we propose a new definition in the frequency domain based on the waveform spectrum. Using an *a priori* information given by nonlinear propagation effects, it is assumed here that real waveform is almost an ideal symmetric *N*-wave with very thin shock front. That is, all the distortions of the waveform are due to the measuring system (Fig. 2.15d) and in particular depend on microphone frequency response, on positioning of the microphone in a baffle, and on diffraction effects on the edges of the microphone. Moreover it is assumed that the effect of measuring system can be described by a smooth function which does not change the position of spectrum minima (say zeros). Thus, to define the half duration of the pulse we can now use the relation between the frequencies of the spectrum minima and its half duration for the ideal *N*-wave. It is given by the solutions of the equation:  $\text{tg}(2\pi fT) = 2\pi fT$ . For example, for the first minimum of the *N*-wave spectrum this leads to  $f_1T = 0.72$  and for the second one -  $f_2T = 1.21$ . The values of half duration, obtained from the first and second minima in experimental spectra were equal to each other with an error not higher than 2 %, that validates the consistency of made assumptions.

Acoustic waveforms were measured at different distances from the source in homogeneous air. At each distance, about 100 waveforms were measured. As the frequency of electric discharge of the spark source was about 1Hz, the time needed for measurement at one distance was about two minutes. Typical waveforms measured at different distances from the spark source are presented in Fig. 2.16. As it was expected, all of them have the form close to the *N*-wave; the peak positive pressure of the pulse becomes smaller while propagating from the source due to the spherical divergence and nonlinear effects; and the shock front rise time and pulse duration – longer.

## § 2.3 Analysis of the effects of turbulence on $N$ -waves

### 2.3.1 Typical measured waveforms. Estimation of the focusing zone width

Typical measured acoustic waveforms, passed through the turbulent layer are presented in Fig. 2.17. The shape of the waveforms measured in laboratory experiment is in a good agreement with sonic boom waveforms registered in real atmosphere [52-55]. Here are shown both the classical  $N$ -wave and  $U$ -wave pulses (a, e) with high amplitude and narrow shock fronts; rounded waves (c) and waves with several shock fronts (d) or several pikes (b) were also observed. Note that all of measured waveforms have a long amplitude tail. Moreover, the maximum amplitude of the wave can be achieved in the tail part, that is the maximum peak

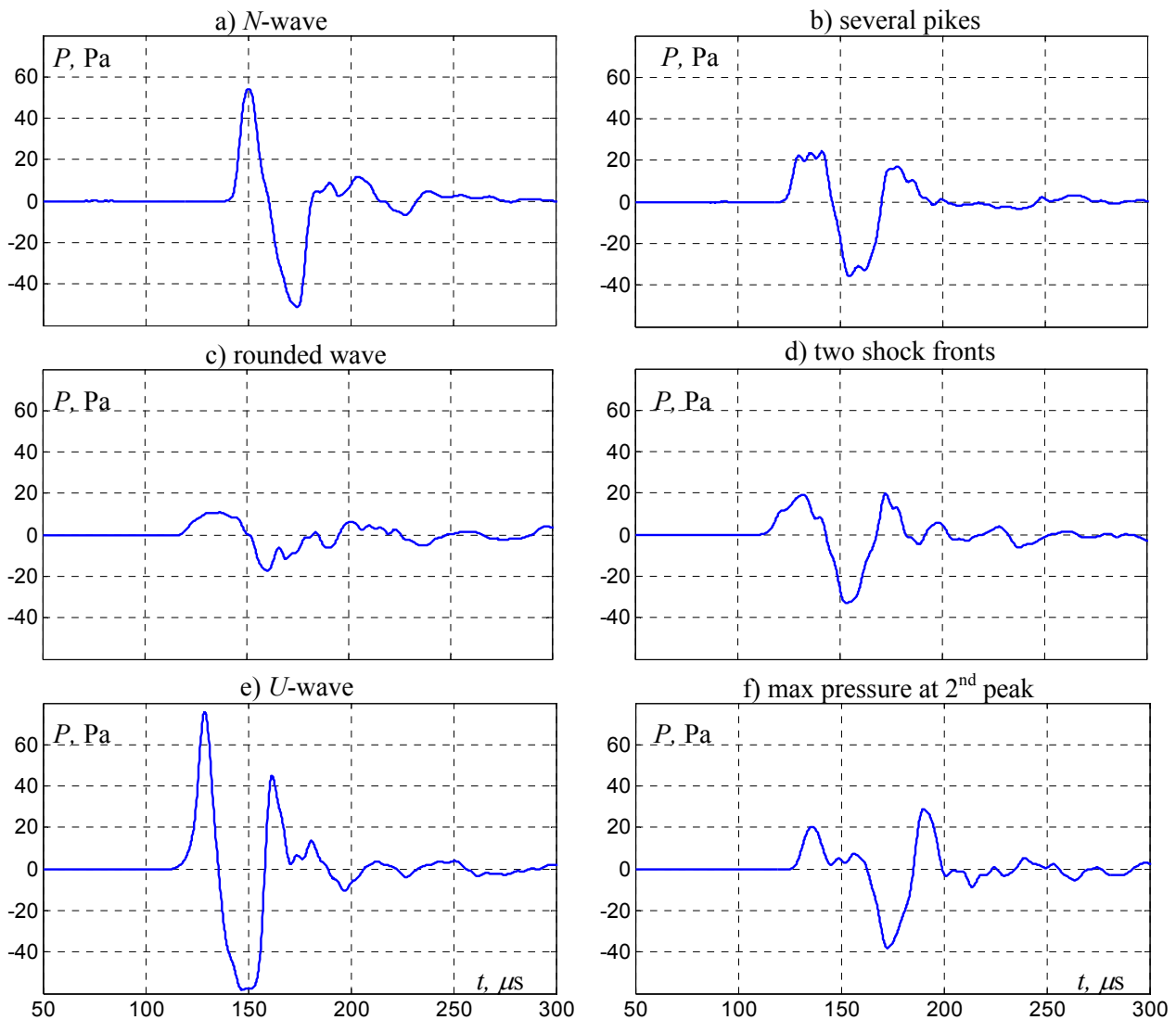


**Fig. 2.17** Typical waveforms measured at the distance 2.19 m from the source after passing the turbulent layer.  $U_{jet} = 30$  m/s.

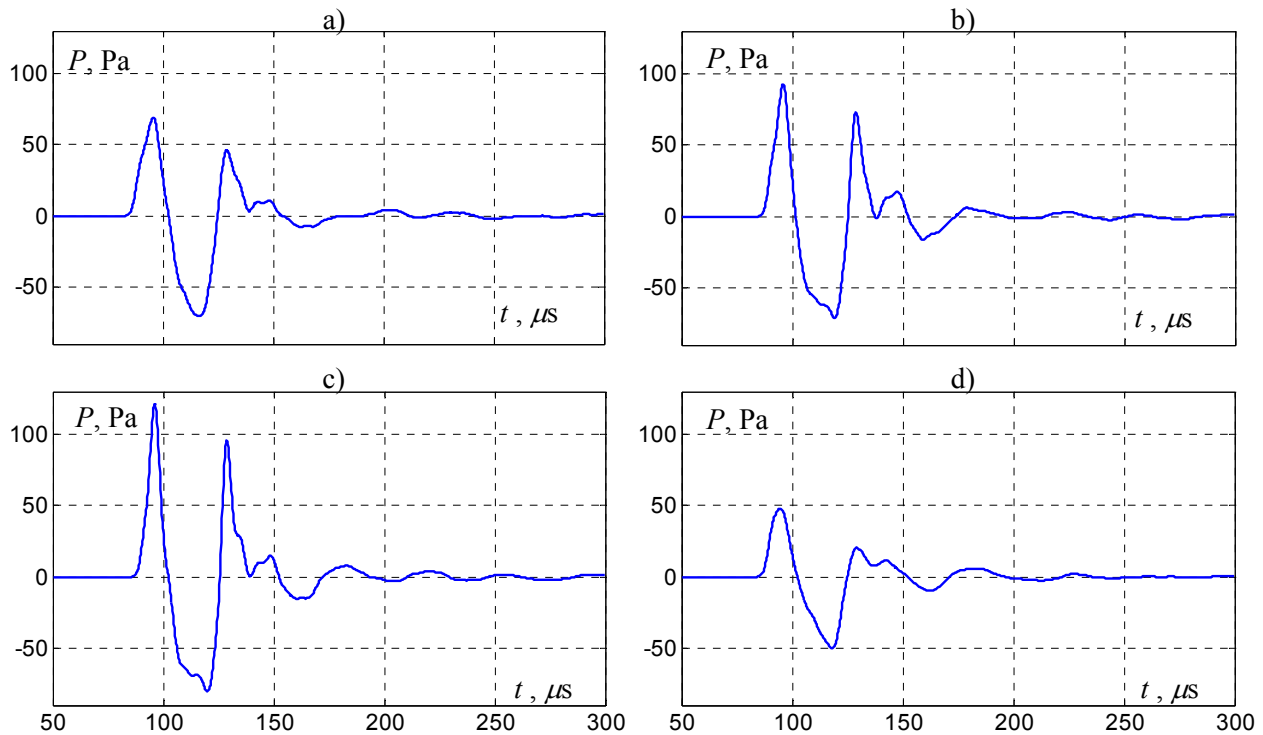


**Fig. 2.18.** Waveforms measured by 4 microphones in the vicinity of the focusing zone at the distance 2.19 m from the source.  $U_{jet} = 20$  m/s

pressure does not always correspond to the first shock front (f).

Having several microphones in one line gives us a chance to estimate the width of the focusing zone at given distance. Three microphones were placed with the spacing of 1 cm between each other (microphones 1, 2, 3 in Fig. 2.13); corresponding measured waveforms are shown in Fig. 2.18a-c. The fourth microphone was located at the distance of 4 cm to the left from the third one. Corresponding measured waveform is shown in Fig. 2.18d. Second microphone is placed at the axis of the acoustic measurement setup. Wave profiles were chosen from the experimental data in such way that they correspond to the area of focusing of the acoustic wave, which was determined by the formation of classical *U*-pulses. Thus, by comparing the waveforms measured by these microphones, the width of the focusing zone in vertical and horizontal directions can be estimated. Waveforms, measured by 1-3 microphones are in a good agreement in shape and in peak amplitudes. Maximum peak positive pressure was measured by the third microphone (Fig. 2.18c) whereas the first microphone gave the amplitude which was 30% less. At the fourth microphone, which was located at a longer distance (4 cm) from the third one, the measured peak amplitude was about 45% less than the maximum one. Therefore, if we suppose that the position of the third microphone corresponds to the centre of the focusing zone, and that its width is defined by the 30% decrease of the amplitude, then the width of the focusing zone is about 4 cm (4.5 wavelengths of the initial *N*-wave). It should be

noted here that the amplitude of the pulse, recorded by different microphones, also depends on the distance travelled by the wave from the source to each of the four microphones. Nevertheless, the difference in propagation distance has a weak influence ( $< 0.03\%$ ) on the wave amplitude due to the long distance from the source as compared to the separation distance between the microphones.

### 2.3.2 Effect of the turbulence intensity on the $N$ -wave statistics, average and peak characteristics

Consider now the statistics of the distorted  $N$ -waves after passing through the turbulent layer. The geometry of the experimental setup is fixed, and only the intensity of the turbulent fluctuations was changed by varying the flow velocity at the exit of the jet. Then, a large number of shock waves, emitted by the spark source at the consecutive time moments, were recorded. As it was mentioned in the introduction, the most important parameters of the sonic boom and shock wave are the peak positive pressure  $p_+$  and the rise time  $t_{0.1-0.9}$ .

Shown in Fig. 2.19 are the dependencies of the mean peak positive pressure values (red curve, Fig. 2.19a), mean rise time of the acoustic wave shock front (Fig. 2.19b), and mean arrival time of the wave front (Fig. 2.19c) on the velocity of the flow at the exit of the jet (turbulence intensity). Experimental data of individual measurement (2000 pulses at each flow velocity) are presented as black points. Data shown here correspond to measurements done by the first

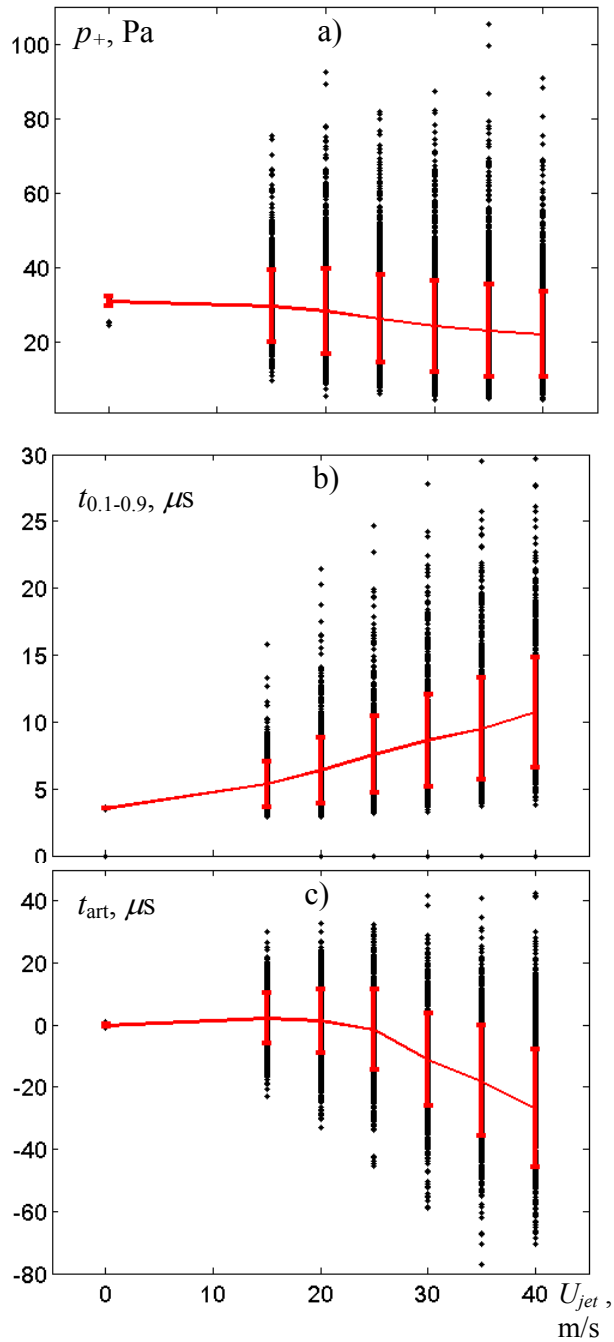


**Fig. 2.19** Mean distributions (red lines) of peak positive pressure a), rise time of the wave front b), and wave front arrival time c) depending on the flow velocity at the exit of the jet  $U_{jet}$  (turbulence intensity) at the distance of 2.19 m from the source. Black points – data of individual measurements. Vertical red segments are the standard deviations of each parameter.

microphone, the other microphones gave similar results. The distance between the source and the receiver was equal to 2.19 m, whereas the width of the developed turbulent layer was about 1.4 m. The longer distance between the source and receiver was chosen in order to avoid the influence of the turbulent fluctuations on them.

On Fig. 2.19a we observe that in the presence of turbulence the dispersion of peak amplitude values becomes very high. Both waveforms with the pressure level of 3-4 times higher than that in the motionless air and waveforms with very low amplitudes are observed. With increasing the flow velocity  $U_{jet}$  the intensity of turbulent fluctuations becomes higher and the mean peak positive pressure level decreases. For example, in the case of motionless atmosphere  $\langle p_+ \rangle = 30.9$  Pa, whereas for  $U_{jet} = 40$  m/s this value is equal to  $\langle p_+ \rangle = 22$  Pa. Note, that the rate of mean pressure amplitude decrease in turbulent medium is sufficiently augmented after passing  $U_{jet} = 20$  m/s flow velocity to its higher values. Presumably, this is connected with the formation of the focusing zones of acoustic wave in the area of measurements at distance 2.19 m from the spark source.

For the rise time of the wave front, determined as the time needed for pressure to pass from 0.1 to 0.9 level of its maximal value, similar results are obtained. Similar to the peak positive pressure, the shock front rise time in turbulent medium varies significantly (Fig. 2.19b). Following the increase of the intensity of the turbulent medium, the mean rise time increases from  $\sim 3.0 \mu s$  in homogeneous air to  $\sim 10.5 \mu s$  for the strongest turbulence. However, the lowest level of the rise time does not exceed  $3 \mu s$ , although in the focusing regions the waveforms with a high amplitude and very short shock fronts are expected [Davy *et al.*, 100].

Turbulent fluctuations affect also the arrival time of the shock front (Fig. 2.19b). Note that fluctuations of the air temperature were included in the analysis of the experimental data and in calculations of the arrival time. For each experimental series of acoustic wave measurements, the arrival time of still medium were calculated using the relation  $t_0 = D/c_0(T)$ . Here the sound speed  $c_0$  depends on the medium temperature,  $c_0(T) = (\gamma RT/\mu)^{1/2}$ , where  $\gamma$  is the specific heats constant,  $R$  is the absolute gas constant,  $\mu$  is the gas molecular weight, and  $D$  is the distance between the spark source and microphone. In this way it was obtained that the mean arrival time of shock wave propagating in the turbulent medium becomes shorter with the increase of the turbulence intensity, i.e. most of the acoustic waves arrive earlier in the presence of turbulence. So in inhomogeneous moving medium with  $U_{jet} = 40$  m/s the acoustic wave arrives on the microphone, in average,  $26 \mu s$  faster than in the motionless medium. This variation in arrival time is of the same order as the duration of the initial pulse ( $25 \mu s$ ). This can be explained by the Fermat least action principle, which in application to acoustics tells that the wave propagates in

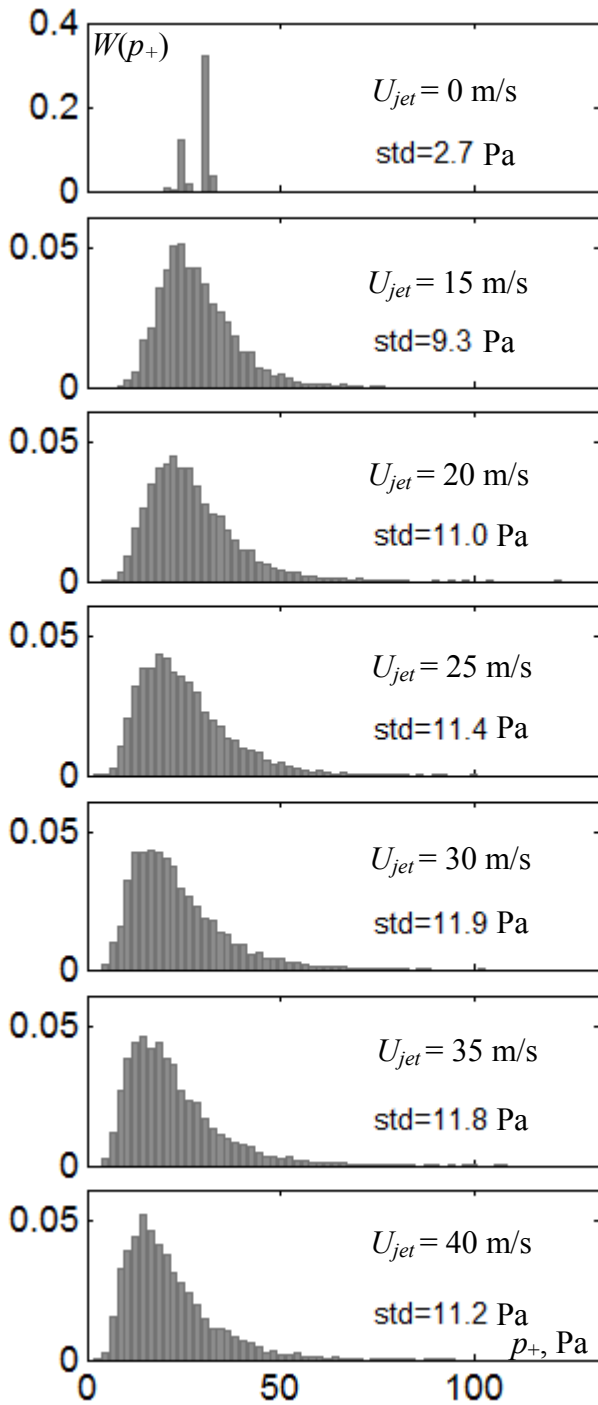


**Fig. 2.20** Probability density distributions of shock wave peak positive pressure  $p_+$  at the distance 2.19 m from the source for various flow velocities  $U_{jet}$  at the exit of the jet. **std** – standard deviation abbreviation. Width of the class is 2 Pa.

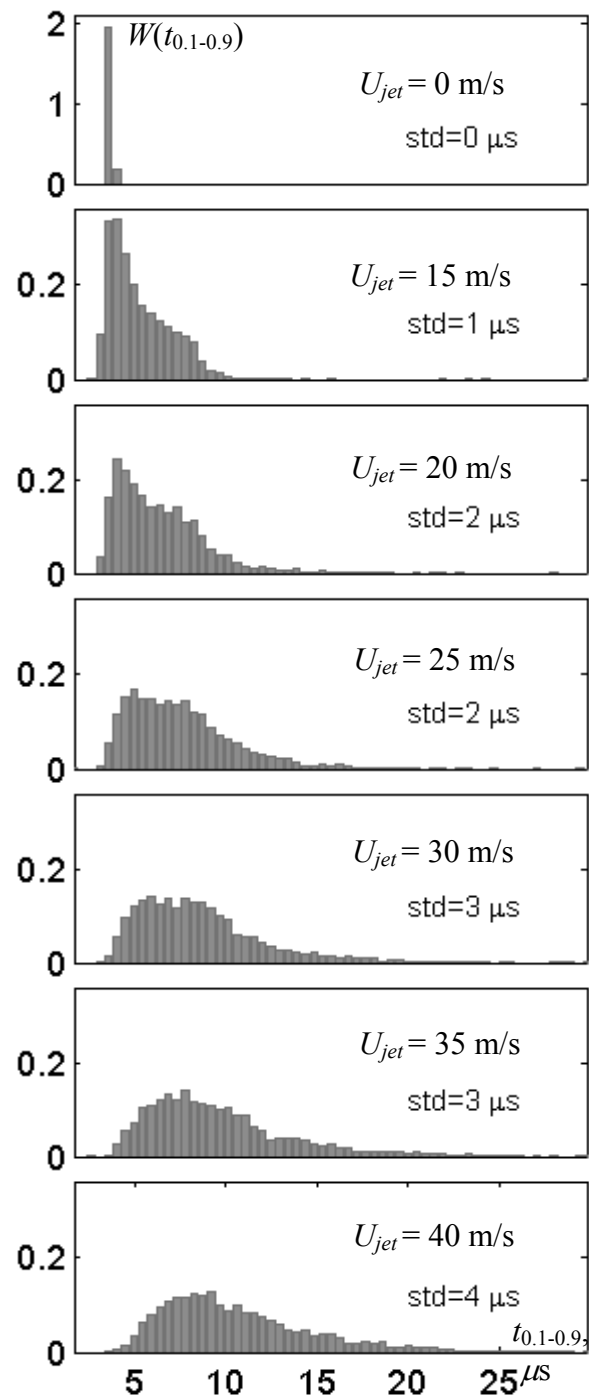


**Fig. 2.21** Probability density distributions of shock wave rise time  $t_{0.1-0.9}$  at the distance 2.19 m from the source for various flow velocities  $U_{jet}$  at the exit of the jet. **std** – standard deviation abbreviation. Width of the class is  $0.5 \mu s$ .

inhomogeneous medium in the way to minimize its arrival time.

To obtain more detailed information about statistics of peak positive pressure, the probability density distributions were calculated using the data for all four microphones (8000 individual measurements at each flow velocity) and are shown in Fig. 2.20. Distribution for  $U_{jet} = 0$  m/s (homogeneous medium) has a finite width due to the small difference in propagation distance between the source and each of the microphones and due to the fluctuations, peculiar to the shock wave generation process by the source of the given type. In addition, all the microphones have different amplitude frequency responses, which affects the pressure estimation from the output voltage, and therefore affects the estimation of the peak positive pressure and the shape of the distribution. In the presence of turbulence, the distributions of peak positive pressure widen substantially and transform into symmetric bell-like shape, with a long tail at high amplitudes. Similar results were obtained in [Ollivier *et al.*, 44]. With increase of turbulence intensity, the maximum of the distribution moves to the smaller amplitudes, as it has been shown for the mean value. Simultaneously with the increase of turbulence intensity the standard deviation of peak positive pressure also increases (standard deviation is marked up on the graph with std abbreviation). The fast increase of the standard deviation from 2.7 Pa in still medium to 11 Pa in a turbulent medium with  $U_{jet} = 20$  m/s is followed by the slow-varying part where its maximum value 11.9 Pa ( $U_{jet} = 30$  m/s) is achieved. At higher turbulence intensities a slight decrease of the wave amplitude standard deviation is observed: the probability density distribution becomes narrower. Note, that at the distance 2.19 m from the spark source it is still possible to measure the amplitudes as high as 120 Pa (Fig. 2.18c), that are more than 4 times higher than the peak pressures measured at the same distance in homogeneous medium.

Distributions of the shock rise time probability densities for different flow velocities at the exit of the jet are shown in Fig. 2.21. In motionless medium, when  $U_{jet} = 0$  m/s, the probability density for the rise time is presented with almost one line, corresponding to the value  $3.0 \mu\text{s}$ . For  $U_{jet} = 15$  m/s, the probability density distribution is already widened by the turbulence, that results in its spreading to longer rise times. Note here that the shape of the distribution became like a right triangle that tells about experimental limitations of measuring short rise times for pulses that form due to focusing.

Rise time values shorter than  $3.0 \mu\text{s}$  are not observed, while  $3.0 \mu\text{s}$  rise time is still most frequently observed as soon as all shorter rise times are recorded as this value. Thus, such cut-off at  $3.0 \mu\text{s}$  can be explained by the limited frequency response of the microphone, which is investigated in details in Chapter 3. Note, that the given microphone frequency response can vary due to aging, due to temperature, and humidity variations. Therefore, the minimum

measured rise time of the wave may vary slightly for the measurements done with the same microphone, but under different air conditions. This value depends also on the positioning of the microphone inside the baffle.

Further increase of flow velocity results in stronger distortion of the  $N$ -wave and in moving of peak probability density to longer rise times. For these turbulence conditions, the triangle shape of the distribution changes to the bell-like shape with a very long tail in the region of wide fronts with the rise time up to 20-25  $\mu s$ . Thus, the rise times of acoustic waves become longer than the minimum rise time resolved by the microphone. Therefore, the transformation of the shape to the bell-like shape is observed. The more intense the turbulent fluctuations are the stronger shock fronts are smeared out.

Obtained results for the  $N$ -wave amplitude and shock front rise time are in a good agreement with the model experiments data, carried out by other authors [7, 40, 44]. The results are also in a good qualitative agreement with the sonic boom measurements in real atmosphere [52 - 55]. Common tendency is that the turbulent fluctuations lead to strong distortion of the initial  $N$ -wave and to weakening in average of most important shock wave parameters, which affects the environment (decrease of mean peak positive pressure, corresponding increase of the mean rise time). However, there exists a probability of measurement of acoustic waves with very high amplitude and short rise time, and this is undesirable due corresponding increase in the sonic boom annoyance. Specific values of probability depend on various factors including the intensity of turbulent fluctuations and the width of the turbulent layer.

### *2.3.3 Effect of propagation distance through turbulent medium on the statistics, average and peak characteristics of the acoustic $N$ -wave*

In addition to investigating the effect of the intensity of turbulent fluctuations on the main acoustic wave parameters, it is also interesting to study the dependence of these parameters on the propagation distance in turbulent medium. For this purpose, it is necessary to place the source of acoustic waves or microphones inside the turbulent velocity field. Microphone, placed in the turbulent flow in addition to the acoustic pressure will measure the hydrodynamic pressure that will lead to the diminishing of its dynamic range and therefore to inevitable error of measurements. If the source is positioned inside the turbulent flow, the parameters of the generated acoustic wave may fluctuate with the velocity ripples, which change the temperature and humidity of the medium around the source.

To estimate the dependence of the main acoustic wave parameters on temperature and humidity of the medium, the acoustic waves were measured beginning with the cold start of the

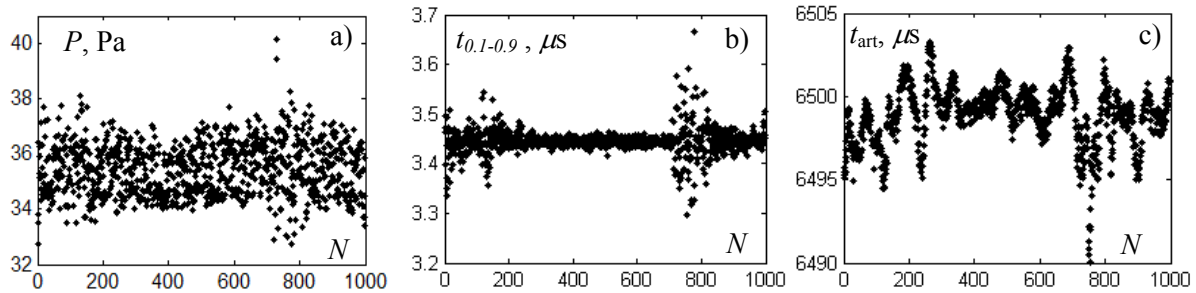


**Fig. 2.22** Distributions of peak positive pressure (a), rise time (b) and arrival time (c) of the shock wave, measured at distance 2.19 m from the spark source during its cold start.  $N$  is the spark consecutive number. source in homogeneous air until the  $N$ -wave generation became stable. The results of peak positive pressure (a), rise (b) and arrival (c) times measurement are presented in Fig. 2.22. It is seen, that the variation of wave parameters with spark number (with time) is very small and can be neglected. The values of the peak positive pressure are mainly enclosed within the 2.5 Pa interval ( $\sim 7\%$  of mean peak positive pressure) which does not depend on time (source heating). Rise time varies mainly within  $0.1\ \mu\text{s}$  interval and arrival time - within  $10\ \mu\text{s}$  interval. Thus, source parameters are not very strong affected by the temperate changes in the environmental conditions like humidity and temperature.

Consider now that the source is placed inside the turbulent field, that is the temperature and humidity of the air in its vicinity depend on the turbulent flow parameters. These parameters vary slightly in time and therefore the source can be considered as stable even inside the inhomogeneous turbulent field. Moreover, characteristic timescale of acoustic wave generation is much shorter than the characteristic timescale of turbulent fluctuations, and, therefore, it is assumed with a good confidence that the spark is not shifted by the medium velocity fluctuations.

According to the previous discussion, it is possible to place the acoustic source inside the turbulent field and to estimate the variation of the pressure level with the distance between the source and the microphone. Changes in environmental parameters (temperature, humidity and turbulent velocity) do not affect significantly the characteristics of the acoustic source and therefore do not change significantly the measured acoustic pressure field. In this configuration we observed fluctuating displacements of the source around its stationary position due to the vibration of the mounting support. However this displacement was of the order of 10 mm for  $U_{jet} = 20\ \text{m/s}$ , and such difference in the propagation path of acoustic wave had a negligible effect on the wave rise time and the wave amplitude. Thermoviscous absorption and nonlinear dissipation will give less than 0.5% change in amplitude on 10 mm at distances longer than 600 mm from the source. Spherical divergence will give a pressure decrease not higher than 2%. Only the arrival time can be strongly affected, as soon as 10 mm of displacement gives about

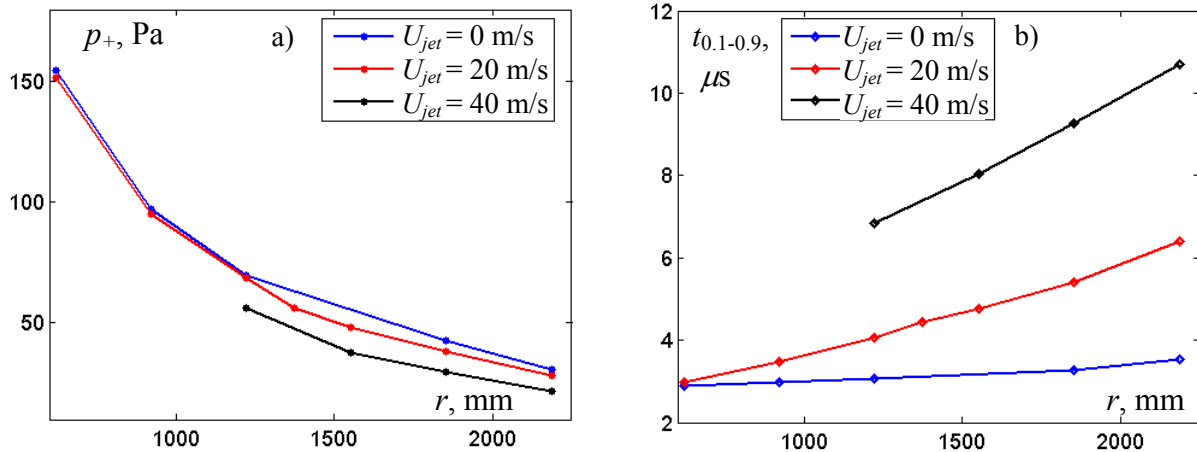


**Fig. 2.23** Dependence of mean peak positive pressure (a) and mean rise time of the wave shock front (b) on the distance of acoustic wave propagation in inhomogeneous turbulent medium of different intensity.

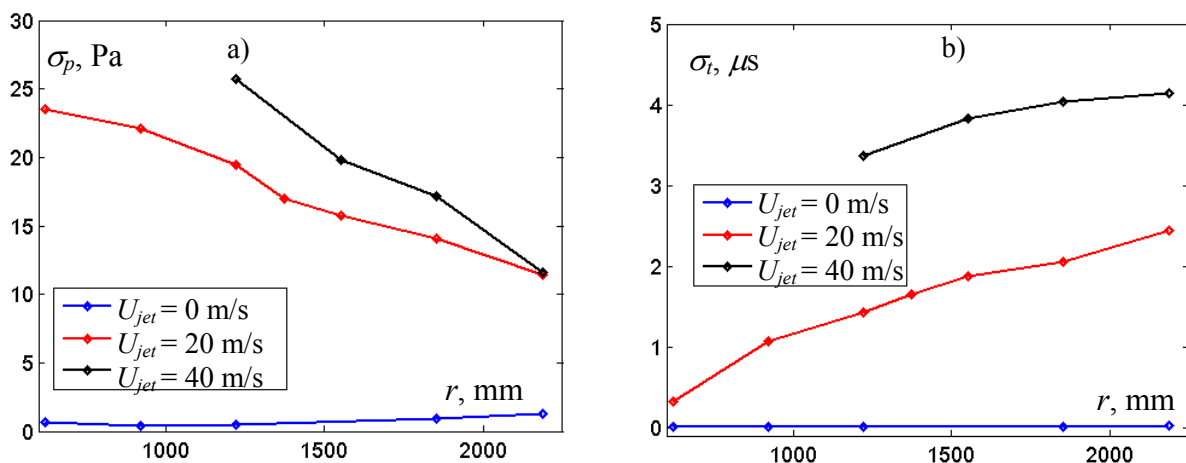


**Fig. 2.24** Dependence of standard deviation of peak positive pressure (a) and rise time of the wave shock front (b) on the distance of the acoustic wave propagation in inhomogeneous turbulent medium of different intensity.

30  $\mu$ s retard in arrival time (30% of arrival time fluctuation, measured with the fixed mounting). Due to the source displacement, it was not possible to move the source further inside the turbulent field than 400 mm for when the jet flow velocity was  $U_{jet} = 40$  m/s.

In Fig. 2.23 are presented the dependencies of acoustic wave mean peak positive pressure and shock front mean rise time on the propagation distance inside the turbulent field for different jet flow velocities (red line –  $U_{jet} = 20$  m/s, black line –  $U_{jet} = 40$  m/s) or in still medium (blue line). Presented data correspond to the measurements by the microphone, situated at the axis of the acoustic experimental setup. At each distance from the source, 2000 distorted waveforms were measured. As it was discussed previously, the peak positive pressure decreases in turbulent field and rise time increases with augmenting flow velocity. These conclusions are confirmed by Fig. 2.23. Same tendency remains with the augmenting the acoustic wave propagation distance.

However, there is also a new point, which is interesting to outline. For propagation distances up to 1200 mm, the mean value of the peak positive pressure in turbulent medium does not differ from that in still medium (for  $U_{jet} = 20$  m/s). The distance, where the difference

between two curves becomes notable, can be associated with the distance of caustics formation, related to the large-scale inhomogeneities (see §5.2-5.3). With the further increase of the distance, the difference between turbulent and still medium cases again becomes smaller. This happens due to the absorption and relaxation effects, which are frequency dependent. The rise time of the wave, measured in still medium, is much shorter than the rise time of the wave, measured in turbulent medium. Therefore, in still medium the waveform contains much higher frequencies, which are faster suppressed by absorption and relaxation effects.

Shown in Fig. 2.24 are standard deviations of characteristic acoustic wave parameters considered in Fig. 2.23. It can be seen that the absolute value of standard deviation of peak positive pressure (Fig. 2.24a) decreases with the distance from the receiver due to suppression of high amplitudes, whereas its relative value  $\sigma_p/\langle p_+ \rangle$  increases. At the distance 1800 mm from the source and  $U_{jet} = 40$  m/s it is almost equal to  $\sigma_p/\langle p_+ \rangle = 1$ . It is obvious that increasing the distance between the source and the microphone will result in an increase of the standard deviation of the shock front rise time (Fig. 2.24b) due to effects of turbulent medium. At the same time, the rise time standard deviation increases due to the formation of very steep shock fronts in the areas of focusing. Thus, probability density distribution of peak positive pressure with distance becomes thinner and probability density distribution for the rise time becomes wider.

### § 2.4 Characteristic scales: atmosphere and laboratory experiment

Characteristic spatial and time scales of sonic boom propagation problem in real turbulent atmosphere and shock waves in laboratory scale experiments are compared in Table 2.1 [52 - 54]. It is seen that with the scaling coefficient equal to 1000, spatial scales of inhomogeneous medium generated in laboratory experiment well coincide with atmospheric turbulence scales. Therefore, in both cases the width of the turbulent layer, through which the acoustic wave

**Table 2.1** Comparison of spatial and time scales of sonic boom problem in atmosphere and shock wave propagation problem in laboratory experiment.

	Atmosphere	Laboratory scaled experiment
Turbulence integral length scale, $L_f$	100-200 m	16-18 cm
Turbulent layer thickness	1-2 km	1.5 – 2 m
Amplitude of velocity fluctuations	0 - 30 m/s	0 - 40 m/s
Peak positive pressure, $p_+$	10 – 800 Pa	10 -1000 Pa
Pulse duration	90-300 ms	30-50 $\mu$ s
Rise time, $t_{0.1-0.9}$	0.5-10 ms	3 – 10 $\mu$ s

propagates, is equal to ten integral length scales of the turbulence:  $L_t \approx 10L_f$ . At the same time, one integral length scale is equal to ten acoustic wavelengths. As for the amplitudes of acoustic pulses, in the laboratory scale experiment they are of the same order as in the field experiments. This parameter determines the influence of nonlinear effects on acoustic wave propagation and therefore should not be scaled. The rise time of the shock front could not be properly compared as soon as in both cases it is determined by the microphone spectral characteristics. In addition, the effects of thermoviscous absorption and effects of relaxation, which in contrast to nonlinear effects change significantly by the transition from the field scale to the laboratory scale. So in the case of laboratory scale experiment the dominant mechanism is the thermoviscous absorption mechanism, whereas in field experiments – relaxation mechanisms [63].

## § 2.5 Conclusion

A new arrangement of the ECL experimental downscaled setup used to investigate the propagation of short acoustic pulses of high amplitude (duration 30  $\mu$ s, amplitude  $\sim 1000$  Pa) in turbulent flow with mean velocity and velocity fluctuations amplitude up to 40 m/s was designed and built up. Scaling relations between characteristic parameters of generated turbulent field and parameters of acoustic pulse are in a good agreement with those of sonic boom and atmospheric turbulent boundary layer. It is shown that the energy spectrum of generated turbulence was very well described by a modified von Karman spectrum. This allows us to conclude that the modified von Karman model can be used in our numerical simulations.

It is shown experimentally that in randomly inhomogeneous moving medium the decrease of mean peak positive pressure of the shock wave, the increase of mean rise time, and the decrease of mean arrival time are observed with increasing the intensity of medium turbulent fluctuations. However, there still exists a probability of observation of very steep shock fronts with very high amplitudes, which are up to 4 times higher than those measured in homogeneous medium at the same propagation distance from the source. In addition, mean peak positive pressure of the pulse starts to decrease faster in turbulent air than in homogeneous air starting from the distance of 1.2 m ( $U_{jet} = 20$  m/s), whereas the shock front rise time augments faster in turbulent medium starting from the shorter propagation distance.

It is shown that the measuring system has a limited frequency response that affects the measurements of the shock fronts in the focusing zones. This limitation explains why the rise times measured at focus are longer than those expected from the theory. Therefore, to estimate

correctly the parameters of the acoustic wave it is necessary to know the frequency response of the measuring system. This problem is addressed in Chapter 3.



## Chapter 3

### **MEASUREMENT AND MODELLING OF SPHERICALLY DIVERGING SHOCK PULSES IN RELAXING AIR. CALIBRATION OF THE MICROPHONE.**

The problem to determine the frequency response of the measuring system in laboratory conditions, posed in the previous chapter, appears to be a very important problem [101 - 106]. In fact the initial characteristics of microphones provided by the manufacturer are modified by aging, or by any others reasons as the changes in environmental conditions of measurements or the use of different settings of microphone (with or without grid, released or mounted in a baffle, different positioning inside the baffle). So the knowledge of the measuring system frequency response becomes necessary in order to have accurate estimation of the measured parameters of the acoustic pulse. To determine these spectral characteristics, the laboratory and numerical experiments on *N*-wave propagation in homogeneous air were conducted.

In the laboratory experiment, we used 1/8 inch *Brüel & Kjaer* microphones with a limited frequency band of 140 kHz to measure acoustic pulses propagating from the spark source. Measurements were done at distances up to 2 m from the source in a quiet ambient room. In the numerical modelling, the modified Burgers equation that includes the combined effects of spherical spreading of the wave, nonlinear waveform distortion, thermoviscous dissipation, and  $N_2$  &  $O_2$  relaxation effects was employed [107]. Initially ideal *N*-waveform with a shock front defined in accordance with physical effects (nonlinearity and thermoviscous absorption) was used as an initial boundary condition to the model given at some distance from the source. Time-domain numerical algorithm was developed to simulate *N*-wave propagation. This combined experimental and modelling approach allowed us not only to calibrate the measurement system but also to validate the modelling *versus* experiment, and to better understand the effects of relaxation, thermoviscous absorption, and acoustic nonlinearity on the *N*-wave distortion under experimental conditions. Note, that investigations presented here were done for the experiment,

conducted at different date and time and under different environmental conditions than in the experiment presented in Chapter 2.

The peculiarity of the calibration method proposed in this work is that it allows obtaining spectral characteristics of the measuring system in a wide band of frequencies at once. This method is based on an *a priori* information about nonlinear propagation of high amplitude pulsed signals. It is known, that due to strong nonlinear effects, the high amplitude acoustic pulse takes the form of an  $N$ -wave with a thin shock front. Therefore, in numerical modelling, the initial conditions can be taken in the form of an ideal  $N$ -wave.

Such approach based on nonlinear propagation effects has been previously used in hydroacoustics for absolute calibration of hydrophones in water by Andreev *et al.* [108]. The approach is based on the assumption that the change in  $N$ -wave amplitude while propagating in the nonlinear medium can be described based on the simple wave equation and the relations of the weak shock theory. Similar to that, exact analytic solution of the simple wave equation for the change of slope in the sawtooth waveform can be also used to calibrate the hydrophones [Andreev *et al.*, 109]. However, these approaches cannot be directly applied to calibrating microphones. In the atmosphere, in addition to nonlinear effects, thermoviscous absorption and relaxation phenomena strongly influence the wave propagation and thus the amplitude or the slope of the waveform.

However, nonlinear calibration methods that employ weak shock theory and propagation in lossless medium have been also used in atmospheric acoustics to determine the sensitivity of the measuring system. These methods are also based on nonlinear propagation of high amplitude pulses: the dependence of the shock front speed [Romanenko, 110] or pulse duration [Wright *et al.*, 43] on the shock amplitude. The frequency dependent absorption and relaxation have not been accounted for in both cases (the speed of the shock front also depends on relaxation effects). In contrast to the previously developed approaches, the method proposed here allows calibration of microphones in dissipative media. Moreover, in addition to measuring system sensitivity, its spectral characteristics (amplitude and phase frequency responses) are also obtained.

### § 3.1 Acoustic measurements. Mean and peak characteristics of the $N$ -wave parameters

Calibration acoustic measurements in still air were conducted using the same experimental setup as described in details in §2.2. Acoustic waveforms were measured at the distances starting from  $r = r_0 = 0.15$  m up to  $r = 2$  m from the spark source. At each distance, 100 waveforms were recorded. The results of the analysis of the  $N$ -shape output voltage from the microphone are summarized in Fig 3.1. The parameters of the electric signal without conversion into pressure (usually found as the ratio between the voltage and the sensitivity measured using a calibrator at 1 kHz, 1Pa) are shown: the calculated mean values of the peak positive voltage (a), half duration (b), shock front rise time (c), and arrival time (d) of the voltage pulse. These values correspond to the analogous parameters of the acoustic waveform. The measurements done for each individual spark are marked with points. We can observe a slight dispersion in the measured wave parameters due to small variations in the spark energy and to its position between the electrodes when flashing. Therefore, maximum standard deviation of peak positive voltage was not bigger than 16 mV (< 3 %), of half duration – 0.25  $\mu$ s (< 2 %), of rise time – 0.03  $\mu$ s (< 1 %), and of arrival time – 0.6  $\mu$ s. Such fluctuations in arrival time correspond to only 0.2 mm displacement of the spark between the electrodes

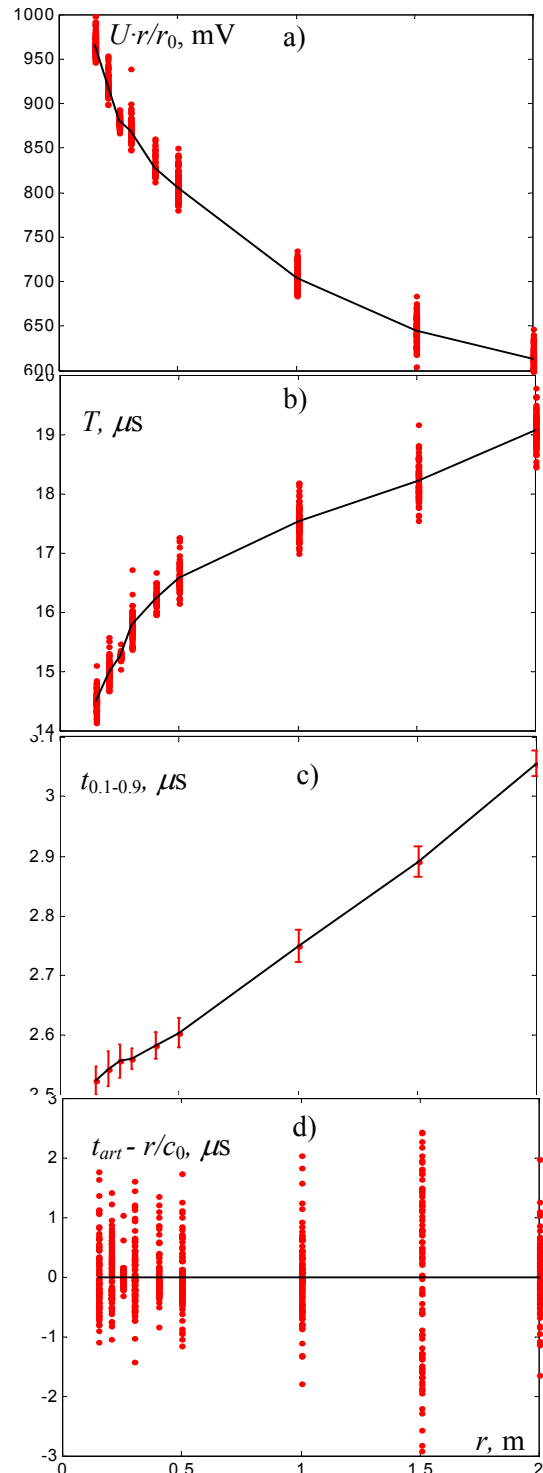


**Fig. 3.1** Dependence of mean acoustic wave parameters (tension pulse parameters) on the distance between the source and the microphone. (a) – mean peak positive pressure, (b) – mean half duration, (c) – mean shock front rise time, (d) – mean relative arrival time. Points – measured parameters of individual pulses.

## § 3.2 Theoretical model

### 3.2.1 Modified Burgers equation for divergent waves in relaxing medium

The Burgers equation, extended to include relaxation processes and spherical divergence of nonlinear wave in homogeneous media can be written in the following form [111]:

$$\frac{\partial p}{\partial r} + \frac{p}{r} = \frac{\beta}{\rho_0 c_0^3} p \frac{\partial p}{\partial \tau} + \frac{b}{2\rho_0 c_0^3} \frac{\partial^2 p}{\partial \tau^2} + \sum_{\nu=1}^M d_\nu \frac{\partial}{\partial \tau} \int_{-\infty}^{\tau} \exp(-(\tau - \tau')/\tau_\nu) \frac{\partial p}{\partial \tau'} d\tau'. \quad (3.1)$$

Here  $p$  is the acoustic pressure,  $r$  is the radial propagation coordinate,  $\tau = t - (r-r_0)/c_0$  is the retarded time,  $c_0$  is the ambient sound speed at low frequencies,  $r_0$  is the reference distance to set boundary conditions,  $\rho_0$  - the air density,  $\beta$  - the coefficient of nonlinearity in air,  $b$  - the coefficient of viscosity,  $M$  - the total number of relaxation processes. Each relaxation process  $\nu$  is characterized by two parameters: relaxation time  $\tau_\nu$  and coefficient  $d_\nu = (c_\infty^\nu - c_0)/c_0^2 = c_\nu/c_0^2$ , where  $c_\infty^\nu$  is the so called frozen sound speed of acoustic signal propagation through the medium with relaxation time much longer than the effective duration of the signal  $T_s \ll \tau_\nu$ . The second term on the left hand side of the Eq. (3.1) is responsible for the spherical divergence of the wave, while the right hand side includes nonlinear effects (first term), dissipation due to thermoviscous absorption of the medium (second term), and relaxation processes (the last term), associated with the excitation of oscillatory energy levels of media molecules [48, 62]. For the Eq. (3.1) to be valid, it is necessary that the ratio  $\lambda/r \ll 1$ . This is true in the current laboratory-scaled experiments ( $\lambda \sim 10$  mm,  $r > 150$  mm).

The number of relaxation processes  $M$  in Eq. (3.1) is equal to the number of molecule types in the propagation medium. Atmosphere consists mainly of nitrogen and oxygen molecules, which define its relaxing properties and corresponding frequency dependence of the sound speed and absorption [48, 62]. The effect of relaxation on the waveform distortion therefore will strongly depend on the frequency content of the shock waves generated in laboratory experiments. The shock waveform and corresponding frequency spectrum that will be further used in simulations as a boundary condition given at the distance  $r_0$  from the source are shown in Fig. 3.2(a,b). The waveform is an ideal  $N$ -shape pulse with infinitely short rise time and main parameters, duration (30  $\mu$ s) and amplitude (1000 Pa), close to those measured experimentally at the nearest distance to the source  $r_0 = 15$  cm. Characteristic relaxation frequencies of oxygen ( $f_1 = 1/(2\pi\tau_1) \sim 26500$  Hz) and nitrogen ( $f_2 = 1/(2\pi\tau_2) \sim 300$  Hz)

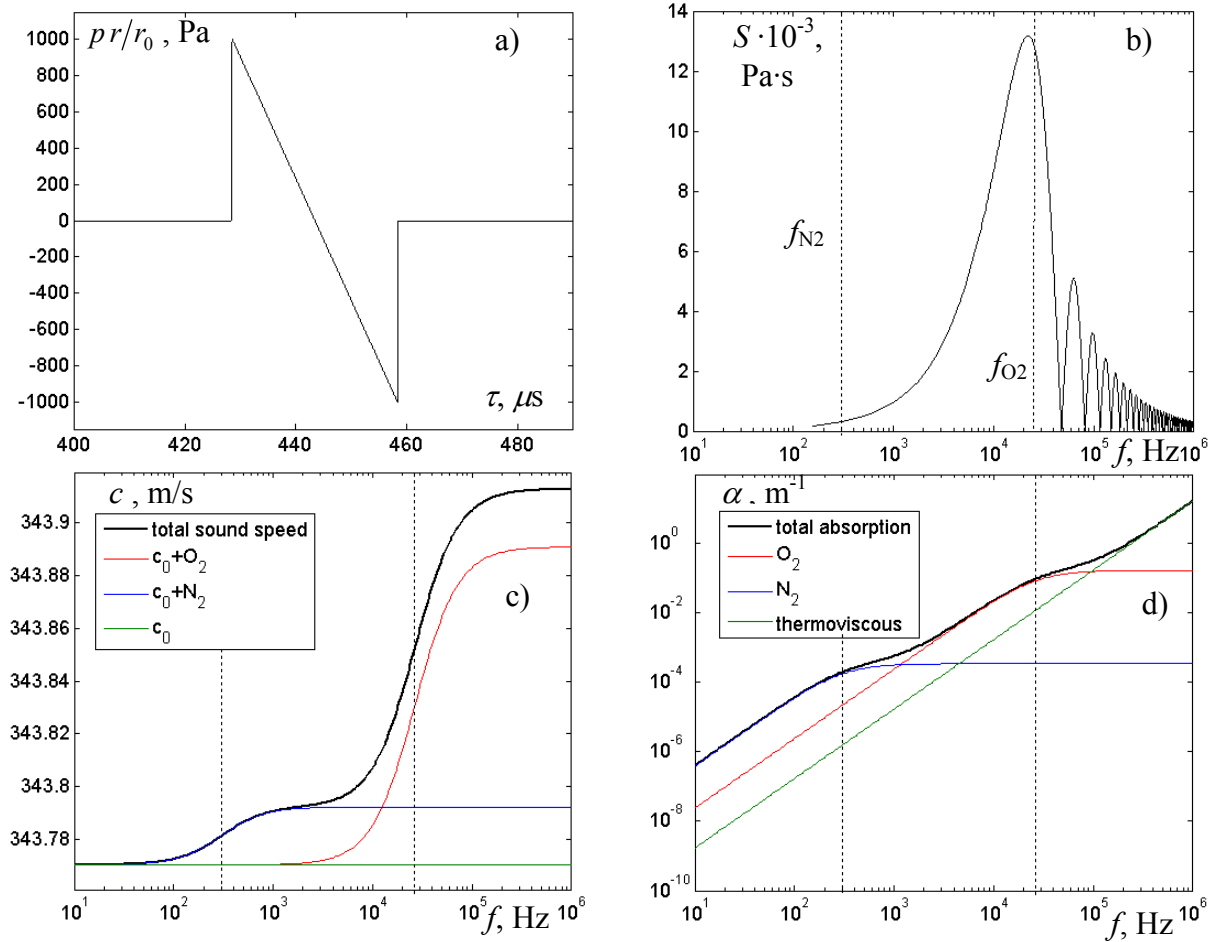


**Fig. 3.2.** Initial  $N$ -pulse waveform (a) and its spectrum (b). Dependence of the sound speed (c) and absorption (d) on frequency due to relaxation in atmosphere. Characteristic relaxation frequencies of oxygen  $O_2$  and nitrogen  $N_2$  are shown with vertical dotted lines.

molecules were calculated according to the humidity (34%) and temperature (20°C) of the experimental conditions and are shown in the Fig. 3.2(b-d) as vertical dotted lines [62].

The relaxation frequency of oxygen lies near the maximum of the  $N$ -wave spectrum, while the nitrogen frequency corresponds to the nearly zero part of the spectrum at low frequencies. The nitrogen relaxation process thus should have very little effect on the shock wave propagation. The frequency dependence of the sound speed and absorption that incorporates the effects of relaxation can be obtained from the linearized Eq. (3.1) [Rudenko *et al.*, 48]:

$$c = c_0 \left[ 1 + c_0 \sum_{\nu=1}^2 \frac{d_{\nu} \cdot (\omega \tau_{\nu})^2}{1 + (\omega \tau_{\nu})^2} \right] \quad \alpha = \frac{b \omega^2}{2 \rho_0 c_0^3} + \sum_{\nu=1}^2 \frac{d_{\nu}}{\tau_{\nu}} \frac{(\omega \tau_{\nu})^2}{1 + (\omega \tau_{\nu})^2}. \quad (3.2)$$

These dependencies are shown in Fig. 3.2, c) and d), respectively. The presence of relaxation will change the wave amplitude due to additional absorption, and also the arrival time of the pulse due to the fact that the shock front is built of high frequencies propagating faster than the ambient sound speed  $c_0$ . The effect of nitrogen on arrival time and amplitude is expected to be negligible in comparison with that of oxygen. The sound speed variations due to  $N_2$

relaxation is about 5 times less than those introduced due to  $O_2$  relaxation (Fig. 3.2c), and the effective increase of absorption for nitrogen  $N_2$  is of three orders less than for oxygen  $O_2$  (Fig. 3.2d).

### 3.2.2 Numerical algorithm

To perform numerical simulations it is convenient to rewrite the Eq.(3.1) in nondimensional form:

$$\frac{\partial V}{\partial \sigma} = V \frac{\partial V}{\partial \theta} + \frac{1}{\Gamma} \exp\left(\frac{x_s}{r_0} \sigma\right) \frac{\partial^2 V}{\partial \theta^2} + \sum_{\nu=1}^2 D_\nu \exp\left(\frac{x_s}{r_0} \sigma\right) \frac{\partial}{\partial \theta} \int_{-\infty}^{\theta} \exp\left(-\frac{\theta-\theta'}{\theta_\nu}\right) \frac{\partial V}{\partial \theta'} d\theta'. \quad (3.3)$$

Here  $V = pr/(p_0 r_0)$  is the dimensionless acoustic pressure,  $\sigma = r_0 \ln(r/r_0)/x_s$  is the spatial dimensionless propagation coordinate,  $x_s = \rho_0 c_0^3 T_0 / \beta p_0$  is the characteristic nonlinear distance;  $\theta = \tau/T_0$  is the dimensionless time,  $\Gamma = 2\beta p_0 T_0/b$  is the Gol'dberg number which determines the relative effect of nonlinearity and thermoviscous absorption;  $\theta_\nu = \tau_\nu/T_0$  is the dimensionless relaxation time and  $D_\nu = \rho_0 c_0^3 d_\nu/\beta p_0 = \rho_0 c_0 c_\nu/\beta p_0$  is the dimensionless relaxation coefficient for the processes  $\nu = 1, 2$ . To avoid limitations of the validity in the model, we kept both oxygen and nitrogen relaxation effects in the Eq. (3.3) and in further numerical simulations. The waveform parameters measured at the closest distance  $r_0$  from the source, such as peak positive pressure  $p_0$  and half duration  $T_0$ , were chosen to be the reference values.

To obtain a solution for the dimensionless pressure  $V$ , the Eq.(3.3) was solved numerically in the time domain using an operator splitting procedure. At each grid step in propagation distance  $\sigma$  the equation was divided in three physically consistent equations, describing different physical effects:

$$\text{nonlinearity} \quad \frac{\partial V}{\partial \sigma} = \frac{1}{2} \frac{\partial V^2}{\partial \theta}, \quad (3.4)$$

thermoviscous absorption

$$\frac{\partial V}{\partial \sigma} = \frac{1}{\Gamma} \exp\left(\frac{x_s}{r_0} \sigma\right) \frac{\partial^2 V}{\partial \theta^2}, \quad (3.5)$$

$$\text{relaxation} \quad \frac{\partial V}{\partial \sigma} = \sum_{\nu=1}^2 D_\nu \exp\left(\frac{x_s}{r_0} \sigma\right) \frac{\partial}{\partial \theta} \int_{-\infty}^{\theta} \exp\left(-\frac{\theta-\theta'}{\theta_\nu}\right) \frac{\partial V}{\partial \theta'} d\theta'. \quad (3.6)$$

Here the simple wave Eq. (3.4) is written in flux conservative form.

At the first step of the algorithm, nonlinear effects, Eq. (3.4), are taken into account using Godunov-type central flux-conservative scheme of the second-order accuracy in time  $\theta$  and first-order accuracy in propagation coordinate  $\sigma$  [Kurganov *et al.*, 112]. This scheme has small

internal viscosity and it is sufficient to have only 2-3 time points per shock to describe its evolution with high accuracy and stability without introducing additional physical absorption to suppress high frequencies (for more details refer to § 4.3.2).

At the second step, previously obtained solution is used as an initial condition to compute thermoviscous dissipation effects, described by Eq. (3.5). An explicit central finite difference scheme of the second-order accuracy in time  $\theta$  and first-order accuracy in propagation coordinate  $\sigma$  is used:

$$V(\sigma + h_\sigma, \theta) = V(\sigma, \theta) + \frac{h_\sigma}{\Gamma} \exp\left(\frac{x_s}{r_0} \sigma\right) (V(\sigma, \theta - h_\theta) - 2V(\sigma, \theta) + V(\sigma, \theta + h_\theta)). \quad (3.7)$$

Finally, at the last step of numerical procedure, the relaxation effects (3.6) are accounted for. To build a numerical model it is convenient to rewrite Eq. (3.6) following the approach presented in the paper [111]:

$$\left(\frac{1}{\theta_v} + \frac{\partial}{\partial \theta}\right) \frac{\partial V}{\partial \sigma} = D_v \exp\left(\frac{x_s}{r_0} \sigma\right) \frac{\partial^2 V}{\partial \theta^2}. \quad (3.8)$$

The Eq. (3.8) is then calculated using the Crank-Nicholson algorithm of the second-order accuracy in time  $\theta$  and spatial propagation coordinate  $\sigma$ .

$$\begin{aligned} -(a+b)V(\sigma - h_\sigma, \theta) + (1+2b)V(\sigma, \theta) + (a-b)V(\sigma + h_\sigma, \theta) = \\ (b-a)V(\sigma, \theta - h_\theta) + (1-2b)V(\sigma, \theta) + (a+b)V(\sigma, \theta + h_\theta) \end{aligned} \quad (3.9)$$

where coefficients  $a = \theta_v / (2h_\sigma)$  and  $b = D_v \theta_v h_\sigma / (2h_\theta^2)$ , and  $h_\sigma$  and  $h_\theta$  are spatial coordinate and time steps, respectively. Boundary conditions at time window edges are given with the following relations:  $V(\sigma + h_\sigma, \theta_{\min}) = V(\sigma, \theta_{\min})$  and  $V(\sigma + h_\sigma, \theta_{\max}) = V(\sigma, \theta_{\max})$ . During numerical modelling the attention should be paid to the selection of the grid steps. Usually the time step is much smaller than the relaxation time of the medium, and therefore coefficient  $a \ll 1$ . If the spatial step is also very small, then the coefficient  $b$  is much smaller than  $a$ :  $b \ll a$ . Therefore, non diagonal elements of the coefficients matrix of the Eqs. (3.9) for different steps are dominant on the diagonal elements. The problem becomes ill-posed, that leads to large numerical errors. Therefore, the spatial grid step along the propagation distance should not be too small.

To validate the algorithm of nonlinear operator modelling, numerical and analytical solutions to the simple wave equation were compared for an ideal  $N$ -wave propagation [47, 48]. To validate the accuracy of the combined nonlinear and relaxation modelling, the numerical results were compared with the stationary Polyakova solution for monorelaxing medium [113]:

$$\theta = \theta_0 \ln \frac{(1+V)^{D_0-1}}{(1-V)^{D_0+1}}, \quad (3.10)$$

where  $\theta_0$  and  $D_0$  are the parameters of the considered relaxation process. Ambiguity in the Polyakova solution for  $D_0 \leq 1$  is eliminated by application of the simple wave theory, which gives the following relation for the shock coordinate:

$$\theta_s = -\theta_0 \ln[4D_0^{1+D_0} (1-D_0)^{1-D_0}] \quad (3.11)$$

In Fig. 3.3 with the red curve is presented the solution to equations (3.10-3.11) in the form of the stationary wave, propagating in the monorelaxing medium with the following characteristic parameters:  $\theta_0 = 1$  and  $D_0 = 0.5$ .

With blue curve, the numerical solution to the Eq. (3.3) is presented. To ensure the stability of the numerical algorithm the calculation was done with accounting for the small but finite thermoviscous absorption  $\Gamma=3000$ , which influences only the width of the shock front, and almost does not affect its amplitude. In addition, the simulations were done for sufficiently long distances  $\sigma$ , where the spherically diverging wave can be assumed as a plane one. At distance  $\sigma = 10$  for the following computational steps:  $h_\sigma = 0.002$  and  $h_\theta = 0.0262$ , the maximum error in numerical solution as compared to the analytic results was less than 1%.

### 3.2.3 Effects of nonlinearity, thermoviscous absorption and relaxation on the acoustic wave propagation

For numerical simulations of nonlinear  $N$ -wave propagation in relaxing medium the specific parameters of the medium, corresponding to those of the laboratory-scaled experiment were set:  $\beta = 1.21$ ,  $b = 4.86 \cdot 10^{-5} \text{Pa} \cdot \text{s}$ ,  $\rho_0 = 1.29 \text{ kg/m}^3$ ,  $c_0 = 343.77 \text{ m/s}$ . The parameters of relaxation processes were calculated using empirical expressions for the relative humidity 34%, temperature 293 K and ambient pressure level of 1 atmosphere:  $c_1 = 0.11 \text{ m/s}$ ,  $\tau_1 = 6.0 \mu\text{s}$  ( $O_2$ ),  $c_2 = 0.023 \text{ m/s}$ ,  $\tau_2 = 531 \mu\text{s}$  ( $N_2$ ) [62]. The boundary condition was set at the distance  $r_0 = 15 \text{ cm}$  as an ideal  $N$ -pulse with characteristic experimental values of amplitude  $p_0 = 1000 \text{ Pa}$  and half-duration  $T_0 = 15 \mu\text{s}$  (Fig. 2.1a). The corresponding values of nondimensional parameters in the Eq. (3.3) are the following:  $\Gamma = 746.9$ ,  $D_1 = 0.04$ ,  $D_2 = 8.43$ ,  $\theta_1 = 0.4$ ,  $\theta_2 = 35.4$ ,  $x_s/r_0 = 4.33$ .

To illustrate the relative effects of nonlinearity, thermoviscous absorption, and relaxation

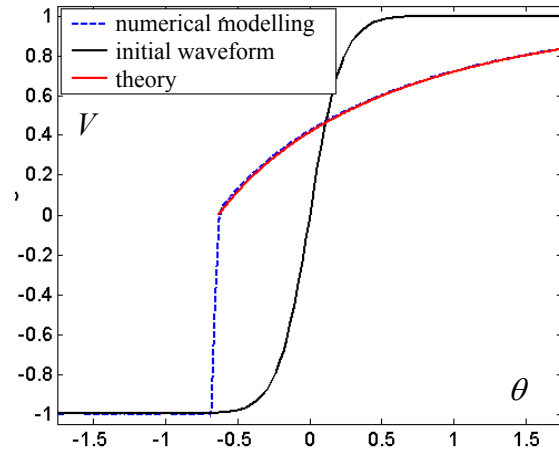


**Fig. 3.3** Comparison of the numerical solution to the Eqs. (3.3) (blue line) with the analytical Polyakova solution for monorelaxing medium in the form of stationary wave (red line). Black line is the initial waveform (hyperbolic tangent)

under experimental conditions, the shock waveforms were calculated numerically at the distance  $r = 6$  m from the source assuming different regimes of propagation (Fig. 3.4). Various physical effects were alternately included into the model. Linear propagation in ideal medium was considered first, then only acoustic nonlinearity was included, then relaxation effects only, thermoviscous absorption only, and finally, all the above-mentioned effects. In order to “exclude” spherical divergence of the wave, the acoustic pressure in all solutions was multiplied by the ratio of the current propagation distance  $r$  to the initial one  $r_0 = 15$  cm from the source. If only the

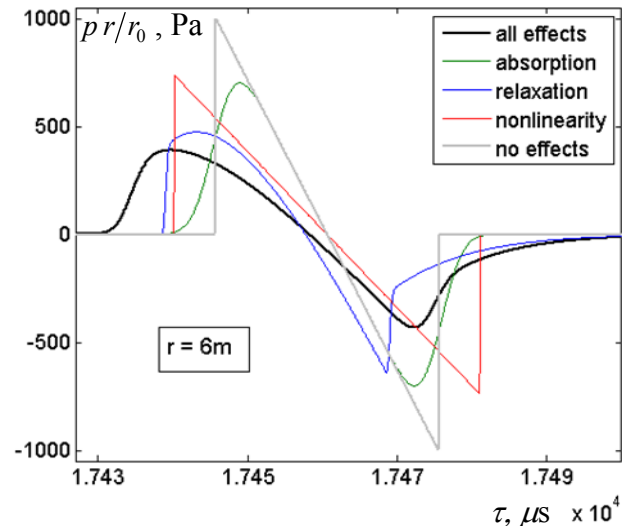


**Fig. 3.4.**  $N$ -pulse waveforms calculated at the distance  $r = 6$  m from the source with alternate account for different physical effects: ideal linear medium (no effects, grey line), nonlinearity only (red line), relaxation only (blue line), thermoviscous absorption only (green line), and all the effects (black line). The waveforms are multiplied by the ratio  $r/r_0$  to exclude spherical divergence of the wave.

divergence of the wave is taken into account in simulations (“no effects”, grey line) the corrected waveform does not change with the propagation distance and thus coincides with the initial waveform shown in Fig. 3.2a). Nonlinear propagation (red line) results in classical lengthening of the  $N$ -pulse and corresponding decrease of the shock amplitude [48]. Relaxation processes (blue line) lead to asymmetric waveform distortion and displacement of both front and distal shocks towards the direction of propagation. The peak value of the rounded positive waveform cycle is reduced more than the peak value in the sharp negative tail of the pulse. The pulse length between the front and distal shock fronts, however, does not noticeably change due to relaxation as both shock fronts move with the same speed of high frequencies.

The sharp structure of shock fronts is also not strongly affected by the relaxation. Thermoviscous absorption substantially reduces the shock amplitude and broadens the shock front without changing the symmetry of the pulse and its duration between the half peak pressure levels (green line). It is seen that all the physical effects, nonlinearity, relaxation, and thermoviscous absorption are of comparable importance in reducing the pulse amplitude and thus should all be taken into account in theoretical modelling. The solution corresponding to this case of “all effects” included in the model is shown as a black line. The contributions of different physical effects to the pulse distortion now are clearly seen from the preceding auxiliary cases. The peak pressure values are determined by nonlinearity, relaxation, and

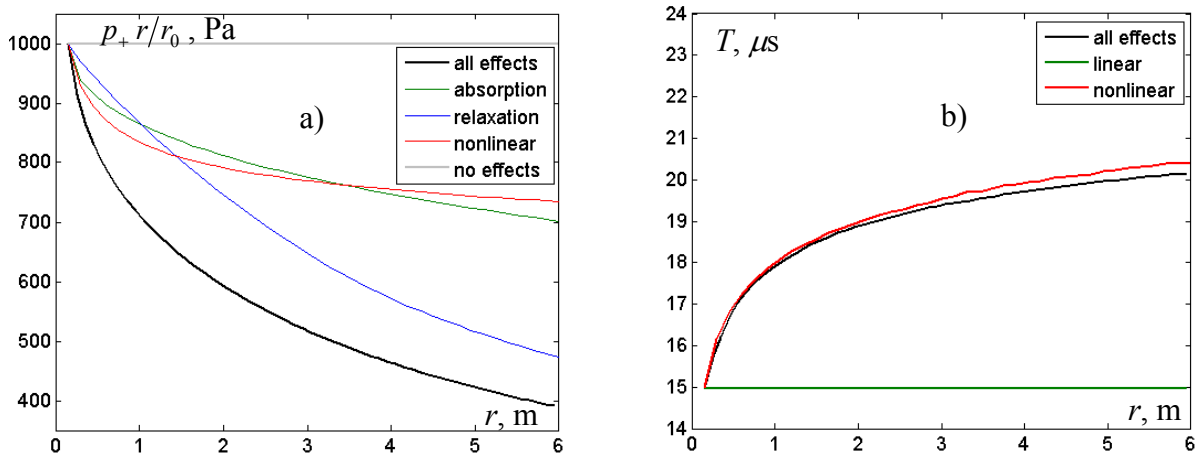


**Fig. 3.5.** Dependence of the peak positive pressure (a) and half duration (b) of the  $N$ -pulse on the propagation distance. Peak positive pressure  $p_+$  is multiplied by the ratio  $r/r_0$  to exclude spherical divergence of the wave.

thermoviscous absorption in comparable extent. The asymmetry of the waveform is due to relaxation and shock broadening is due to thermoviscous absorption. The pulse duration increases mainly due to nonlinear propagation. As nonlinear effects depend on the initial pulse amplitude, this effect gives an opportunity for absolute calibration of the microphone sensitivity based on the measured pulse lengthening at different distances [43].

The relative effects of nonlinearity, relaxation, and absorption on the peak positive pressure  $p_+$  and half pulse duration  $T$  over the propagation path are shown in more details in Fig. 3.5. It is seen that for the peak pressure  $p_+$  nonlinear effects dominate over the relaxation and absorption in diminishing the pulse amplitude up to the distance of approximately 2 meters from the source (Fig. 3.5a). Beyond this distance, nonlinear absorption on the shocks becomes much lower as the shock amplitude decreases due to spherical divergence of the pulse, and the relaxation and absorption effects therefore start to be dominant.

Shown in Fig. 3.5b are the results of simulations for the half pulse duration  $T$  versus the propagation distance  $r$ . As the  $N$ -waveform is strongly asymmetric it is difficult to define its duration correctly in the time domain. Moreover, in case of experimental data, the waveforms are affected by the microphone response and by diffraction on the edges of the microphone. It is proposed here to define the duration of the pulse in the frequency domain by matching the positions of the minima in the calculated or measured pulse spectrum with those in the spectrum of an ideal  $N$ -wave with an infinitely thin front (Fig. 3.2a, b). This definition relies on the assumption that all linear waveform distortions additional to nonlinear lengthening can be represented as multiplication of the pulse spectrum by a transfer function that changes smoothly with frequency and does not shift zero values of the  $N$ -wave spectrum and, consequently, these minima. In contrast to the peak positive pressure which was significantly affected by both nonlinear and relaxation/absorption effects, the pulse duration changes mainly due to the

nonlinear propagation of shock fronts. Small influence of relaxation/absorption processes is observed due to suppression of nonlinear effects by lowering the pulse peak pressure values. However, this influence is almost negligible (Fig. 3.5b). The characteristic scale of nonlinear propagation can be also defined here as an interval with the high gradient of the pulse lengthening curve and is about 2 meters too. Note that the characteristic nonlinear distance estimated here is only applicable for the current experimental conditions, pulse amplitude and duration.

### § 3.3 Calibration of measuring system based on nonlinear effects

To simulate the experiment, an ideal  $N$ -waveform was taken as a boundary condition at the distance of the first measured waveform  $r_0 = 0.15$  m. The initial amplitude and duration of the  $N$ -wave were obtained by matching the duration of pulses measured at various distances from the source and those predicted theoretically at the same distances. As it was previously discussed in § 3.2, the duration of pulses in both cases was calculated from the position of nulls in their spectra. For theoretical predictions, the

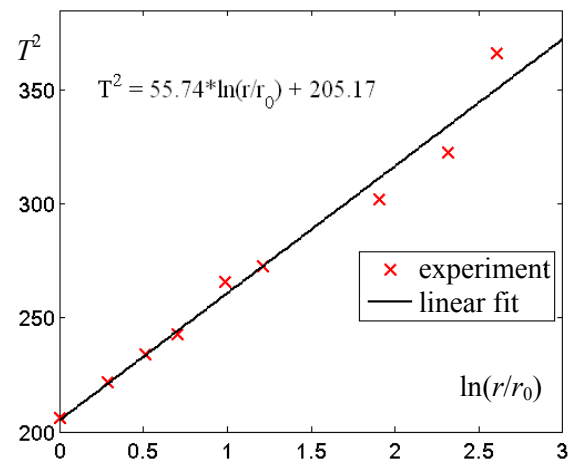


**Fig. 3.6** Linear fit for the squared half duration of the pulse. Correlation coefficient is equal to  $R=0.975$ .

dependence of the dimensionless pulse half duration  $T_n$  versus propagation distance was obtained from the exact analytic solution to the simple wave equation for  $N$ -pulse, Eq. (3.4):

$$T_n = \sqrt{1 + \sigma}, \tag{3.12}$$

or in dimension coordinates

$$T = T_0 \sqrt{1 + \frac{\beta}{\rho_0 c_0^3} \frac{p_0}{T_0} r_0 \ln\left(\frac{r}{r_0}\right)}. \tag{3.13}$$

Here we rely on the results shown in Fig. 3.5b that the change in the pulse duration was mainly due to nonlinear effects, not relaxation or absorption. The two unknown parameters  $T_0$  (initial half duration) and  $p_0$  (peak pressure) of the solution (3.13) which relates linearly  $T^2$  to  $\ln(r/r_0)$  were obtained by fitting the experimental values using the method of least squares. Definition of the initial  $N$ -wave parameters using this method showed a good accuracy as soon as the correlation coefficient was  $R = 0.975$  (Fig. 3.6). Thus, the initial half duration was found to be  $T_0 = 14.32 \mu\text{s}$  and peak positive pressure  $p_0 = 1148$  Pa at the distance of  $r_0 = 0.15$  m from the

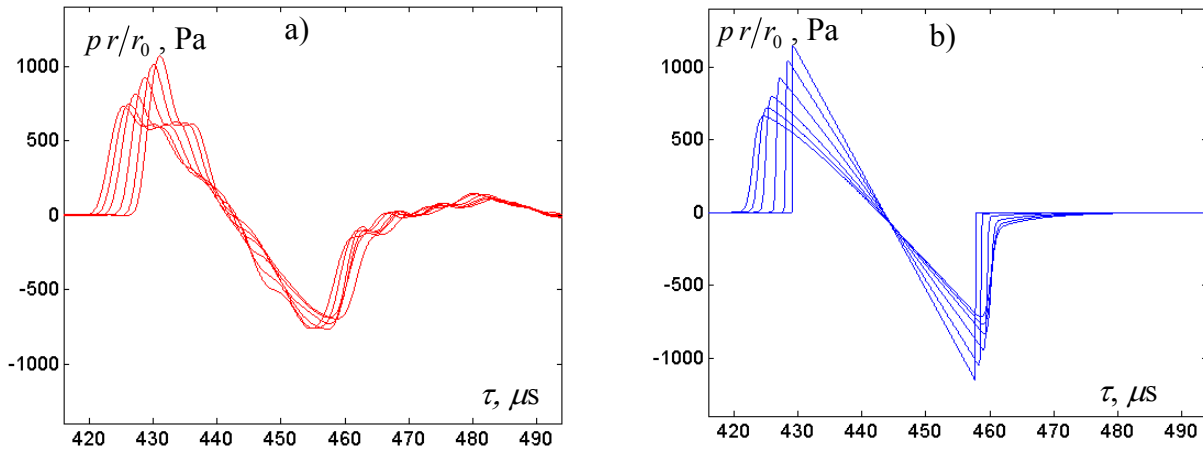


**Fig. 3.7.** Measured (a) and calculated (b)  $N$ -waves at different distances from the source 0.15, 0.3, 0.5, 1, 1.5, and 2 m. Monotonic decrease of the pulse amplitude corresponds to the increase of the propagation distance.

source. For these parameters of the experiment dimensionless coefficients in Eq. (3.3) are:  $\Gamma = 857.4$ ,  $D_1 = 0.035$ ,  $D_2 = 7.34$ ,  $\theta_1 = 0.419$ ,  $\theta_2 = 37.08$ ,  $x_s / r_0 = 3.77$ .

The measured and calculated waveforms are presented in Fig. 3.7(a,b) at the radial distances  $r = 0.15$ , 0.3, 0.5, 1.0, 1.5, and 2 meters, which in the case of experiment were measured with  $\pm 3$  mm error. The experimental waveforms have much more complex structure with several oscillations on the back slope as compared with the calculated  $N$ -waves. The rise times of the measured shock fronts are much longer than those of the calculated ones. These differences between experimental and simulation results can be attributed to the microphone and amplifier limited frequency response, and to the diffraction effects on the edges of the baffle and microphone as there was still a small gap between them.

### § 3.4 Amplitude and phase frequency characteristics of measuring system

In order to check the agreement between the experimental and numerical waveforms it is necessary to know the frequency response of the measurement system, that is the microphone filtering, including diffraction effects, and the response of the amplifier. The frequency response of the measurement system was calculated here as a ratio between the complex spectra of the measured and of the calculated pulses, taken at the same distances from the source. The resulting amplitude frequency response is sufficiently stable for different sparks and presented in Fig. 3.8a (blue line – is the average over the ensemble of derived responses). Obtained response is compared to that of the microphone itself obtained from the manufacturer datasheet (red line). It is seen that the system amplitude frequency response is flat up to 10 kHz, then continues with some  $\pm 3$  dB oscillations, and ends with frequency cut-off at about 150-200 kHz. The structures

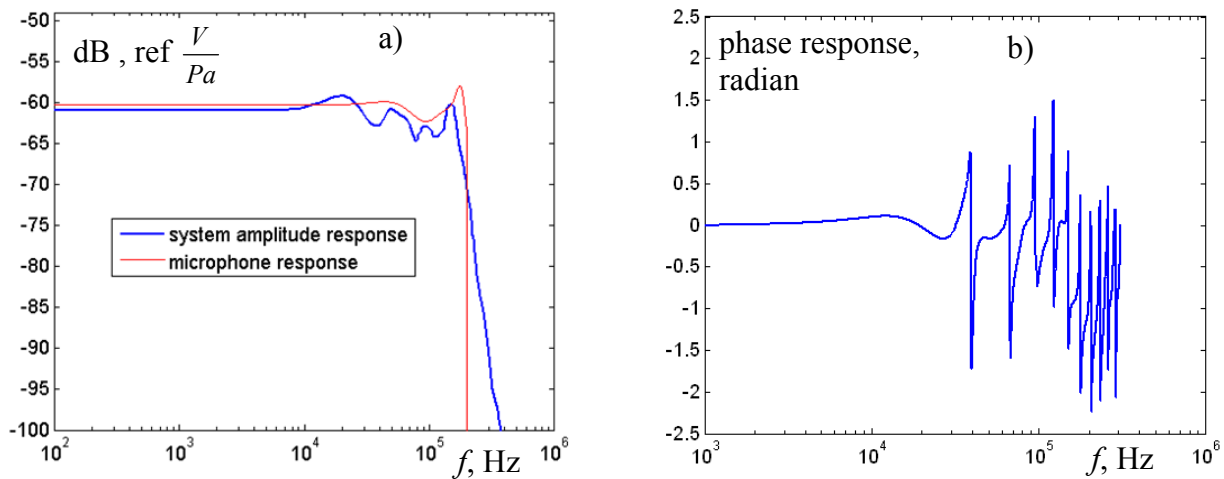


**Fig. 3.8.** Averaged amplitude frequency response (a) and random sample of phase response (b) calculated for the total measuring system (blue line) and response of the microphone, provided by the manufacturer (red line)

of the curves of both filters, calculated and provided by the manufacturer, are pretty close to each other. Distortions of the measured waveforms are, therefore, mainly due to the frequency response of the microphone. The difference between the curves on the plateau is less than 1 dB. Both curves show the microphone resonance at about 100 kHz. However, some additional oscillations in the system amplitude frequency response (compared to the microphone response) are observed between 10 kHz and the cut-off. More difficulties are encountered with the definition of the phase frequency response, as soon as it showed not so good stability from pulse to pulse due to fluctuations of spark characteristics, such as position of formation, energy and size. It appeared that the phase frequency response is very sensitive to these fluctuations. Moreover the comparison with the microphone phase response itself could not be done because manufacturer does not provide necessary data. Note, that derived using described method sensitivity of the microphone  $S = 0.89$  mV/Pa differs greatly from that, obtained by means of the monotone calibrator at frequency 1 kHz with the pressure level 1 Pa:  $S = 0.494$  mV/Pa. A sample of the system phase frequency response is presented in Fig. 3.8b. It shows sufficiently good stability from spark to spark up to 30-40 kHz, giving about zero radian value. At higher frequencies the phase response could not be found by averaging responses for different waves (sparks) because the variation of the curve shapes at these frequencies become very strong. Therefore, in following calculations the phase response was not used. To be able to estimate correctly the phase response of the system, the stability of the source should be increased.

Shown in Fig. 3.9a are the experimental waveform, measured at the distance  $r_0 = 0.15$  m from the source (red line), the initial ideal  $N$ -wave (blue line), and the initial  $N$ -wave filtered (black line) with the calculated amplitude response. It is seen, that after filtering, the ideal  $N$ -wave with infinitely small rise time and high peak positive pressure, transforms to the waveform with the shape and peak positive pressure much closer to the experimental ones. However there

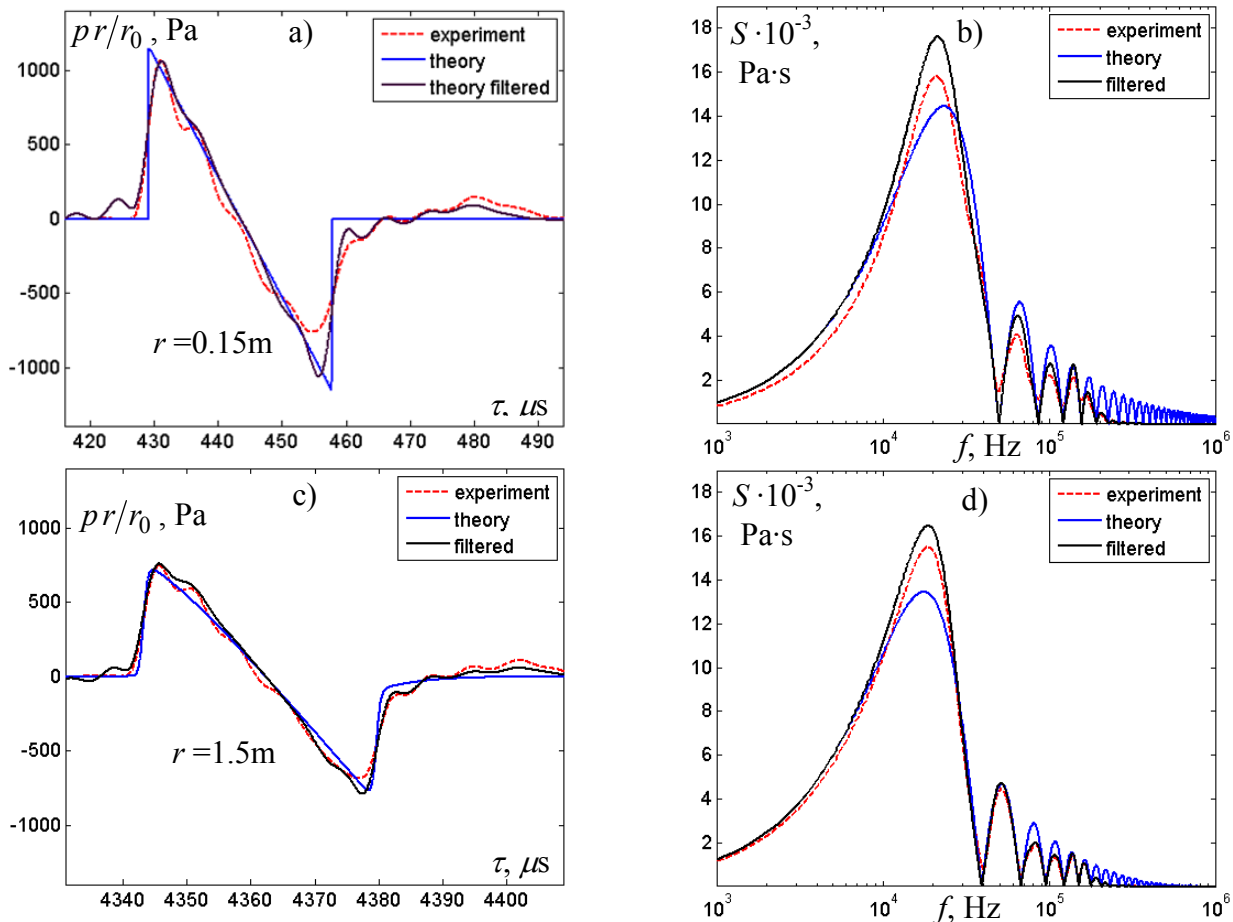


**Fig. 3.9.** Experimental (red line) and theoretical (blue line)  $N$ -pulse waveforms and corresponding spectra at the initial distance  $r_0 = 0.15$  m (a, b) and at the distance  $r = 1.5$  m from the source (c, d). Filtered theoretical waveforms and spectra are shown with the black lines.

is still a difference in the peak negative pressure level which could be explained by the fact that we did not take into account the phase characteristics of the measuring system response. The oscillating structure and disturbances before the shock front are also due to the filtering artefacts. Frequency spectra that correspond to the presented waveforms are shown in Fig. 3.9b. A good agreement between the positions of spectrum minima is achieved in all three cases. Note, that as it was discussed earlier, the filtering does not change these positions and thus the characteristic duration of the pulse.

The waveforms, measured and calculated at the distance  $r = 1.5$  m from the source, are compared in Fig. 3.9c. It is seen that the peak pressure values, both positive and negative, are close to each other for all three waveforms, including the filtered one. However, strong difference in the steepness (rise time) of the shock front is observed between the experimental pulse and the theoretical one, simulated without further filtering. Application of the amplitude filtering to the calculated waveform results in much better agreement in the rise time with the experiment (black and red lines). Shock front steepness of the filtered numerical signal almost coincides with the measured one. The positions of local minima of the spectra and thus the durations of all three pulses, also agree very well (Fig. 3.9d).

§ 3.5 N-wave characteristic parameters. Comparison of experimental data with the results of numerical modelling

The effect of filtering and more detailed comparison of the peak positive pressure, duration and rise time of the measured and modelled signals over propagation distances are presented in Fig. 3.10(a,b,c). The difference in peak positive pressure between the calculated signal (blue line) and measured one (red crosses) becomes almost negligible after applying the amplitude frequency filter (phase component of the filter equal to zero, as discussed previously) to the calculated waveform (black line with circles). As it was already shown, the duration of the wave does not change with the filtering. This can be seen in Fig. 3.10b where the pulse half durations extracted from filtered (circles) and nonfiltered (blue line) waveforms coincide with each other. The rise time (Fig. 3.10c) was measured as the time between 2 points on the shock front, corresponding to  $0.1 p_+$  and  $0.9 p_+$  pressure values. After applying the filter the difference between predicted and measured values of rise time becomes reasonable: smaller than  $0.5 \mu s$ . In comparison, without applying the filter, the front width of the theoretical wave was 10 times smaller, than that of the experimental wave.

A very good agreement between the results of numerical modelling with additional filtering and laboratory-scaled experiment data was obtained therefore for the main shock pulse

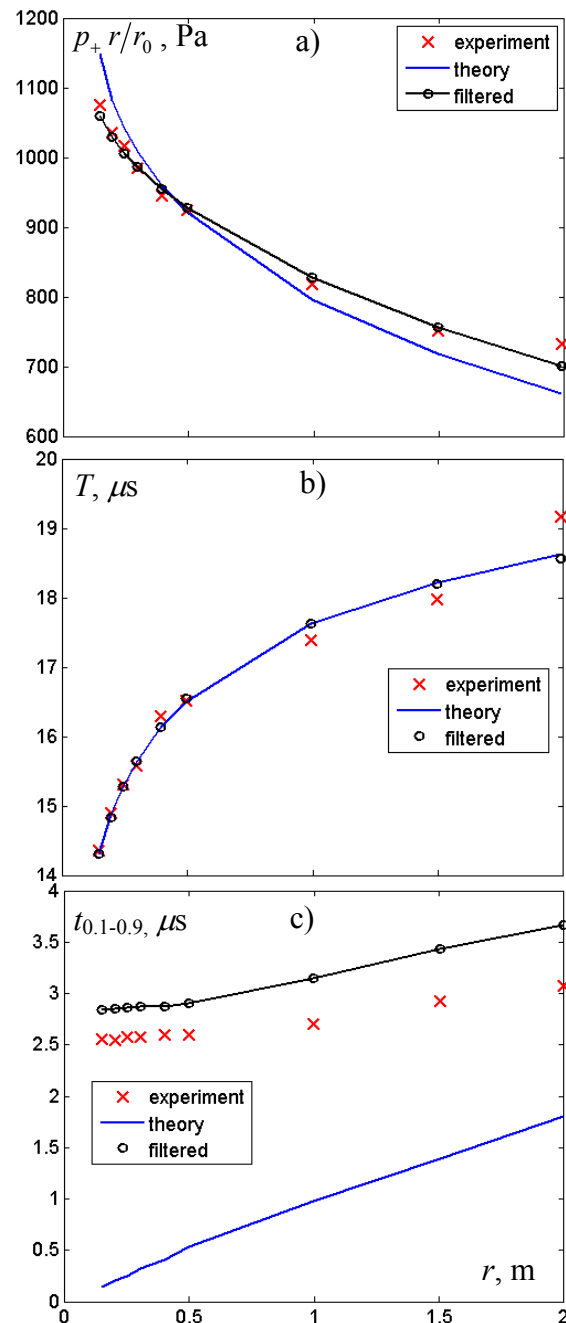


Fig. 3.10. Dependence of peak positive pressure (a), half duration (b) and rise time (c) of the wave on propagation distance. Blue line – calculated results, red crosses – measured results, black circles – calculated results with filter applied.

parameters. Small discrepancies in pulse amplitude and half duration, and bigger difference in the rise time of the experimental and theoretical pulses were observed. This is due to the fact that the system phase frequency response was not taken into account.

### § 3.6 Conclusion

Nonlinear propagation of short duration ( $30 \mu\text{s}$ ) and high amplitude (1100 Pa at 15 cm from the source)  $N$ -waves in homogeneous standard atmosphere was studied numerically and experimentally. The Burgers equation extended to describe nonlinear spherically divergent waves in relaxing media was employed in the numerical analysis. Numerical simulations performed with alternative inclusion of different physical effects showed the relative importance of thermoviscous absorption, relaxation, and acoustic nonlinearity on the  $N$ -waveform distortion for the conditions of the laboratory experiment. The peak positive pressure was shown to be dependent on both nonlinear absorption and linear relaxation/absorption phenomena, whereas only nonlinear effects were shown to be dominant in the pulse lengthening.

The amplitude and duration of  $N$ -pulses generated experimentally were calibrated. Pulse duration was defined from the position of the first nulls in the spectra of the measured signal. Peak pressure was calculated by matching the experimental and analytic curves of nonlinear  $N$ -pulse lengthening over the propagation distances. Nonlinear modelling of  $N$ -pulse propagation was performed for the experimental conditions. Some distortion of the measured signals as compared to the modelled waveforms occurred due to the limited bandwidth of the measuring system. The distortion was mainly in changing the peak pressure of the pulse, widening the rise time of the shock front, and appearance of additional oscillations.

The frequency response of the measuring system was calculated as a ratio between the spectra of experimental and calculated signals and found to be close to the response of the microphone itself provided by the manufacturer (the last one is measured using an electrostatic actuation). The frequency response has a plateau up to 10 kHz and a cutoff at about 150-200 kHz. Application of the calculated amplitude response to the numerical waveforms resulted in even better agreement between simulations and experiment. Application of an appropriate phase frequency response may further advance the filtering procedure. To estimate the phase response more accurately, improvement of the source pulse to pulse stability and more accurate measurements of the propagation are needed.

Numerical analysis showed that for the existing experimental arrangement, nonlinear effects can not be neglected up to the distances of 2 meters, at which the pressure level is higher

---

than 70 Pa. This remark is very important for scale experiments designed to simulate sound propagation in halls or streets because nonlinear effects are usually not wanted for these applications [114]. On the other hand, it is possible to extend this developed and calibrated experimental set-up to investigate nonlinear shock wave fields in turbulent media, like it would be for sonic booms outdoor propagation. Numerical and experimental results obtained in this chapter for *N*-wave propagation in homogeneous atmosphere are shown to be in a good agreement thus validating the model, the numerical algorithm, the filtering, and the calibration methods.



## Chapter 4

### **NONLINEAR EVOLUTION EQUATION OF KHOKHLOV-ZABOLOTSKAYA TYPE FOR THE DESCRIPTION OF ACOUSTIC WAVE PROPAGATION IN INHOMOGENEOUS MOVING MEDIA**

For theoretical description of acoustic signals propagating in turbulent atmosphere it is necessary to have a model, which accounts both for the nonlinear and diffraction effects, the effects of thermoviscous absorption, and the effects related to the vector nature of turbulent fluctuations. A good model has already been proposed and successfully used for the description of nonlinear - diffraction processes in inhomogeneous media; it is known as an extension of the nonlinear evolution parabolic equation of Khokhlov – Zabolotskaia - Kuznetsov type [30-33]. However, the nonlinear equations presented in literature do not account for the vector behaviour of the moving inhomogeneous medium, i.e. they do not account for the medium velocity fluctuations transverse to the acoustic wave propagation direction. Therefore, current chapter of the dissertation is devoted to the derivation of a modified evolution equation in the parabolic approximation of the diffraction theory; it will describe all the physical effects previously mentioned here, including the vector properties of inhomogeneous moving medium. With such complete model, it becomes possible to simulate the propagation of high amplitude short pulses in randomly inhomogeneous moving medium and to calculate, for example, precise values of the statistical distributions, mean and peak characteristics of the acoustic pressure field. To obtain the solution of this generalized KZK equation a numerical algorithm, based on the operator splitting procedure, is developed. In this development most attention is paid to an accurate modelling of the propagation of steep shock fronts, formed due to the nonlinear focusing of an initial periodic signals or pulses.

### § 4.1 Theoretical model. Parabolic equation for nonlinear sound waves in inhomogeneous moving media.

A rigorous way to incorporate the effects of a velocity field into an evolution model equation is to start with the fundamental equations of fluid mechanics and to derive a wave equation that accounts for fluctuations in sound speed, density, and all components of the velocity of the moving medium. This has been done for the case of linear waves [4, 12, 28] and the equation that describes acoustic wave propagation through scalar and vector type inhomogeneities is:

$$\frac{d}{dt} \frac{\partial}{\partial t} \left( \frac{1}{\rho c^2} \frac{dp}{dt} \right) - \nabla \cdot \frac{\partial}{\partial t} \left( \frac{\nabla p}{\rho} \right) + 2 \frac{\partial u_i}{\partial x_j} \frac{\partial}{\partial x_i} \left( \frac{1}{\rho} \frac{\partial p}{\partial x_j} \right) = 0 \quad (4.1)$$

Here  $p$  is the acoustic pressure,  $x_i$  ( $i = 1, 2, 3$ ) – are the components of a position vector  $\mathbf{r} = (x, y, z)$  in Cartesian coordinates,  $c$  is the sound speed in the medium of interest;  $\rho$  is the density;  $t$  is the time,  $u_i$  is the component of the medium velocity along the coordinates  $x$ ,  $y$ , and  $z$ .

The variables  $p$ ,  $c$ ,  $\rho$ ,  $\mathbf{u}$  are functions of time  $t$  and coordinates  $x, y, z$ .  $\nabla = (\partial/\partial x, \partial/\partial y, \partial/\partial z)$ , and  $d/dt = \partial/\partial t + (\mathbf{u} \cdot \nabla)$ . Beyond the usual paradigm of linear lossless acoustics the only restriction on the use of this equation is that the Mach number associated with the flow velocity should be small:  $|\mathbf{u}|/c_0 \ll 1$ , where  $c_0$  is the ambient sound speed.

Here the method of slowly varying amplitude [47, 48] is used to reduce the Eq. (4.1) to the linear parabolic equation. According to this method the solution is represented in the form  $p = p(\tau = t - x/c_0, X = \varepsilon x, Y = \sqrt{\varepsilon} y, Z = \sqrt{\varepsilon} z)$ , where  $\tau$  is the retarded time and  $\varepsilon$  is a small parameter. In this representation the direction of Cartesian axis  $x$  becomes the initial direction of the wave propagation. The derivatives in the Eq. (4.1) are transformed as:

$$\begin{aligned} \partial/\partial t &\rightarrow \partial/\partial \tau, \quad \partial^2/\partial t^2 \rightarrow \partial^2/\partial \tau^2, \quad \partial/\partial x \rightarrow -1/c_0 \partial/\partial \tau + \varepsilon \partial/\partial X, \\ \partial^2/\partial x^2 &\rightarrow 1/c_0^2 \partial^2/\partial \tau^2 - 2\varepsilon/c_0 \partial^2/\partial X \partial \tau + \varepsilon^2 \partial^2/\partial X^2 \\ \partial/\partial y &\rightarrow \sqrt{\varepsilon} \partial/\partial Y, \quad \partial^2/\partial y^2 \rightarrow \varepsilon \partial^2/\partial Y^2, \quad \partial/\partial z \rightarrow \sqrt{\varepsilon} \partial/\partial Z, \quad \partial^2/\partial z^2 \rightarrow \varepsilon \partial^2/\partial Z^2 \end{aligned} \quad (4.2)$$

After substituting the relations (4.2) into the Eq. (4.1), neglecting the terms of order  $\varepsilon^2$  in the stretched coordinates  $(X, Y, Z)$ , and returning back to the original coordinates  $(x, y, z)$ , one obtains:

$$\begin{aligned}
 & \left[ \frac{2}{c_0} \frac{\partial^2}{\partial x \partial \tau} - \Delta_{\perp} + \left( \frac{1}{c^2} - \frac{1}{c_0^2} \right) \frac{\partial^2}{\partial \tau^2} - \frac{2u_x}{c^2 c_0} \frac{\partial^2}{\partial \tau^2} + \frac{2}{c^2} (\mathbf{u}_{\perp} \nabla_{\perp}) \frac{\partial}{\partial \tau} + \right. \\
 & \left. + \left( \frac{2}{c^2} u_x \frac{\partial}{\partial x} + \frac{2}{c_0^2} \frac{\partial u_x}{\partial x} \right) \frac{\partial}{\partial \tau} - \frac{1}{\rho c_0} \frac{\partial \rho}{\partial x} \frac{\partial}{\partial \tau} + \frac{1}{\rho} \nabla_{\perp} \rho \cdot \nabla_{\perp} - \frac{2}{c_0} \left( \nabla_{\perp} u_x + \frac{\partial \mathbf{u}_{\perp}}{\partial x} \right) \nabla_{\perp} - \right. \\
 & \left. \int \left( 2 \sum_{i=2}^3 \sum_{j=2}^3 \frac{\partial u_i}{\partial x_j} \frac{\partial^2}{\partial x_i \partial x_j} \right) d\tau + \frac{1}{\rho} \frac{\partial \rho}{\partial x} \frac{\partial}{\partial x} - \frac{4}{c_0} \frac{\partial u_x}{\partial x} \frac{\partial}{\partial x} + 2 \int \left( \frac{\partial \mathbf{u}_{\perp}}{\partial x} + \nabla_{\perp} u_x \right) \frac{\partial}{\partial x} \nabla_{\perp} d\tau \right] p = 0 \quad (4.3)
 \end{aligned}$$

Here  $u_x$  is the longitudinal component of the flow in the medium,  $\mathbf{u}_{\perp} = (u_y, u_z)$  is the transverse component of the flow, and  $\nabla_{\perp} = (\partial/\partial y, \partial/\partial z)$ . During the derivation it was assumed that all inhomogeneities are slowly varying in space, i.e.  $\partial\rho/\partial X_i$ ,  $\partial c/\partial X_i$  and  $\partial u_j/\partial X_i$  are of the order of  $\varepsilon$ . We also suppose that the inhomogeneities known *a priori* are specified at the time corresponding to the crossing through moment of the acoustic wave and remain unchanged during the passage of the acoustic wave. In this case the sound speed, density, and velocity fields can be considered as functions of spatial coordinates only:  $c = c(x, y, z)$ ,  $\rho = \rho(x, y, z)$ , and  $\mathbf{u} = \mathbf{u}(x, y, z)$ , i.e. they are “frozen” in time. Equation (4.3) is the most complete linear parabolic equation, which describes the propagation of sound waves in inhomogeneous moving media. For harmonic waves it can be cast in a form identical to the equation derived by Ostashev with the same enumeration of terms [4].

Equation (4.3) is still rather complicated for numerical modelling. Actually in this equation there are six physical parameters assumed to be of the same order of smallness. These parameters are: i)  $1/kL$ , where  $L$  is the characteristic scale of inhomogeneity and  $k$  is the acoustic wave number; ii) the acoustic Mach number  $p/c_0^2 \rho_0$ ; iii) the flow Mach number  $|\mathbf{u}|/c_0$ ; iv)  $\Delta c/c_0 = (c - c_0)/c_0$  is the parameter associated with scalar inhomogeneities of the sound speed; v)  $\Delta\rho/\rho_0$  is the parameter associated with variations in density, and vi) the angle between the direction of wave propagation and the  $x$  axis.

To simplify Eq. (4.3), let us do an analysis of the relative order of magnitude of the derivatives, i.e. :

$$\frac{\nabla \rho}{\rho} \sim \frac{\nu}{L} \quad \frac{1}{c_0} \left| \frac{\partial u_i}{\partial r_j} \right| \sim \frac{|\mathbf{u}|_{\max}}{c_0 L} = \frac{M}{L} \quad \frac{\partial}{\partial \tau} \sim \omega$$

where parameter  $\nu = |\rho - \rho_0|/\rho_0$  characterizes the density variations,

$L$  is the characteristic scale of the inhomogeneity,  $\omega$  is the frequency of wave parameters change. For density variations the following relation is almost always valid  $\nu \ll 1$  [4]. The spatial derivative of the acoustic pressure in the direction of the wave propagation is proportional to  $\partial p / \partial x \sim A / L$ , where  $A$  is the amplitude value of sound pressure in the medium of propagation. The spatial derivative in transverse direction is characterized by the angle of acoustic rays declination from the direction of wave propagation due to diffraction, as soon as pressure contains the phase factor  $\exp(i\mathbf{k}\mathbf{r}) = \exp(ik_0 \sin \beta \cdot \mathbf{e} \cdot \mathbf{r}) = \exp(ik_0 \beta \cdot \mathbf{e} \cdot \mathbf{r})$ . Here the  $\mathbf{e}$  vector is the unit vector in the direction of the projection of wave vector  $\mathbf{k}$  on the  $yz$  plain. Thus,  $\nabla_{\perp} p \sim Ak_0 \beta_m$  where  $k_0 = 2\pi / \lambda$  and  $\beta_m$  is the maximum ray declination angle.

Using these estimations to simplify the Eq. (4.3) and dividing each term by  $(k_0)^2$  one can obtain the following orders of magnitude:

1.  $2 / (k_0 L) \sim 1.6 \cdot 10^{-1}$
2.  $\beta_m^2 \sim 9.8 \cdot 10^{-2}$
3.  $2 \cdot \Delta c / c_0 \sim 1.2 \cdot 10^{-1}$
4.  $2M \sim 8.8 \cdot 10^{-2}$
5.  $2M\beta_m \sim 2.8 \cdot 10^{-2}$
6.  $2M / (k_0 L) \sim 7.0 \cdot 10^{-3}$
7.  $\nu / (k_0 L) \sim 1.3 \cdot 10^{-3}$
8.  $\nu\beta_m / (k_0 L) \sim 4.3 \cdot 10^{-4}$
9.  $2M\beta_m / (k_0 L) \sim 2.2 \cdot 10^{-3}$
10.  $2M\beta_m^2 / (k_0 L) \sim 6.9 \cdot 10^{-4}$
11.  $\nu / (k_0 L)^2 \sim 1.1 \cdot 10^{-4}$
12.  $4M / (k_0 L)^2 \sim 1.1 \cdot 10^{-3}$
13.  $2M\beta_m / (k_0 L)^2 \sim 1.8 \cdot 10^{-4}$

For the previous estimations the following parameters of the atmosphere were used:  $\Delta c = 20$  m/s,  $|\mathbf{u}|_{\max} = 15$  m/s, and  $\nu = 1.7 \cdot 10^{-2}$  that corresponds to changes in ambient temperature equal to 5K. It was also supposed that  $\beta_m = \pi / 10$  (maximal acceptable angle of rays declination from the axis due to the limitation of parabolic approximation) and  $\lambda / L = 0.5$ .

Thus we retain in the Eq. (4.3) only terms 1-5, which are of order  $1/kL$  and neglect terms containing combinations of any previous small parameters. In addition, we keep the term 7,

related to density variations, because in the absence of any sound speed fluctuations or medium flow this term becomes the most significant.

The resulting linear parabolic wave equation is obtained using the approximate relation  $1/c^2 - 1/c_0^2 = 2\Delta c/c_0^3$ :

$$\frac{\partial}{\partial \tau} \left[ \frac{\partial p}{\partial x} - \frac{\Delta c + u_x}{c_0^2} \cdot \frac{\partial p}{\partial \tau} + \frac{1}{c_0} \mathbf{u}_\perp \nabla_\perp p - \frac{p}{2\rho} \frac{\partial \rho}{\partial x} \right] = \frac{c_0}{2} \Delta_\perp p, \quad (4.4)$$

Equation (4.4) accounts for the acoustic wave propagation in a 3D inhomogeneous moving media. In the absence of inhomogeneities, i.e. if  $\Delta c$ ,  $\Delta \rho = 0$  and  $\mathbf{u} = 0$ , it simplifies to the well known parabolic approximation of diffraction [Vinogradova *et al.*, 47].

In the final step of the derivation of a nonlinear parabolic equation it is usually considered that the terms describing nonlinearity and attenuation may be included into the linear parabolic equation additively [30, 47, 48]. This can be justified on the basis that the nonlinear and attenuation terms are small and so any interaction with the other terms will necessarily be of higher order of smallness, and so within the framework described here can be neglected. Finally, we get the following nonlinear parabolic wave equation of the KZK type:

$$\frac{\partial}{\partial \tau} \left[ \frac{\partial p}{\partial x} - \frac{\beta}{c_0^3 \rho_0} p \frac{\partial p}{\partial \tau} - \frac{\Delta c + u_x}{c_0^2} \cdot \frac{\partial p}{\partial \tau} + \frac{1}{c_0} (\mathbf{u}_\perp \nabla_\perp p) - \frac{p}{2\rho} \frac{\partial \rho}{\partial x} - \frac{b}{2c_0^3 \rho_0} \frac{\partial^2 p}{\partial \tau^2} \right] = \frac{c_0}{2} \Delta_\perp p \quad (4.5)$$

where  $\beta$  is the coefficient of nonlinearity and  $b$  is the coefficient of viscosity. The thermoviscous absorption term  $b/(2c_0^3 \rho_0) \cdot \partial^2 p / \partial \tau^2$  can be replaced by more general linear operator  $L(p)$  if it is necessary to account for relaxation or other losses [Cleveland *et al.*, 115].

Equation (4.5) is a KZK type of equation, which models the combined effects of diffraction, nonlinearity, attenuation; and has been generalized to account for sound speed and density inhomogeneities, and flow inhomogeneities. In Eq. (4.5) the first term accounts for propagation, the second term - for nonlinear distortion, the third term - for sound speed (scalar) and axial flow (vector) inhomogeneities, the fourth term - for transverse flow (vector) inhomogeneities, the fifth term - for density (scalar) inhomogeneities, and the sixth term - for absorption. The right-hand side of Eq. (4.5) accounts for diffraction effects. What is new here, that is the addition of the fourth term, which accounts for the transverse flow effect.

In dimensionless coordinates and 2D Cartesian geometry the modified KZK equation excluding scalar inhomogeneities can be represented as:

$$\frac{\partial}{\partial \theta} \left[ \frac{\partial V}{\partial \sigma} - NV \frac{\partial V}{\partial \theta} - 2\pi U_\parallel \cdot \frac{\partial V}{\partial \theta} + U_\perp \frac{\partial V}{\partial \rho} - L[V] \right] = \frac{1}{4\pi} \frac{\partial^2 V}{\partial \rho^2} \quad (4.6)$$

Here  $V=p/p_0$  is the acoustic pressure normalized by its initial amplitude value,  $\theta=\omega_0 \tau$  is dimensionless time,  $\omega_0 = 2\pi c_0 / \lambda$  is the characteristic frequency of the acoustic wave,  $\lambda$  is

the acoustic wavelength,  $\sigma = x/\lambda$  is the normalized propagation distance,  $\rho = y/\lambda$  is the normalized transverse coordinate,  $U_{\parallel} = u_x/c_0$  normalized axial flow,  $U_{\perp} = u_y/c_0$  normalized transverse flow,  $N = 2\pi\beta p_0 / c_0^2 \rho_0 = \lambda / x_s$  is the dimensionless nonlinear parameter, where  $x_s = c_0^3 \rho_0 / \beta p_0 \omega_0$  is the shock formation distance for a harmonic plane wave.  $L[V]$  is the linear operator which governs frequency dependent losses, and in the case of thermoviscous absorption and relaxation processes modelling can be written as:

$$L[V] = A \frac{\partial^2 V}{\partial \theta^2} + \sum_{v=1}^2 D_v \frac{\partial}{\partial \theta} \int_{-\infty}^{\theta} \exp\left(-\frac{\theta - \theta'}{\theta_v}\right) \frac{\partial V}{\partial \theta'} d\theta', \quad \text{where } A = 2\pi^2 b / (c_0 \rho_0 \lambda) \quad \text{is the}$$

dimensionless parameter of thermoviscous absorption,  $D_v = 2\pi c_v / c_0$  and  $\theta_v = \omega_0 \tau_v$  are the force and time of the oxygen and nitrogen relaxation processes for  $v = 1, 2$  respectively. If an acoustic pulse is propagating instead of a periodic signal for the normalization of equation parameters the duration of the pulse is used:  $(2T_0) = 2\pi/\omega_0$ .

To determine the orders of dimensionless parameters in Eq. (4.6) let us consider the propagation of the acoustic pulse in two cases of interest: laboratory scale experiments [7, 40, 43, 44] and field experiments [52 - 55]. Measured both in laboratory and field experiments sound pressure amplitudes and medium velocity fluctuation amplitudes are about than  $p_0 \sim 1000$  Pa and  $u_{x,y} \sim 20$  m/s (Table 2.1). Thus under the normal atmosphere conditions for dimensionless parameter of nonlinearity one can obtain the value  $N \sim 0.06$ , and for the velocity fluctuation dimensionless parameter  $U_{\perp, \parallel} \leq 0.05$ . Thermoviscous absorption parameter appears to be strongly dependent on the acoustic pulse length, which in laboratory experiment is about  $\lambda \sim 1.2$  cm, and in field experiments  $\lambda \sim 50$  m (of the order of the length of the airplane). Therefore, dimensionless absorption parameter varies according to the type of experiment: laboratory scale experiment ( $A \sim 1.5 \cdot 10^{-4}$ ) and field experiment ( $A \sim 3.6 \cdot 10^{-8}$ ).

It should be noted here that parabolic evolution Eq. (4.6) with  $U_{\perp} = 0$ , was previously used in literature for the description of acoustic pulse propagation in media with only scalar inhomogeneities (1.18) [31]. From this point of view, the novelty of Eq. (4.6) consists in accounting for the transverse winds and turbulent fluctuations of medium velocity, which may sufficiently affect the propagation of acoustic signals in turbulent atmosphere. In addition, the numerical solutions obtained in [31], correspond to the initial condition in the form of  $N$ -wave with very wide front (7% of the wavelength), which is chosen in order to simplify the simulations, but does not fit real physical effects (front width is  $< 0.4\%$  of wavelength). Moreover, in the computations an algorithm, which introduces a very strong artificial dissipation, was used (for details refer to §4.3).

### § 4.2 Self similarity property of the KZK type equation

Equation (4.6) has no analytical solutions, but there exist some important properties of similarity, that can be used to obtain series of solutions of the Eq. (4.6) if only one numerical solution is known. Generally, the motion of the medium is represented as a mean motion with superposition of various fluctuations of velocity. According to this, the components of the total velocity can be written in the form:  $U_{\parallel} = U_{\parallel}^0 + \tilde{U}_{\parallel}$  and  $U_{\perp} = U_{\perp}^0 + \tilde{U}_{\perp}$ , where variables with a tilde are velocity fluctuations and variables with zero index – the mean motion of the medium.

Let us consider a field of vector inhomogeneities with a mean motion governed by the following laws:  $U_{\parallel}^0 = B(\sigma) \cdot \rho + C(\sigma)$  and  $U_{\perp}^0 = D(\sigma)$ ; and arbitrary random fluctuations  $\tilde{U}_{\parallel}$  and  $\tilde{U}_{\perp}$ . It can be shown that using the following transformation of variables:

$$\theta_1 = \theta + \theta_{01}(\sigma) + \theta_{02}(\sigma) \cdot \rho, \quad \sigma_1 = \sigma, \quad \rho_1 = \rho + \rho_0(\sigma), \quad (4.7)$$

where unknown functions  $\theta_{01}(\sigma)$ ,  $\theta_{02}(\sigma)$ ,  $\rho_0(\sigma)$  can be obtained as the solutions of a system of differential equations:

$$\frac{d\theta_{02}}{d\sigma} = 2\pi B, \quad \frac{d\theta_{01}}{d\sigma} = 2\pi C - D\theta_{02} + \frac{1}{4\pi}\theta_{02}^2, \quad \frac{d\rho_0}{d\sigma} = -D + \frac{1}{2\pi}\theta_{02}, \quad (4.8)$$

it is possible to completely exclude the mean motion of the medium from the parabolic equation, and in the same time to keep the modified fluctuating components:

$$\frac{\partial}{\partial \theta_1} \left[ \frac{\partial V}{\partial \sigma_1} - NV \frac{\partial V}{\partial \theta_1} - 2\pi \tilde{U}_{\parallel}^1 \cdot \frac{\partial V}{\partial \theta_1} + \tilde{U}_{\perp}^1 \cdot \frac{\partial V}{\partial \rho_1} - A \frac{\partial^2 V}{\partial \theta_1^2} \right] = \frac{1}{4\pi} \frac{\partial^2 V}{\partial \rho_1^2} \quad (4.9)$$

where

$$\begin{aligned} \tilde{U}_{\parallel}^1(\sigma_1, \rho_1) &\equiv \tilde{U}_{\parallel}(\sigma_1, \rho_1 - \rho_0(\sigma_1)) + \frac{1}{2\pi} \theta_{02}(\sigma_1) \cdot \tilde{U}_{\perp}(\sigma_1, \rho_1 - \rho_0(\sigma_1)) \\ \tilde{U}_{\perp}^1(\sigma_1, \rho_1) &\equiv \tilde{U}_{\perp}(\sigma_1, \rho_1 - \rho_0(\sigma_1)) \end{aligned} \quad (4.10)$$

Note, that according to the Eqs (4.10), fluctuations of the medium flow in the transverse direction have an influence on the speed of sound of the wave. This can be interpreted physically as follows: as the phase front turns, the transverse flow is no longer perpendicular to the normal to the front, the flow projection onto the wave vector becomes nonzero, and therefore the transverse flow component results in a change of the wave phase speed. In contrast, the projection of the longitudinal flow onto the normal to the steered wave vector does not manifest itself as a transverse flow, presumably because this is a large angle effect which is not accounted for by the parabolic approximation.

Consider an example of a layered inhomogeneous media described by the law  $U_{\parallel}^0 = B_0 \cdot \rho + C_0$  and  $U_{\perp}^0 = 0$ , where  $B_0$  and  $C_0$  are arbitrary constants (horizontal flow with linearly changing amplitude in transverse direction). This leads to the following change of variables:

$$\theta_1 = \theta - C_0 \cdot \sigma + \frac{1}{12\pi} B_0^2 \cdot \sigma^3 - B_0 \cdot \sigma \cdot \rho, \quad \sigma_1 = \sigma, \quad \rho_1 = \rho - \frac{1}{4\pi} B_0 \cdot \sigma^2, \quad (4.11)$$

from which it can be deduced that the axis of the beam has a parabolic trajectory and the phase front turns due to the presence of flow. In the case of a purely transverse flow, i.e.  $U_{\parallel}^0 = 0$  and  $U_{\perp}^0 = D(\sigma)$ , the change of variables takes the form

$$\theta_1 = \theta, \quad \sigma_1 = \sigma, \quad \rho_1 = \rho - \int_0^{\sigma} D(\sigma') d\sigma'. \quad (4.12)$$

In this case, the axis of the sound beam has a trajectory governed by the function  $D(\sigma)$ , but the wave front does not turn. In geometrical acoustics this leads to the noncollinearity of phase and group velocities.

### § 4.3 Numerical algorithms

The parabolic evolution Eqs (4.5, 4.6) are still sufficiently complicated for deep theoretical analysis and, therefore, they need to be solved numerically. Depending on the temporal characteristics of the transmitted signal, different approaches can be employed for numerical modelling. Time domain approach is more convenient for modelling the propagation of pulsed signals [31, 115, 116], like sonic booms in atmosphere or intense shock waves emitted by explosive sources in the ocean [9], and spectral method approach is better suited for solving equations governing periodic wave propagation, such as acoustic waves used in noninvasive ultrasound surgery [1, 49, 117, 118]. In this work both spectral and time domain algorithms are developed and used for numerical computations.

#### 4.3.1 Frequency domain approach to model periodic waves with shocks

To obtain the solution of the Eq. (4.6) the spectral numerical algorithm presented in [Khokhlova *et al.*, 117] for axially symmetric beams has been generalized to 2D Cartesian geometry [Averiyanov *et al.*, 11]. Representing the solution in the form of the Fourier series

expansion:  $V(\sigma, Y, \theta) = \sum_{n=-\infty}^{\infty} C_n(\sigma, \rho) \exp(-in\theta)$  and substituting it to the Eq. (4.6) yields a set of coupled nonlinear differential equations for the complex amplitudes  $C_n$ :

$$\begin{aligned} \frac{\partial C_n}{\partial \sigma} &= \frac{i}{4\pi m} \frac{\partial^2}{\partial \rho^2} C_n - \frac{in}{2} N \sum_{k=-\infty}^{\infty} C_k C_{n-k} - An^2 C_n - i \cdot 2\pi m U_{\parallel} C_n - U_{\perp} \frac{\partial C_n}{\partial \rho} = \\ &= L_D + L_N + L_A + L_I \end{aligned} \quad (4.13)$$

where  $C_n(\sigma, \rho)$  is the complex amplitude of the  $n^{\text{th}}$  harmonic ( $-\infty < n < \infty$ ),  $C_{-n} = C_n^*$  ( $C_n^*$  denotes the complex conjugate of  $C_n$ ).

To guarantee the stability of the numerical algorithm (4.13) at the stage of developed shocks, an absorption term that represents either the physical thermoviscous absorption or artificially added absorption is included in the algorithm. The absorption is necessary to smoothen the shock front in nonlinear regime of acoustic wave propagation [Kasheeva *et al.*, 119]. Otherwise, the formed shock front becomes too steep for its accurate description using prescribed finite number of Fourier harmonics, and the Gibbs oscillations occur – numerical error – at the wave profile. For stability purposes it is also possible to use absorption, proportional, for example, to the fourth or to the sixth power of frequency. Such choice could be justified by the fact that according to the Rayleigh law, in the media with small scale internal structure absorption is proportional to fourth power of frequency. However, using these laws of absorption leads to the formation of physical oscillations at the waveform [120 - 123]. Chosen here is the quadratic law of frequency dependent absorption that does not introduce any additional distortions to the waveform, and corresponds to the absorption law in water and air, where the propagation of nonlinear waves is studied. During the integration of Eqs. (4.13) the absorption coefficient  $A$  is selected to be as small as possible to maintain the stability of simulations and to get more realistic results.

The set of equations (4.13) is solved for the harmonic amplitudes  $C_n$  using a frequency domain numerical algorithm based on the operator splitting procedure [11, 117]. The amplitudes  $C_n$  of the first  $n \leq N_{max}$  harmonics are calculated using a marching algorithm in the  $\sigma$  direction. At each step  $h_{\sigma}$  the, right-hand side of equations (4.13) is split into four operators:  $L_D =$  diffraction,  $L_N =$  nonlinearity,  $L_A =$  absorption, and  $L_I =$  inhomogeneity, and these operators are applied sequentially. At the first fractional step, the set of equations  $\partial C_n / \partial \sigma = L_D$  is solved independently for each harmonic component  $n$  using a second order Crank-Nicholson implicit algorithm. The obtained results are then used as a boundary condition for the second fractional step at which nonlinearity effects are included independently for each spatial grid point,  $\partial C_n / \partial \sigma = L_N$ , using a fourth order Runge-Kutta algorithm. At the third fractional step the

absorption term,  $\partial C_n / \partial \sigma = L_A$ , is calculated by applying the exact solution  $C_n(\sigma + h_\sigma) = C_n(\sigma) \exp(-An^2 h_\sigma)$ . The effects of inhomogeneities are accounted at the last fractional step,  $\partial C_n / \partial \sigma = L_I$  using an exact solution for the longitudinal component and the second order Lax-Wendroff numerical algorithm for the transverse component of the velocity field [Press *et al.*, 124].

Spatial steps in the numerical modelling are chosen according to the characteristic spatial scales of the acoustic field (wavelength, width of the focal waist) and so the stability of the algorithm is guaranteed. The value of the absorption coefficient  $A$  is chosen to provide the stability of the solution in accordance with the number of harmonics retained in the calculations and the maximum amplitude of the shock wave achieved. In its turn, the absorption coefficient is determined due to the time limits for the calculation of the acoustic field realization. For example, to calculate the acoustic wave nonlinear ( $N=0.05$ ) propagation through the inhomogeneity with a characteristic outer scale equal to  $L = 3\lambda$  and a mean square medium velocity of fluctuations equal to  $u_{rms} = 3$  m/s, the numerical grid step along the propagation coordinate is set to  $h_\sigma = 2.5 \cdot 10^{-2}$  and the numerical grid step along the transverse direction is set to  $h_\rho = 2.0 \cdot 10^{-2}$ . Calculations are conducted for  $N_{max} = 150$  harmonics, and according to that, the absorption parameter is chosen to be equal to  $A = 0.002$ . For a specific problem, the coefficient is determined by the properties of the medium, and the appropriate number of harmonics would have to be chosen for that case. It is also important for numerical simulations to choose correctly the width of the computational window in transverse direction, as soon as the reflected acoustic waves from the boundaries may lead to distortions of the investigated acoustic field. So for the calculation of a realization with dimensions  $40\lambda$  in transverse direction and  $60\lambda$  in longitudinal direction the width of the computational window was chosen to be  $L_{window} = 60\lambda$ . Reliability of obtained results was checked by the change of the computational window width, by diminishing the chosen spatial grid steps by a factor of two and by increasing the number of harmonics used. Thus, the obtained numerically acoustic field differed from the previously calculated field not more than on 1 %.

#### 4.3.2 Time domain approach to model propagation of single shock pulses

To investigate the propagation of an acoustic pulse with a thin shock front typical for an  $N$ -shaped intense sound wave, a separate algorithm was developed. To construct an initial  $N$ -

wave pulse it is useful to note that, in the absence of inhomogeneities, the parameters of the wave are governed by the Burgers equation [Vinogradova *et al.*, 47]:

$$\frac{\partial V}{\partial \sigma} - NV \frac{\partial V}{\partial \theta} = A \frac{\partial^2 V}{\partial \theta^2} \quad (4.14)$$

which has an exact solution in quasistationary form. This means that the solution to the Eq. (4.14) is given by shocks formed according to the simple wave equation (Eq. (4.14) with  $A=0.0$ ) but smoothed with the stationary solution to the Burgers equation.

Following our discussion, to solve the evolution Eq. (4.6) it is essential to set the initial condition in the form of a quasistationary solution. In this way at least two physical effects will be accounted for. Thus, the initial condition is an  $N$ -wave with smoothed shock front, which width is determined by nonlinear (wave amplitude) and thermoviscous effects:

$$V_0 = \frac{\theta}{2\pi} \left[ \tanh\left(\frac{N}{4A}(\theta - \pi)\right) - \tanh\left(\frac{N}{4A}(\theta + \pi)\right) \right] \quad (4.15)$$

The duration of the initial pulse is equal to  $2\pi$  and the shock front width (rise time) is approximately equal to  $10A/N$ , that corresponds to changes in pressure on the shock from 10% to 90% of its amplitude. With  $A/N \rightarrow 0$  quasistationary solution (4.15) becomes an ideal  $N$ -wave with amplitude  $V_0=1.0$ .

As it was mentioned previously, to model the propagation of acoustic pulses it is more convenient to use the time domain approach for numerical modelling. As in the spectral approach, it is based on the operator splitting procedure. According to this method at each grid step in propagation distance  $\sigma$  the equation is split in five physically consistent equations, describing different physical effects, each of which is solved independently:

nonlinearity	$\frac{\partial V}{\partial \sigma} = \frac{N}{2} \frac{\partial V^2}{\partial \theta},$	(4.16)
--------------	--	--------

thermoviscous absorption	$\frac{\partial V}{\partial \sigma} = A \frac{\partial^2 V}{\partial \theta^2},$	(4.17)
--------------------------	--	--------

convection in wave propagation direction	$\frac{\partial V}{\partial \sigma} = 2\pi U_{\parallel} \cdot \frac{\partial V}{\partial \theta}$	(4.18)
--	--	--------

convection in transverse direction	$\frac{\partial V}{\partial \sigma} = -U_{\perp} \frac{\partial V}{\partial \rho}$	(4.19)
------------------------------------	--	--------

diffraction	$\frac{\partial V}{\partial \sigma} = \frac{1}{4\pi} \int \frac{\partial^2 V}{\partial \rho^2} d\theta$	(4.20)
-------------	---	--------

In addition, if it is necessary to account for relaxation effects on the acoustic wave propagation, then the set of equations (4.16-4.20) should be supplemented by one more equation, analogous to Eq. (3.6) and written as follows in 2D geometry :

relaxation processes	$\frac{\partial V}{\partial \sigma} = \sum_{\nu=1}^2 D_{\nu} \frac{\partial}{\partial \theta} \int_{-\infty}^{\theta} \exp\left(-\frac{\theta - \theta'}{\theta_{\nu}}\right) \frac{\partial V}{\partial \theta'} d\theta'$	(4.21)
----------------------	---	--------

At the first step of the numerical procedure, diffraction is taken into account (4.20) using six point implicit Crank-Nicholson finite difference (CNFD) algorithm of second order in respect to the space coordinates [Lee, 125]. At this step, for the integration over time, the trapezoidal rule written in the following form is used:

$$\int_0^{\theta} f(\theta) d\theta = \Delta\theta \sum_{l=1}^{n-1} f_l + \frac{1}{2}(f_0 + f_n) \quad (4.22)$$

Using (4.22) and substituting derivatives in their differential form into the Eq. (4.20) one can get the following set of equations:

$$-\frac{\alpha}{16}Q(\sigma_{i+1}, \rho_{j+1}, \theta_n) + (1 + \frac{\alpha}{8})Q(\sigma_{i+1}, \rho_j, \theta_n) - \frac{\alpha}{16}Q(\sigma_{i+1}, \rho_{j-1}, \theta_n) = \frac{\alpha}{8}[R(\sigma_i, \rho_{j+1}, \theta_n) - 2R(\sigma_i, \rho_j, \theta_n) + R(\sigma_i, \rho_{j-1}, \theta_n)] + 2V(\sigma_i, \rho_j, \theta_n) \quad (4.23)$$

where

$$Q(\sigma_{i+1}, \rho_{j-1}, \theta_n) = V(\sigma_{i+1}, \rho_{j-1}, \theta_n) + V(\sigma_i, \rho_{j-1}, \theta_n)$$

$$R(\sigma_i, \rho_j, \theta_n) = \sum_{k=1}^{n-1} Q(\sigma_n, \rho_j, \theta_k) \quad (4.24)$$

$$\alpha = \frac{h_\theta h_\sigma}{\pi h_\rho^2}$$

For the derivation, it is assumed that there are no distortions at the edges of the time domain and that the boundaries in transverse direction are ideally rigid, that is the boundary is assumed to be as ideally reflective surface:

$$V(\sigma_i, \rho_j, \theta_n) = 0 \text{ for } n = 0 \text{ and } n = N_{max}$$

$$V(\sigma_i, \rho_{j+1}, \theta_n) = V(\sigma_i, \rho_{j-1}, \theta_n) \text{ for } j = 0 \text{ and } j = J_{max} \quad (4.25)$$

In the left hand side of the Eqs. (4.23) the unknown terms of the  $i+1$  layer are gathered together, whereas in the right hand side the known terms from the previous layer  $i$  are collected. Definitive matrix of the set of equations (4.23) has a three diagonal form, and therefore, the solution can be found using the well-known Thomas sweep algorithm [Press *et al.*, 124].

The result obtained at this step is then used as a boundary condition for the second fractional step when nonlinearity effects (4.16) are included independently for each spatial grid point. In this purpose, the six point explicit conservative Godunov type algorithm of the second order accuracy in time and first order accuracy in propagation distance is used [Kurganov *et al.*, 112]. According to this algorithm the solution to the Eq. (4.16) at the layer  $i+1$  is represented in the following form :

$$V^{i+1}_n = V^i_n - N \frac{h_\sigma}{h_\theta} (H^i_{n+1/2}(\sigma) - H^i_{n-1/2}(\sigma)) \quad (4.26)$$

where the numerical fluxes  $H_{n\pm 1/2}^i$  passing through the numerical grid cell centres are given at layer  $i$  with relations:

$$H_{n+1/2}^i(\sigma) = -\frac{1}{4} \left( (V_{n+1/2}^+)^2 + (V_{n+1/2}^-)^2 \right) - \frac{a_{n+1/2}^i(\sigma)}{2} \left[ V_{n+1/2}^+(\sigma) - V_{n+1/2}^-(\sigma) \right] \quad (4.27)$$

To obtain the solution of the second order accuracy in time, in the presented algorithm the piecewise linear reconstruction is used to estimate the pressure values  $V(\sigma_i, \theta_n)$  to the write  $V_{n+1/2}^+$  and to the left  $V_{n+1/2}^-$  from the numerical grid knot  $(i, n)$ :

$$\begin{aligned} V_{n+1/2}^+ &= V_{n+1}^i(\sigma) - \frac{h_\theta}{2} (\partial V / \partial \theta)_{n+1}^i \\ V_{n+1/2}^- &= V_n^i(\sigma) + \frac{h_\theta}{2} (\partial V / \partial \theta)_n^i \end{aligned} \quad (4.28)$$

In (4.27), solution derivatives on time at the  $i^{\text{th}}$  layer of the propagation coordinate are chosen in such way that their absolute values appear to be minimal in the set of possible derivative differential representations: left, right and central derivatives with mass coefficient  $1 \leq \beta \leq 2$ . Such selection of the derivative value provides better stability of the numerical algorithm:

$$(\partial V / \partial \theta)_n^i = \min \text{mod} \left( \beta \frac{V_n^i - V_{n-1}^i}{h_\theta}, \frac{V_{n+1}^i - V_{n-1}^i}{2h_\theta}, \beta \frac{V_{n+1}^i - V_n^i}{h_\theta} \right) \quad (4.29)$$

Where the *min mod* function is the standard minimum modulus function.

If a better accuracy is needed, the mass coefficient should be set to  $\beta = 2$ , whereas  $\beta = 1$  introduces to the algorithm additional grid absorption and makes the algorithm more stable. And, finally, the local numerical flux speed in the grid cell is defined as:

$$a_{n+1/2}^i(\theta) = \max \left| V_{n+1/2}^-, V_{n+1/2}^+ \right| \quad (4.30)$$

The presented algorithm possesses a good stability and allows computing the propagation of thin shock fronts with a good accuracy. In the following paragraph we present the detailed comparison of the Godunov type algorithm with the two other numerical algorithms, widely used in literature to model the nonlinear effects.

One of these algorithms is the algorithm based on the exact implicit Poisson's solution to the simple wave equation  $V = V(\theta + NV\sigma)$  [111, 125, 126]. A numerical solution at each knot of the nonuniform grid is given by the simple relation  $V(\sigma + h_\sigma, \theta) = V(\sigma, \theta + NVh_\sigma)$  [111, 125]. Therefore, an interpolation from the non uniform to uniform time grid is then necessary. Commonly used linear interpolation reduces the accuracy of the algorithm to the second order in time  $(h_\theta)^2$  and also introduces strong numerical dissipation which accumulates with distance. Moreover, this method has several disadvantages and hidden dangers. Being used for the prediction of the shock wave evolution in lossless media it will result in the incorrect shock front

position (it will not move) giving only decrease of its amplitude with distance. Even if artificial or physical absorption is introduced, it is necessary to have sufficient number of grid points per shock front to obtain a correct solution. In addition, during the propagation of the acoustic wave the number of grid points per shock front should not be less than the minimal possible number.

Thus, if the numerical grid is uniform in time, one will get a huge amount of grid points per wave, as soon as the width of the shock is very small in comparison with the wave duration. As we discussed previously the width of the front (rise time) can be estimated with the value  $10A/N$ . This value varies approximately from 0.4% of the wave duration in the model experiment to 0.0001% of wave duration for sonic booms propagating in real atmosphere. Therefore, having even 10 points per shock in the first case will result in about 2500 points per wave, what in one's part will result in very high time consumption, especially in the case of 2D or 3D calculations.

Thus, being limited with the wish to obtain sufficient accuracy from one side and minor time contribution from the other, three different numerical algorithms to solve the nonlinear term in parabolic Eq. (4.6) are compared here. With the aim to find the most effective numerical method, the following algorithms of simple wave Eq. (4.16) modelling are tested:

- 1) widely used approach built on the basis of the exact solution to the simple wave equation  $V(\sigma_{i+1}, \theta_n) = V(\sigma_i, \theta_n + NVh_\sigma)$ ;
- 2) second order in time and first order in distance explicit finite difference conservative algorithm [122]  $V(\sigma_{i+1}, \theta_n) = V(\sigma_i, \theta_n) + \frac{Nh_\sigma}{4h_\theta} [V(\sigma_i, \theta_{n+1})^2 - V(\sigma_i, \theta_{n-1})^2]$ ;
- 3) central flux-conservative Godunov type scheme of the second-order accuracy in time and first-order accuracy in propagation coordinate (4.26-4.30).

At that stage, according to the discussion related to the first algorithm, the comparison is done for waves propagating in the nonlinear dissipative medium, i.e. the classical Burgers Eq. (4.14) is solved. The absorption introduced here plays the role of artificial absorption necessary to provide the stability and accurateness of the algorithm. For all the algorithms the absorption is calculated using Crank-Nicholson algorithm of the second order. For each case of wave propagation presented here, spatial grid step is chosen according to the conditions of stability and convergence of the solution. The initial waveform is chosen according to the quasistationary solution (4.14) with the following physical parameters: nonlinearity parameter is equal to  $N=0.06$ , absorption parameter is equal to  $A=1.5 \cdot 10^{-4}$  that is in accordance with the laboratory experiment. Therefore the amplitude of the initial wave is equal to  $V_0=0.988$  and the shock front rise time is equal to  $10A/N=0.025$  (0.4% of wave duration which is equal to  $2\pi$ ).

Shown in Fig. 4.1 are the positive half periods of the calculated waveforms. The calculations were made using previously discussed numerical algorithms and varying the number of grid points per shock front of the  $N$ -wave. The results of numerical modelling are compared with the quasistationary solution to Burgers equation (4.15) at the distance  $\sigma=157$  (at this distance the ideal  $N$ -pulse becomes twice longer). It is seen (Fig. 4.1a), that to obtain more or less accurate solution in the case of the first proposed algorithm, it is necessary to have more than 50 grid points per shock front of the initial pulse, or as equal, 12000 grid points per wave duration. This leads to very strong time consumption. If the number of grid points per initial shock is chosen to be smaller, the position of the wave front, its amplitude and rise time are predicted incorrectly. If one is interested only in the wave amplitude and duration, it is still possible to use this algorithm, having not very strong numerical error. However, if the shock rise time is of interest, then this algorithm can easily give an error of more than 100%, if wave propagation is calculated even with more than 20 grid points per shock. The second proposed algorithm – conservative finite difference scheme – is much better suited to solve the Burgers Eq. (Fig. 4.1b). With only 7 grid points per initial shock a good accuracy of main wave parameters determination is achieved: the error does not exceed 0.2% when comparing with quasistationary solution to the Burgers equation. However, further decrease of grid point number per shock front leads to the formation of Gibbs instabilities on the waveform. To suppress these instabilities, additional artificial absorption needs to be introduced. However, it will result in shock front widening. Finally, it appeared that Godunov type scheme (Fig. 4.1c) is the best suited to perform desired calculations of  $N$ -wave propagation in nonlinear dissipative medium.

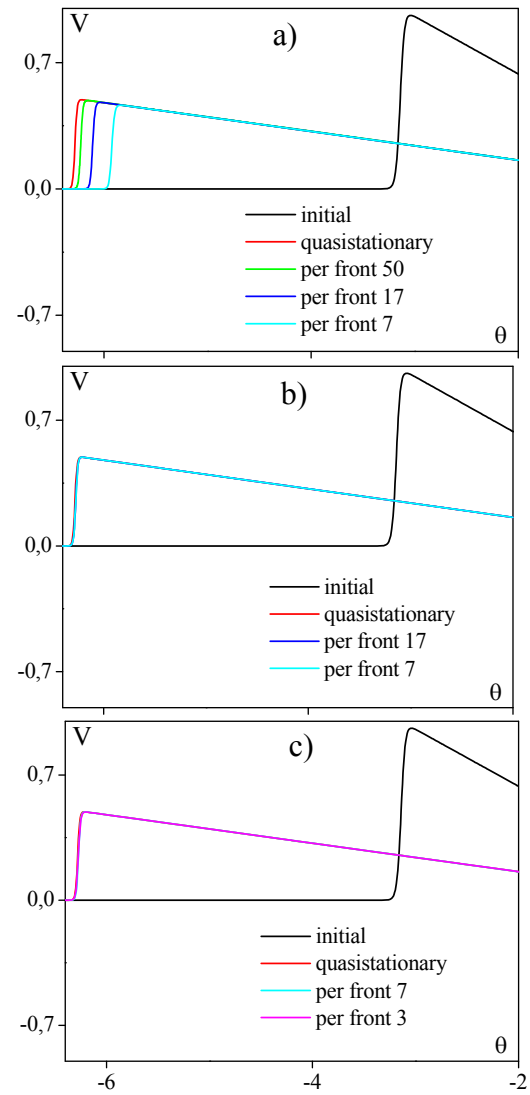


**Fig. 4.1** Comparison of nonlinear waveforms, calculated at the distance  $\sigma=157$  using different numerical algorithms and varying the number of grid points per shock front of the wave. a) – implicit numerical algorithm built on the basis of the exact solution to the simple wave equation, b) – explicit finite difference conservative algorithm, c) Godunov type explicit conservative algorithm.

This algorithm gives good results even with only 3 grid points per wave shock front. At that stage, the numerical error of main wave parameters estimation (peak positive pressure, duration and rise time) does not exceed 0.2%. (Optimal relation between time step and spatial step in lossless media in the sense of both time contribution and accuracy is  $h_\sigma < [3, 4] h_\theta$ ). It should be noted that the presented algorithm describes very good the nonlinear propagation of acoustic pulses even in lossless media (without introducing the absorption). In this case of acoustic  $N$ -wave propagation in the medium without dissipation, its peak positive pressure and duration are estimated with a very high accuracy, whereas the minimal value of the shock front rise time is limited with 3 grid points, that can be explained by small internal viscosity of the algorithm.

The problem of optimal numerical algorithm selection occurs also at the third step of numerical procedure, while computing the convection of sound wave in the direction of its propagation due to the presence of medium velocity fluctuations Eq. (4.18). As in the previous case, three different numerical algorithms are compared: 1) an explicit algorithm built on the basis of the exact solution  $V(\sigma_{i+1}, \theta_n) = V(\sigma_i, \theta_n + 2\pi U_{\parallel} h_\sigma)$  to the transport equation, 2) the Lax-Wendroff explicit numerical algorithm [Press *et al.*, 124], and 3) an explicit numerical algorithm, built on the basis of frequency domain exact solution for complex amplitudes (see below). To estimate the accuracy of each algorithm, the numerical solutions are compared to the exact solution i.e.: the step solution for the transport equation  $V = V(\theta + 2\pi U_{\parallel} \sigma)$ . Here, like previously, the first implicit method appears to be too much dissipative when not sufficient grid points per shock front is used. Moreover, to obtain sufficiently good accuracy in computations, the stronger limitations on the number of grid point per shock front is needed. For example, a 4% accuracy is achieved only if in the calculations a minimum of 80 grid points per shock are used.

The second method (Lax-Wendroff) allows to obtain an accurate solution for the computation done with  $n = 50$  grid points per initial shock front (in this case the error in main wave parameters estimation is not greater than 3% as compared to the exact solution). Further decrease in grid point number per shock front leads to the formation of Gibbs oscillations.

The most efficient algorithm, in the sense of getting better accuracy paying less time contribution, is the third algorithm despite of the necessity of direct and inverse Fourier transforms realization. It allows obtaining a good accuracy (less than 1% error) having only 2-3 grid points per initial wave front. Moreover, the use of this method allows also accounting for frequency dependent thermoviscous absorption [Averiyanov *et al.*, 122] and relaxation effects almost without additional time consumption:

$$C_n(\sigma + h_\sigma) = C_n(\sigma) \exp(-An^2 h_\sigma - i \cdot 2\pi m U_{\parallel} h_\sigma - n^2 h_\sigma \sum_{v=1}^2 \frac{D_v \theta_v}{1 + n^2 \theta_v^2} - in^3 h_\sigma \sum_{v=1}^2 \frac{D_v \theta_v^2}{1 + n^2 \theta_v^2}) \quad (4.31)$$

In addition, as soon as the spectrum of real function is symmetric, the number of harmonics used is two times smaller than the actual number of time grid points per wave duration. The limitations of this method consist only in the use of at least 2-3 points per wave front at all stages of propagation. Thus, at the third step of the global numerical procedure (4.16)-(4.21), the following effects are accounted for: convection in the direction of the wave propagation (4.18), frequency dependent thermoviscous absorption (4.17) and relaxation effects (4.21).

At the last step of the numerical procedure the convection in the direction, transverse to the direction of the wave propagation (4.19) is taken into account. As the acoustic pressure field does not have emphasized shocks in the transverse direction, the transport equation is solved numerically using the Lax-Wendroff explicit algorithm [Press *et al.*, 124] of the second order accuracy in both spatial directions, transverse and longitudinal to the wave propagation:

$$V_j^{i+1} = V_j^i - \frac{h_\sigma}{2h_\rho} U_{\perp} [V_{j+1}^i - V_{j-1}^i - \frac{h_\sigma}{h_\rho} U_{\perp} (V_{j+1}^i - 2V_j^i + V_{j-1}^i)] \quad (4.32)$$

Thus, to model the formation of the acoustic field in the medium with  $N=0.05$  and  $A=0.00034$  the following parameters of numerical simulations are chosen (the method of appropriate numerical parameters selection is described in Appendix B):  $h_\sigma = 2.5 \cdot 10^{-2}$  and  $h_\rho = 2 \cdot 10^{-2}$  are the steps in longitudinal and transverse directions, respectively. Numerical grid steps are chosen to provide a good stability of the numerical algorithm, and to describe accurately the fine structure of the field (to have a good resolution). For example, not less than 10 grid points in each direction are used to describe the focal spot.

The number of time grid points within the wave duration is chosen to be  $n=1024$ . This amount is quite enough to accurately describe the shock front rise time even in the wave foci. The accuracy of the total procedure was checked by the comparison with numerical solutions calculated with different steps (see, Appendix B). So, for twice smaller numerical steps the relative error between main parameters of two solutions was not higher than 3%. In addition, to avoid the influence of parasitic reflections from the edges of numerical domain, the spatial computational window in transverse direction is chosen to be larger ( $L_{window} = 400 \lambda$ ) than the area of interest ( $L_{area} = 370 \lambda$ ).

#### § 4.4 Benchmark solutions and validation of the model

In general, derived evolution parabolic Eq. (4.6) is valid only for relatively small angles of diffraction  $\theta_m \ll 1$  and, therefore, it is valid only for the acoustic wave propagation through big size inhomogeneities for which  $kl \gg 1$ , where  $k$  is the wave number and  $l$  is the inhomogeneity size [47, 127]. However, in the investigated problems of acoustic signals propagating through different type of inhomogeneities, their characteristic sizes appear to be often of the order of the wavelength. In this case of the presence of small inhomogeneities the validity of the parabolic Eq. (4.6) is questionable. Therefore, to test the validity of the theoretical model and numerical algorithm, let us consider first the example of linear propagation of an initially plane harmonic wave through a singular focusing scalar Gaussian inhomogeneity of one wavelength size:  $U_{\parallel}^0 = U_0 \exp(-(\sigma - 10)^2 - \rho^2)$  and  $U_{\perp}^0 = 0$  in the Eq. (4.6). A value of  $U_0 = 0.03$  was used which resulted in the sound speed in the centre of inhomogeneity about 3% lower than the background sound speed  $c_0$  (see Fig. 4.2a). This kind of inhomogeneity was chosen to compare the obtained results with a solution to the more precise wide-angle parabolic equation [Dallois *et al.*, 25] and to the parabolic equation solved in the time domain [115, 128], and thus to check the accuracy of

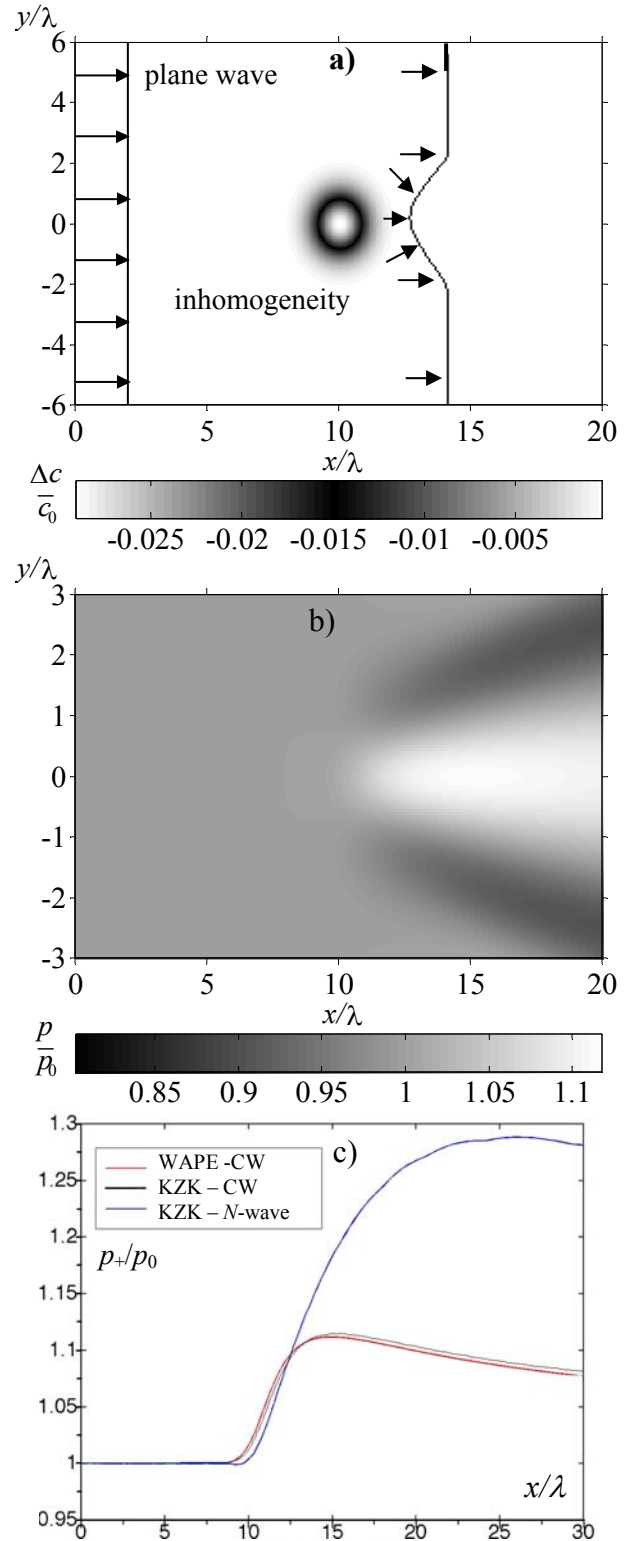


**Fig. 4.2.** (a) Sound speed map for a medium with a single scalar focusing Gaussian inhomogeneity with  $\Delta c_{max}/c_0 \sim 3\%$  and (b) corresponding distribution of peak acoustic pressure resulting from linear continuous wave (CW) propagation through the inhomogeneity. (c) distributions of the pressure amplitude, obtained along the symmetry axis by solving KZK type Eq. (4.6) and wide angle parabolic equation (WAPE).

the theoretical model and of the numerical scheme.

During the propagation of the acoustic wave through the sound speed inhomogeneity an initially plane wave front distorts, resulting in the wave focusing and formation of areas with increased pressure (Fig. 4.2b). The areas of defocusing and corresponding decrease of the pressure amplitude are also formed along with creation of wave defocusing regions. Shown in Fig. 4.2c are the peak pressure distributions at the axis passing through the centre of the Gaussian inhomogeneity in the direction of the initial wave propagation. Pressure distribution (black line) is calculated for the propagation of the continuous wave (CW) using the numerical procedure (4.13) for the KZK type equation (4.6). Red line corresponds to the solution to the wide angle parabolic equation – WAPE-CW [Dallois *et al.*, 25] for continuous wave, and black curve describes the distribution of an  $N$ -wave peak pressure calculated along the same axis using the KZK-type equation (4.6). It is seen, that the amplitude of the continuous wave along this axis is in a good agreement with the solution obtained based on wide angle parabolic approximation. The difference in the results was less than 3% when the spatial marching steps  $h_\sigma$  and  $h_\rho$  were set to a value of 50 points per acoustic wavelength. Thus the nonlinear evolution equation of the KZK type, derived in this work, can be used for the acoustic field computations in inhomogeneous media with characteristic scales of the order of acoustic wavelength.

After checking the accuracy of the derived evolution equation, let us compare the acoustic pattern with the distribution of acoustic rays (for details about geometrical acoustics equation refer to Appendix A) in the inhomogeneous medium with only one scalar Gaussian fluctuation presented  $U_{||}^0 = U_0 \exp\left[-\frac{(x-10)^2 - y^2}{R^2}\right]$ , where  $R$  is the characteristic size [Khokhlova *et al.*, 129]. It is known that geometrical acoustics is not valid for description of sound wave propagation through small size inhomogeneities. For comparison, different sizes of inhomogeneity are considered: small size  $R=1.5\lambda$  (Fig. 4.3a), intermediate size  $R=3\lambda$  and large size  $R=5\lambda$  inhomogeneities. The value of fluctuation amplitude is chosen to be  $U_0 = 0.06$ . Such inhomogeneity by its physical properties resembles the defocusing lens [130, 131]. The incidence of initially plane harmonic wave in linear regime on defocusing Gaussian inhomogeneity is considered.

The results of numerical modelling are presented in Fig. 4.3. As expected for small size inhomogeneities (Fig. 4.3a – the diameter is equal to 3 acoustic wavelengths), the differences between the positions of focusing areas due to parabolic equation and rays consolidation positions, obtained using the geometrical acoustics equations, are clearly notable (Fig. 4.3b). For larger scale inhomogeneities (Fig. 4.3c and d) the agreement between the two solutions becomes much better. Nevertheless, for all three investigated inhomogeneities, the geometrical acoustics

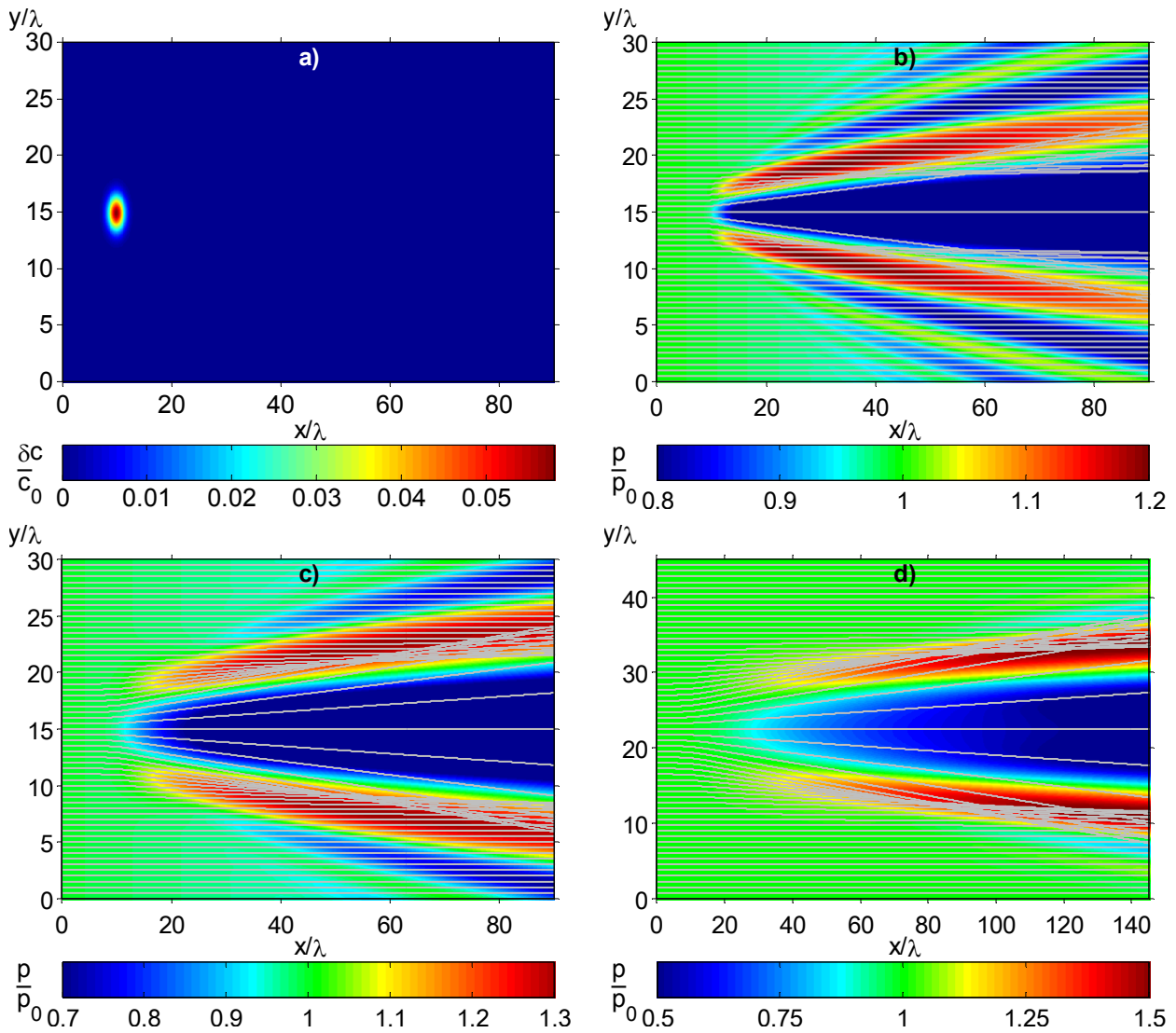


**Fig. 4.3.** Comparison of peak pressure distributions in the solution to wave Eq. (4.6) with the distributions of acoustic rays obtained using geometrical acoustics equations for propagation of plane acoustic wave through the single scalar Gaussian inhomogeneities (a) of different sizes:  $R = 1.5\lambda$  (a,b),  $R = 3\lambda$  (c),  $R = 5\lambda$  (d) and same disturbance amplitude  $U_0 = 0.06$ .

does not show the existence of secondary focusing and defocusing zones (rays are straight there), since they are formed due to diffraction effects.

## § 4.5 Conclusion

In this Chapter, a new parabolic evolution equation for describing the propagation of nonlinear sound waves in inhomogeneous moving media was derived. This equation is an extension of the KZK-type equation for nonlinear beams generalized for arbitrary inhomogeneous media. In particular, the component of medium motion that is transverse to the wave propagation direction was taken into account. The assumptions invoked in deriving this

generalized equation were that the fluctuations in the medium properties varied slowly in space and in time, and that the sound speed or velocity fluctuations were small in magnitude as compared to the sound speed. The diffraction is modelled using the parabolic approximation which restricts the validity of the solution to collimated beams and is generally accepted to be a good model for sound with propagation direction within 20 degrees of the axis [Tjøtta *et al.*, 127]. Therefore, this model is appropriate for considering the inhomogeneities that primarily result in scattering in the forward direction. The derived parabolic equation was found to have properties of similarity, which allows finding solutions for certain types of medium mean motion in the presence of small fluctuations using the solution for effective fluctuations.

A numerical algorithm, which allows the investigation of a wide number of problems of intense periodic wave or pulse propagation through different types of inhomogeneities, was developed. In particular, this algorithm allows computing an acoustic  $N$ -wave propagation in inhomogeneous moving medium with account for the diffraction and nonlinear effects, thermoviscous absorption, and also for the effects, caused by the influence of longitudinal and transverse components of the medium vector inhomogeneities. The advantage of the developed algorithm is that it allows computing the propagation of acoustic waves with thin shock fronts, using only 3 grid points per its front. In comparison with the widely used Texas code for solving the KZK equation [Lee, 125], the algorithm developed here gives much better resolution of the wave shock front structure, without having a significantly increase of the computational time. However, to find the solution to the parabolic equation high time expenses are still needed. For example, the calculation time of one realization 120 x 500 wavelength under conditions, described in this chapter, as long as about 85 hours of machine time at HP AlphaServer 128



## Chapter 5

### **NONLINEAR AND DIFFRACTION EFFECTS DURING THE PROPAGATION OF ACOUSTIC SIGNALS IN RANDOMLY INHOMOGENEOUS MOVING MEDIUM (Numerical modelling)**

This chapter of the dissertation is devoted to the numerical calculation and investigation of nonlinear propagation of acoustic signals in inhomogeneous moving media. Propagation of periodic signals and acoustic  $N$ -pulses is considered. Based on the modelling results, the influence of nonlinear and diffraction effects on the acoustic field structure and random caustics formation is investigated. The role of characteristic scale and intensity of the inhomogeneous moving medium fluctuations and influence of the transverse component of velocity field on the acoustic wave propagation is revealed. As an example of the propagation media one realization of random velocity field with Gaussian energy spectrum is presented. The results of simulations of acoustic wave propagation in random media with modified von Karman energy spectrum, a more realistic energy spectrum for atmospheric turbulence, are also presented. Finally, results of the simulations for the  $N$ -wave propagation in turbulent air under conditions of the laboratory scale experiment are compared to the measured data (Chapter 2).

#### **§ 5.1 Periodic waves**

##### *5.1.1 Nonlinear versus linear effects of random focusing in an inhomogeneous moving medium*

The longitudinal and transverse components of one typical realization of random velocity field with Gaussian energy spectrum are shown in Fig. 5.1. Corresponding

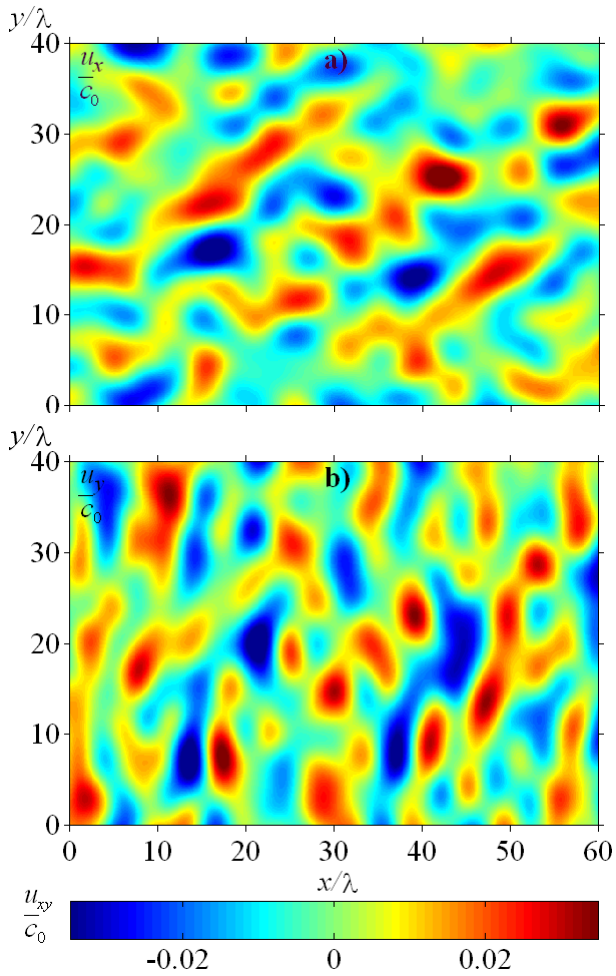


**Fig. 5.1.** (a) Longitudinal and (b) transverse components of the random velocity field with Gaussian energy spectrum. Characteristic length of inhomogeneities  $L = 3\lambda$ , and root mean square velocity  $u_{rms} = 2.5$  m/s.

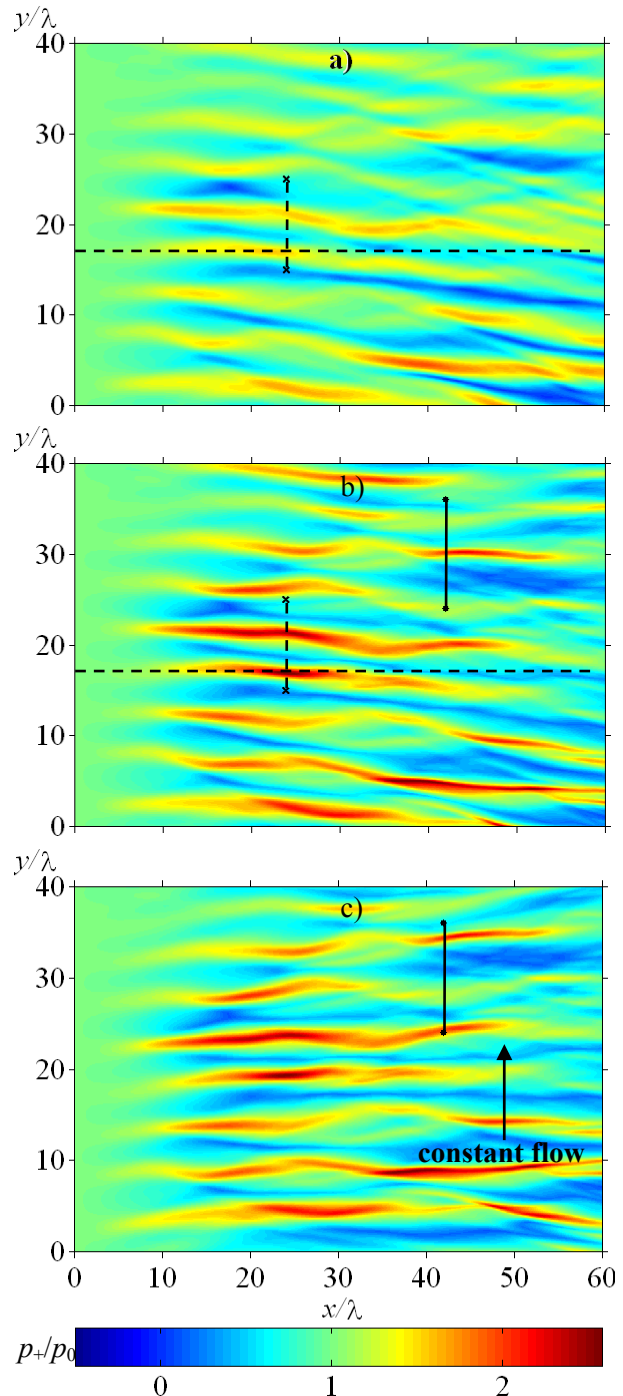


**Fig. 5.2.** Spatial patterns of the peak positive pressure corresponding to (a) linear ( $N = 0$ ) and (b) nonlinear ( $N = 0.05$ ) propagation of an initially plane harmonic wave through the randomly inhomogeneous moving medium. (c) The result for nonlinear propagation ( $N = 0.05$ ) in the presence of an additional transverse constant flow  $U_{\perp}^0 = 0.1$ . Vertical solid line shows the location for the transverse field presented in Fig. 5.6, dashed vertical line - for the transverse distributions shown in Fig. 5.3, and dashed horizontal line - for the longitudinal distributions in Fig. 5.4.

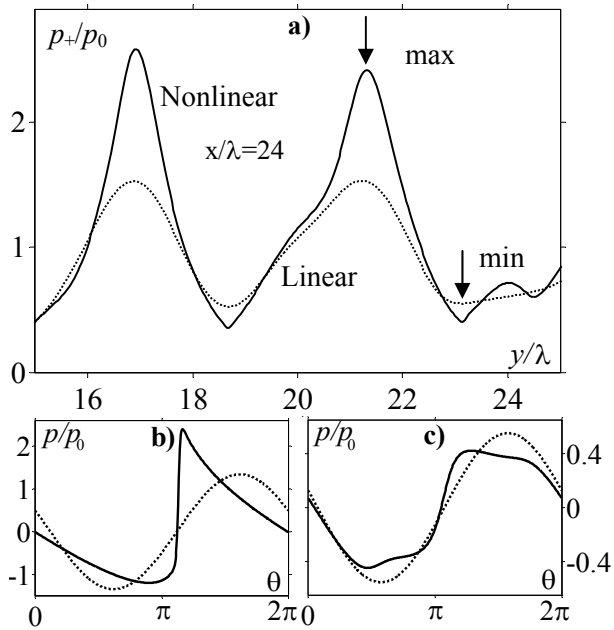


**Fig. 5.3.** (a) Transverse distributions of the peak positive pressure at a distance  $x/\lambda = 24$  along the dashed segments shown in Fig. 5.2 for linear ( $N = 0$ , dotted line) and nonlinear ( $N = 0.05$ , solid line) propagation. (b) Linear and nonlinear waveforms at locations of maximum positive pressure  $x/\lambda = 24$ ,  $y/\lambda = 21.3$  (indicated as max in (a)). (c) Waveforms at the pressure minimum,  $x/\lambda = 24$ ,  $y/\lambda = 23.15$  (indicated as min in (a)).

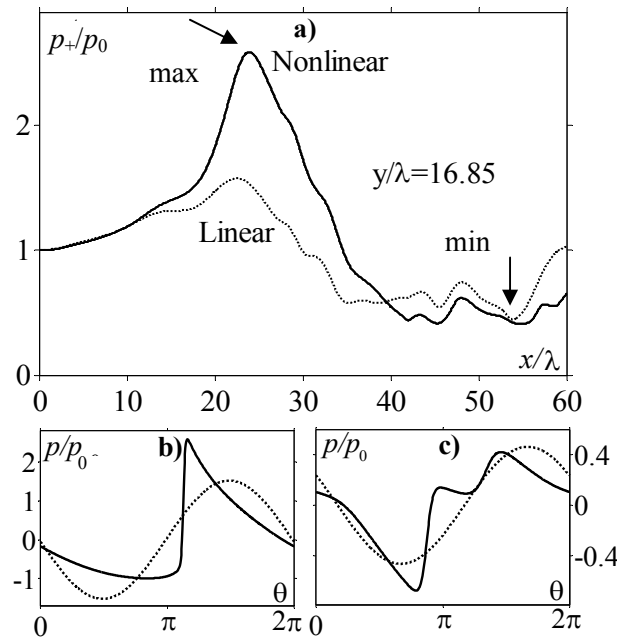


**Fig. 5.4.** (a) Longitudinal distributions of the peak positive pressure for linear ( $N = 0$ , dotted line) and nonlinear ( $N = 0.05$ , solid line) propagation along the dashed line  $y/\lambda = 16.85$  shown in Fig. 5.2. (b) Linear and nonlinear waveforms at locations of maximum positive pressure,  $x/\lambda = 24$ ,  $y/\lambda = 16.85$  (indicated as max in (a)). (c) Waveforms at the pressure minimum,  $x/\lambda = 54$ ,  $y/\lambda = 16.85$  (indicated as min in (a)).

distributions of acoustic peak positive pressure patterns, in case of linear ( $N = 0$ ) and nonlinear ( $N = 0.05$ ) propagation of an initially plane harmonic wave through this inhomogeneous medium velocity field are presented in Fig. 5.2. Note that both longitudinal and transverse components of the velocity field were included in the numerical simulations. No absorption was applied in the case of linear propagation, and in the case of nonlinear propagation the absorption coefficient was equal to  $A = 0.002$ . Qualitatively the morphology of the acoustic field can be predicted based on the data shown in Fig. 5.1, that is, regions of decreased effective sound speed result in focusing and regions of increased effective sound speed result in defocusing (analogous to a divergent lens). Indeed the formation of focusing regions and shadow areas due to random focusing and defocusing of the wave is clearly observed in Fig. 5.2a-c. Regions of increased pressure do follow regions of the minimum values of the velocity field. The maximum positive peak pressure  $p/p_0 = 2.6$  is reached in the case of nonlinear propagation compared to  $p/p_0 = 1.5$  in the case of linear propagation. In spite of the additional absorption on the shocks, the maximum of the peak positive pressure in nonlinear case is higher than that for the linear one even at the distances of 60 wavelengths (three shock formation lengths).

To illustrate the effect of acoustic nonlinearity on the wave propagation in randomly inhomogeneous medium, two one-dimensional distributions of peak positive pressure across and

along the travelling coordinate  $x$  are presented in Figs.5.3 and 5.4. The solutions correspond to the linear ( $N=0$ , dotted curves) and nonlinear ( $N=0.05$ , solid curves) propagation within the dashed line intervals shown in Fig. 5.2a, and Fig. 5.2b. It is clearly seen that nonlinearity results in much higher peak pressures in focal regions, tightening of the width of the increased pressure area, and a shift of the maximum peak pressure in both the longitudinal and transverse directions. Even at ranges of 3 shock formation distances, despite the existence of strong nonlinear dissipation on the shocks, the regions of increased pressure level are observed due to the transverse redistribution of the acoustic energy (see Fig. 5.2). Linear and nonlinear waveforms that correspond to locations of the maximum and minimum in the peak pressure distributions are also shown in Figs 5.3 and 5.4. In the focal regions (Figs 5.3b and 5.4b) typical asymmetric distortion of the waveform with a developed shock front, increased positive peak and smoothed negative part of the waveform was observed in the case of nonlinear propagation. In regions of pressure minima the nonlinear waveforms (Figs 5.3c and 5.4c), still demonstrated significant distortion, but in this case shocks were not present presumably because the higher harmonics components appeared due to scattering from the focused regions.

The effective absorption of acoustic energy, with and without the presence of random inhomogeneities, can be compared using the intensity dependence on the propagation distance. The intensity is normalized to its initial value (at  $x=0$ ) and averaged over the transverse coordinate at every step in propagation distance  $x$ . Figure 5.5 shows the results for linear propagation in either homogeneous or inhomogeneous absorptive medium (upper solid curve), for nonlinear propagation in a homogeneous medium using weak shock theory (WST, dotted upper) and with absorption explicitly modelled (Burgers, dotted lower), and for nonlinear propagation in randomly inhomogeneous medium (NPE – nonlinear parabolic equation, lower solid curve). Some energy dissipation ( $\sim 20\%$  at the distance of 60 wavelengths) in case of linear propagation is due to inclusion of the same absorption ( $A = 0.002$ ) as used in the nonlinear simulations. The Burgers and NPE nonlinear simulations show similar energy

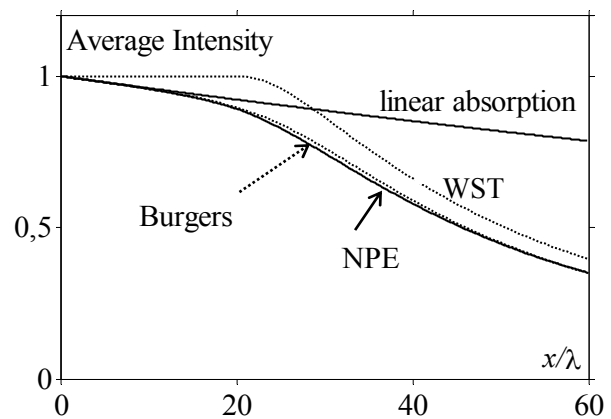


**Fig. 5.5.** Dependence on distance of propagation for the wave intensity averaged over the transverse coordinate for: linear propagation in a dissipative medium, nonlinear propagation governed by weak shock theory (WST), nonlinear plane wave propagation in a dissipative medium (Burgers equation), and nonlinear propagation in moving inhomogeneous dissipative media governed by the nonlinear parabolic equation (NPE). Parameters of simulations are  $N = 0.05$ ,  $A = 0.002$ ,  $N_{max} = 150$

loss as the linear simulations for distances up to one shock formation distance (about 20 wavelengths for  $N = 0.05$ ). After this range the main contribution to the energy loss (~60 - 70%) is due to strong nonlinear absorption at the shocks. Note that the energy dissipation in a nonlinear homogeneous medium (Burgers equation) is almost the same as in nonlinear inhomogeneous medium (NPE). A small difference can be noticed only between one and two shock formation distances (20 – 40 wavelengths). The presence of inhomogeneities thus does not lead to significant changes in energy losses. The use of weak shock theory does not model the energy losses at small distances and at long ranges appears to be offset by an amount similar to the linear losses (Fig. 5.5).

### 5.1.2 *Effect of the transverse component of turbulent velocity field: vector versus scalar contributions of inhomogeneities*

Spatial structure of the acoustic field (Fig. 5.2, a and b) is formed mainly due to the presence of the longitudinal component  $U_{\parallel}$  of the random velocity field. The transverse component  $U_{\perp}^0$  acts as a flow, which shifts randomly the focusing and shadow zones in the direction perpendicular to the direction of the wave propagation. Note, that for the chosen characteristics of inhomogeneities (relatively small scale  $L = 3\lambda$  and not high value of the hydrodynamic Mach number  $M = \max(U_{\parallel}, U_{\perp}) = 0.03$ ) the inclusion of random transverse velocity component in the computation did not noticeably change the resulting structure of acoustic field. The effect of transverse velocity component, however, becomes stronger when the scale of inhomogeneities  $L$  increases, in particular, in the presence of a constant flow in the transverse direction. Let us consider here, as an example, a combination of a random velocity field (Fig. 5.1) with the constant transverse flow  $U_{\perp}^0 = 0.1$ . Simulations were done for nonlinear wave propagation with nonlinearity parameter  $N = 0.05$ . The results of simulations are presented in Fig. 5.2c as the peak positive pressure pattern. Note, that in this case, the flow shifts not only the acoustic field, but also the random velocity inhomogeneity. Therefore, when the uniform flow was superimposed on the random field velocity distributions the random field was transformed to account for the spatial shift of the inhomogeneities in the transverse direction (due to the presence of the flow). The resulting velocity field  $U_{\perp} = U_{\perp}^0 + \tilde{U}_{\perp}(\sigma, \rho - U_{\perp}^0 \sigma)$  then was used in the simulations of the acoustic field, Eq. (4.6), in which the constant velocity  $U_{\perp}^0$  was also included. A noticeable shift of the field towards the direction of the flow without changing the morphology of the field is clearly observed. Note, that the results for the acoustic field in the presence of constant flow, Fig. 5.2c, can be also obtained without additional

simulations, but using the numerical results for the case without the flow (but with shifted random inhomogeneities (4.10)) and analytic transformations (4.7, 4.8), that exclude the mean flow from the parabolic Eq. (4.6).

To illustrate the effect of shifting the nonlinear acoustic field by the constant flow without changing its spatial structure, three one-dimensional transverse distributions are presented in Fig. 5.6. The location of the distributions is denoted by the transverse solid line shown in Fig. 5.2 (b and c) at a distance

$x/\lambda = 42$ . In Fig 5.6 the black curve is the peak positive pressure modelled with the presence of only random inhomogeneities, the red curve is the result in the presence of inhomogeneities and uniform flow  $U_{\perp} = U_{\perp}^0 + \tilde{U}_{\perp}(\sigma, \rho - U_{\perp}^0 \sigma)$  based on the analytic transformation (4.10), and the blue circles - the purely numerical result in the presence of inhomogeneities and uniform flow. It is seen that transformation is in excellent agreement with the direct numerical results. This provides an additional verification of the algorithm developed for modelling the effect of the transverse component of the velocity field.

### 5.1.3 Diffraction effects: ray tracing and acoustic field patterns obtained with the KZK equation

As it has been mentioned in §4.4, the geometrical acoustics approach does not accurately describe the positions of increased pressure level areas for simple inhomogeneous structures, especially of small size. Let us now consider the propagation of an initially plane linear harmonic wave through the random inhomogeneity with Gaussian energy spectrum (Fig. 5.7a) and a sufficiently large characteristic scale  $L=3\lambda$ . The corresponding acoustic field peak positive pressure pattern is shown in Fig. 5.7b together with the rays paths distribution (grey lines), which are the solutions to the eikonal equation (Appendix A1). During the acoustic wave propagation through inhomogeneous medium, the caustics form. Their positions can be estimated by the consolidation of a large amount of the acoustic rays in a small spatial region. According to

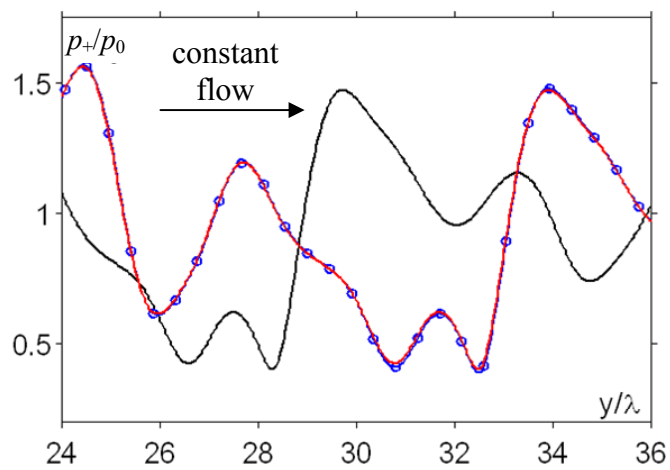


**Fig. 5.6** Distributions of peak positive pressure along the transverse segments (solid lines) shown in Fig. 5.2b and Fig. 5.2c at the distance  $x/\lambda = 42$ . Black curve – propagation through random velocity field (Fig. 5.2b), red curve – analytic transformation of the numerical solution to account for additional constant flow, blue circles – full numerical solution in the case of the flow presence (Fig. 5.2c).

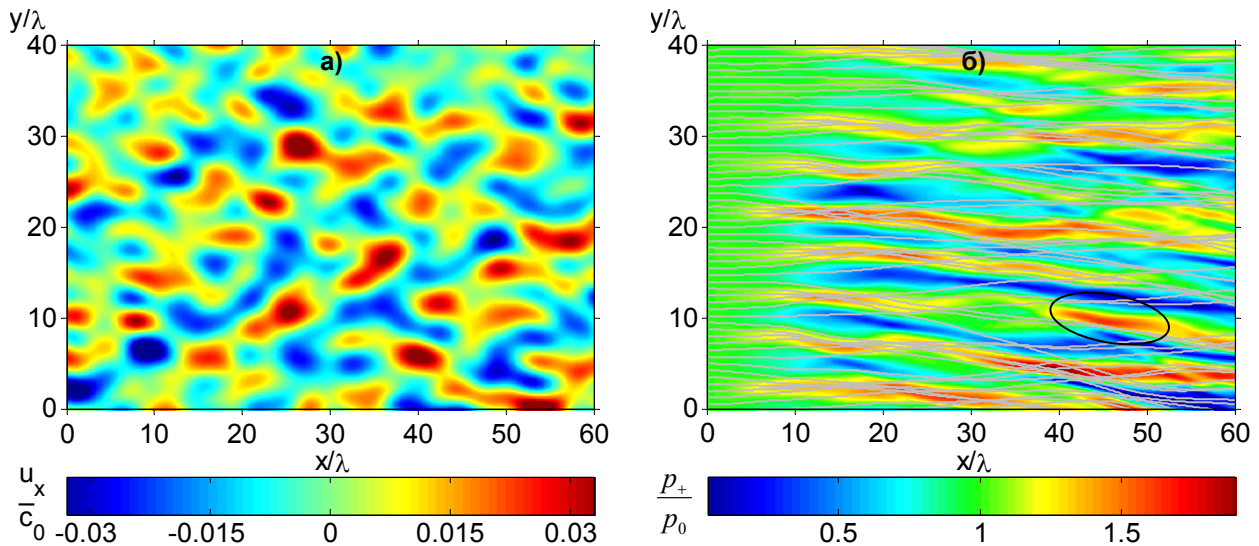


**Fig. 5.7** a) – longitudinal component of a random inhomogeneous velocity field with Gaussian energy spectrum and  $u_{rms} = 2.5$  m/s,  $L=3\lambda$ . b) – corresponding spatial distribution of peak positive pressure in the case of linear wave propagation and ray paths – grey lines – solutions of the eikonal equation.

the properties of caustics, their positions should correspond to the areas of increased level pressure at the acoustic field pattern. However, similar to the case of simple scalar Gaussian inhomogeneities (§4.4), the caustic positions, predicted by the ray acoustics, and increased pressure level areas positions are not in a good agreement. Agreement between two theories is achieved only for first caustics and increased level pressure regions (see the caustics at the distance  $\sim 15$  wavelengths, Fig. 5.7b). Estimations of secondary focusing and defocusing areas positions are far from each other. This can be explained by the fact that first areas of focusing and corresponding caustics are formed by plane acoustic wave, which had not enough time to diffract on inhomogeneities. That is why at short distances, the areas of rays densification do correspond to the pressure maxima of acoustic field. Further, with increasing distance, the diffraction effects accumulate along the propagation path of the wave. Geometrical acoustics does not account for these effects, and therefore, its predictions of secondary caustics positions may not be accurate, and they appear to be shifted compared to the locations of the maxima of the acoustic pressure field. For example, in some cases, according to geometrical acoustics approach, there should be a decrease of acoustic pressure, but parabolic Eq. (4.6) predicts an opposite effect (focusing zone near  $x/\lambda = 45$ ,  $y/\lambda = 11$ ).

#### 5.1.4 Effect of spatial correlation lengths and intensity of the turbulence on acoustic field characteristics

In previous paragraph of this Chapter, the random inhomogeneities with the characteristic scale equal to  $L=3\lambda$  have been considered. However, in realistic problems, the inhomogeneities

with longer and shorter scales are also of importance. For example, in aeroacoustics, the propagation of sonic booms with length of the order of 50 m is considered. And the atmosphere inhomogeneities have an outer scale of several hundred meters. Consequently we investigate the propagation of an acoustic wave through the random inhomogeneity with a characteristic scale  $L = 5\lambda$  or 250 m, and a mean square velocity  $u_{rms} = 7.4$  m/s. In Fig. 5.8a the longitudinal component of random velocity field is presented. Corresponding spatial distribution of the peak positive pressure in nonlinear regime ( $N = 0.1$ ) of initially plane harmonic wave propagation is shown in Fig. 5.8b. Numerical modelling was done using 100 first harmonics. The necessary artificial absorption was set to be  $A = 0.0052$  to provide the stability of the algorithm. In the case of large scale inhomogeneities, areas of increased level pressure are positioned with longer

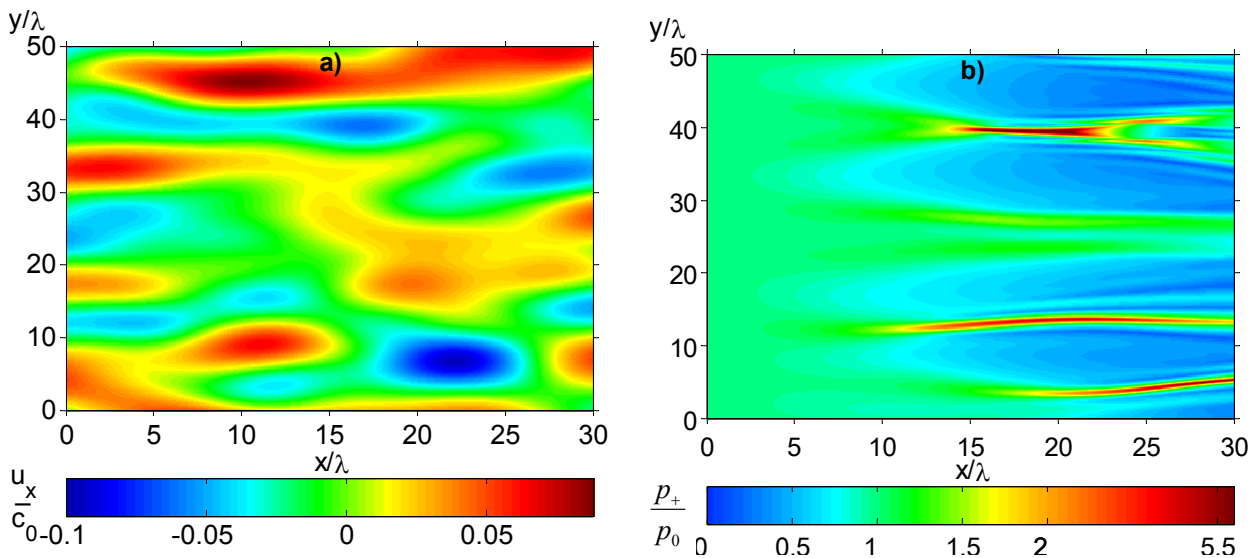


**Fig. 5.8:** a) – longitudinal component of a random velocity field ( $u_{rms} = 7.4$  m/s,  $L = 5\lambda$ ) and b) – corresponding spatial distribution of the peak positive pressure ( $N = 0.1$ ,  $A = 0.0052$ ,  $N_{max} = 100$  harmonics). Both longitudinal and transverse components of the velocity field are taken into account.

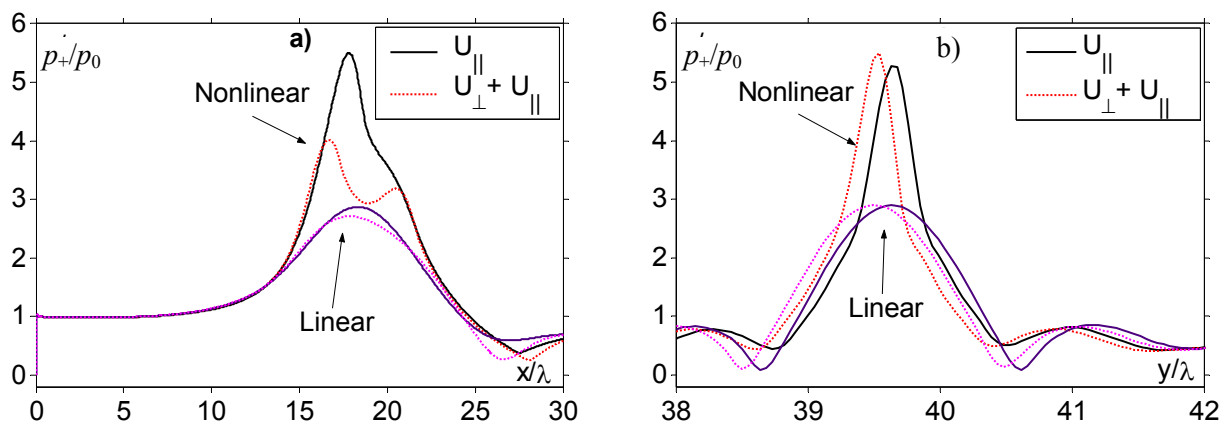


**Fig. 5.9** Peak positive pressure distributions in longitudinal direction along the line  $y/\lambda = 39.5$  (a) and in transverse direction along the line  $x/\lambda = 17.5$  (b) in both linear ( $N=0.0$ ) and nonlinear ( $N=0.1$ ) regimes. Calculations are done with account for both longitudinal and transverse components of inhomogeneous field (dotted curves) or only with account for the longitudinal one (solid curves).

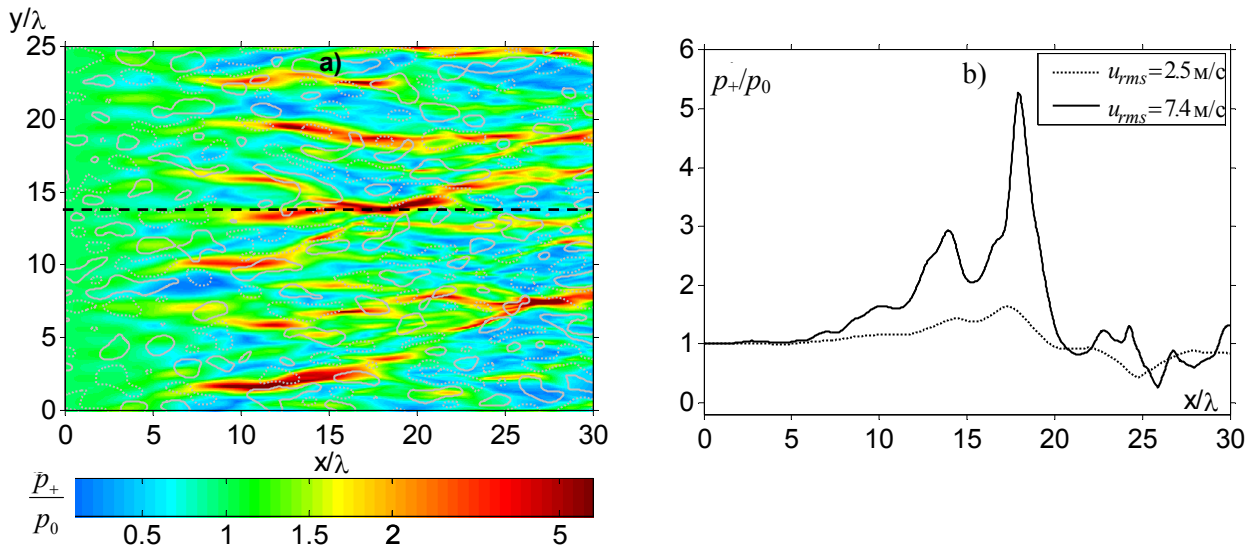


**Fig. 5.10.** a) Spatial distribution of peak positive pressure and longitudinal component of medium velocity fluctuations (grey contour lines). Dashed contours correspond to  $u_x/c_0 = -0.04$  level, and solid contours to  $u_x/c_0 = 0.04$  level. b) peak positive pressure distributions along dashed line in Fig. 5.10a calculated for different value of turbulent fluctuations intensities:  $u_{rms} = 7.4$  m/s and  $u_{rms} = 2.5$  m/s

spacing in transverse direction; they are of larger longer and their amplitude is higher. Moreover, very wide regions of wave defocusing are observed.

In order to determine the influence of the transverse component of the random velocity field on acoustic field structure, the simulations were performed with account for both velocity components or with account only for transverse one  $U_{\perp}$ . The results of the simulations are presented in Fig. 5.9 as the longitudinal and transversal peak positive pressure distributions. Presented data are taken along the lines  $y/\lambda = 39.5$  and  $x/\lambda = 17.5$  respectively. Due to the influence of transverse fluctuations the focal regions appear to be shifted both in longitudinal and transverse directions. This shift is shorter than the half of the wavelength. It is clear, that with the increase of turbulent fluctuations scale, the effect of acoustic field structure shifting by  $U_{\perp}$  will become stronger.

Consider now the nonlinear ( $N=0.1$ ) propagation of initially plane harmonic wave through a random inhomogeneous field with a characteristic scale  $L$  equal to the acoustic wavelength  $L = 1 \lambda$ . Corresponding peak positive pressure spatial distribution is shown in Fig. 5.10a with the colour pattern. Grey contour lines denote fluctuation levels of the longitudinal velocity component. Solid contours correspond to positive level of velocity fluctuations  $u_x/c_0 = 0.04$ , and dashed contours – to negative level of fluctuations  $u_x/c_0 = -0.04$ . The root mean square velocity of the random field is equal to  $u_{rms} = 7.4$  m/c. The artificial absorption is set to be  $A = 0.0028$  and  $N_{max} = 100$  harmonics to ensure the stability of numerical simulations. We observed that the decrease of characteristic scale of the

inhomogeneity fluctuations leads to the decrease of the wave amplitude in the focal spots. So, for example, for small scale inhomogeneity (Fig. 5.10a) in focusing areas the maximum peak positive pressure value  $p/p_0=5.2$  is reached, that is less than that for larger scale inhomogeneity  $p/p_0=5.8$  (Fig. 5.8a). One more point of difference is that in the case of small scale inhomogeneities the focal areas are formed closer to the source. In both cases the most intense focusing is observed in focal areas, which are formed at the distance of shock wave formation for acoustic plane wave ( $x_s=20\lambda$ ). In fact, if focal regions are formed closer to the source, the acoustic wave does not have time during the propagation to develop higher harmonics and so enhance the focusing effect.

It can be expected, that the change of root mean square velocity fluctuations (turbulence intensity) with retaining the same structure of the inhomogeneity will result in change of acoustic field characteristics. Shown in Fig. 5.10b are the peak positive pressure distributions calculated along the dashed line (Fig. 5.10a) for two levels of turbulence intensity:  $u_{rms} = 2.5$  m/s (dashed line) and  $u_{rms} = 7.4$  m/s (solid line). It is seen, that an increase of fluctuations intensity results in a significant increase of the peak positive pressure (up to four times in considered case) in the focal spot with tiny changes of the acoustic field structure.

## § 5.2 Acoustic pulses. *N*-waves

### 5.2.1 Parameters of simulations, 2D patterns of randomly inhomogeneous velocity field

In this section the acoustic *N*-wave propagation through the random inhomogeneous moving media with Gaussian energy spectrum is considered. For the computation of acoustic ray distribution and acoustic field pattern, the random velocity field of the medium was considered as “frozen”, i.e. it did not depend on time. These assumptions do not limit the validity of shown results and made conclusions. Dimensionless nonlinearity parameter *N* and absorption parameter *A* are taken to be  $N=0.05$  and  $A=0.00034$  if it is not stated otherwise. Chosen nonlinearity parameter is close to its value in physical experiments (both laboratory and field), whereas absorption parameter is about two times larger than that in laboratory experiment, as soon as it is chosen according to the time limitations and to guarantee numerical algorithm stability. Characteristic scale of fluctuations is set to be  $L=4\lambda$  and mean square velocity is equal to  $u_{rms} = 3$  m/s. Typical example of random velocity field is shown in Fig. 5.11 as distributions for longitudinal (a) and transverse (b) components.

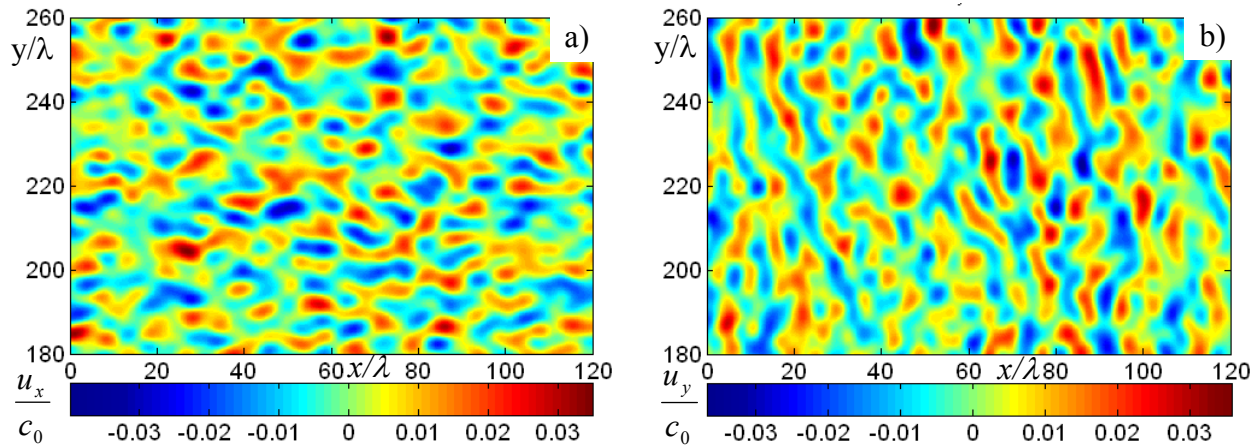


**Fig. 5.11** Longitudinal a) and transverse b) components of the random velocity field with Gaussian energy spectrum. Characteristic fluctuation scale is equal to  $L=4\lambda$ , and mean square velocity is equal to  $u_{rms} = 3 \text{ m/s}$

### 5.2.2 Diffraction effects: ray tracing and acoustic field patterns obtained with the KZK equation

In Fig. 5.12a is shown a distribution of acoustic ray paths (solution to the set of geometrical acoustics equations (Appendix A2-A8)) in the considered inhomogeneous medium. Multiple areas of acoustic ray concentration and intersection are observed, that gives us information about the existence of sufficiently high levels of acoustic pressure in these regions due to narrowing of the ray tubes. Corresponding spatial distribution of the peak positive pressure in the field of propagating *N*-wave (solution to the parabolic Eq. (4.6)) is shown in Fig. 5.12b together with the levels of medium velocity fluctuations (overlaid contour lines). It is seen that due to the presence of inhomogeneities, the acoustic wave energy is redistributed in space, forming regions with higher and lower pressure. Regions of increased peak positive pressure occur directly after the areas of the medium where effective sound speed  $c_0+u_x$  is less than its ambient value  $c_0$  (fluctuations of medium velocity are negative). This is consistent with the fact that these regions should act as focusing lenses by distorting the phase front of the wave. In spite of strong nonlinear dissipation of the wave energy, the peak positive pressure of the *N*-wave in these regions was more than three times the initial value of the incident wave amplitude. Due to random focusing and defocusing effect, the formation of multiple focal zones is observed. Random foci, however, occur mainly at relatively short distances,  $\sigma = x/\lambda < 60$ . This is in contrast with the results obtained for harmonic wave propagation where focusing regions occurred over all studied propagation distances [Averiyanov *et al.*, 11]. For single pulses propagating in an inhomogeneous medium, the increasing difference in the path lengths results in a lengthening of the pulse, in a widening of the shock front, and in a corresponding decay of

the peak pressure. For harmonic waves the periodic nature means that large differences in travel time can still result in constructive interference. For the  $N$ -wave propagation occurrence of high pressures far from the source is a rare phenomenon, but some relatively high level focusing zones are still observed even at longer distances (see e.g., Fig. 5.12b,  $\sigma = x/\lambda = 110$ ).

Shown in Fig. 5.12c is an expanded view of the focal region denoted by the black rectangle in Fig. 5.12b. Overlaid on the peak positive pressure pattern are the ray paths (grey curves) and locations of first (solid grey circles) and second caustics (solid red circles) obtained with geometrical acoustics equations (Appendix A2-A8). The ray paths clearly show focusing and formation of caustics, and are agree qualitatively with the parabolic equation prediction of high pressure levels. However, the positions of caustics obtained in the high frequency limit of geometrical acoustics do not coincide with the position of maximum values of acoustic pressure. Moreover, due to the fact that diffraction is neglected, some caustics, given by geometrical acoustics approach appear in the regions, where the wave amplitude is small. Good agreement for the regions of focusing is achieved mainly for the first caustics, whereas for the second (red solid circles) and higher order caustics nonlinear geometrical acoustics gives incorrect positions of high-level pressure zones. Thus, diffraction effects play very important role in formation of the acoustic field pattern and need to be considered in theoretical models to

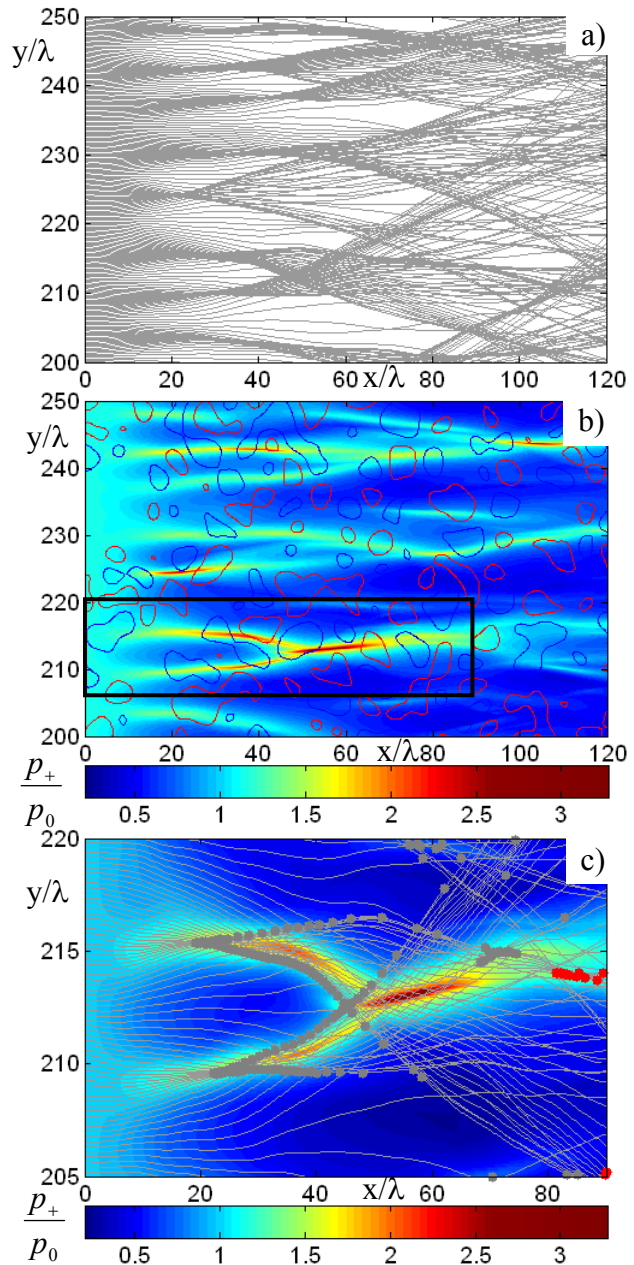


**Fig. 5.12** a) - acoustic rays distribution in inhomogeneous moving medium with Gaussian energy spectrum (Fig. 5.11), b) corresponding acoustic field pattern (peak positive pressure) with marked turbulence levels  $u_x/c_0 = \pm 0.009$  (red - positive, blue - negative), c) expanded view of the peak positive pattern with overlaid rays distribution and caustic locations (grey points - first caustics, red points - second caustics) comparison. Area of expansion is marked with black rectangle in Fig. 5.12b

get realistic results.

Note that in the laboratory scale experiment the turbulent layer was about 1-1.5 m thick (see Table 2.1). Therefore the shock *N*-wave of 1.2 cm length if it goes straight will propagate over a distance about 100-120 wavelengths through the turbulent layer. Therefore, the simulation data that correspond to 100-120 wavelengths is representative of laboratory scale sonic boom propagation.

While propagating through the turbulent medium, acoustic waveform changes its shape due to the combined effect of nonlinearity, diffraction, thermoviscous absorption, effect of inhomogeneities. For example, Fig. 5.13 shows waveforms measured at various locations along the axis  $y/\lambda = 212$ . It is shown there, how an initially ideal *N*-wave distorts while passing through the caustic

(focal area). Distortion results in formation of waveforms having various complex shape: rounded waveforms, waves with several shock fronts, and very long pressure tails. Rounded waveforms ( $x/\lambda = 40$ ), waveforms with two distinct shock fronts ( $x/\lambda = 83$ ), and waves with long pressure tails ( $x/\lambda = 115$ ) are more likely to be observed in the regions with low level pressure (defocusing zones). On the contrary, in areas of high level acoustic pressure (focusing zones) waveforms with several peaks ( $x/\lambda = 51$ ) and classical *U*-shaped waves ( $x/\lambda = 56$ ) are observed. In agreement with this, steeper shock fronts are observed in focusing zones due to higher amplitudes and stronger nonlinear effects. However, nonlinear distortion of the wave occurs also in the regions of low level pressure due to scattering of higher harmonics from the caustics. At longer distances in the turbulent medium, the pulse elongates due to the large variety in travel paths through the medium. This pulse spreading in time makes it very unlikely for the medium to effectively refocus the wave and produce a large amplitude wave at longer distance.

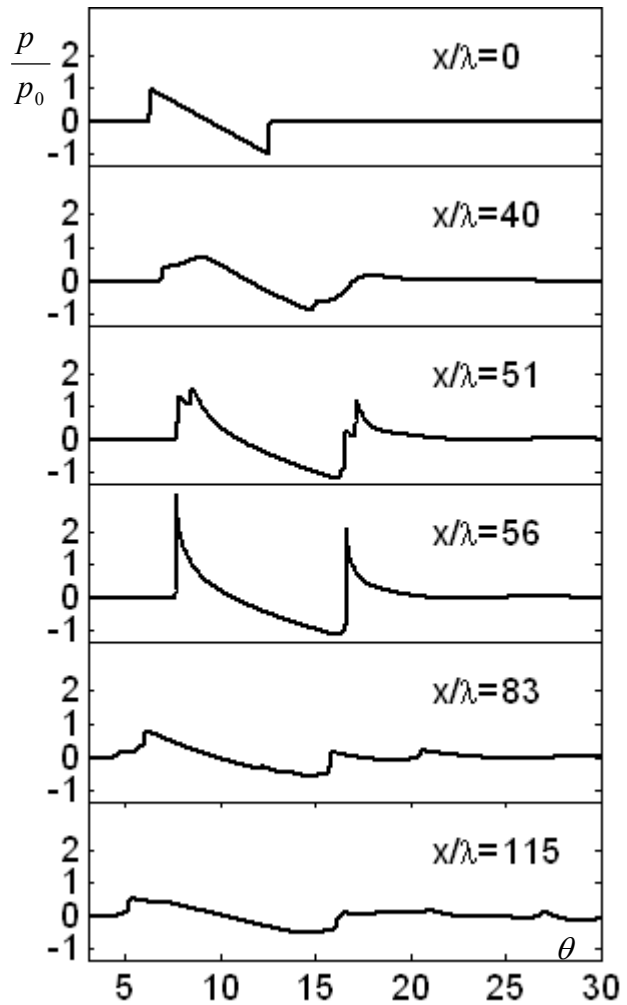
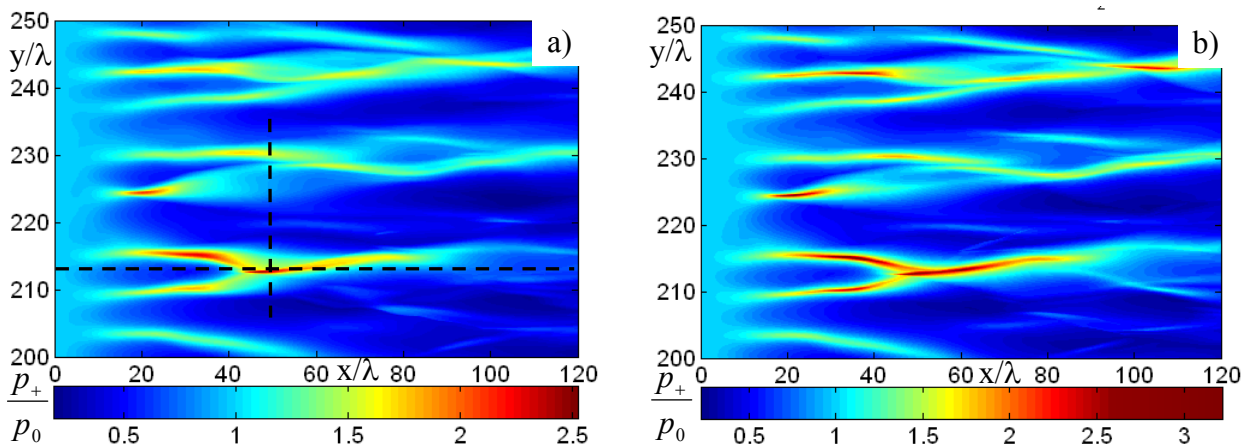


Fig. 5.13 Waveforms, measured at various locations along  $y/\lambda = 212$  axis while passing through the caustic

### 5.2.3 Nonlinear versus linear effects on random focusing in an inhomogeneous medium

Nonlinear effects play an important role in formation of the acoustic field in turbulent air. His role was investigated by comparison of peak positive pressure patterns for linear ( $N=0$ , Fig. 5.14a) and nonlinear ( $N=0.05$ , fig5.14b) propagation of an initially plane  $N$ -wave through inhomogeneous medium. At a first glance, acoustic pattern structures are not that much different. Nonlinearity effects appear mainly as an increase of peak positive pressure in focal regions due to more effective focusing of higher harmonics produced by nonlinear interaction. In the focal region the peak positive pressure in the case of nonlinear propagation is up to 30% higher than that in the case of linear propagation of the wave even at longer distances (up to 5 nonlinear distances  $x_s = 20\lambda$ ). However, the presence of turbulence dominates all images and in each case the focusing ability is severely curtailed for  $x/\lambda > 80$  due to dispersion of the pulse. More detailed comparison of nonlinear and linear regimes of  $N$ -wave propagation in turbulent media is presented in Fig. 5.15, where distributions of the peak positive pressure along horizontal (a) and vertical (b) dashed lines (Fig. 5.14) are presented. Two nonlinear regimes, corresponding to  $\sim 1000$  Pa ( $N = 0.05$ , red curve) and 500 Pa ( $N = 0.025$ , blue curve) of initial  $N$ -wave amplitude are considered as well as linear regime of propagation (black curve). It is seen, that along chosen lines, higher peak pressure corresponds to stronger nonlinearity. Maximum peak pressure level is achieved in nonlinear regime with  $N = 0.05$ , whereas minimum peak pressure is at about the same level in all three cases. It can be noted that the locations of maximum peak pressure are differently shifted in longitudinal direction depending on the value of nonlinearity parameter, whereas in transverse direction the peak position shift is negligible. Nonlinearity also results in a little smaller and clearer defined focal spots due to the smaller focal region associated with



**Fig. 5.14** Peak positive pressure spatial distributions corresponding to (a) linear ( $N = 0$ ) and (b) nonlinear ( $N = 0.05$ ) propagation of an initially plane acoustic  $N$ -wave through the randomly inhomogeneous moving medium (Fig. 5.11). Peak pressure distributions along dashed lines are shown in Fig. 5.15.

higher frequencies.

Shown in Fig. 5.15c are the maximum in transverse direction peak positive pressure distributions found in the range from  $y=20\lambda$  till  $y=380\lambda$  for linear and nonlinear regimes of shock wave propagation. It is seen that in the nonlinear regime maximum peak positive pressure usually dominates that in linear regime, i.e. moderate nonlinearity enhances focusing. Increasing nonlinearity from  $N = 0.0$  up to some “critical” point increases the focal amplitudes. Further increase of nonlinearity parameter will increase nonlinear dissipation at the shock front of the acoustic wave that will result in amplitude decrease. In our simulations this critical point lies somewhere between  $N = 0.025$  and  $N = 0.05$  as soon as peak pressure in the second case is in average smaller than in the first case. Thus, the dependence of focusing efficiency on nonlinearity parameter value is non monotonic. In general, nonlinearity will enhance focusing effects of acoustic wave in randomly inhomogeneous medium only if the following condition is valid. Characteristic nonlinear distance, which determines the value of nonlinear dissipative effects at the acoustic wave shock front, should be sufficiently small in comparison with the distance of the first

caustics (focal areas) formation. In other words, at the distance of first caustics formation the acoustic wave amplitude should not be drastically suppressed by nonlinear dissipation. However, under some circumstances, better focusing may be observed even in the case of very strong nonlinear effects ( $N = 0.05$ ): focal region at distance  $x/\lambda = 56$ . Presumably, this happens due to the additional phase shift given by nonlinear lengthening of the pulse. This phase shift equilibrates random arrivals that result in strong enhancement of the focusing.

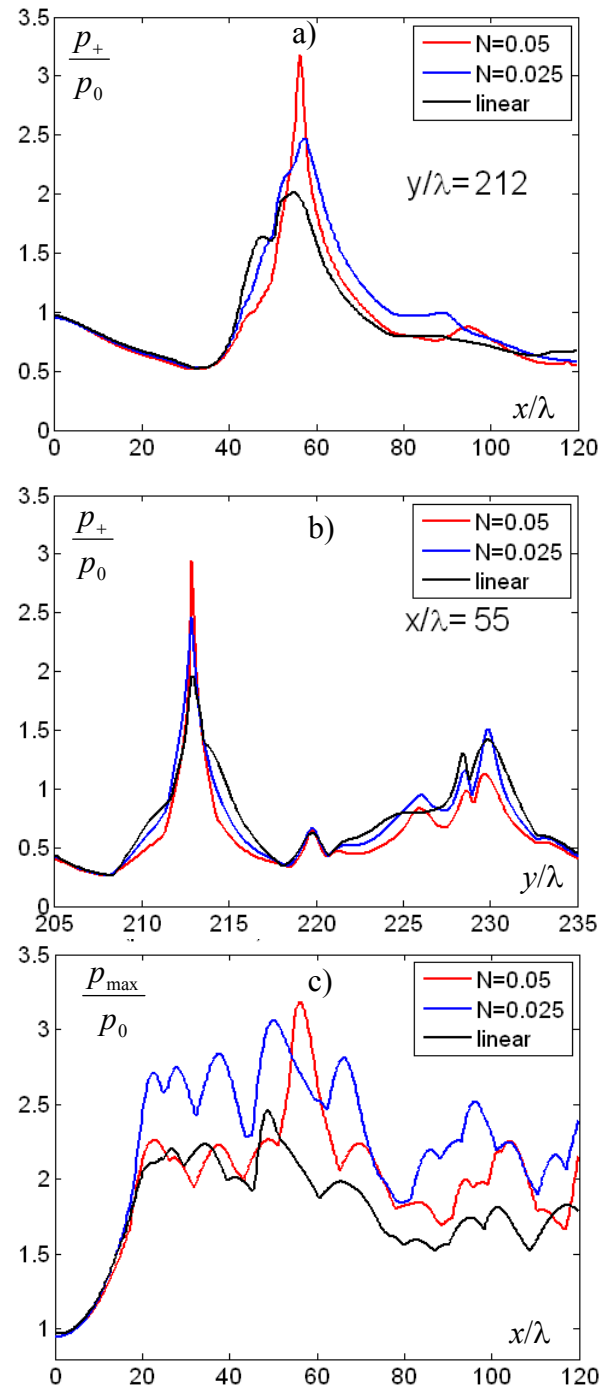


**Fig. 5.15.** Peak positive pressure distribution along horizontal a) and vertical b) dashed lines shown in Fig. 5.14a. c) – Maximum over  $y$  axis peak positive pressure distribution along  $x$  axis.

In geometrical acoustics approach for 2D randomly inhomogeneous medium this distance (where probability density of the first caustic occurrence have a maximum) is given by the inhomogeneous medium parameters [Blanc-Benon *et al.*, 132]: root mean square velocity of fluctuations  $u_{rms}$  and inhomogeneity characteristic scale  $L$ :

$$(x / \lambda)_{caust} = L \cdot \left( \frac{11.7c_0^2}{300\pi^{1/2}(u_{rms})^2} \right)^{1/3} \approx 26.3, \quad (5.1)$$

Thus the condition of focusing enhancement in the caustic will be given by  $x_s > x_{caust} = 26.3\lambda$ . In our simulations  $x_s = 20\lambda$  and  $x_s = 40\lambda$ , respectively, for  $N = 0.05$  and  $N = 0.025$ . One more reason for the dramatic effect of nonlinearity can be also that strong nonlinear dissipation faster suppresses the high-level narrow peaks.

Another phenomenon, related to the nonlinearity effect is that, for the same medium of propagation, the positions of peak pressure maxima in Fig. 5.15c are different for the considered nonlinear and linear regimes. Moreover, the shifts in locations of maxima are not constant and fluctuate from one peak to another. This can be explained by the fact, that wave energy redistribution depends on the relation between characteristic nonlinear distance and distance of caustic formation.

It has been already shown that under influence of the combined effects of diffraction, nonlinearity, thermoviscous dissipation, and effect of inhomogeneity the initial ideal  $N$ -wave distorts to obtain various shapes. To investigate the influence of nonlinear effect on waveform distortion, linear ( $N=0.0$ ) and nonlinear ( $N=0.05$ ) waveforms measured at different points of the acoustic pressure field are presented in Fig. 5.16. In the focal point (Fig. 5.16a) the classical transformation of  $N$ -wave to  $U$ -wave is shown. The  $U$ -wave amplitude is higher than that of the initial  $N$ -wave, and depends on the width of the  $N$ -wave shock front. Both linear and nonlinear waveforms are strongly distorted due to focusing effects. However, in the nonlinear case the peak positive pressure of the  $U$ -wave is more than 50% higher than the linear prediction value, the shock front is narrower, and the pulse duration is longer as compared to the linear one. In some points of shadow zones or in transition zones (Fig. 5.16c, d) even at not very large distances one can observe that nonlinear waveforms have lower amplitudes than linear ones, due to the effect of nonlinear dissipation. Another interesting phenomenon is that even in shadow zones of low level pressure (Fig. 5.16c) waveforms with sufficiently steep shock fronts can be observed due to scattering of higher harmonics at caustics. Both linear and nonlinear waveforms have very long tails as soon as inhomogeneities introduce multiple paths and different time delays. Such complex pulse structure is formed after superposition of waves. In some cases it was possible for the pressure amplitude in the tail to exceed the amplitude of the direct wave and

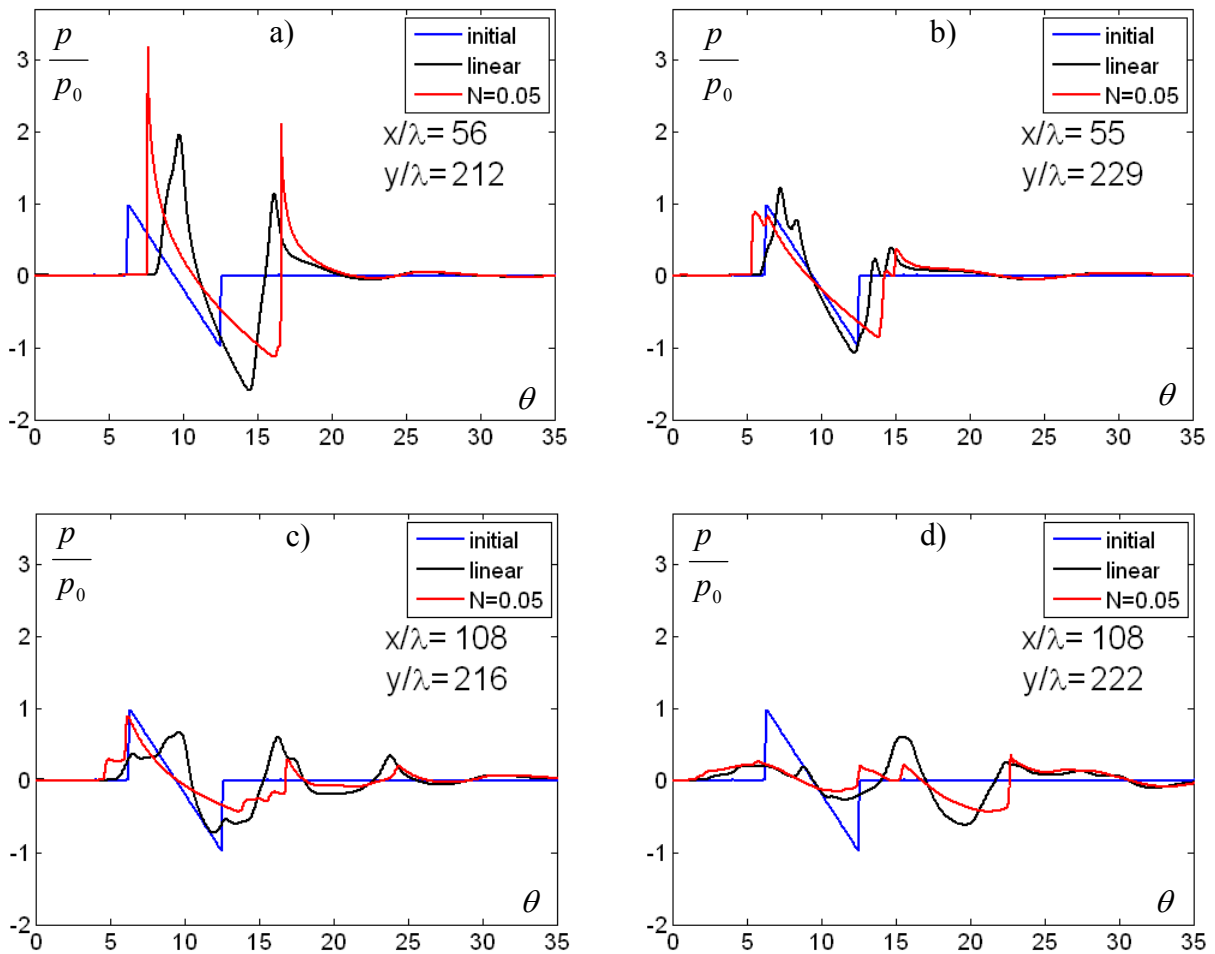


**Fig. 5.16** Typical linear ( $N=0.0$ ) and nonlinear ( $N=0.05$ ) waveforms measured in different points of the acoustic pressure pattern including (a) focal zones and (b)-(d) shadow areas. Initial *N*-wave is shown with the blue curve.

to form there sufficiently steep shock (Fig. 5.16d). Generally, the tail of the wave is sufficiently long outside focusing regions, whereas in focusing zones formed *U*-waves have a very short pressure tail. For all waveforms, nonlinear effects result in steepening of the pulse front and lengthening of the wave. However, in spite of nonlinear steepening, the predicted waveforms in the shadow zones always had longer shock fronts than the initial waveform, apparently due to the influence of inhomogeneities.

#### 5.2.4 Influence of randomly inhomogeneous medium on statistics, average and peak characteristics of the acoustic *N*-wave

Complex acoustic field structure in turbulent medium is characterized by peak and average values of *N*-wave parameters. Peak values have been partially considered in previous discussion. Therefore this section is devoted to the investigation of the acoustic field average characteristics behaviour, and behaviour of their statistical distributions. Computation of average values and statistical distributions is based on the ergodicity hypothesis and includes the analysis

of the numerical data for the acoustic field, calculated for  $N$ -wave propagation through one very wide realization of random inhomogeneous field. The width of the medium realization (about 100 inhomogeneity scales) is chosen in such way, that the result of acoustic wave parameters averaging over the full realization width is equal to the result of averaging over the half width of the same realization. In addition, calculations of acoustic field statistics are also performed for other realization of velocity inhomogeneities, determined by different set of random modes (different starting number in the random generator).

In Fig. 5.17 are shown the distributions of  $N$ -wave mean peak positive pressure (Fig. 5.17a), mean rise time (Fig. 5.17b), and mean arrival time (Fig. 5.17c) along the propagation distance. Linear ( $N=0.0$ , dashed lines) and nonlinear ( $N=0.05$ , solid lines) distributions in turbulent (blue) medium are compared with those obtained for motionless (black) linear and nonlinear media. With red lines are shown the standard deviations of the considered wave parameters in turbulent medium. Main effect of nonlinearity here is to decrease mean peak positive pressure, to decrease mean rise time and to shorten mean arrival time of the  $N$ -wave due to pulse widening.

If the turbulent field (blue curves) is accounted for in calculations, behaviour of average parameters changes. At sufficiently short distances before caustics, formation averages behave as if there were no turbulence at all. Then, if the peak positive pressure is considered, the rate of pressure decrease becomes stronger and achieves its maximum somewhere at a distance of the order of the first caustic formation distance ( $x/\lambda = 26$ ). It is obvious that around this

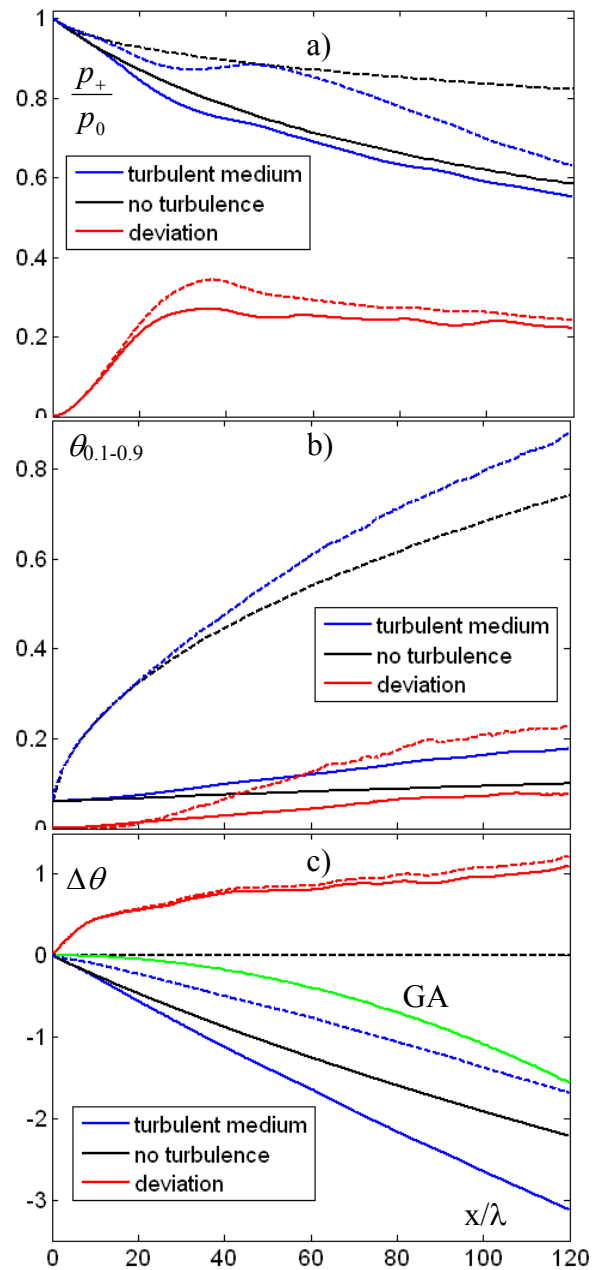


**Fig. 5.17.** Mean peak positive pressure (a), mean rise time (b), and mean arrival time shift (c) of an  $N$ -wave propagating in turbulent medium in linear ( $N=0.0$  dashed lines) and nonlinear ( $N=0.05$  solid lines) regimes. Red lines – standard deviations of considered wave parameters in turbulent medium. Green line – 2<sup>nd</sup> order approximation of geometrical acoustics for mean arrival time

distance, the local minimum of mean peak positive pressure should occur, as soon as the focusing zones are well localized and their total area is much smaller than area of defocusing zones, where the wave amplitude is sufficiently small. At the same distance, the maximum of standard deviation is also achieved, and its slow decrease replaces its fast growth. At longer distances, the rate of mean peak positive pressure decrease takes the form of the inverse square root of distance. Therefore, the curve goes further along the distribution of peak positive pressure in still medium, but at a bit lower level. Local minima corresponding to the caustics formation at longer distances are not observed due to their uniform distribution over the distance. To the contrary, two curves even approach each other. This rapprochement is due to the faster dissipation of signal in motionless medium, as soon as it contains higher frequencies (its front is much steeper).

The influence of the turbulent field on the *N*-wave rise time is different. At longer distances, after formation of first caustics, it tends, in contrast to nonlinear effects, to increase wave rise time due to multiple arrivals of the scattered waves. The rate of rise time increase in turbulent medium both in linear and nonlinear cases is faster than that in medium with no turbulence. The effect of turbulence is quite strong here: at  $x/\lambda = 120$  from the source the mean rise time  $\theta_{0.1-0.9} = 0.06$  is about 3 times larger than its initial value  $\theta_{0.1-0.9} = 0.177$ . In motionless medium the augmentation is only 1.65 times from:  $\theta_{0.1-0.9} = 0.06$  till  $\theta_{0.1-0.9} = 0.099$ . Thus the rise time is not only defined by the shock amplitude, like it would be in still medium, but also by effects of turbulence, which contrarily to nonlinear effects tend to elongate the shock front. Concerning the standard deviation of the rise time, it increases faster in the linear regime of the sound wave propagation than in nonlinear one. Thus, nonlinearity effects decrease variations of the rise time, caused by turbulence.

Average arrival time (Fig. 5.17c) is also strongly affected by the turbulent inhomogeneities. Both in linear and nonlinear cases of *N*-wave propagation, effects of turbulence cause its faster arrival. Obviously, this is due to the least action principle, which in application to the geometrical acoustics gives Fermat principle: the wave path minimizes the travel time of the wave. But one may note that in the case of nonlinear propagation (solid lines) this effect is much smaller than that in the case of linear propagation (dashed lines). Maximal average arrival time shortening due to Fermat principle in linear case equals  $\Delta\theta = -1.7$  (difference between arrival time values in motionless and turbulent media), while in nonlinear case  $\Delta\theta = -0.9$ . Thus, nonlinear effects in considered cases decrease the effect of turbulence on arrival time by a factor of 2. It is also interesting to note, that in geometrical acoustics approximation it is possible to evaluate mean arrival time analytically at the second order [Iooss *et al.*, 133], which in current

experiment conditions (2D Cartesian geometry, random field with Gaussian energy spectrum)

and in dimensionless coordinates gives:  $\Delta\theta = -\sqrt{\pi^3} \frac{u_{rms}^2}{c_0^2} \frac{\sigma^2}{L}$  postulating a parabolic dependence

of arrival time shortening on propagation distance. Corresponding graph is shown in Fig. 5.17c with green line. In contrast to geometrical acoustics approximation results, parabolic approximation gives almost linear law of arrival time shortening, that tells about significant role of diffraction. One of the possible explanations to this difference is also that mean arrival time is calculated in geometrical acoustics only up to the second order [Iooss *et al.*, 133].

In Fig. 5.18a are shown the peak positive pressure probability density distributions. All figures are scaled between minimum and maximum observed values of the peak pressure. It can be seen, that initially narrow at short distance probability distribution becomes wider at longer distances. Distribution peak moves in the direction of peak positive pressure decrease accordingly with the behaviour of its mean, shown with vertical red line. Nevertheless, regardless common tendency of peak pressure reduction, there exist a small probability of high level values occurrence, which are more than 3 times higher than initial one.

In Fig. 5.18(b-d) are shown the characteristic parameters of the peak positive pressure distributions. They are: mean and standard deviation values (b), skewness (c) and excess (d) factors. The distance of the first caustics formation, obtained in the geometrical acoustic approximation (5.1), is shown with the vertical line. The skewness factor is a measure of the asymmetry of the probability distributions in comparison with the Gaussian distribution. If it is positive, the distribution right hand side contains more values than the left hand side. Thus the skewness factor should be sufficiently high at distances of most intense focusing of the wave, where the probability density distribution is most asymmetric. The excess factor gives a relative measure of “peakedness” of a given probability density distribution. The excess factor of the normal distribution is equal to 0. Higher excess value means that more of the variance is due to the infrequent extreme deviations, as opposed to the frequent modestly-sized deviations. So the excess factor should be very high, where the most intense focusing is observed, as soon as this gives infrequent extreme deviations.

Intense focusing should occur somewhere near the distance of the first caustic formation. In fact, as it is seen in the Fig. 5.18(b-d), the standard deviation, skewness and excess factors of the peak positive pressure increase rapidly from zero to some characteristic value at the distance of first caustics formation, predicted by means of geometrical acoustics approximation. It means that the probability distribution becomes wider and obtains a long asymmetric pressure tail in the higher-pressure level part. So a good agreement is achieved between the distance of the first

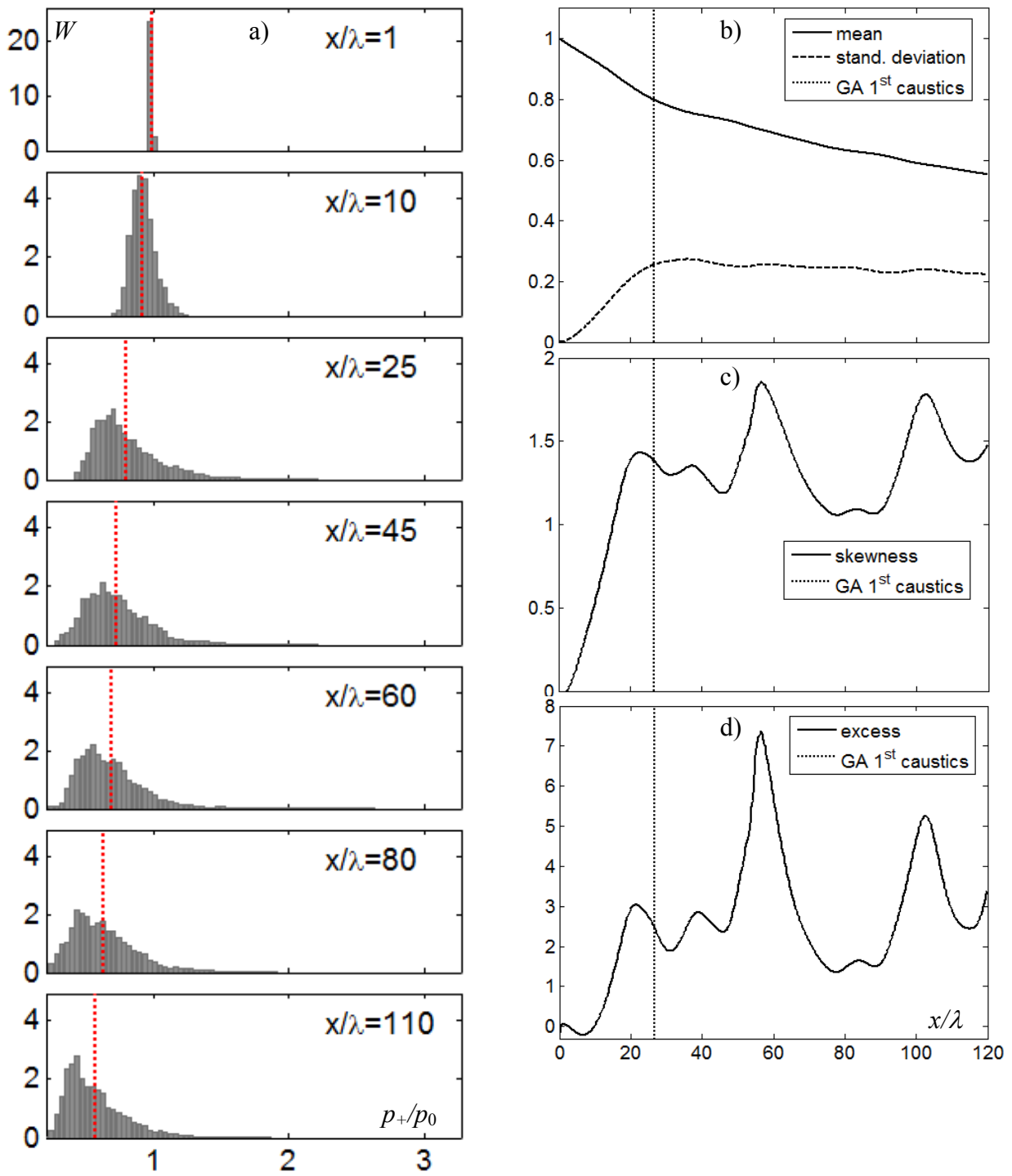


**Fig. 5.18.** (a) Peak positive pressure probability density distributions at different distances from the source. Vertical red line is the mean value. Class width equals to 0.04. (b), (c), (d) – mean and standard deviation, skewness and excess parameters distributions over the propagation distance. Vertical dotted line is the prediction of the 1<sup>st</sup> caustics formation distance in the geometrical acoustics approximation.

caustic formation and characteristic focusing distance of the acoustic wave. The only parameter which seems to be not significantly affected by the wave focusing is the mean peak positive pressure.

Further with distance, the mean peak positive pressure does not vary a lot and its standard deviation seems to achieve its saturation level. Contrary to that, the skewness and excess factors are subjected to the strong change while wave propagates through the randomly inhomogeneous medium. It appeared that the strongest fluctuations in these parameters correspond to the most intense focusing of the acoustic wave. For example, a peak of skewness and kurtosis factors at the distance of  $x/\lambda = 60$  corresponds to the focalization coefficient, equal to  $p_+/p_0 = 3.2$  (note, that this focalization was not captured by the geometrical acoustics, Fig. 5.12c). The second peaks are situated at the distance  $x/\lambda = 105$  from the source. This distance can be associated with the second wave of focusing ( $2^{\text{nd}}$  caustics formation distance - red points in Fig. 5.12c).

In Fig. 5.19 are presented the probability density distributions of the acoustic wave shock front rise time and arrival time at different distances from the source. It is seen, that in agreement with the peak positive pressure decrease the rise time probability density distribution maximum moves towards higher values of the parameter. Nevertheless, there still exists a notable probability of very short rise time observation which is smaller than initial one: minimum observed rise time, measured in the focal zone, is almost 3 times smaller than the initial one and is equal to  $(\theta_{0.1-0.9})_{\min} = 0.022$ . As for the arrival time probability density distribution, it becomes very wide with distance showing earlier arrivals up to  $-5.25 = -1.67\pi$ , what is more than 3/4 of a period.

### 5.2.5 *Effect of the transverse component of turbulent velocity: vector versus scalar contributions of inhomogeneities*

In the parabolic evolution Eq. (4.6) a new term, which accounts for the transverse component of a random velocity field has been introduced. To estimate the influence of lateral fluctuations and winds on formation of acoustic field structure, two types of computation have been done: with account for both longitudinal and transverse fluctuation components and with account only for longitudinal component of the random velocity field. Results of numerical simulations are shown in Fig. 5.20, where maximum of peak positive pressure distributions over  $x$  axis (Fig. 5.20a) or over  $y$  axis (Fig. 5.20b) are presented. One can see, that transverse component of the random velocity field under considered conditions (Gaussian energy distribution with scale  $L = 4\lambda$  and  $u_{rms} = 3$  m/s) results in insignificant changes in the peak

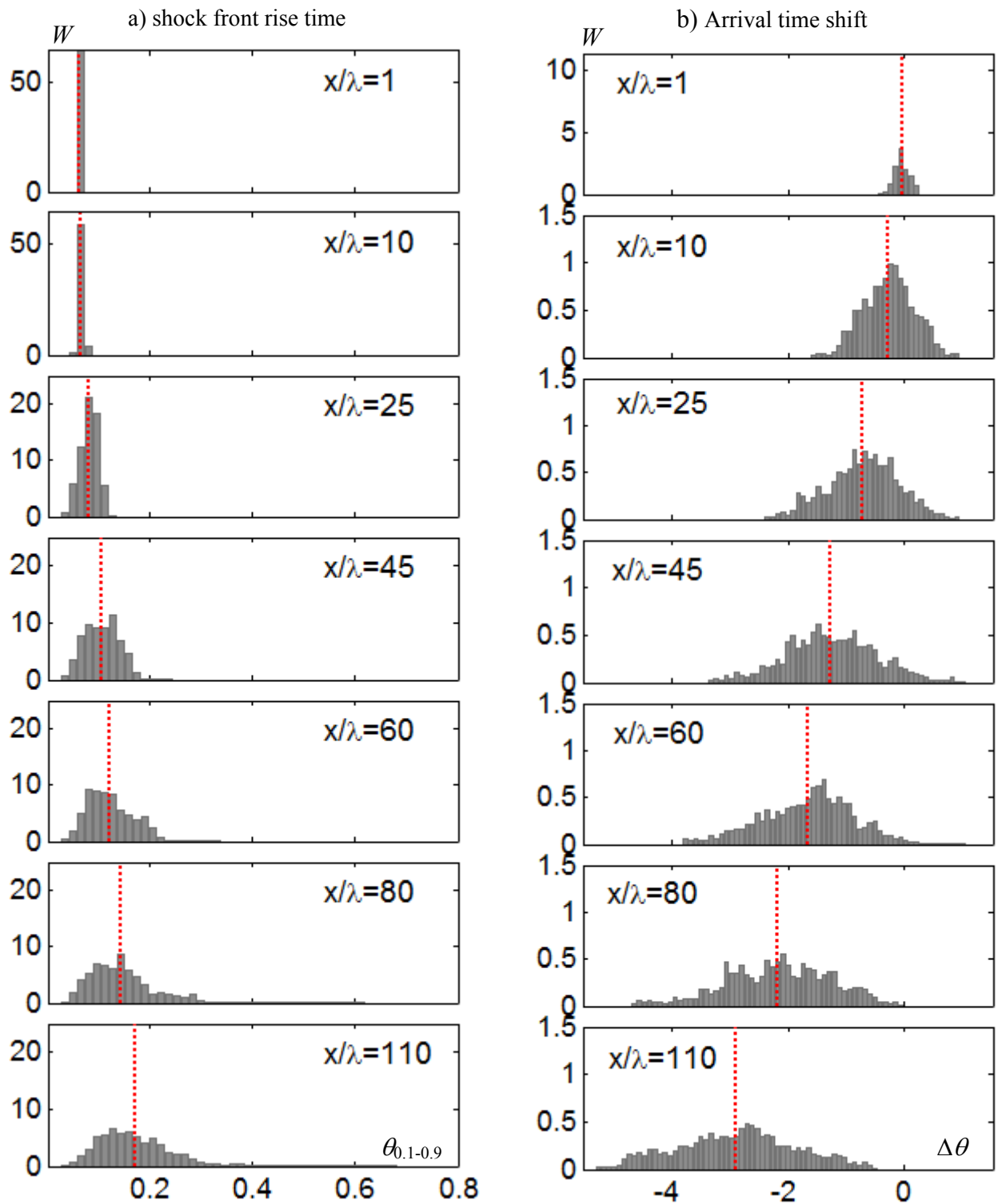


**Fig. 5.19.** Shock front rise time (a) and arrival time (b) probability density distributions at different distances from the source. Class width equals to (a) – 0.16, (b) – 0.09. Vertical red line is the mean value of the considered parameter.

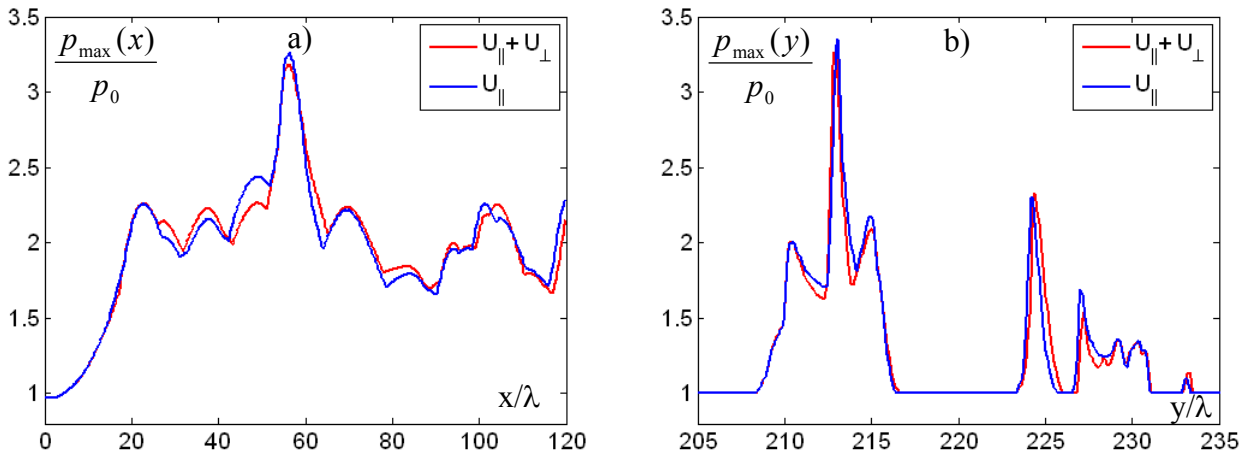


**Fig. 5.20** Peak positive pressure distributions calculated with or without account for the transverse component of the random velocity field. a) maximal over  $y$  axis distribution plotted along  $x$  axis, b) maximal over  $x$  axis distribution plotted along  $y$  axis

positive pressure. Nevertheless, this term should be kept in the equation. For more intense and larger scale inhomogeneities, especially in the presence of lateral winds, the influence of this term is predicted to be much stronger.

#### 5.2.6 Effect of spatial correlation lengths and turbulent kinetic energy distribution law on acoustic field characteristics

In this section propagation of the acoustic  $N$ -wave through the random inhomogeneous moving media with a modified von Karman energy spectrum (Fig. 1.2e-g), which describes multi scale turbulent medium fluctuations, is considered. Outer scale and intensity of the turbulent field are chosen to be the same as for the considered previously inhomogeneity with Gaussian energy spectrum:  $L_0 = 4\lambda$  and  $u_{rms} = 3$  m/s. Inner scale is equal to  $l_0 = 2.4\lambda$  and is chosen according to the limits of parabolic approximation. Dimensionless nonlinear coefficient  $N$  and absorption coefficient  $A$  are taken to be  $A = 0.00034$  and  $N = 0.05$  if it is not stated otherwise. The resulting peak positive pressure pattern is presented in Fig. 5.21 showing multiple focusing and defocusing of the acoustic wave. The random focusing occurs here at shorter distances, as compared to the Gaussian type medium inhomogeneity, and the overall structure of the acoustic field obtains additional tiny structure due to presence of small scales in the turbulent field [Wert *et al.*, 95].

Mean peak positive pressure and arrival time distribution are in qualitative and even quantitative agreement with that obtained for the acoustic  $N$ -wave propagation through the inhomogeneity with Gaussian energy spectrum and will not be presented in this document. It is only worth to introduce the mean rise time distributions (Fig. 5.22). From the comparison of mean distributions, calculated for the acoustic wave propagation through the media with

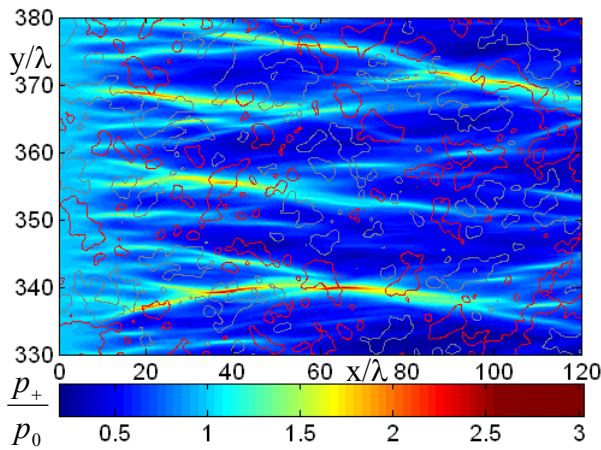


**Fig. 5.21** Peak positive acoustic pressure distribution formed in inhomogeneous field with von Karman energy spectrum (Fig. 1.2e-g). Levels of turbulence intensity are marked with red – positive and grey – negative contours ( $u_x / c_0 = \pm 0.009$ ).

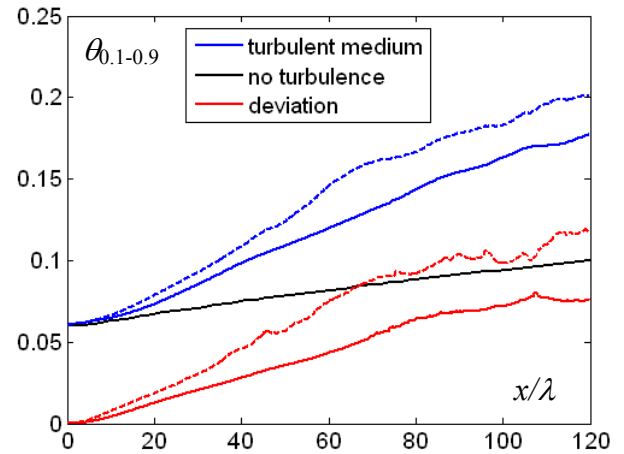


**Fig. 5.22** Mean acoustic wave rise time distributions in random medium with Gaussian (solid lines) or Karman (dashed lines) energy spectra. Red curves – corresponding standard deviations. Black line – rise time in motionless medium.

different energy spectra, one can see that in the case of multi scale inhomogeneity the shock front rise time is smeared out more effectively. This means that the shock front width is mainly determined by the smaller scale inhomogeneities. The influence of transverse component of the random velocity field becomes very significant in that case. In Fig. 5.23 are shown maximal over  $x$  axis (a) and maximal over  $y$  axis (b) peak positive pressure distributions calculated with account for both components of random velocity field (red curves) and with account only for longitudinal component (blue curves). It is seen that contrary to random inhomogeneity with Gaussian energy spectrum, the transverse component of the random field with a modified von Karman energy spectrum has a significant influence on peak characteristics of the acoustic field. Due to the presence of lateral medium velocity fluctuations the focal regions are shifted both in longitudinal and transverse directions. Moreover additional focusing zones may occur. In

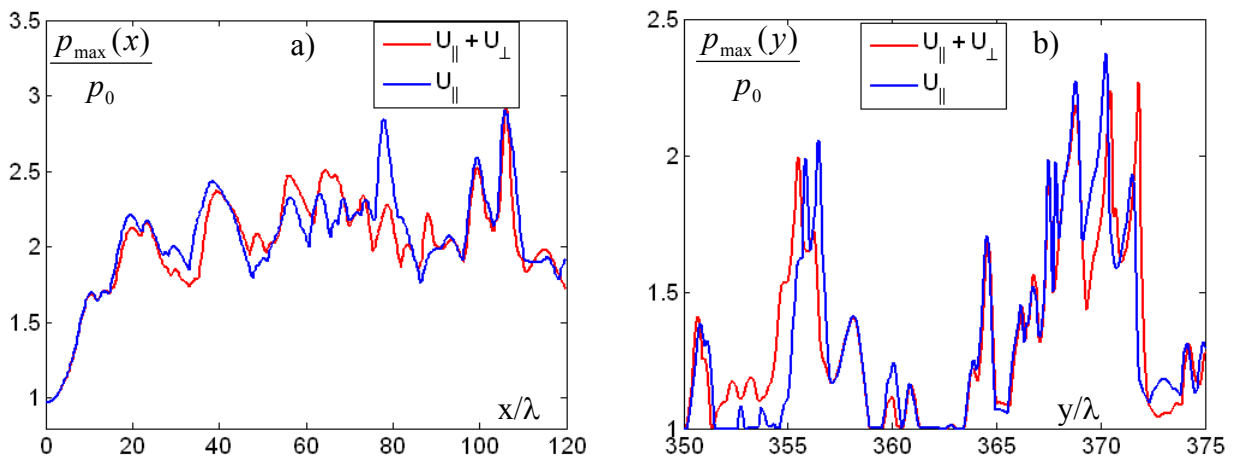


**Fig. 5.23.** Peak positive pressure distributions calculated with or without account for the transverse component of random velocity field. (a) maximal over  $y$  axis distribution plotted along  $x$  axis, (b) maximal over  $x$  axis distribution plotted along  $y$  axis

addition, some focal regions may disappear (Fig. 5.23a,  $x/\lambda = 80$ ), whereas in others the focusing may become more intense (Fig. 5.23b,  $y/\lambda = 372$ ). Thus, to correctly predict peak and average characteristics of the acoustic field in randomly inhomogeneous moving medium with a modified von Karman energy spectrum, transverse component of the velocity field need to be included in the model of acoustic wave propagation.

### § 5.3 Comparison of numerical model results with experimental data

For the numerical modelling of an  $N$ -wave propagation in randomly inhomogeneous moving air with account for the relaxation effects, the parameters of the medium are chosen according to the laboratory scale experiment conditions:  $\varepsilon = 1.21$ ,  $b = 4.86 \cdot 10^{-5} \text{ Pa}\cdot\text{s}$ ,  $\rho_0 = 1.29 \text{ kg/m}^3$ ,  $c_0 = 335 \text{ m/s}$ . Relaxation parameters were calculated using empirical formulas for 85% humidity, 278 K temperature and atmospheric pressure equal to 1 atm.:  $c_1 = 0.1174 \text{ m/s}$ ,  $\tau_1 = 6.9 \mu\text{s}$  ( $O_2$ ),  $c_2 = 0.0214 \text{ m/s}$ ,  $\tau_2 = 641 \mu\text{s}$  ( $N_2$ ) [Pierce, 62]. As the initial condition, the plane  $N$ -wave with the characteristic for the experiment pressure amplitude  $p_0 = 950 \text{ Pa}$  and duration  $(2T_0) = 25 \mu\text{s}$  at distance  $r_0 = 15 \text{ cm}$  from the spark source were chosen (these values are determined according to the method, presented in §3.2). The  $N$ -wave shock front rise time is determined according to nonlinear and dissipation effects. Dimensionless parameters in Eq. (4.6) are, thus, equal to:  $N = 0.05$ ,  $D_1 = 0.0022$ ,  $D_2 = 0.0004$ ,  $\theta_1 = 1.73$ ,  $\theta_2 = 161.1$ . The absorption coefficient is chosen in order to maintain the stability of the numerical algorithm during the optimization procedure (§4.3, Appendix B) and is equal to  $A = 0.00034$ , that is twice the absorption parameter in experimental environment. Numerically generated randomly inhomogeneous medium velocity field has a modified von Karman energy spectrum shape with an inner scale equal to  $l_0 = 2.0 \text{ cm} = 2.4\lambda$  and an outer scale equal to  $L_0 = 19.3 \text{ cm} = 23\lambda$  (§2.3). Outer scale is chosen in accordance with the experimentally generated turbulence scale, whereas chosen inner scale is much longer due to the limitations of the used parabolic approximation. So, in Fig. 5.24 are presented the turbulent fluctuations energy distribution and acoustic wave energy distribution over wave numbers. Blue curve corresponds to the used in simulations 2D modified von Karman spectrum ( $L_0 = 19.3 \text{ cm}$ ,  $l_0 = 2 \text{ cm}$ ). Note, that the energy containing part of the modified von Karman spectrum lies at lower wave numbers ( $K \in [2, 40] \text{ m}^{-1}$ ) than the main energy part of the acoustic wave spectrum ( $[40, 170] \text{ m}^{-1}$ ). Thus, the parabolic approximation should be valid in the presented conditions of propagation. Numerical simulations are provided for wide realizations ( $240\lambda \times 1000\lambda$ ) of random field with different intensity of turbulent

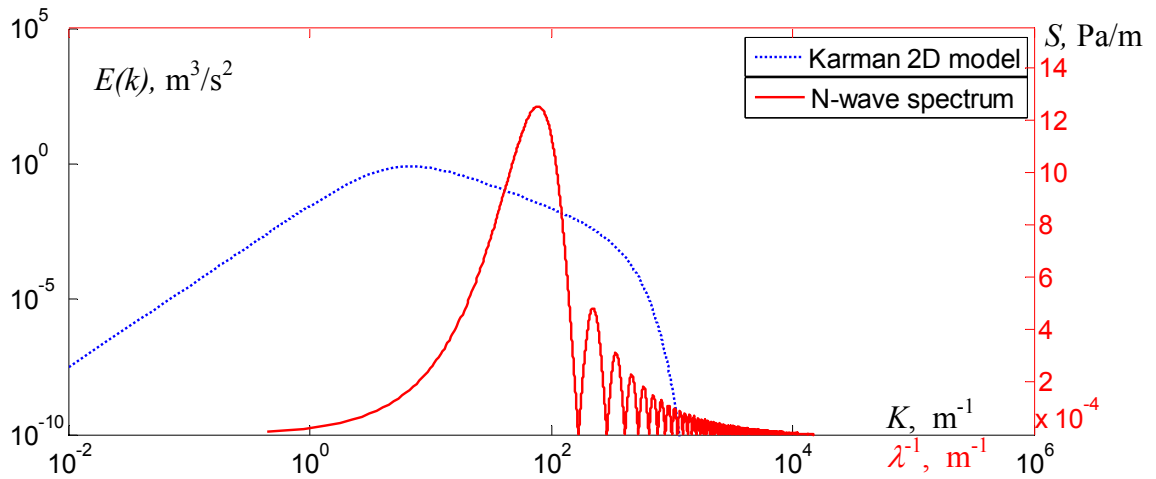


**Fig. 5.24** Comparison of characteristic scales in 2D modified von Karman energy spectrum of turbulent medium ( $L_0 = 19.3$  cm,  $l_0 = 2$  cm, blue) with the spectrum of the modelled initial  $N$ -wave ( $\lambda = 0.85$  cm, red curve, red y-axis)

fluctuations in agreement with our laboratory scale experiment. Root mean square velocity of fluctuations varied from  $u_{rms} = 0$  m/s up to  $u_{rms} = 4.0$  m/s, that corresponds to  $U_{jet} = 10 u_{rms} = 40$  m/s at the exit of the jet in the experiment (Fig. 2.9). Note also, that in our computations it is assumed that the turbulent field exists at all distance of the acoustic wave propagation path (from 15 cm to 2.19 m) and is isotropic everywhere, whereas in the laboratory scale experiment the turbulent field is isotropic only at distances 40 cm – 170 cm from the source and is anisotropic and unstationary in the outside region.

In Fig. 5.25 are shown the experimental (Fig. 5.25a) and calculated (Fig. 5.25b) probability densities distributions of relative peak positive pressure  $\langle p_+ \rangle / \langle p_+^0 \rangle$  in the field of acoustic  $N$ -wave at the distance of 2.19 m from the source, calculated for different intensities of turbulent fluctuations (different flow velocities at the exit of the jet  $U_{jet}$ ) [Averiyanov *et al.*, 134]. Here  $\langle p_+^0 \rangle$  is the mean value of peak positive pressure of the wave, propagating in motionless medium. Red dashed lines correspond to the mean values of the peak positive pressure in turbulent medium. Standard deviations of the acoustic pressure fluctuations are designated with *std* and their numerical values are printed in the figure. Simulations are done based on time domain numerical algorithm, presented in §4.3, and using amplitude frequency response of the measuring system obtained for current laboratory experiment using method, described in Chapter 3. Even if the laboratory scale experiment is a fully 3D experiment, whereas the numerical modelling is done only in 2D representation, the results of peak positive pressure measurements are in a good qualitative agreement. In both case the peak positive pressure probability density distributions have a bell like shape with a long pressure tail in the direction of  $\langle p_+ \rangle / \langle p_+^0 \rangle$  increase. Distributions maxima move in the direction of pressure

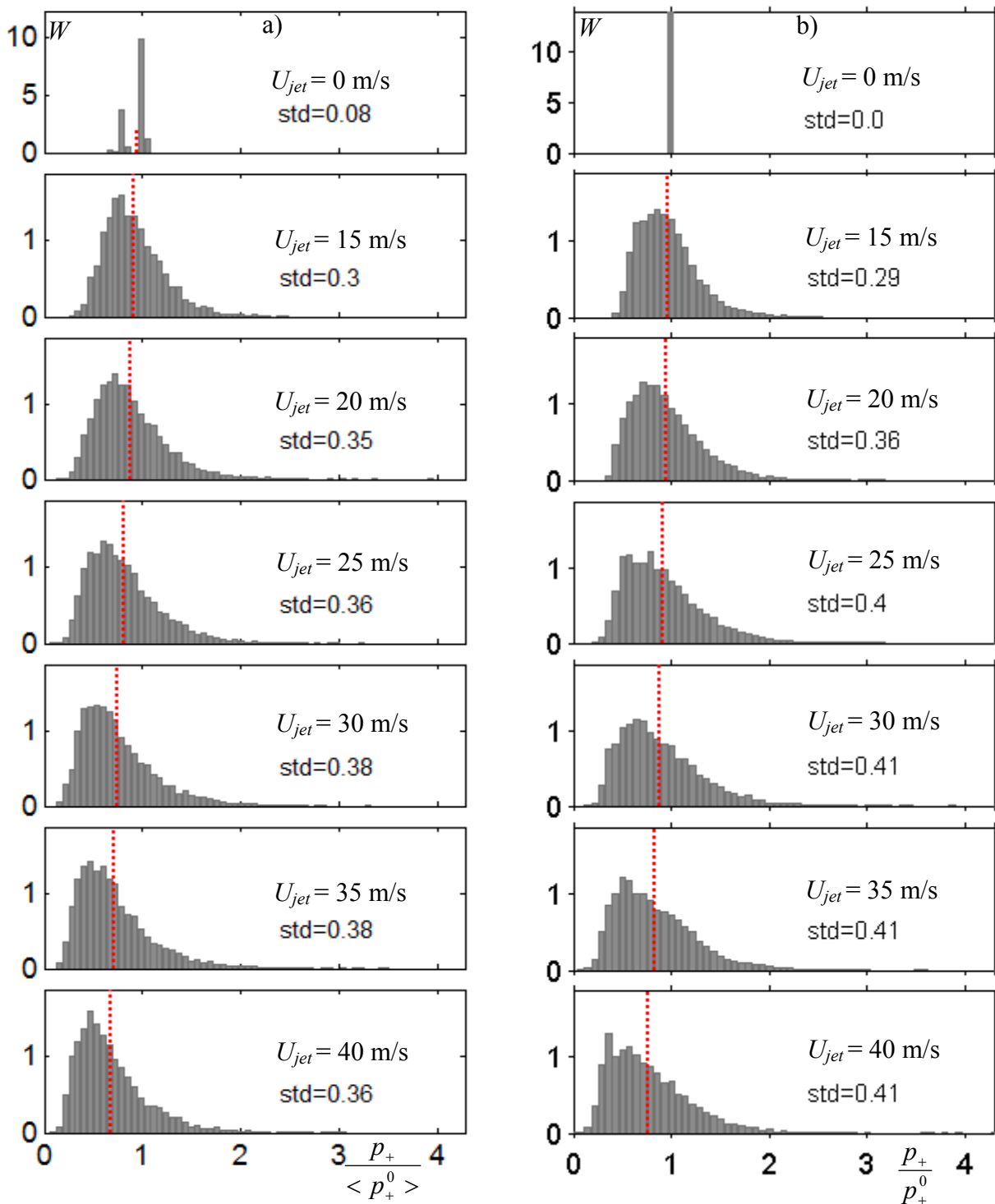


**Fig. 5.25.** Experimental (a) and modelled (b) relative peak positive pressure  $p_+ / \langle p_+^0 \rangle$  probability distributions obtained at distance of 2.19 m from the source. Flow velocity at the exit of the jet  $U_{jet}$  varies from 0 m/s to 40 m/s.  $\langle p_+^0 \rangle$  is the mean value of the peak positive pressure, measured at the same distance in motionless medium. Red dashed lines correspond to the mean value of the pressure amplitude in turbulent medium. With designation *std* the standard deviation is shown. Class width equals to 0.07.

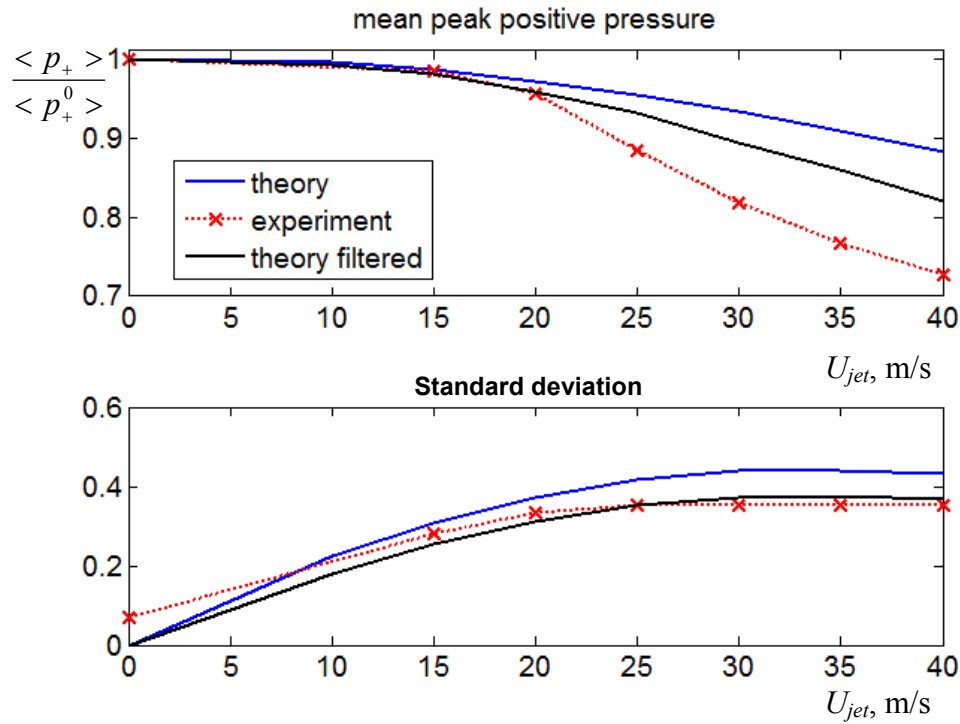


**Fig. 5.26** Dependence of the peak positive pressure of the acoustic wave and its standard deviation, measured at the distance 2.19 m from the source, on the flow velocity at the exit of the jet  $U_{jet}$  (turbulence intensity). Red curve – experimentally measured values, blue curve – results of simulation, black curve – result of simulations, to which the measuring system frequency response was applied.

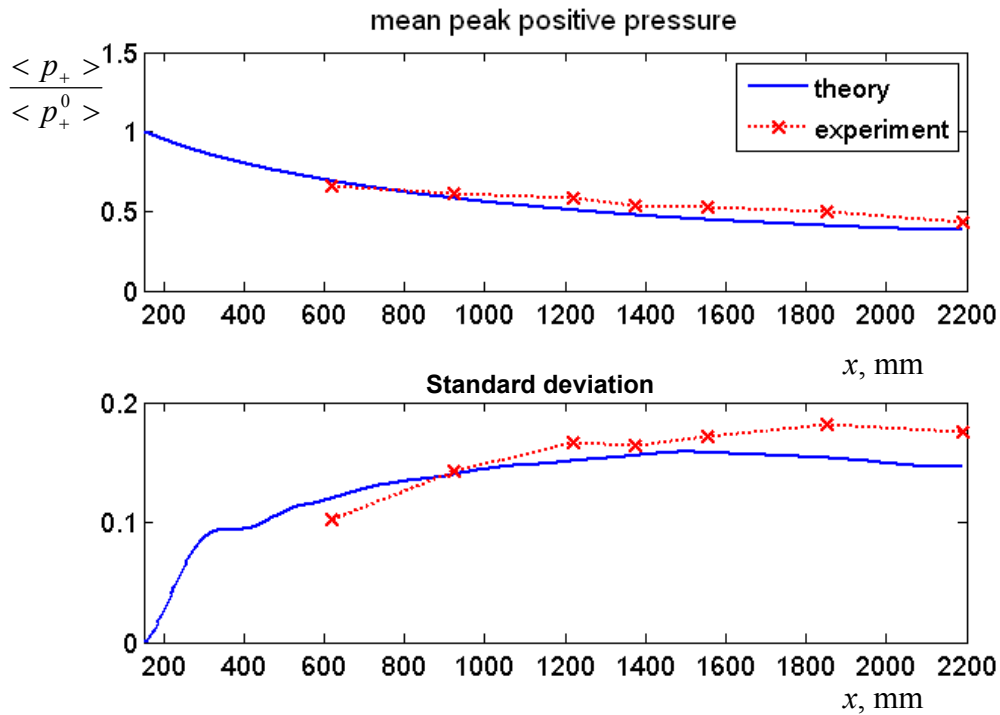


**Fig. 5.27** Dependence of the peak positive pressure of the acoustic wave and its standard deviation on the distance from the source ( $U_{jet} = 20$  m/s). Red curve – experimentally measured values, which are multiplied by the  $r/r_0$  value to exclude the spherical divergence effects, where  $r_0 = 150$  mm. Blue curve – results of the simulation.

decrease with augmenting the turbulent fluctuations intensity. At the same time, one can observe the formation of peak positive pressure values, which are up to 4 times higher than in the motionless medium. These values correspond to measurements in the vicinity of focal spots.

It should be noted also, that in both experiments the same regularity of different shape waveforms formation is observed according to their amplitude position in the probability density distribution. So, if  $p_{+}/\langle p_{+}^0 \rangle \in [0, 1]$ , then the formation of rounded waveforms and waveforms with several shock fronts and very long pressure tails are mainly observed. For  $p_{+}/\langle p_{+}^0 \rangle \in [1, 2]$  the classical  $N$ -waves and waves with two shock fronts, which also have long pressure tails are observed. If  $p_{+}/\langle p_{+}^0 \rangle \in [2, 3]$ , then waves with several peaks of high amplitude are formed, that tells about proximity of the focal spot. Finally, in the focal spot itself ( $p_{+}/\langle p_{+}^0 \rangle \in [3, 4]$ ) the formation of classical  $U$ -waves of high amplitude and thin shock front is observed

As for the mean characteristics of the acoustic wave, the influence of randomly inhomogeneous moving medium is to decrease mean peak positive pressure with increase of turbulence intensity (Fig. 5.26). So, the relative pressure level  $\langle p_{+} \rangle / \langle p_{+}^0 \rangle$  in the case of maximum flow velocity decreases on 27 % in laboratory scale experiment, and on 12 % in numerical modelling and 18% when the measuring system frequency response (§3.4) is applied to the results of simulations. Moreover, the standard deviation of measured parameter in both cases increases monotonically up to flow velocities  $U_{jet} = 30$  m/s, where its saturation is observed, i.e. it does not notably change further with the flow velocity increase. In the laboratory scaled experiment, the maximal standard deviation of the peak positive pressure relative fluctuations is equal to 0.38, and in numerical experiment – 0.41.

Comparison of obtained experimental and numerical data clarifies the physical meaning of the inflection on mean peak positive pressure curve (Fig. 5.26) at flow velocity  $U_{jet} = 20$  m/s. It is related to the focusing of the acoustic wave. As soon as an effective area of focusing zones is much smaller than the total area of decreased pressure regions, mean peak positive pressure in turbulent medium decreases. The strongest decrease is observed at a distance of first caustics formation, described by large-scale inhomogeneities, as soon as such inhomogeneities result in strongest focusing. For example, in Fig. 2.23a, mean peak pressure decrease at a distance 1200 mm ( $U_{jet} = 20$  m/s) from the source correspond to the distance of first caustic formation, associated with large-scale inhomogeneities  $L_0 = 19.3$  cm. At this distance, which equals to 1532 mm, one can see that difference between peak pressure in still medium and turbulent medium achieves its maximum. Further with distance, difference between mean peak pressures

becomes smaller due to faster dissipation of waves in motionless medium, as soon as they contain higher frequencies (have steeper shock fronts). The stronger turbulence intensity is, the stronger is the focusing. Therefore, if the turbulent field is enough intense, the difference between two curves will be sufficiently large even at longer distance: dissipation mechanism will not have enough time to suppress difference in amplitude. Thus, in our example (Fig. 5.26) turbulence created by the flow  $U_{jet} = 15$  m/s is not enough intense and difference in amplitudes is fully suppressed. And starting only from  $U_{jet} = 20$  m/s dissipative mechanisms only decrease the difference but do not have time to fully suppress it.

In addition to the dependence of the peak positive pressure on turbulence intensity, its dependence on propagation distance is presented in Fig. 5.27, where a good agreement between experimental and theoretical data is obtained. Thus, the quantitative agreement between results of numerical modelling and laboratory scale measurements is even achieved and enhanced by using the measurement system frequency response.

A small difference in peak pressure in laboratory and numerical experiments can be partially explained by the fact, that measurement of high amplitude acoustic waves is sufficiently difficult to realize from the technical point of view as soon as they are located in very thin focal areas. To measure a large number of waveforms (for a good statistics) a huge amount of microphones or long duration experiments are needed, and that is not always possible. This can explain why mean amplitude value of acoustic wave in laboratory scale experiment decrease faster than in numerical experiment. Comparison of the shock front rise time and arrival time statistics in both experiments is not yet possible due to strong influence of nonlinear effects, which are differently pronounced in 2D and 3D geometries.

In Fig. 5.28 are shown the probability density distributions of arrival time, obtained in laboratory scale experiments (a) and in numerical simulations using parabolic Eq. (4.6) at the distance 2.19 m from the source and with varying velocity of the air flow at the exit of the jet  $U_{jet}$  (turbulence intensity). With red vertical lines are shown the mean values of the arrival time and its standard deviation is noted on the figures using designation *std*. In both cases, the arrival time is normalised by the initial duration of the wave ( $2T_0$  in experiment and  $2\theta_0 = 2\pi$  in modelling). In both cases the probability density distribution becomes wider with increasing the intensity of the turbulent fluctuations and moves towards faster arrivals, which is consistent with the Fermat principle of arrival time minimization. A more detailed comparison of mean arrival time and its standard deviation in theory and experiment is presented in Fig. 5.29. In addition to the measured data and results of numerical simulations based on the parabolic Eq. (4.6), the geometrical acoustics prediction for the arrival time in turbulent medium is presented in the figure with green

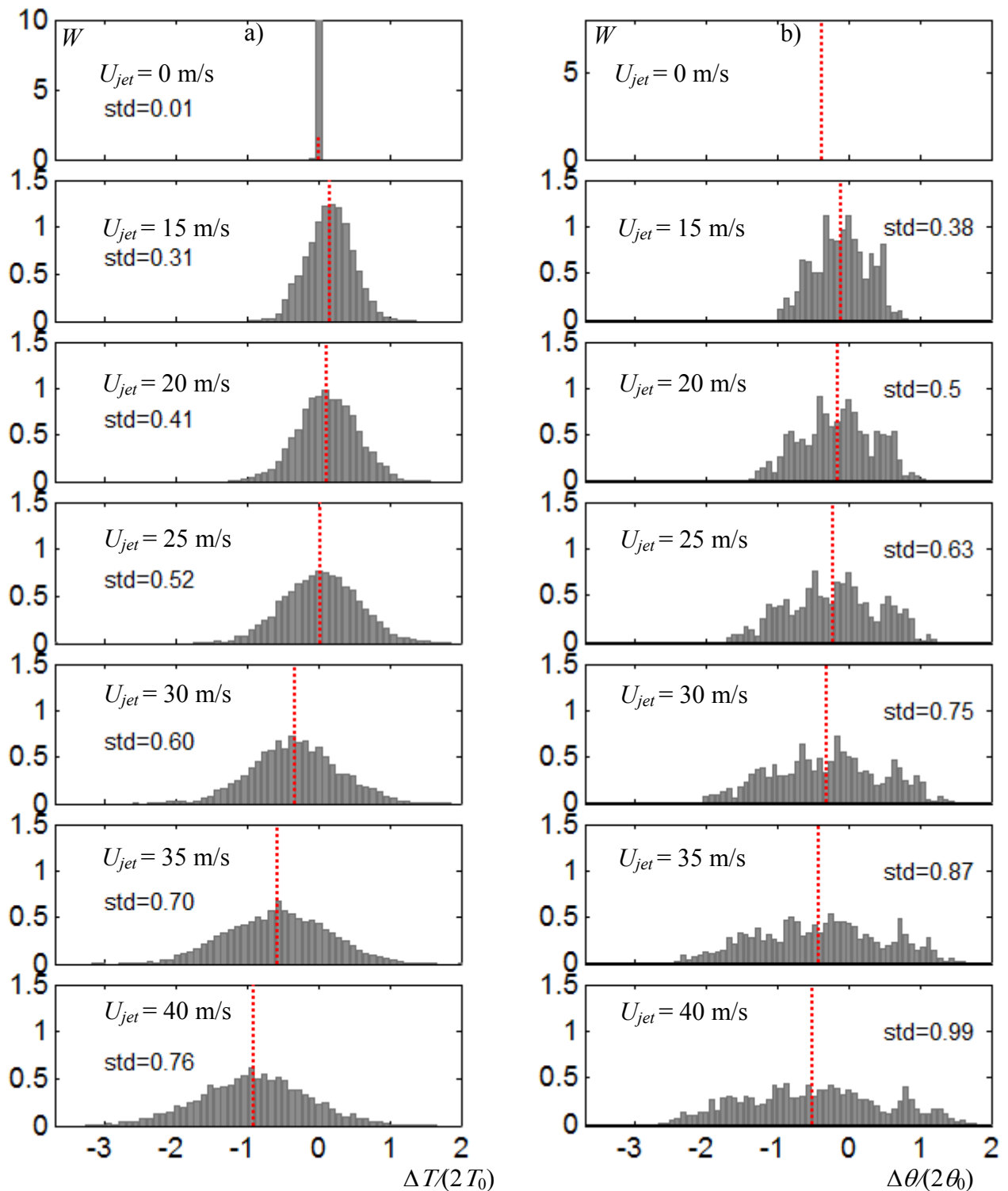


**Fig. 5.28.** Experimental (a) and modelled (b) arrival time probability density distributions measured at distance of 2.19 m from the source varying the flow velocity at the exit of the jet  $U_{jet}$  (turbulence intensity). Red dashed lines correspond to the mean value of the arrival time in turbulent medium. With designation *std* the standard deviation is shown. Class width equals to 0.095.

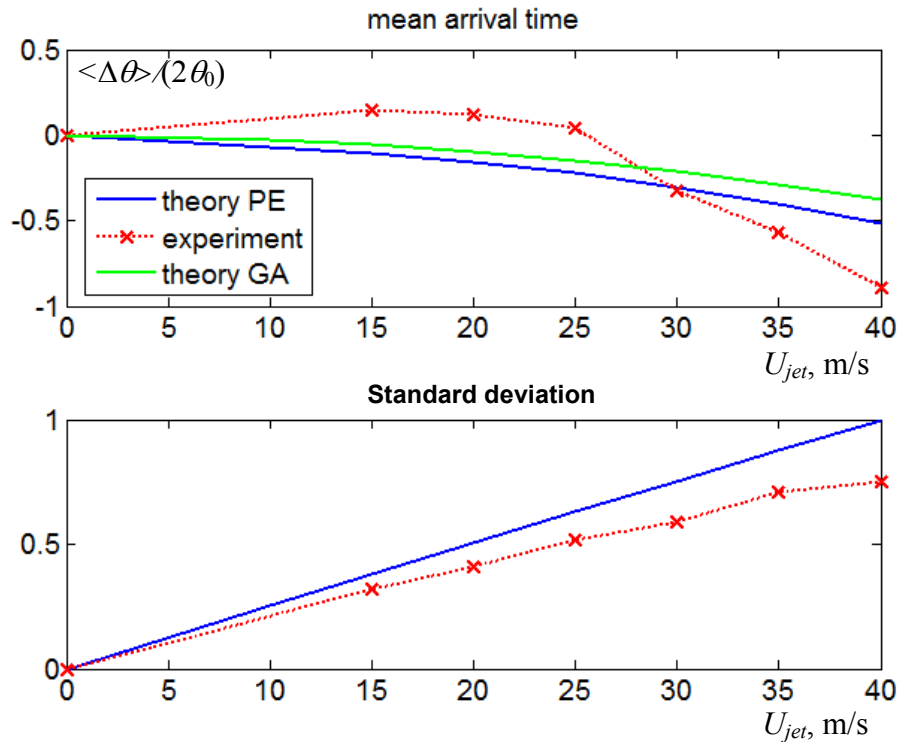


**Fig. 5.29** Dependence of the mean arrival time of the acoustic wave and its standard deviation, measured at the distance 2.19 m from the source, on the flow velocity at the exit of the jet  $U_{jet}$  (turbulence intensity). Red curve – experimentally measured values, blue curve – results of simulation using parabolic equation (PE), green curve – values given by geometrical acoustics approach (GA).

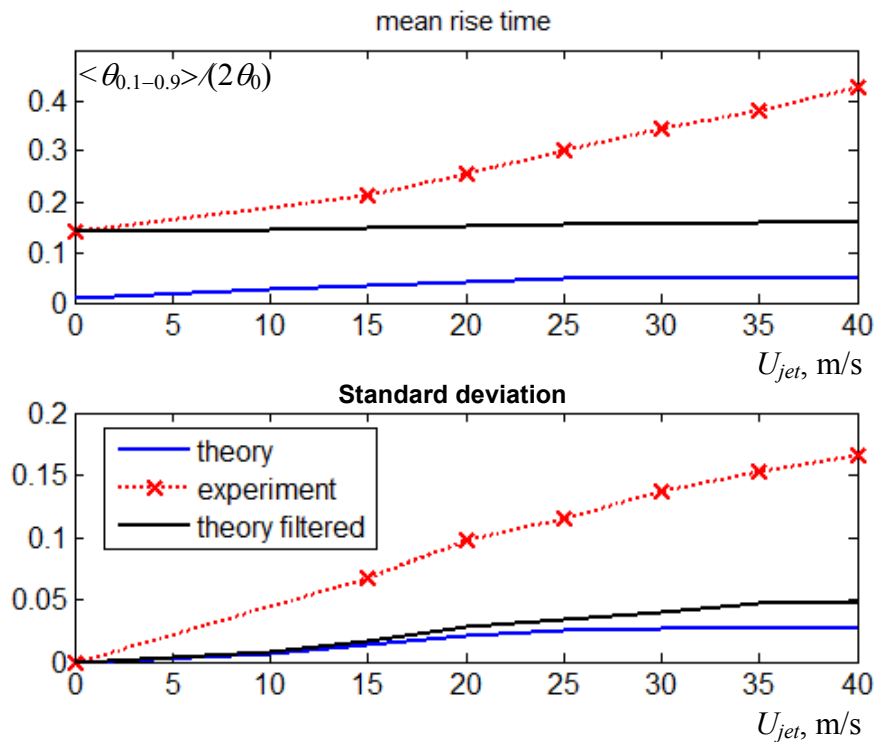


**Fig. 5.30** Dependence of the mean rise time of the acoustic wave and its standard deviation, measured at the distance 2.19 m from the source, on the flow velocity at the exit of the jet  $U_{jet}$  (turbulence intensity). Red curve – experimentally measured values, blue curve – results of simulation using parabolic equation, black curve – result of simulations, to which the measuring system frequency response was applied.

line [Iooss *et al.*, 133]. Parabolic equation predicts a bit faster arrival time of the acoustic wave in turbulent medium than the geometrical acoustics approach. The qualitative agreement between experimentally and theoretically obtained mean values and standard deviations is not so good here as for the peak positive pressure as soon as the arrival time is very sensitive to temperature variations and to any error of its measurement.

Such agreement between the results of 3D laboratory scale experiment and 2D numerical modelling confirms the validity of the derived parabolic evolution model (4.6) and developed numerical algorithm for the description of nonlinear acoustic wave propagation in inhomogeneous moving media. Nevertheless, such parameter of the acoustic wave as the shock front rise time (Fig. 5.30) can not be easily compared with theoretical predications due to strong difference of nonlinear propagation effects in 2D and 3D geometry (fast spherical divergence of the wave decrease the strength of amplitude dependent nonlinear effects). Even applying the measuring system frequency response to the calculated rise time does not give the same rate of its increase. However, the order of the “filtered” rise time is the same as that of the experimental one.

It is also useful to plot a cumulative probability curves which follow from the probability density distributions, presented above (Fig. 5.25), by using the following integration

$$P_c(a) = \int_a^{\infty} W(x) dx, \quad (5.2)$$

Cumulative probability  $P_c$  shows the probability pressure levels measurement which are higher than  $a$ . The results of integration are shown in Fig. 5.31 for both experimental (Fig. 5.31a) and theoretical measurements (Fig. 5.31b). With red solid and red dashed curves, the probabilities in laboratory measurements and probabilities given by theoretical predictions in still air are shown. The theoretical curve represents a step with 100% probability of relative pressure levels

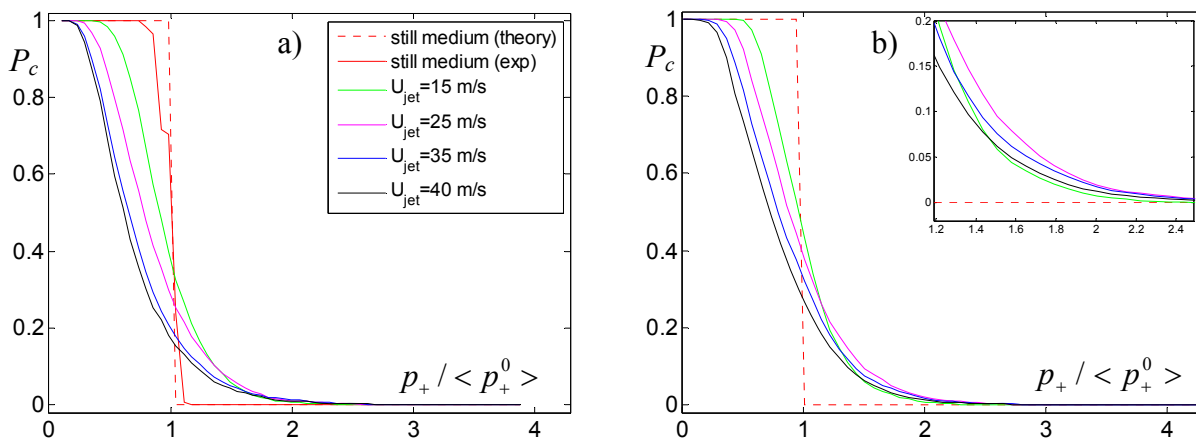


**Fig. 5.31** Cumulative probability  $P_c$  of normalized peak positive pressure calculated using the laboratory scale experiment data (a) and data from numerical modelling (b). Results are presented for different turbulence intensities.

observation higher than [0 1] and zero probability of observation of pressure levels higher than  $(1, \infty)$ . In contrast, experimental probability curve is smoothed around theoretical shock due to the slight instabilities of the spark source and due to the integration over data, measured by four microphones, which, in general, have different frequency responses. Results, obtained for the turbulent medium, are presented for four different turbulence intensities. Turbulence effect results in smoothing of the cumulative probability curve around the theoretical step-like shape (in still air). In general, low level pressure occurrence probability  $P_c(a < 1.0)$  becomes smaller, whereas the probability of high level pressure observation  $P_c(a > 1.0)$  becomes larger. The higher the turbulence intensity ( $U_{jet}$ ) is, the stronger the probability curves are smoothed and the longer tails they have. The cumulative probability  $P_c(a)$  for  $a < 1.0$  decreases with increasing the turbulence intensity. However, for  $a > 1.0$  peak positive pressure observation probability measured in high intensity turbulence starts to dominate that, measured in low intensity turbulence. In Fig. 5.26b in the zoomed area, one can see that the green curve ( $U_{jet} = 15$  m/s) reaches the zero value probability faster than other curves, corresponding to higher intensity turbulence. Thus, the higher the intensity of the turbulence is, the higher is the probability of high-level pressure observation. Relative pressure level higher than three is observed only in  $P_c(a = 3.0) = 0.1\%$  cases maximum ( $U_{jet} = 40$  m/s), whereas for  $U_{jet} = 15$  m/s this probability is already equals to zero. Cumulative probability for pressure levels higher than two is much higher and is equal to  $P_c(a = 2.0) = 2\%$ . This maximum is reached for  $U_{jet} = 25$  m/s. Minimum occurrence probability is reached for  $U_{jet} = 15$  m/s and is equal to  $P_c(a = 2.0) = 0.7\%$ . It is interesting, that probability of pressure level occurrence like in still medium drops down from  $P_c(a = 1.0) = 100\%$  in still medium to  $P_c(a = 1.0) = 27.44\%$  in turbulent medium, depending on its intensity. The highest probability here corresponds to the less intense turbulent fluctuations.

Finally, in Fig. 5.32 are shown the theoretical probabilities of high acoustic wave amplitudes observation in turbulent medium, which two times exceed the value of the peak pressure at the same distance but in motionless medium. These values are calculated for different turbulence intensities (different flow velocities  $U_{jet}$ ) along the propagation

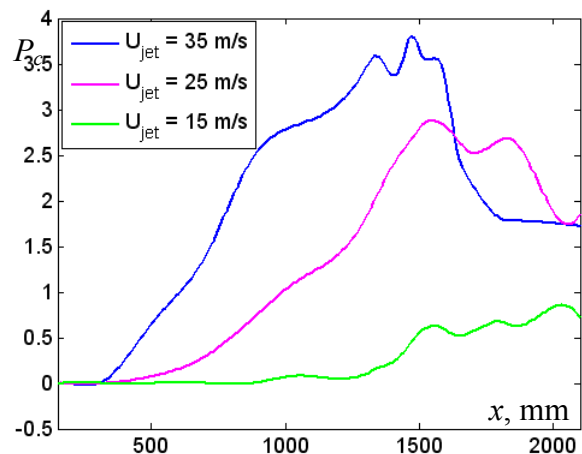


**Fig. 5.32** Cumulative probability  $P_c$  of peak positive pressure measurement, which two times exceeds the acoustic wave amplitude measured in motionless medium at the same propagation distance. Results are presented for different turbulence intensities.

coordinate of the acoustic wave. The highest probability is achieved in the case of the most intense turbulence and equals about 4%. With the decrease of turbulence intensity, the maximum probability decreases and moves towards longer distances in agreement with distance of occurrence of the strongest focusing, which is defined here by the largest scale inhomogeneities  $L = 23 \lambda = 193$  mm. This distance can be estimated in geometrical acoustics approach using (5.1) and is equal to 1060 mm, 1320 mm, 1840 mm from the source respectively for  $U_{jet} = 35$  m/s, 25 m/s, 15 m/s. Thus, predicted by geometrical acoustics distances are in a quite good agreement with the presented results, which were calculated using diffraction model.

## § 5.4 Conclusion

The propagation of an initially plane harmonic wave and  $N$ -pulse in nonlinear randomly inhomogeneous moving media was investigated numerically. Random inhomogeneities were generated using Gaussian and von Karman energy spectra. The results of simulations were compared to those obtained using the geometrical acoustics (eikonal equation). It was shown that the prediction of caustics and shadow zones by geometrical acoustics only partially corresponds to the regions of high and low pressure levels predicted with the nonlinear parabolic wave equation. The discrepancy between the results of the models increases for smaller size of inhomogeneities and for longer distances of propagation in randomly inhomogeneous media.

The simulations showed, that in the case of single-scale inhomogeneities with Gaussian energy spectrum the acoustic field was primarily affected by the fluctuations of the flow component parallel to the wave propagation direction. Contrarily to that, in the case of multi scale inhomogeneities with modified von Karman energy spectrum, the transverse component of the random velocity field was sufficiently noticeable. Moreover, influence of transverse component of the velocity field becomes even stronger for larger scale inhomogeneities and in the case of lateral winds. Therefore transverse to the wave propagation direction component of the turbulent flow need to be accounted for in order to correctly predict peak and average characteristics of the acoustic field.

It was shown, that for the case where nonlinearity has a length scale of higher or same order as the caustic formation distance, the focusing of the wave was enhanced even in the presence of strong nonlinear dissipation, that is, the focal regions have higher peak pressure and are more localized. If nonlinear length scale is very small, strong nonlinear dissipation suppresses peak pressure before the wave focuses, and therefore decrease of pressure amplitude in caustics is observed.

In the focal regions the waveforms were classical in shape: harmonic wave transforms to obtain a shock fronts, cusped positive peak, and smooth negative trough; *N*-wave transforms to the *U*-wave with high amplitude and thin shock front. In the shadow zones of small pressure amplitudes the presence of nonlinearity can also be observed as the waveforms have sufficiently steep shocks. In the case of *N*-wave propagation in random medium, formation of following waveforms were observed outside the focusing zones: picked waves, rounded waves and waves with several shock fronts with long pressure tails due to multi path propagation in the medium.

Random properties of the inhomogeneous moving medium have been shown to have twofold influence on the parameters of the acoustic field. On the one hand, statistically, mean peak positive pressure of the acoustic wave in turbulent medium decreases and mean rise time increases in comparison with them in the medium without turbulence, what is desirable. But on the other hand, due to the focusing, there occurs a small probability of measurement of very steep shock fronts with very high amplitudes. These results, confirm the tendency which were previously observed in experiments of Lipkens [7,40-42] and Ollivier *et al.* [44], and preliminary numerical simulations of Blanc-Benon *et al.* [31]. When acoustic wave propagates in random medium with von Karman energy spectrum the rate of mean rise time increase becomes even higher than in the medium with Gaussian energy spectrum. This effect is related to the presence of smaller size inhomogeneities which determine the widening of the front. However, there still exists non zero probability of very short rise times occurrence. It is shown that influence of turbulent medium on mean arrival time decrease with distance is smaller in the case of nonlinear propagation of the wave than in linear one.

The energy of the acoustic wave that propagated through the inhomogeneous medium was very close to that predicted by plane wave theory indicating that transverse redistribution of the energy into higher (with extra absorption) and lower (with less absorption) pressure regions did not result in average in significant change of nonlinear energy losses.

When experimental and numerical data for *N*-wave propagation in inhomogeneous moving medium were compared, it was shown that despite of different geometry of numerical (2D) and laboratory (3D) experiments, the results of measurements of peak positive pressure are in a good agreement, including the shape of statistical distributions, obtained values of peak and mean pressure and also the values of standard deviations.



## CONCLUSION

The main goal of this work was the experimental and numerical investigation of nonlinear-diffraction effects during the propagation of high amplitude acoustic signals through randomly-inhomogeneous moving medium. In experimental study, the aim was to build an experimental setup which allows investigating of shock wave propagation in turbulent medium under the conditions of multiple focusing caused by large-scale inhomogeneities. Previously conducted experiments did not give complementary information about focusing at long distances, defined by large scales in turbulence spectrum. However, such focusing is the most intense one, and, therefore, results in very high-pressure amplitude levels and very steep shock fronts. Moreover, the scaling of previous experiments was too high, and absorption effects were very strong and dominant on nonlinear propagation. Thus, a new laboratory scale experimental setup was built for the investigation of the propagation of short shock pulses of high amplitude (duration 30  $\mu$ s, amplitude up to 1000 Pa) in a turbulent airflow with mean velocity up to 20 m/s. It is shown that the energy spectrum of created turbulent field is well described by modified von Karman energy spectrum. Parameters of the turbulent flow were defined as: mean square velocity  $u_{rms} \in [0, 4]$  m/s, outer scale  $L_0 \in [200, 220]$  mm, inner scale  $l_0 \in [1.25, 1.7]$  mm, integral scale  $L_f \in [166, 182]$  mm.

Analysis of the experimental data showed, that the measurement system had a limited frequency response at higher frequencies. As soon as system response may vary due to using specific geometry of the experimental setup, due to air conditions or due to aging, it became necessary to develop a method of on-place measurement system calibration. Previously developed for non dissipative media calibration methods, based on nonlinear propagation phenomena, can not be used for calibration in air due to strong influence of thermoviscous absorption and relaxation effects. Based on numerical modelling of modified Burgers equation it was shown that in the experimental conditions and for the characteristic parameters of generated shock wave the decrease of the wave amplitude is equally dependent on nonlinear effects,

relaxation processes and on effects of thermoviscous absorption, whereas lengthening of the  $N$ -pulse is determined only by nonlinear effects. Thus, based on nonlinear lengthening of the  $N$ -pulse, a new experimental method of wide band microphone calibration in dissipative media was proposed and validated both numerically and experimentally. For the determination of pulse duration, a definition, based on the positions of the nulls in the pulse spectrum, was proposed. This method allows obtaining spectral characteristics of the measuring system at a wide frequency band simultaneously. The proposed method of nonlinear calibration of wide band microphones in dissipative media and conducted experiments under the conditions of multiple caustics formation, allows not only to describe the acoustic signal propagation in inhomogeneous medium, but also to validate developed theoretical model and numerical algorithm by comparison of experimental data with the results of simulations.

In theoretical study, the aim was to develop the nonlinear parabolic equation model, which accounts for the component of the medium velocity field transverse to the direction of wave propagation. Up to date, the effect of transverse winds were studied only in approximation of nonlinear geometrical acoustics, which does not account for diffraction effects, or in the wide angle parabolic approximation, which is limited to linear effects. Thus, incorporating both the nonlinear-diffraction effects and effects of transverse winds in one theoretical model, which, moreover, allows efficient numerical modelling, will give a powerful technique for investigation of intense sound wave propagation in inhomogeneous moving medium. In this work, starting from the exact equations of linear acoustics of inhomogeneous moving medium a nonlinear parabolic equation of the KZK type was derived. This equation contains a new term, which accounts for the influence of the medium velocity component in the direction transverse to the acoustic wave propagation. The validity of the derived equation is limited to smooth inhomogeneities, which primarily result in scattering in the forward direction up to 20 degrees of axis.

The parabolic equation has no analytical solutions and has to be solved numerically. However, it was found to have properties of similarity, which allows finding solutions for certain types of medium mean motion in the presence of small fluctuations using the solution for effective fluctuations. Numerical algorithm which allows solving obtained evolution equation in two dimensions, was developed using a split-step numerical method. Numerical procedure for each physical term was optimised to have a good accuracy of the solution, and, at the same time, to have reasonable computational time. Depending on the temporal characteristics of the transmitted signal, two approaches were employed for numerical modelling: time domain approach - for pulsed signals propagation and spectral approach - for periodic wave propagation.

Both algorithms allow computing of narrow shock fronts propagation in inhomogeneous moving media with account for the effects of diffraction, nonlinearity, thermoviscous absorption and relaxation. The validity of our theoretical and numerical models was investigated for the case of acoustic wave propagation through a simple focusing Gaussian inhomogeneity of one wavelength radius.

Propagation of acoustic signals in 2D randomly inhomogeneous media with Gaussian or modified von Karman energy spectra was then investigated. The random velocity field was modelled using the random Fourier modes method. It was shown that the spatial structure, peak and mean characteristics of the acoustic field in randomly inhomogeneous moving media are defined by the combined influence of nonlinear and diffraction effects. The advantages of the nonlinear-diffraction approach in comparison with the approximation of geometrical acoustics were demonstrated. It was determined, that nonlinear effects lead to essential change in the coefficient of field concentration in the random focusing areas. Moreover, regardless strong dissipation of the energy on the shock front, random focusing can result in considerable increase of pressure amplitude and in steepening of the wave front even at long distances such as several nonlinear distances  $x_s$ .

The influence of the random velocity field component, which is transverse to the acoustic wave propagation, on the acoustic field structure was investigated numerically by accounting in simulations whether both fluctuation components (longitudinal and transverse) or only transverse one. It was shown, that characteristic structure of the acoustic field in turbulent flow is formed mainly due to the influence of the longitudinal to the wave propagation direction component of the random velocity field. Transverse fluctuations lead to changes of the acoustic field structure in both longitudinal and transverse directions, and their influence increases with the growth of characteristic scale of the turbulent medium.

The influence of random focusing effect on the statistics of powerful acoustic shock pulse propagating in randomly inhomogeneous moving medium was investigated experimentally and numerically. Results of simulations, done in the conditions of the laboratory scale experiment, showed a very good qualitative and even quantitative agreement with the experimental data. Comparison was done after applying derived frequency response of the measuring system to the numerical data. Both experimentally and numerically, it was shown that turbulent medium results in considerable decrease of mean peak positive pressure (up to 30% at 2 m from the source), in increase of the mean rise time of the shock front (3-4 times), and in faster in average arrival of the  $N$ -wave (more than 15  $\mu\text{s}$  gain) in comparison with the same parameters of the wave propagating in motionless medium. At the same time in areas of focusing, acoustic pulses

with more than 4 times increase in the amplitude and corresponding decrease in the rise time were measured. For the first time the combined influence of nonlinear-diffraction effects on the statistics of wide band acoustic field in randomly inhomogeneous moving medium was investigated. It was shown that nonlinear effects decrease the value of relative changes in mean characteristics of the wave propagating in turbulent media in comparison with that in still medium.

As a continuation of this work, various possible prolongations can be proposed. The first possible continuation is the development of the numerical method in three dimensions, which accounts for all described previously effects, including the effects of transverse winds. In fact, if randomly fluctuating transverse component of the medium velocity field has been shown to have an important impact on the propagation of the acoustic wave in two dimensions, it will be even more pronounced in three dimensions, as shown by experiments. Moreover, 3D simulations should lead to even better agreement between theory and experiment. However, 3D simulations will be time consuming. Therefore, to ameliorate the code and finally to have reasonable computation time, the absorbing boundary layer of PML type (Perfectly Matched Layer) should be integrated in the algorithm, which will negotiate the reflections from the boundaries of the computational domain.

One more continuation of this work concerns the development of numerical algorithm, which also accounts for the effects of scalar inhomogeneities like variations of density and temperature, and also for the stratification of the atmosphere. This model could be used for the investigation of sound wave propagation at long distances; and for the investigation of transverse wind and diffraction effects on the acoustic pressure fields in shadow zones. Implementation of impedance boundaries into the code will also allow investigating sound reflection from the ground surface.

One more branch of possible future investigations is related to the amelioration of the wide band microphones calibration method in dissipative medium, taking into account relaxation effects. This could be done by means of better characterisation of the spark source and enhancement of the measuring procedure. Work in the direction of spark source amelioration in order to make it more stable as well as the work to create a wide band high frequency microphone (up to 200 kHz) is also possible.

## Appendix A : GEOMETRICAL ACOUSTICS APPROACH

### Eikonal equation in geometrical acoustics approach. Ray paths and caustics.

For acoustic wave propagation in inhomogeneous moving media, geometrical acoustics approach is used to trace acoustic rays and to determine exact caustic positions along ray paths. The classical formulation of geometrical acoustics is well known and given by the transport and eikonal equations which accounts also for moving media. Note that both in linear and nonlinear acoustics the eikonal equation has the same form [20]. If nonlinear propagation of the acoustic wave is considered, the nonlinear effects are accounted for by the transport equation. Thus, both in linear and nonlinear acoustics, rays are the solutions to the eikonal equation, which follows [14, 21, 62]:

$$(\nabla\psi)^2 = n^2\left(1 - \frac{\mathbf{u}}{c_0} \nabla\psi\right)^2 \quad (\text{A1})$$

where  $\psi=\psi(x,y,z)$  is the eikonal,  $n=c_0/(c_0+\Delta c)$  is the coefficient of refraction,  $\Delta c$  is the fluctuation in the speed of sound (scalar inhomogeneity),  $\mathbf{u} = (u_x, u_y, u_z)$  is the velocity field of the medium (vector inhomogeneity), and  $\nabla = (\partial / \partial x, \partial / \partial y, \partial / \partial z)$ .

Eikonal Eq. (A1) is a nonlinear first order partial differential equation of the Hamilton-Jacobi type [14, 135]. Taking the Hamiltonian in the form  $H = k - n(1 - \mathbf{k}\mathbf{u}/c_0)$ ,  $\mathbf{k} = \nabla\psi$ , the eikonal equation can be reduced to the characteristic set of coupled differential equations for acoustic rays, which in the absence of scalar type inhomogeneities ( $n=1$ ) take the form:

$$\frac{dx_i}{dt} = \frac{c_0 k_i}{(1 - \mathbf{p}\mathbf{u}/c_0)} + u_i \quad (\text{A2})$$

$$\frac{dk_i}{dt} = -k_j \frac{\partial}{\partial r_i} u_j \quad (\text{A3})$$

Here the variable  $t$  parameterizes the ray and is analogous to time,  $\mathbf{r} = (x, y, z)$  is the location of the ray in space,  $\mathbf{k}$  is the nondimensional wave vector,  $\mathbf{p}=\mathbf{k}/|\mathbf{k}|$  is the unit vector in the direction of wave vector and indices  $i$  and  $j$  show the  $x, y, z$ , component of the corresponding vector.

The ray trajectory is completely determined by the knowledge of medium inhomogeneities and by initial conditions given at the time  $t = 0$ . For a plane wave and 2D Cartesian geometry these initial conditions take the form:

$$\mathbf{r}(t = 0) = \begin{pmatrix} x(t = 0) \\ y(t = 0) \end{pmatrix} = \begin{pmatrix} 0 \\ y_0 \end{pmatrix}$$

$$\mathbf{k}(t = 0) = \frac{1}{1 + u_x / c_0} \begin{pmatrix} 1 \\ 0 \end{pmatrix} \quad (\text{A4})$$

The spatial distribution of the rays is a qualitative indicator of the local intensity of the acoustic field linked to the focusing or defocusing of the rays. To define caustics locations precisely, one needs to find points where the cross section area of the ray tube vanishes. In linear description, these points correspond to infinite acoustic pressure levels. In reality, the acoustic pressure at the caustic is limited by various physical mechanisms, as for example by diffraction [47, 62]. Anyway, caustics serve as indicators of increased pressure levels. The ray tube section in 2D geometry can be defined by means of geodesic element  $\mathbf{R} = (\partial \mathbf{r} / \partial y_0)_t$ . The geodesic elements describe the evolution of the wave front along each ray and are given by [Candel *et al.*, 136]:

$$\frac{dR_i}{dt} = \frac{c_0}{k} \left( Q_i - \frac{k_i k_m}{k^2} Q_m \right) + R_j \frac{\partial u_i}{\partial r_j} \quad (\text{A5})$$

$$\frac{dQ_i}{dt} = -Q_j \frac{\partial u_j}{\partial r_i} - k_j R_m \frac{\partial^2 u_j}{\partial r_i \partial r_m} \quad (\text{A6})$$

where  $\mathbf{Q} = (\partial \mathbf{k} / \partial y_0)_t$  and designates ‘conjugate’ elements.

The appropriate initial conditions for the system of equations (A5)-(A6) are given by:

$$R(t = 0) = \begin{pmatrix} 0 \\ 1 \end{pmatrix} \quad (\text{A7})$$

$$Q(t = 0) = \frac{\partial k(t = 0)}{\partial y_0} \begin{pmatrix} 1 \\ 0 \end{pmatrix} = \frac{p_x^2}{c_0} \frac{\partial u_x}{\partial y} \begin{pmatrix} 1 \\ 0 \end{pmatrix} \quad (\text{A8})$$

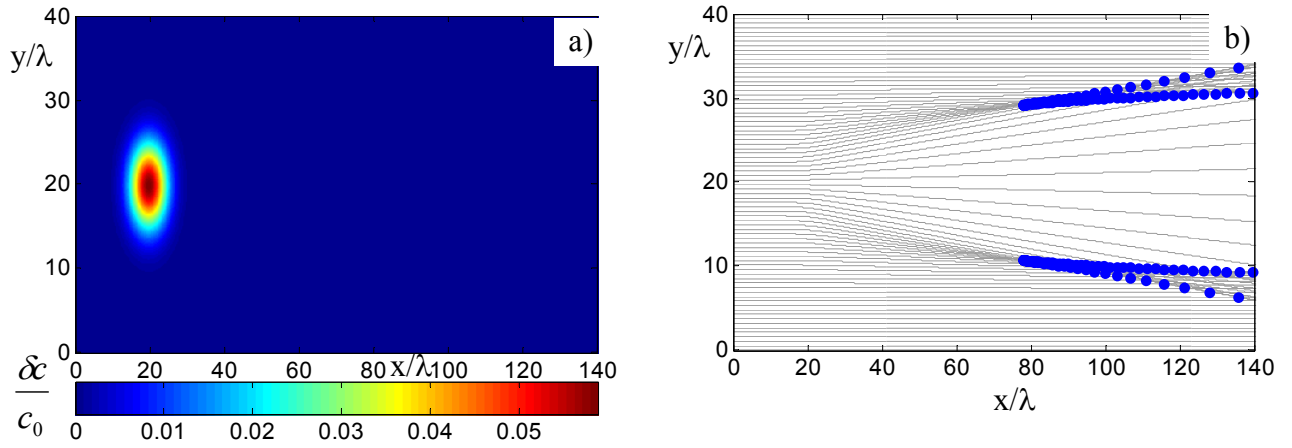


**Fig. A1.** a) an example of scalar Gaussian inhomogeneity with radius  $R=5\lambda$  and amplitude  $M = \delta c / c_0 \sim 0.06$ . b) acoustic ray paths and caustics corresponding to the plane acoustic wave propagation through presented inhomogeneity

Thus, position of the caustics are defined by the condition  $\mathbf{R}=0$ , i.e. when geodesic element  $\mathbf{R}$  vanishes, the acoustic pressure becomes infinite.

The system of equations (A2-A8) is solved numerically in 2D geometry using Runge-Kutta fourth order finite-difference algorithm [Press *et al.*, 124]. The time step for the Runge-Kutta solver was chosen to ensure 40 steps across the length scale of the inhomogeneity. In Fig. A1 is shown an example of acoustic rays passing through the defocusing scalar Gaussian inhomogeneity

$$\frac{\delta c}{c_0} = M \exp\left(-\frac{(\mathbf{r} - \mathbf{r}_0)^2}{R^2}\right) \quad (\text{A9})$$

With characteristic radius  $R=5\lambda$  and fluctuation amplitude  $M = (\delta c / c_0)_{\max} \sim 0.06$ . The centre of the inhomogeneity is situated at  $\mathbf{r}_0 / \lambda = (20, 20)$

After passing the inhomogeneity the acoustic wave phase front distorts, that lead to the formation of increased and decreased pressure levels. Regions with high concentration of acoustic rays correspond to high-pressure levels (infinite pressure in caustics – blue points). Regions with low rays intensity correspond to the low level pressure areas.



## **Appendix B : NUMERICAL GRID STEPS**

### **Selection of grid steps in time domain numerical algorithm for nonlinear parabolic equation**

To get an accurate numerical solution of the parabolic Eq. (4.6), appropriate grid steps in the numerical algorithm should be chosen for each particular problem. This appendix concerns the selection of numerical grid steps, computational window widths and artificial absorption for the time domain algorithm (§4.3.2). In general, there are two ways how to select the grid steps. If there are no computational time limits, the first way is used. All numerical steps are chosen in accordance with the physical effects, governing the acoustic wave propagation. This way gives an exact solution of the problem, but it results in a very long time of computation. Second way is usually used, if computation time is limited. In order to have reasonable computation time, one needs to limit physical effects. That is, for example, to introduce a small artificial absorption, which permits using larger numerical steps. Such method allows faster computation by means of introducing a small physical error into the solution. In this work, the second method was mainly used to solve the parabolic Eq. (4.6) and is further described.

As it was discussed in our numerical simulations of Chapter 4 (see §4.3), a long time calculation of the acoustic wave propagation is the result of a high time resolution, required to obtain a good description of shocks structure, occurring during the propagation. High time resolution needs a huge number of time points. Let us now consider that the maximum number of grid points per duration of the wave, due to calculation time limitations, is chosen to be equal to  $n = 256$ . From this follows the time step:  $h_\theta = 2\pi/n = 0.0246$  as soon as the period of the initial wave is equal to  $T = 2\pi$ . The problem now is to introduce modified physical parameters which permit to obtain the solution with minimal numerical error. Taking into account, that the width of the shock front in the still medium is described by quasistationary solution to the

Burgers Eq. (4.14), and that it should be taken not less than 3 points per shock to describe it properly (§4.3.2), the following relation can be obtained:  $10A/N \geq 3h_\theta$ , where  $A$  and  $N$  are the absorption and nonlinearity parameters respectively. In the problem of the acoustic shock wave propagation, investigated in this dissertation, the nonlinearity parameter is equal to  $N = 0.05$  and the absorption parameter is equal to  $A \sim 1.5 \cdot 10^{-4}$  (laboratory scale experiment). Substitution of these values into the presented relation makes it invalid. Therefore, one of the physical parameters should be changed. Usually in numerical methods, the absorption parameter is increased, as soon as it makes the numerical algorithm more stable and also results only in minor changes in the computed field [122]. Thus, from the relation, mentioned above, it follows  $A \geq 3Nh_\theta/10$ , from where follows the minimal absorption coefficient value:  $A = 3.6 \cdot 10^{-4}$ . Obtained value is of the same order as in laboratory scale experiment. However, using this value will result in proper description of shocks propagating only in homogeneous medium. If inhomogeneous medium is presented, the focalization of the acoustic wave, and therefore the increase of the acoustic pressure in the focal spots should be accounted for. The higher the pressure in the focal spot is, the narrower is the shock front due to the nonlinear effects. Therefore, the  $A$  coefficient should be modified according to the focalization ratio to describe properly the shock front even at the caustics. Thus, if estimated focalization ration is equal to two (this can be estimated from benchmark tests), the minimal absorption coefficient should be equal to  $A = 2 \cdot 3.6 \cdot 10^{-4} = 7.2 \cdot 10^{-4}$ .

Further, as soon as appropriate absorption coefficient value is found, the spatial step in the direction of wave propagation  $h_\sigma$  should be defined. In this purpose, a 1D propagation model based on the modified Burgers equation (Eq. (4.6) without diffraction term and transverse convection term) is considered. Such model allows more precise investigation of acoustic wave propagation using different grid steps and does not need long computational time. Numerical step is further selected in agreement with the condition of minimal difference between computed solution and “exact” numerical solution for the following physical phenomena: nonlinearity, absorption, relaxation and convection in the direction of the acoustic wave propagation. The “exact” solution is chosen as a solution, which can be considered as unchangeable with the decrease of a given numerical step. This spatial step was found to be equal  $h_\sigma = 0.5h_\theta$ . Let us define now the spatial step, which will result in a small numerical error of calculated wave parameters in comparison with the exact numerical solution. Let this error be not higher than 3%. The most difficult area in the simulations is the focal spot and its vicinity, where the highest amplitude and the steepest shock front is formed. Thus, if propagation is well described in focal spots, it will be described with even better accuracy outside them. Therefore, according to the

physical problem, the acoustic wave propagation is calculated using the following physical and numerical parameters:  $N = 0.05$ ,  $A = 3.6 \cdot 10^{-4}$  (restriction to the focalization),  $D_1 = 0.0022$ ,  $D_2 = 0.0004$ ,  $\theta_1 = 1.73$ ,  $\theta_2 = 161.1$ ,  $h_\theta = 0.0246$  and varying value of the spatial step  $h_\sigma = h_\theta$ ,  $h_\sigma = 4h_\theta$ ,  $h_\sigma = 10h_\theta$ ,  $h_\sigma = 20h_\theta$ . Relative numerical errors are then calculated for the amplitude of the acoustic wave and for the rise time of its front:  $\varepsilon = (\alpha - \alpha_{exact})/\alpha_{exact}$ , where  $\alpha$  is the investigated parameter and  $\alpha_{exact}$  its “exact” numerical value. In the Table B1 are presented maximal and mean errors for the peak pressure and for the rise time over the propagation distance  $\sigma = 230$ . It is seen, that the required accuracy ( $\varepsilon < 3\%$ ) is achieved when using spatial grid step  $h_\sigma = 4h_\theta$ . Numerical errors in this case are equal to 2.2% for the rise time and 0.36% for the peak amplitude. Note also, that even if only about two grid points per wavelength are used ( $h_\sigma = 20h_\theta = 0.492$ ), the numerical error does not exceed 10% level. In order to compare with, in Table B2 the numerical errors calculated using  $n = 512$  (instead of  $n = 256$ ) points per wave duration are shown ( $h_\theta = 0.0123$ ,  $A = 1.8 \cdot 10^{-4}$ ). In this case, like in previous one, the required accuracy of numerical solution is achieved for spatial step  $h_\sigma = 4h_\theta$ , what is equivalent to about 10 grid knots per wave duration. Thus, spatial step  $h_\sigma = 4h_\theta$  was chosen to preserve a good accuracy of the numerical solution.

At the last step of the procedure, the spatial grid step in the direction, transversal to the acoustic wave propagation, is selected according to the minimal characteristic scales of the problem. They are the wavelength, the turbulence inner scale and the characteristic transverse scale of the focal regions. The turbulence inner scale, due to the limitations of the parabolic approximation, is usually chosen to be longer, than the wavelength. At the same time, there no limitations on the characteristic transverse scale of the focal region, and therefore it can be

**Table B1.** Dependence of relative error on the numerical grid step in propagation direction.  $h_\theta = 0.0246$ ,  $A = 3.6 \cdot 10^{-4}$

	$h_\sigma = h_\theta$	$h_\sigma = 4h_\theta$	$h_\sigma = 10h_\theta$	$h_\sigma = 20h_\theta$
$\varepsilon_{peak\ pressure}$	$1.6 \cdot 10^{-3}$	$3.6 \cdot 10^{-3}$	$1.0 \cdot 10^{-2}$	$4.3 \cdot 10^{-2}$
$\varepsilon_{rise\ time}$	$4.5 \cdot 10^{-3}$	$2.2 \cdot 10^{-2}$	$5.4 \cdot 10^{-2}$	$8.8 \cdot 10^{-2}$

**Table B2.** Dependence of relative error on the numerical grid step in propagation direction.  $h_\theta = 0.0123$ ,  $A = 1.8 \cdot 10^{-4}$

	$h_\sigma = h_\theta$	$h_\sigma = 4h_\theta$	$h_\sigma = 10h_\theta$	$h_\sigma = 20h_\theta$
$\varepsilon_{peak\ pressure}$	$1.3 \cdot 10^{-3}$	$2.6 \cdot 10^{-3}$	$6.0 \cdot 10^{-3}$	$4.0 \cdot 10^{-2}$
$\varepsilon_{rise\ time}$	$6.6 \cdot 10^{-3}$	$2.1 \cdot 10^{-2}$	$4.7 \cdot 10^{-2}$	$1.1 \cdot 10^{-1}$

shorter than the wavelength. Due to the experience, the transverse length scale of the focal region can be as short as a  $\lambda/2$  (see, for example, Fig. 5.12c). To describe precisely the acoustic

pressure and to have a good resolution of the acoustic field parameters in the vicinity of focal region, the number of grid points per focal waist should not be less than 10, and therefore not less than 20 grid points per unity. Thus, in our simulations in agreement with this, the spatial step in transverse direction was chosen to be equal to  $h_\rho = 0.04$  (25 grid points per wavelength). Moreover, chosen in this way spatial numerical step is in the agreement with the relation  $U_\perp \cdot h_\sigma / h_\rho \leq 1$ , which limits the validity of the Lax-Wendroff scheme used for the description of the velocity field transverse component.

To validate our choice for the numerical grid step, the simulations of the acoustic wave propagation through the randomly inhomogeneous moving medium (modified von Karman spectrum,  $u_{rms} = 4.0$  m/s,  $L_0 = 23\lambda$ ,  $l_0 = 2.4\lambda$ ) were done using the transverse spatial grid step equal to  $h_\rho = 4.0 \cdot 10^{-2}$ , to  $\frac{1}{2} h_\rho$  and to  $2h_\rho$ . The results of simulations are presented in Table B3 as observed maximal and mean relative errors in determination of the acoustic wave peak positive pressure and its rise time. As soon as an exact analytical solution is not available, the obtained results were compared to the “exact” numerical solution, calculated with the following steps:  $h_\theta = 0.0246$ ,  $h_\sigma = 2h_\theta$ ,  $h_\rho = 0.02$  at different points of the acoustic field. It follows from the comparison, that for the chosen steps ( $h_\theta = 0.0246$ ,  $h_\sigma = 4h_\theta$ ,  $h_\rho = 4.0 \cdot 10^{-2}$ ) the numerical error in determination of the peak positive pressure values does not exceed 3.0% and thin shock front rise time values - 3.1%.

**Table B3.** Dependence of relative error on the spatial grid steps in propagation and transverse directions.  $h_\theta = 0.0246$ ,  $A = 7.2 \cdot 10^{-4}$ ,  $h_\sigma = 4h_\theta$ ,  $h_\rho = 4.0 \cdot 10^{-2}$

	$\frac{1}{2}h_\sigma, h_\rho$	$h_\sigma, \frac{1}{2}h_\rho$	$h_\sigma, h_\rho$	$h_\sigma, 2h_\rho$	$2h_\sigma, h_\rho$	$2h_\sigma, 2h_\rho$
$\mathcal{E}_{peak\ pressure, \max}$	0.03	0.013	0.03	0.132	0.056	0.146
mean	$3.8 \cdot 10^{-4}$	$1.6 \cdot 10^{-3}$	$1.7 \cdot 10^{-3}$	$4.0 \cdot 10^{-3}$	$6.6 \cdot 10^{-3}$	$7.4 \cdot 10^{-3}$
$\mathcal{E}_{rise\ time}$	0.016	0.036	0.031	0.09	0.093	0.094
max	$2.7 \cdot 10^{-3}$	$5.9 \cdot 10^{-3}$	$6.5 \cdot 10^{-3}$	$1.5 \cdot 10^{-2}$	$1.5 \cdot 10^{-2}$	$2.4 \cdot 10^{-2}$
mean						

If a smaller time step was chosen to calculate the acoustic wave propagation in the inhomogeneous moving medium, the appropriate spatial grid steps and the value of absorption coefficient can be easily found, using the analysis, presented above. Let us, for example, make a calculation of acoustic wave propagation using  $n = 512$  grid points per its duration. Then, the time grid step  $h_t = 2\pi/n = 0.0123$  and absorption coefficient value becomes equal to  $A = 3.6 \cdot 10^{-4}$ . According to the Table B1, B2, and corresponding discussion, the spatial grid step in the direction of propagation is equal to  $h_\sigma = 4h_\theta \approx 0.05$ . As soon as the width of the focal region should not change, the spatial grid step in transverse direction is remains intact and is equal to

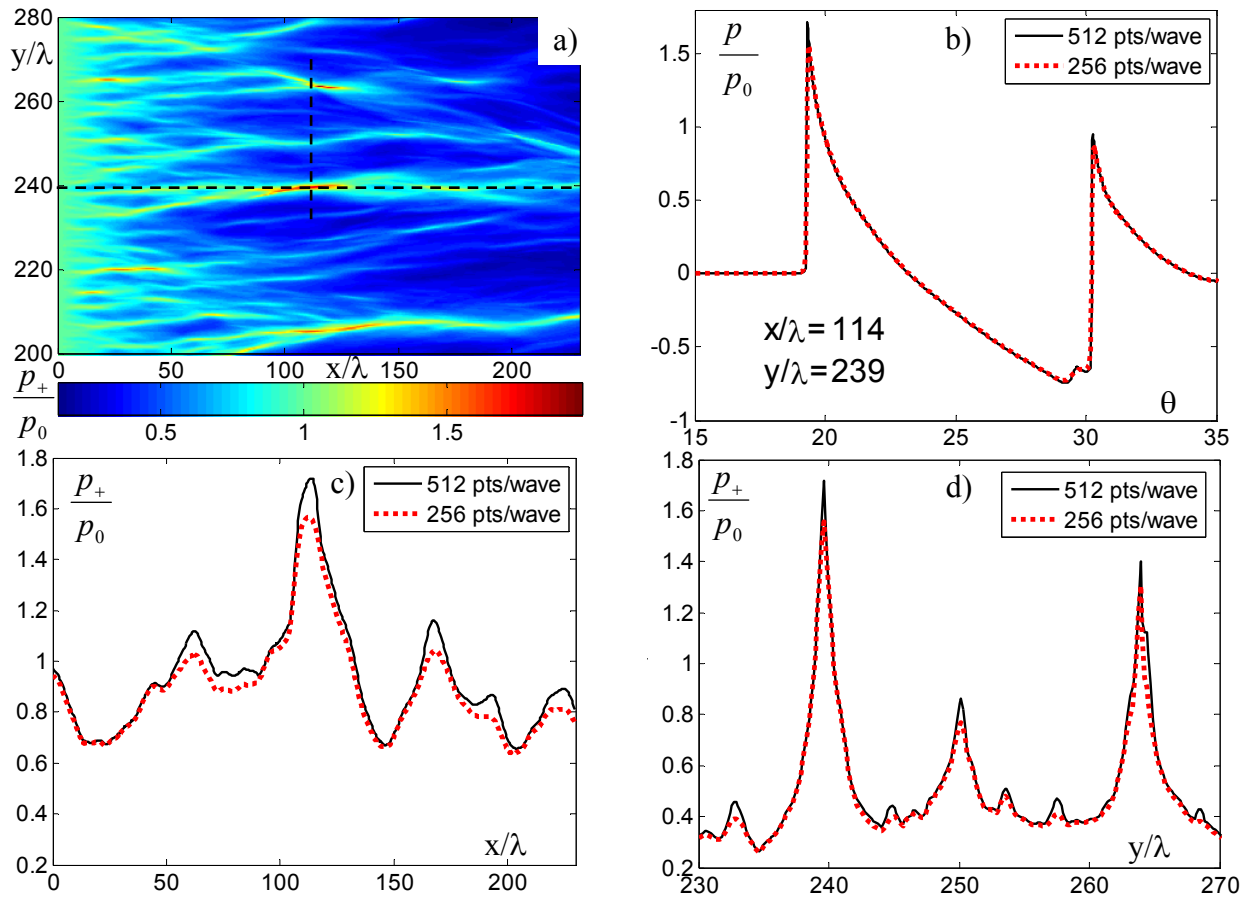


**Fig. B1** Comparison of waveforms (b), longitudinal (c) and transverse (d) distributions of the peak positive pressure field (a), measured along dashed lines and calculated taking 256 (dotted line) or 512 (solid line) time grid points per duration of the wave.

$h_p = 0.04$ . In Fig. B1 are presented the distributions of the peak positive pressure in longitudinal (c) and transverse (d) directions, measured along corresponding dashed lines (a) together with waveforms (b), calculated at the focal spot ( $x/\lambda = 114.1$ ,  $y/\lambda = 239.9$ ) taking 256 (dotted line) or 512 (solid line) time grid points per wave duration. It can be clearly seen, that having more time grid points leads to stronger focusing, and therefore to the formation of higher peak pressures and steeper shock fronts. This also allows us to decrease the absorption coefficient, being closer to its value for the conditions of the laboratory scale experiment.

After choosing the spatial and temporal grid steps there still remains a question concerning boundary conditions. In the simulations, reported here, the computational window in transverse spatial direction is chosen sufficiently large to avoid influence of reflections from the boundaries on the investigated field. According to the validity limit of the parabolic approximation used in this work, the maximal supported angle of sound beam declination from the axis is equal to  $20^\circ$  [Tjøtta *et al.*, 127]. Thus, to avoid reflection from the boundaries it is needed to make a computational window larger than the region of interest on  $\sigma_{max} \cdot \tan(20^\circ)$  from each side, where  $\sigma_{max}$  is the maximal distance of propagation. As for the time domain computational window size, it is much more difficult to define, as soon as two phenomena

should be taken into account: elongation of the pulse according to the nonlinear effects and variation of the wave arrival time due to presence of inhomogeneities. The first effect can be estimated using the weak shock theory, where as the second effect is very difficult to predict. The arrival time depends strongly on scale and intensity of the inhomogeneous medium and also on the propagation distance and, therefore, can be defined only experimentally. In the calculations, presented in this dissertation, faster arrivals of the acoustic pulse in inhomogeneous medium were observed. The maximum arrival time shift was obtained for the most intense large scale turbulence with dimensionless root mean square velocity  $U_{rms} = 0.012$  (4.00 m/s) and spatial scale  $L_0/\lambda = 23$  and is equal to  $6.4\pi$  at propagation distance  $230 \lambda$ . The second temporal boundary should be chosen in agreement with the length of the pulse tail, which is of interest. In this work, for example, a tail part not smaller than four wave periods ( $8\pi$ ) was investigated.

## **Appendix C : SYNTHÈSE DES RÉSULTATS**

### **INTRODUCTION**

La propagation d'ondes acoustiques intenses dans un milieu hétérogène en mouvement est un problème important pour plusieurs applications modernes de l'acoustique théorique et expérimentale, telles que la diffusion d'ultrasons de puissance dans les tissus biologiques hétérogènes avec la présence entre autre des vaisseaux sanguins, la propagation de l'onde de choc du bang sonique à travers les couches turbulentes de l'atmosphère près de la terre et celle des ondes produites par des sources explosives dans l'océan fortement fluctuant. La structure du champ acoustique non linéaire propagé dépend fortement du caractère hétérogène du milieu de propagation, et notamment de la présence des diverses inhomogénéités, y compris, des vents ou des courants, des champs turbulents, ainsi que des gradients de densité et de température. Pour toutes les applications indiquées, la définition de la structure spatio-temporelle du champ acoustique est importante pour plusieurs raisons. Par exemple, cela permet d'estimer le niveau de la pression acoustique près de la surface de la terre, ou d'estimer les effets provoqués par les ultrasons sur les tissus biologiques. Et il est alors souhaitable d'avoir en plus la possibilité de prédire les caractéristiques des signaux acoustiques transmis telles que les valeurs du pic et des moyennes de la pression ainsi que celles du temps de montée du front d'onde. Pour réaliser cela, une modélisation théorique, qui prend en considération les effets apportés par les inhomogénéités du milieu, par la diffraction, par la non linéarité acoustique, par l'absorption thermo visqueuse et par les phénomènes de relaxation est strictement nécessaire.

Malgré des exemples si divers de propagation du son dans les milieux hétérogènes, les modèles théoriques décrivant le processus de formation du champ acoustique et de sa propagation en milieu inhomogène sont très proches ; on peut néanmoins distinguer deux types d'inhomogénéités permettant de définir deux catégories de milieu : d'une part les milieux avec des inhomogénéités « scalaires » ( fluctuations spatiales de la vitesse du son et de la densité du

milieu provoquée, par exemple, par des changements de la température ou de la concentration du sel dans l'océan, ou par des changements de nature du tissu biologique); et d'autre part les milieux avec des inhomogénéités « vectorielles » (fluctuations spatiales de la moyenne vitesse des particules du milieu, par exemple, en conséquence de la présence des tourbillons, du vent ou des courants). Une analyse avec un modèle théorique complet, dans lequel les inhomogénéités de type vectoriel sont prises en considération, est très complexe à mettre en œuvre. L'approche traditionnelle que l'on trouve dans la littérature, consiste au remplacement du milieu réel en mouvement par un milieu hypothétique immobile pour lequel la vitesse du son est remplacée par une vitesse effective du son, qui prend en considération seulement la composante de la vitesse du milieu dans la direction de propagation de l'onde acoustique ; le milieu inhomogène mobile est donc modélisé comme un milieu inhomogène de type scalaire. Néanmoins, si la composante transversale du champ de la vitesse (par rapport à la direction de propagation) est non nulle, elle peut provoquer par convection le déplacement transversal du champ acoustique et l'altération des zones de focalisation du champ et des caustiques, et, donc, peut fortement influencer la propagation de l'onde acoustique dans le milieu en mouvement.

L'étude théorique du problème de la propagation des impulsions acoustiques de forts niveaux dans une atmosphère hétérogène en mouvement est une tâche très complexe, c'est pourquoi les résultats théoriques sont souvent obtenus dans le cadre de modèles simplifiés, comme par exemple l'approche de l'acoustique géométrique. Dans cette approximation haute fréquence, les effets non linéaires sont alors examinés dans les milieux contenant des inhomogénéités aussi bien scalaires que vectorielles, et des solutions analytiques ont été développées seulement pour les milieux stratifiés. Cependant, un grand désavantage de cette approche est que l'acoustique géométrique néglige les effets de diffraction. Ce n'est que récemment, avec le développement de méthodes numériques performantes, que les problèmes de diffraction ont commencé à pouvoir être traités. Ainsi, pour la propagation linéaire du son dans les milieux hétérogènes mobiles, les équations d'évolution ont été récemment dérivées dans l'approche parabolique de la théorie de diffraction, et cela en conservant la nature vectorielle de la vitesse de convection du milieu. La propagation non linéaire du son dans les milieux contenant des inhomogénéités scalaires a été également examinée dans le cadre de l'approximation parabolique. Le cas des milieux contenant des inhomogénéités vectorielles, telles que des tourbillons à diverses échelles ou des vents avec une composante transversale de vitesse significative, à notre connaissance n'a pas été étudié en utilisant une approximation parabolique non linéaire. De même les effets combinés de la propagation non linéaire et les effets de diffraction intrinsèques aux divers types d'inhomogénéités aléatoires ont été que très peu

envisagés jusqu'à présent. Ainsi, les problèmes non linéaires diffractifs de propagation des signaux à large bande dans les milieux aléatoires et hétérogènes en mouvement sont d'actualité.

Quant à l'étude expérimentale en milieu extérieur de la propagation des signaux acoustiques de fortes amplitudes, par exemple dans la couche limite atmosphérique, elle est particulièrement délicate compte tenu notamment de la complexité des mesures des champs aérodynamique et acoustique, et du manque de contrôle des conditions expérimentales. De plus dans le cas de la propagation du bruit émis par un avion supersonique, il est difficile d'effectuer un nombre important de mesures indispensable à une analyse statistique. C'est pourquoi depuis une vingtaine d'année les travaux de la littérature se sont concentrés sur la réalisation d'expériences à l'échelle dans des conditions de laboratoire. En effet dans les conditions de laboratoire, les paramètres de la source sonore et ceux des champs turbulents sont bien contrôlés, ce qui donne la possibilité de faire des études plus exactes. Les résultats des mesures d'une telle expérience permettent non seulement la description qualitative des irrégularités de propagation des impulsions acoustiques dans le milieu hétérogène en mouvement, mais aussi ils sont à la base d'une validation des modèles théoriques développés et des simulations numériques associées. L'une des perspectives de ce travail est alors d'obtenir des estimations quantitatives des pics de pression acoustiques et des temps de montées des chocs formés lors de la propagation des bangs soniques dans la turbulence atmosphérique.

## OBJECTIFS

L'objectif de cette thèse est de développer des méthodes théoriques et expérimentales pour l'étude de la propagation non linéaire des signaux acoustiques dans les milieux hétérogènes en mouvement. Dans cette perspective nous avons retenu les objectifs intermédiaires suivants:

1. Le développement d'un dispositif expérimental en soufflerie anéchoïque et l'étude de la propagation d'impulsions acoustiques – ondes en  $N$  – à travers un jet turbulent dans des conditions de laboratoire.
2. Le développement d'un modèle théorique de la propagation des signaux non linéaires acoustiques dans des milieux hétérogènes mobiles, sur la base d'une équation de type Khokhlov-Zabolotskaya-Kuznetsov, en tenant compte des effets diffractifs, dissipatifs et des processus de relaxation.
3. Le développement d'un algorithme numérique permettant la résolution d'une équation parabolique de type Khokhlov-Zabolotskaya-Kuznetsov et la modélisation

de la propagation dans un milieu hétérogène en mouvement de signaux non linéaires périodiques ou impulsifs avec des fronts très raides.

4. L'analyse de l'influence relative des effets non linéaires, dissipatifs et des effets de relaxation sur la propagation d'une onde acoustique en  $N$  dans un milieu homogène afin d'élaborer une méthode de calibration des microphones utilisés dans l'expérience.
5. L'étude expérimentale et théorique de l'influence des effets non linéaires et de diffraction, ainsi que celle des focalisations aléatoires, sur la propagation d'une onde acoustique en  $N$  dans un milieu hétérogène en mouvement à partir d'une analyse statistique des paramètres principaux du champ acoustique (maximum de niveaux de pression, temps de montée, temps d'arrivée).

Cette thèse en co-tutelle a été accomplie avec le soutien d'une bourse du Président de la Fédération de Russie, d'une bourse de thèse en cotutelle du Gouvernement Français distribuée par l'ambassade de France en Russie, d'une bourse de la Société d'Acoustique des Etats-Unis, et dans le cadre des programmes de recherche RFBR № 06-02-16860 INTAS № 05-1000008-7841, et scientific schools RF № NSH-4449.2006.2.

## SYNTHESE DES RESULTATS

Le premier chapitre présente la bibliographie sur les études expérimentales (§1.1) et théoriques (§1.2) de propagation de signaux acoustiques intenses dans un milieu turbulent. Les mesures effectuées « in situ », ainsi que les mesures faites en laboratoire montrent notamment qu'il est possible d'observer la formation des régions de forte focalisation (§1.1). Il est également possible d'obtenir des maxima de pics de pression du champ acoustique qui sont deux ou trois fois plus grands que ceux, enregistrés dans un milieu homogène en l'absence de turbulence. Le §1.2 traite de la bibliographie, consacrée à la description des modèles mathématiques principaux de propagation des ondes acoustique non linéaires à travers des milieux inhomogènes en mouvement. Il est montré, que des résultats quantitatifs sont obtenus seulement dans le cadre des modèles simplifiés, à savoir pour l'essentiel dans l'approximation de l'acoustique géométrique non linéaire des milieux stratifiés. Récemment, pour la modélisation numérique de la propagation des ondes acoustiques dans les milieux hétérogènes, les équations gouvernant l'évolution du champ de pression acoustique dans l'approximation parabolique de la théorie de la diffraction ont commencé à être utilisées. L'avantage évident de tels modèles est qu'ils prennent en compte les effets de diffraction. Toutefois, la description théorique de cette approche parabolique est limitée dans la littérature soit à des problèmes linéaires de propagation des ondes acoustique dans les milieux en mouvement, soit à la description des champs acoustiques non linéaires dans les milieux avec prise en compte uniquement des hétérogénéités scalaires. Ainsi, à notre connaissance, la description quantitative des champs acoustiques non linéaires et diffractifs dans les milieux hétérogènes en mouvement n'a pas encore été faite. Un sommaire des modèles principaux décrivant des milieux aléatoires et hétérogènes, ainsi que des milieux turbulents, est exposé dans le §1.3. L'attention principale est donnée à un modèle de modes Fourier orientées aléatoirement, où le champ aléatoire de la vitesse du milieu turbulent est modélisé de la façon suivante:

$$\mathbf{u}(\mathbf{r}) = \sum_{j=1}^{J_{\max}} \tilde{\mathbf{U}}(\mathbf{K}_j) \cos(\mathbf{K}_j \cdot \mathbf{r} + \phi_j) , \quad (1)$$

$$\tilde{\mathbf{U}}(\mathbf{K}_j) \cdot \mathbf{K}_j = 0 . \quad (2)$$

Où  $\mathbf{K}_j$  et  $\phi_j$  sont respectivement le vecteur et la phase de  $j^{\text{ème}}$  mode de Fourier. L'angle aléatoire  $\theta_j$  entre  $\mathbf{K}_j$  et l'axe  $x$ , ainsi que des valeurs de la phase  $\phi_j$  sont choisis pour chaque mode de Fourier à partir de distributions indépendantes uniformes sur un intervalle  $[0, 2\pi]$ . L'équation (2)

correspond à la condition d'incompressibilité du champ de vitesse synthétisée. L'amplitude de chaque mode aléatoire  $|\tilde{\mathbf{U}}(\mathbf{K}_j)|$  dans l'équation (1) est déterminée par le spectre d'énergie cinétique  $E(K)$  du modèle de turbulence considéré:  $|\tilde{\mathbf{U}}(\mathbf{K}_j)| \sim \sqrt{E(K) \Delta K}$ ,  $K = |\mathbf{K}|$ . Si un assez grand nombre de modes de Fourier dans l'équation (1) est considéré, chacun d'entre eux choisi conformément à l'équation (2) avec  $\theta_j$  et  $\phi_j$  distribués uniformément, le champ résultant de vitesse  $\mathbf{u}(\mathbf{r})$  sera statistiquement homogène et isotrope, et aura le spectre d'énergie cinétique prescrit. Il est supposé de plus pour cette modélisation du champ aléatoire et homogène de la vitesse que le temps de propagation de l'onde acoustique dans le milieu turbulent est beaucoup plus court que l'échelle caractéristique de l'évolution temporelle de la turbulence ; c'est-à-dire que le champ turbulent est considéré comme "gelé" (indépendant du temps).

Sur la figure C1 est présenté un exemple d'une réalisation du champ turbulent de la vitesse, calculé sur la base de 300 modes de Fourier régulièrement distribués entre  $0.01/L$  et  $9.0/L$  pour un spectre énergétique gaussien:

$$E(K) = \frac{1}{8} u_{rms}^2 K^3 \cdot L^4 \exp\left(-\frac{K^2 \cdot L^2}{4}\right) \quad (3)$$

où  $u_{rms}^2 = 9 \text{ m}^2/\text{s}^2$  est la variance des fluctuations de la vitesse,  $L = 4\lambda$  est une échelle spatiale caractéristique de l'hétérogénéité et  $\lambda$  est la longueur d'onde acoustique de l'onde qui se propage dans le milieu inhomogène considéré. Sur la figure C1 (a, b) sont présentées les distributions

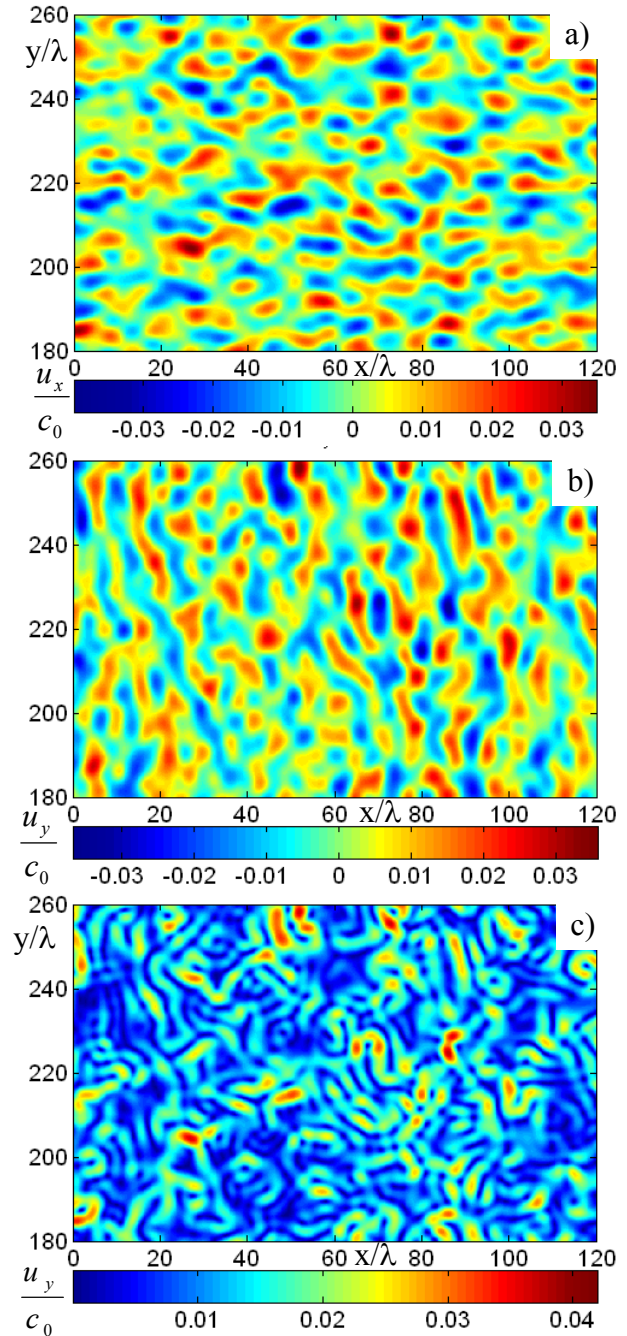


**Fig. C1** Exemple d'une réalisation du champ aléatoire de la vitesse du milieu turbulent avec un spectre énergétique Gaussien. a) - composante longitudinale des fluctuations de la vitesse, b) - composante transversale des fluctuations de la vitesse, et c) - valeur absolue des fluctuations de la vitesse.

spatiales des composants longitudinale et transversale des fluctuations de la vitesse du milieu, et sa valeur absolue est donnée sur la figure C 1c. De cette façon, chaque réalisation synthétisée du milieu aléatoire et hétérogène se caractérise par la forme de son spectre énergétique, par la moyenne quadratique de vitesse des

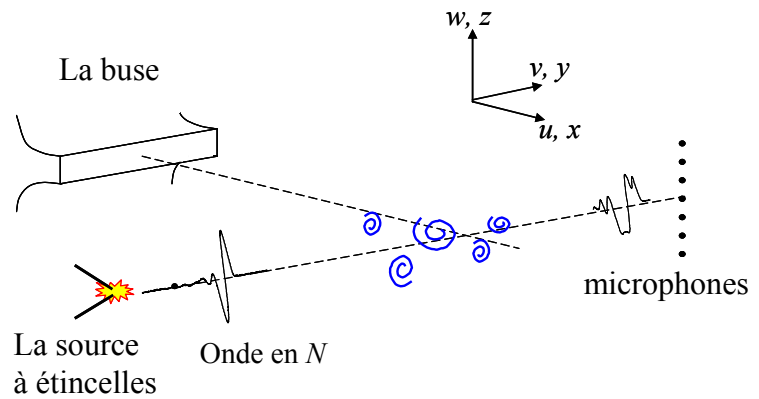


**Fig. C2** Représentation schématique de la géométrie du dispositif expérimental

fluctuations, par l'échelle caractéristique et par l'ensemble des modes aléatoires associés au nombre servant à l'initialisation du générateur de nombres aléatoires. Une telle méthode permet de calculer la propagation des ondes acoustiques avec diverses conditions initiales ou avec différentes méthodes de simulation, mais en considérant toujours la propagation à travers la même réalisation du milieu hétérogène.

**Le deuxième chapitre** de la thèse est consacré à la description du dispositif expérimental et à la mesure dans des conditions contrôlées de laboratoire des valeurs du maximum du pic du champ acoustique, ainsi que des caractéristiques moyennes et statistiques de l'onde acoustique après le passage de la couche turbulente. Le dispositif expérimental mis au point permet de générer des champs de vitesse turbulents pleinement développés, ainsi que les impulsions acoustiques de type d'onde en  $N$ , qui sont propagées dans l'inhomogénéité suivant la direction perpendiculaire au jet turbulent (figure C 2). L'expérience a été réalisée dans la soufflerie anéchoïque de l'École Centrale de Lyon.

**Dans le paragraphe §2.1** est présenté la partie de l'expérience physique consacrée à la création et à la mesure des champs turbulents développés. L'un des objectifs principaux de ce paragraphe, est la recherche d'un plan de mesure, où le champ turbulent est entièrement développé ; pour cela on mesure les caractéristiques statistiques du jet turbulent (variance, densité spectrale) et les fonctions de corrélation spatiales des fluctuations dans le but de définir les échelles intégrales des fluctuations. Dans le plan ainsi défini, les mesures acoustiques seront réalisées.

Pour la création du jet turbulent bidimensionnel pleinement développé, nous utilisons l'un des ventilateurs de la soufflerie subsonique (0 - 160 m/s, 15 kg/s, 350 kW). Le jet sortant d'une buse rectangulaire de dimensions 160 x 1400 mm, est guidé entre deux baffles en bois verticaux afin d'assurer un développement correct du jet et obtenir à une distance de la buse

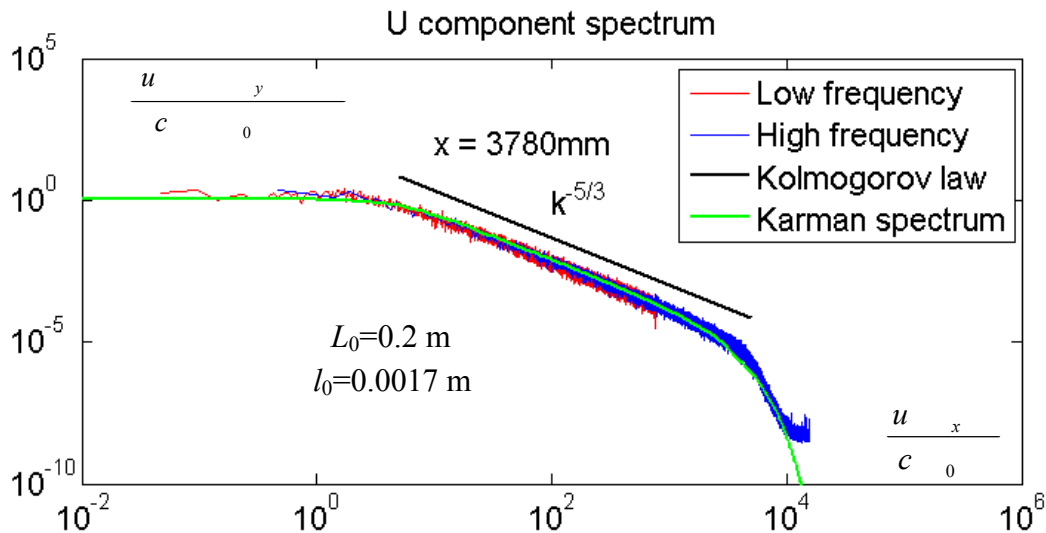


**Fig. C3** Comparaison de la densité spectrale des fluctuations longitudinales de vitesse mesurée avec les valeurs théoriques obtenues pour un spectre de von Kármán modifié et la loi de décroissance en puissance «-5/3» de Kolmogorov dans la zone inertielle de turbulence. Les mesures ont été faites sur l'axe de la buse et à la distance  $x = 3780$  mm

d'environ 3 mètres une turbulence pleinement développée. L'intensité des fluctuations de vitesses formées est une fonction de la vitesse moyenne du jet  $U_{jet}$  à la sortie de la buse, vitesse qui varie de 0 m/s jusqu'à 40 m/s. De plus, les échelles caractéristiques des fluctuations sont définies par la géométrie et les dimensions de la buse. Les mesures des fluctuations turbulentes de vitesses transversales et longitudinales sont effectuées par anémométrie à fil chaud en utilisant des sondes croisées DANTEC 55P51. La calibration de ces sondes est réalisée dans le domaine laminaire près de la buse en utilisant en complément des mesures de vitesse avec un tube de Pitot.

Le spectre des fluctuations de vitesse longitudinales mesurées à la distance  $x = 3780$  mm de la buse correspond aux estimations théoriques obtenues avec un spectre de von Kármán modifié (figure C 3). Le spectre de von Kármán modifié se caractérise par une échelle externe  $L_0$  et une échelle interne  $l_0$  des fluctuations, les valeurs desquelles peuvent être définies par la comparaison de la forme analytique du spectre avec celle de l'expérience, soient :  $L_0 \approx 0.2$  m,  $l_0 \approx 1.7$  mm. De plus, à partir du spectre unidimensionnel des fluctuations de vitesse longitudinale du jet turbulent il est possible d'estimer l'échelle intégrale longitudinale des fluctuations de vitesse, qui dans notre cas est égale à :  $L_f = L_{11}^{(1)} = \pi E(k=0)/(u_{rms})^2 \in [150, 170]$  mm ; on notera que cette valeur coïncide avec l'échelle intégrale déterminée par l'intégration de la fonction de corrélation mesurée :  $L_f = 2L_g \in [166, 182]$  mm, où  $L_f$  et  $L_g$  sont respectivement les longueurs de corrélation longitudinale et transversale.

Les paramètres définissant l'intensité des fluctuations de la vitesse sont leurs moyennes quadratiques  $u_{rms}$  et  $v_{rms}$ . Dans le plan où s'effectueront des mesures acoustiques, les quantités

$u_{rms}$  et  $v_{rms}$ , en fonction de la vitesse moyenne du jet en sortie de la buse, se modifient selon la loi suivante établie empiriquement :  $u_{rms} = 0.23U_{mean} \approx 0.115U_{jet}$  et  $v_{rms} = 0.19U_{mean} \approx 0.095U_{jet}$  de 0 m/s jusqu'à 4.6 m/s, où  $U_{mean}$  est la vitesse moyenne du jet dans le plan indiqué. On notera que ces valeurs sont conformes aux travaux de E. Gutmar et I. Wygnanski, sur le jet plan turbulent ([98]).

Dans le **paragraphe §2.2** nous décrivons le dispositif expérimental utilisé pour la génération des ondes acoustiques en  $N$  de durée courte (30  $\mu$ s) et de grande amplitude (1000 Pa), ainsi que la méthode de mesure après traversée de la couche turbulente. Pour la formation des impulsions acoustiques on utilise la source à étincelles constitués de deux électrodes de tungstène. L'enregistrement digital des signaux de pression acoustique est réalisé à partir de quatre microphones *Bruël&Kjær* 1/8" à large bande et alimentés par un amplificateur *Bruël&Kjær* dont la bande passante a été augmentée jusqu'à 200 kHz. Pour chaque distance de propagation et pour chaque vitesse axiale du jet, nous avons utilisé 2000 « claquements » d'étincelle afin d'obtenir un nombre assez grand d'onde en  $N$  indispensable pour effectuer une analyse statistique rigoureuse. Nous nous sommes intéressés en particulier aux valeurs moyennes, et aux densités de probabilités des différentes grandeurs caractérisant l'onde en  $N$ . Les résultats de mesure sont présentés sous la forme des signatures temporelles caractéristiques et des distributions de probabilité du maximum de pression du choc avant, du temps de montée et de la durée de l'onde (§2.2, §2.3).

Sur la figure C 4a, les valeurs moyennées du pic positif de la pression  $p_+$  sont présentées en fonction de la vitesse axiale du jet  $U_{jet}$  mesurée en sortie de la buse. Les points noirs représentent les valeurs instantanées (2000 impulsions à chaque vitesse du jet). L'onde acoustique est mesurée à une distance de 2.19 m de la source avec une distance de traversée dans le milieu turbulent de 1.4 m. Une très forte dispersion de la pression du pic peut être observée en présence de la turbulence. On remarque également qu'il est possible d'obtenir des maxima de la pression qui sont 3 à 4 fois plus grand que le niveau mesuré en absence de la turbulence (même à la distance maximale 2.19 m), ainsi que des valeurs très faibles. Avec la croissance de la vitesse du jet  $U_{jet}$  l'intensité des fluctuations turbulentes de vitesse se renforce, ce qui entraîne une réduction de la valeur moyenne du maximum du pic de pression. Par exemple, pour l'atmosphère homogène  $\langle p_+ \rangle = 30.9$  Pa, mais à  $U_{jet}=40$  m/s la valeur moyenne devient  $\langle p_+ \rangle = 22$  Pa. Sur la figure C 4b les distributions de la densité de probabilité des valeurs du pic positif de la pression sont présentées en fonction de la vitesse axiale du jet. La distribution à  $U_{jet} = 0$  m/s (le milieu homogène) a une largeur limitée, due à une petite différence de trajet acoustique entre la source

et des différents microphones, ainsi qu'aux fluctuations inhérentes au procédé de génération de l'onde acoustique par claquement d'une source à l'étincelle. En présence de la turbulence, les distributions de l'amplitude du maximum du pic de pression s'élargissent considérablement, et leurs formes ressemblent à une cloche asymétrique avec des valeurs significatives vers les grandes amplitudes. La valeur maximale de la distribution se déplace vers les petites amplitudes avec l'augmentation de  $U_{jet}$ , ce qui correspond à la diminution de la valeur moyenne de la pression acoustique du pic  $\langle p_+ \rangle$ . Simultanément avec l'augmentation de l'intensité des fluctuations turbulentes, l'écart type de la pression du pic positif augmente d'une valeur de 2.7 Pa jusqu'à une valeur de 11.9 Pa (obtenue pour  $U_{jet} = 30$  m/s); après avoir passé cette valeur  $U_{jet} = 30$  m/s, l'écart type diminue lentement.

Des tendances similaires sont obtenues pour le temps de montée, défini comme le temps nécessaire pour que l'amplitude du choc avant passe d'une valeur de  $0.1 \langle p_+ \rangle$  à  $0.9 \langle p_+ \rangle$ . En présence du champ turbulent le temps de montée varie considérablement. Avec l'augmentation de la valeur efficace des fluctuations de vitesse turbulentes, la moyenne du temps de montée passe de  $3 \mu s$  pour le milieu homogène jusqu'à  $10.5 \mu s$  pour le milieu inhomogène. Cependant, la valeur inférieure des fluctuations ne descend pas en dessous de  $3 \mu s$ , ce qui peut sans doute s'expliquer par la limite en haute fréquence des microphones utilisés.

Pour le temps d'arrivée de l'onde en  $N$ , qui se propage dans le milieu turbulent, on observe, qu'avec l'augmentation de l'intensité des fluctuations turbulentes, l'onde acoustique

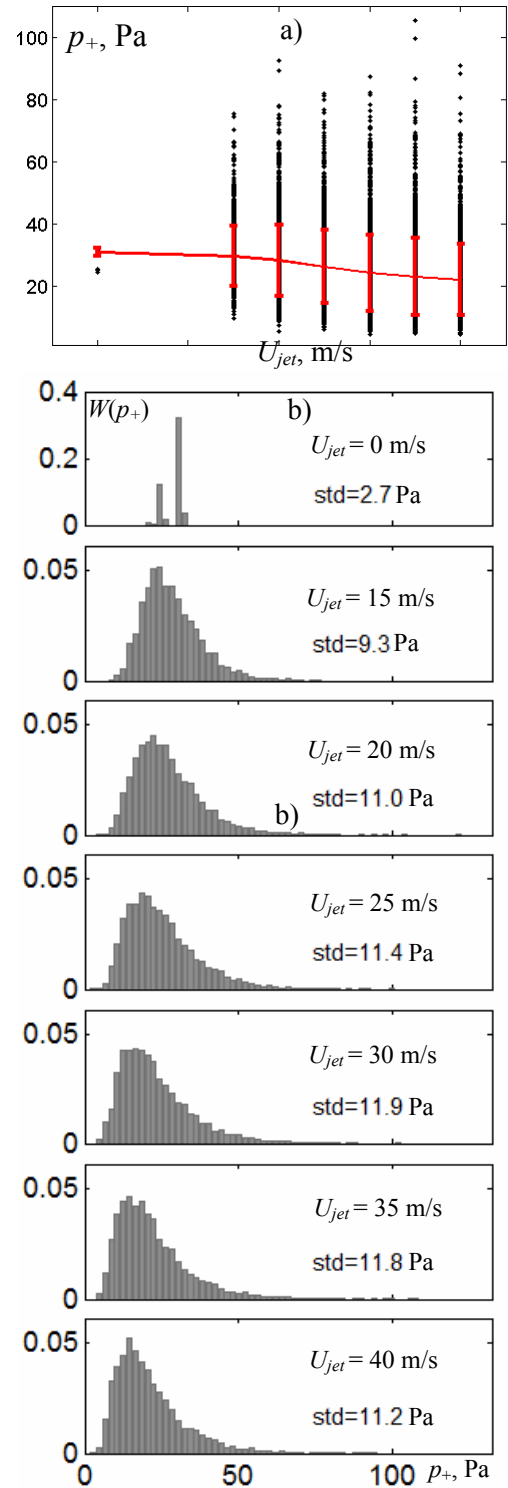


**Fig. C4** Evolution du pic positif de la pression  $p_+$ , à une distance de 2,19m de la source, avec la vitesse axiale du jet  $U_{jet}$  : (a) valeurs moyennes et (b) distributions de la densité de probabilité

arrive plus tôt. Cet effet est conforme au principe de Fermat. Ainsi, dans le milieu hétérogène lorsque  $U_{jet} = 40$  m/s, l'onde acoustique arrive sur le microphone en moyenne  $26 \mu\text{s}$  plus tôt que dans le milieu homogène.

L'influence de la distance de propagation dans le milieu turbulent pour deux vitesses moyenne du jet ( $U_{jet} = 20$  m/s,  $U_{jet} = 40$  m/s) sur les caractéristiques de l'onde acoustique en  $N$  est aussi analysée.

Dans le **paragraphe §2.4** nous comparons les caractéristiques du jet plan turbulent ainsi que celles de l'onde de choc produite avec le système à étincelles utilisée dans notre expérience en soufflerie anéchoïde avec les données d'expériences réalisées « in situ » pour l'étude de la propagation du bang sonique dans l'atmosphère. Cela nous permet de vérifier que la transposition d'échelles est acceptable. Au **paragraphe §2.5** sont présentées les conclusions du 2<sup>ème</sup> chapitre du travail de thèse.

Le **troisième chapitre** de la thèse est consacré à la mise au point d'une méthode de calibration du dispositif de mesure d'une impulsion acoustique de très courte durée, telle que celle émise par la source à étincelles, et à la caractérisation de la réponse en fréquence du système de mesure. L'analyse menée dans ce chapitre repose en partie sur une simulation numérique de la propagation non linéaire des ondes en  $N$  dans un milieu homogène en prenant compte sur les effets de relaxation.

Le **paragraphe §3.1** présente pour une onde en  $N$  les résultats des mesures du maximum du pic positif de pression, du temps de montée du front de choc avant, de la durée et du temps d'arrivée de l'onde acoustique qui se propage dans un milieu homogène avec relaxation. Les mesures ont été faites en variant la distance de propagation de 15 cm jusqu'à 2 m de la source à étincelle, et en utilisant 100 étincelles pour définir les valeurs moyennes. Comme le profil temporel de l'onde acoustique mesurée est proche d'une forme idéale d'onde en  $N$ , nous proposons de définir sa durée à partir de la position des minima de pression dans le spectre ainsi que nous le faisons dans le cas des simulations numériques (voir §3.2). Cette définition de la durée de l'impulsion à partir des minima du spectre, possède une série des avantages en comparaison avec la définition standard dans le domaine temporel. En effet les petites perturbations du profil de l'onde en  $N$  introduites par le système de mesure ne modifient pas les positions des zéros dans son spectre, puisque ces perturbations peuvent être représentées dans le domaine fréquentiel comme la multiplication du spectre idéal de l'onde par une fonction de transfert.

Dans le **paragraphe §3.2**, nous explicitons la modélisation numérique de l'équation modifiée de Burgers, que nous utilisons pour effectuer l'analyse théorique de la propagation des

ondes en  $N$  sphériques de forte amplitude dans un milieu homogène avec prise en compte des effets de relaxation. L'équation d'évolution de la pression acoustique se met sous la forme :

$$\frac{\partial p}{\partial r} + \frac{p}{r} = -\frac{\beta}{\rho_0 c_0^3} p \frac{\partial p}{\partial \tau} + \frac{b}{2\rho_0 c_0^3} \frac{\partial^2 p}{\partial \tau^2} + \sum_{v=1}^M d_v \frac{\partial}{\partial \tau} \int_{-\infty}^{\tau} \exp(-(\tau - \tau')/\tau_v) \frac{\partial p}{\partial \tau'} d\tau'. \quad (4)$$

Ici  $p$  est la pression acoustique,  $r$  est la coordonnée radiale,  $\tau = t - (r-r_0)/c_0$  est le temps retardé,  $c_0$  est la vitesse du son de référence,  $r_0$  est la distance de la source à laquelle les conditions initiales sont connues,  $\rho_0$  est la densité de l'air,  $\beta$  est le coefficient de non linéarité de l'air,  $b$  est le coefficient de la viscosité,  $M$  est le nombre total des processus de relaxation retenus. Chaque  $v^{\text{ème}}$  processus de relaxation peut être caractérisé par deux paramètres : d'une part le temps de relaxation  $\tau_v$  et d'autre part le coefficient  $d_v = (c_\infty^v - c_0)/c_0^2 = c_v/c_0^2$ , où  $c_\infty^v$  est définie comme une vitesse du son limite correspondant à la propagation du signal acoustique dans un milieu pour lequel le temps de relaxation du milieu  $\tau_v$  est bien plus grand que la durée caractéristique du signal acoustique  $T_s \ll \tau_v$  (i.e. hypothèse d'un milieu gelé).

L'équation (4) est résolue numériquement dans le domaine temporel en utilisant une décomposition des opérateurs différentiels en fonction des phénomènes physiques qu'ils prennent en compte (effet non linéaire, dissipation, relaxation moléculaire) ; une telle approche permet d'utiliser pour chacun des opérateurs différentiels le schéma numérique le plus adapté à une résolution performante. De plus il est alors possible d'obtenir non seulement la solution de l'équation (4) complète, mais aussi des solutions partielles de cette équation avec n'importe quel effet physique au choix. Cela donne la possibilité d'estimer l'influence relative des effets non linéaire et dissipatif, ainsi que l'effet de la relaxation sur l'amplitude et la durée de l'impulsion acoustique propagée. Les comparaisons que nous avons effectuées montrent que l'amplitude de l'onde dépend de tous les effets indiqués ci-dessus, mais, que dans le même temps, sa durée est définie uniquement par les effets non linéaires.

De cette façon, la durée de l'impulsion acoustique dans les conditions de l'expérience de laboratoire peut être définie à partir des relations de la théorie des chocs faibles, et ceci permet donc de calibrer la source à étincelles qui produit l'onde en  $N$  en utilisant la durée du signal calculée avec prise en compte des effets non-linéaires (Equation 3.13 §3.3) soit :

$$T = T_0 \sqrt{1 + \frac{\beta}{\rho_0 c_0^3} \frac{p_0}{T_0} r_0 \ln\left(\frac{r}{r_0}\right)}$$

En utilisant une méthode des moindres carrés pour analyser les résultats expérimentaux, les valeurs suivantes de l'amplitude et de la durée du profil d'onde en  $N$  à la distance 15 cm de la

source ont été obtenues :  $T = 28.64 \mu\text{s}$ ,  $p_0 = 1148 \text{ Pa}$ , et ceci avec un coefficient de corrélation  $R = 0.975$ .

**Dans le paragraphe §3.4**, sur la base des données obtenues par simulation numérique effectuée dans les conditions physiques de l'expérience, nous avons obtenue la réponse dans le domaine fréquentielle du système de mesure. Cette caractéristique est calculée en faisant le rapport entre le spectre des impulsions modélisées et le spectre mesuré avec l'un des microphones *Bruël&Kjær* 1/8". On observe alors que l'amplitude de ce rapport est très proche de la réponse en fréquence du microphone fournie par le constructeur sur la bande fréquentielle allant de 0 à 140 kHz.

La comparaison des profils des ondes, mesurées expérimentalement aux diverses distances de la source, avec ceux, calculés en appliquant le filtre obtenu en fréquence, a montrée un bon accord pour tous les paramètres caractéristiques : l'amplitude, la durée et le temps de montée du choc (§3.5). De cette façon, il est obtenu, que le temps de montée du choc minimal dans l'expérience de laboratoire soit défini par la bande limitée fréquentielle du système de mesure et égal environ à  $\sim 2.5\text{-}3 \mu\text{s}$ . **Le paragraphe §3.6** résume les résultats principaux et les conclusions de ce chapitre trois du travail de thèse.

**Le chapitre quatre** du travail de thèse est consacré dans une première partie au développement d'une équation d'évolution non linéaire décrivant la propagation des signaux acoustiques dans les milieux hétérogènes tridimensionnels et en mouvement, en tenant compte de la composante transversale de la vitesse de milieu par rapport à la direction de propagation de l'onde. Dans la deuxième partie de ce chapitre, l'algorithme numérique que nous avons développé, qui permet de décrire précisément la propagation des fronts de choc dans les milieux hétérogènes, est présenté.

**Dans le paragraphe §4.1** l'équation parabolique modifiée de type Khokhlov-Zabolotskaya-Kuznetsov est obtenue en précisant les hypothèses nécessaires à sa dérivation. Cette équation prend en considération les effets non linéaires et diffractifs, les effets de l'absorption thermo visqueuse, et les effets liés à la présence des hétérogénéités scalaires et vectorielles de milieu. Elle s'écrit sous la forme :

$$\frac{\partial}{\partial \tau} \left[ \frac{\partial p}{\partial x} - \frac{\beta}{c_0^3 \rho_0} p \frac{\partial p}{\partial \tau} - \frac{\Delta c + u_x}{c_0^2} \cdot \frac{\partial p}{\partial \tau} + \frac{1}{c_0} (\mathbf{u}_\perp \cdot \nabla_\perp p) - \frac{p}{2\rho} \frac{\partial \rho}{\partial x} - \delta \frac{\partial^2 p}{\partial \tau^2} \right] = \frac{c_0}{2} \Delta_\perp p \quad (5)$$

où  $x$  est la direction de propagation de l'onde,  $c$  et  $\rho$  sont respectivement la vitesse du son et la densité du milieu ambiant,  $u_x$  est la composante longitudinale de vitesse et  $\mathbf{u}_\perp = (u_y, u_z)$  sont les composantes transversales des fluctuations de vitesse du milieu,  $\Delta c = c - c_0$  est l'écart de vitesse du son dans le milieu due aux inhomogénéités scalaires,  $\delta = b/(2\rho_0 c_0^3)$  est le coefficient

d'absorption thermo visqueuse du son. S'il est nécessaire de prendre en considération les effets de relaxation ou d'autres pertes dissipatives, le terme, décrivant l'absorption  $\delta \partial^2 p / \partial \tau^2$ , peut être remplacé par un opérateur linéaire de type général  $L(p)$ . A notre connaissance, l'équation (5) n'a jusqu'à présent jamais été utilisée dans la littérature. Ici, un nouveau terme a été incorporé, qui prend en considération les composantes du mouvement du milieu perpendiculaires à la direction de propagation de l'onde acoustique.

En dérivant cette équation, nous avons considéré que les fluctuations des caractéristiques du milieu varient lentement dans l'espace et dans le temps, et que les fluctuations de la vitesse du son et la vitesse du milieu sont petites en comparaison avec la vitesse du son. En outre, nous faisons l'hypothèse classique que l'approche parabolique de la théorie de la diffraction peut être considérée comme une bonne modélisation de la propagation du son dans les directions angulaires pas plus grandes que  $\pm 20^\circ$  autour de l'axe de propagation, et qu'elle assure l'exactitude des solutions obtenues seulement pour les faisceaux bornés en négligeant les effets de rétrodiffusion.

Ensuite dans le travail de thèse une formulation adimensionnelle de l'équation (5) est écrite dans un système de coordonnées cartésiennes pour une onde acoustique se propageant dans un milieu inhomogène bidimensionnel de type uniquement vectoriel, c'est-à-dire à  $\Delta c, \Delta \rho = 0$ . Nous montrons dans le **paragraphe §4.2**, que cette équation d'évolution ainsi écrite, possède les propriétés d'autosimilarité. Il est alors possible d'exprimer la solution de cette équation d'évolution pour certains types de mouvement moyen du milieu inhomogène sous réserve que l'on connaisse une solution numérique pour un milieu inhomogène équivalent ayant des fluctuations similaires.

**Dans le paragraphe §4.3** nous détaillons les deux catégories de méthodes numériques, temporelle ou spectrale, que nous avons mis en œuvre dans nos simulations numériques, le choix de la méthode de résolution étant adapté à la nature du signal acoustique initial. L'approche spectrale de la modélisation convient plus particulièrement pour la description de propagation des signaux périodiques (par exemple, au diagnostic et à la chirurgie ultrasonore), et l'approche temporelle est plus adaptée à la modélisation de la propagation des signaux courts de type impulsion (par exemple le bang sonique dans l'atmosphère et l'océan). Comme nous l'avons fait précédemment, et pour chacune de ces deux approches la méthode numérique de résolution repose sur une décomposition des opérateurs différentiels en fonction des phénomènes physiques qu'ils prennent en compte ce qui permet d'utiliser pour chaque terme le schéma numérique le plus adapté à une résolution performante.

Pour étudier la propagation des ondes périodiques, la condition initiale est mise sous la forme d'un signal sinusoïdal et la solution de l'équation (5) est obtenue comme une série de Fourier. Après substitution de la forme générale de la solution dans l'équation d'évolution (5) on obtient le système non linéaire couplé des équations pour les amplitudes des harmoniques  $C_n$  de l'onde initiale. Les équations obtenues sont résolues pour chacune des harmoniques. Pour la première étape de l'algorithme numérique nous intégrons l'opérateur de diffraction avec un schéma de type Crank - Nicholson. À la deuxième étape, les effets non linéaires sont pris en considération : pour chaque nœud de la maille numérique selon la coordonnée transversale (par rapport à la direction d'avancement), le système non linéaire des équations couplées pour les harmoniques est résolu en utilisant une méthode Runge-Kutta du quatrième ordre. À la troisième étape, nous utilisons la solution exacte qui prend en compte l'influence de l'absorption thermo visqueuse et de la relaxation, ainsi celle de la composante longitudinale des fluctuations de la vitesse du milieu (i.e. dans la direction de propagation de l'onde acoustique). À la quatrième et dernière étape, pour prendre en compte les fluctuations transversales de la vitesse du milieu, le schéma de Lax – Wendroff est utilisé. Des simulations numériques sont alors effectuées pour la propagation de l'onde acoustique dans un milieu caractérisé par les paramètres adimensionnels de non linéarité égal à  $N = 2\pi\beta p_0 / c_0^2 \rho_0 = \lambda / x_s = 0.05$  et d'absorption égal à  $A = (2\pi)^2 c_0^2 \delta / \lambda = \lambda / x_d = 0.002$  où  $x_s$  et  $x_d$  sont les distances caractéristiques respectivement des effets non linéaires et des effets de dissipation thermo visqueuse. Dans ces simulations, le pas de la maille numérique selon la coordonnée le long de l'axe du faisceau est  $h_x / \lambda = 2.5 \cdot 10^{-2}$  et le pas selon la coordonnée transversale est  $h_y / \lambda = 2.0 \cdot 10^{-2}$ . Les calculs sont réalisés avec  $N_{\max} = 150$  harmoniques.

Pour étudier la propagation des signaux de type d'impulsion, nous utilisons un profil initial sous la forme d'une onde en  $N$  définie comme la solution stationnaire de l'équation de Burgers, avec prise en compte des effets non linéaires et dissipatifs, qui s'écrit sous la forme :

$$V = \frac{\theta}{2\pi} \left[ \tanh\left(\frac{N}{4A}(\theta - \pi)\right) - \tanh\left(\frac{N}{4A}(\theta + \pi)\right) \right] \quad (6)$$

où  $V=p/p_0$  est l'amplitude adimensionnelle de la pression,  $\theta=2\pi\tau / T_0$  - le temps adimensionnel,  $p_0$  et  $T_0$  sont respectivement les valeurs caractéristiques de l'amplitude de la pression et de la durée de l'impulsion. L'épaisseur du front (le temps de montée) d'une telle onde est de l'ordre de grandeur de  $10A/N$ . Dans les conditions de notre expérience en laboratoire  $A \sim 1.5 \cdot 10^{-4}$  et  $N=0.05$ , ainsi l'épaisseur du front est égale à  $10A/N=0.025$ , soit seulement 0.4% de la durée de l'impulsion. Pour ce qui concerne la modélisation numérique nous sommes donc obligé de

prendre un grand nombre de points par maille pour avoir un maximum de précision sur la prédiction de l'évolution du front de choc ; cela a pour conséquence une forte augmentation du temps de calcul nécessaire à l'intégration de l'équation (5). Pour la construction d'un schéma numérique optimal, tant du point de vue de l'exactitude de la solution, que de l'efficacité de l'algorithme en temps de calcul, la comparaison de différents schémas numériques prenant en compte les effets non linéaires et les effets liés à la convection dans la direction longitudinale a été faite. Le modèle finalement retenu est décrit ci-dessous.

À la première étape de l'algorithme numérique les effets de diffraction sont pris en compte dans les calculs sur la base de l'algorithme de Crank - Nicholson du deuxième ordre selon les coordonnées spatiales. Le résultat, obtenu à cette première étape, est utilisé ensuite à titre de condition initiale pour les calculs des effets non linéaires à chaque nœud du maillage du domaine de calcul numérique. Pour cela un schéma conservatif de type de Godunov du deuxième ordre en temps et le premier ordre selon la coordonnée de la propagation est adopté. À la troisième étape, trois effets physiques sont pris en compte à la fois : la convection en direction de propagation de l'onde, l'absorption thermo visqueuse et les effets de relaxation. Pour cela le schéma numérique est construit dans le domaine spectral sur la base de la solution exacte obtenue pour les amplitudes complexes des harmoniques. À la dernière étape de l'itération, sur la base d'un schéma numérique de Lax - Wendroff du deuxième ordre, la convection dans la direction, transversal à la propagation de l'onde est finalement prise en compte. L'avantage de l'algorithme présenté ici est de permettre le calcul en utilisant seulement 2 à 3 nœuds de maillage sur le front de choc en ayant une diffusion numérique très faible. L'algorithme développé donne une bonne résolution de la structure du front de l'onde de choc sans pratiquement augmenter le temps du calcul.

Pour nos simulations numériques du champ acoustique, nous utilisons les valeurs suivantes des coefficients de non linéarité et de l'absorption  $N = 0.05$  et  $A = 0.00034$ . Les pas spatiaux du maillage du calcul ont été choisis conformément à la condition de stabilité d'algorithme et pour avoir une résolution précise des structures à petite échelle du champ acoustique (pas moins que 10 points sur la plus petite échelle) soient :  $h_x / \lambda = 2.5 \cdot 10^{-2}$  et  $h_y / \lambda = 2 \cdot 10^{-2}$ . Le nombre de points de discrétisation du profil de l'onde en temps est  $n=1024$  ; il est très largement surestimé ce qui permet de garantir la prédiction du temps de montée du choc d'onde même dans la région de focalisation. Pour confirmer ces choix, nous avons diminué d'un facteur deux les pas numériques d'intégration indiqués, et nous avons vérifié que la nouvelle solution donnait un écart qui reste inférieur à 3%. Les détails sur la sélection des pas de maillage pour l'algorithme numérique obtenu sont donnés dans l'annexe B. La bonne précision

de l'algorithme numérique et la validité du modèle parabolique développés ont également été confirmées par des calculs de tests concernant la propagation d'onde à travers des homogénéités simples ; nous avons également comparé nos résultats avec des résultats existants, obtenus à partir de calculs avec une équation parabolique à grand angle (§4.4). Dans le paragraphe §4.5 les résultats principaux et les conclusions générales selon le chapitre quatre du travail de thèse sont décrit.

Le cinquième chapitre du mémoire de thèse est consacré à l'analyse des calculs numériques, notamment à l'étude de la propagation des signaux non linéaires acoustiques dans les milieux aléatoires inhomogènes en mouvement. La propagation d'ondes acoustiques périodiques (§5.1), ainsi que la propagation d'impulsions acoustiques prenant la forme d'une onde en  $N$  (§5.2) sont envisagées. L'influence relative des effets non linéaires et des effets de diffraction sur la

structure spatiale du champ acoustique propagé et sur l'occurrence de caustiques aléatoires est étudiée en détail à partir des résultats des simulations numériques fournis pour les valeurs de pic et les valeurs moyennes, ainsi que pour les distributions statistiques des paramètres caractéristiques de l'onde acoustique (temps de montée, maximum de pression, durée, etc...). L'influence de la taille des échelles caractéristiques et de l'intensité des fluctuations aléatoires du milieu hétérogène en mouvement, ainsi que l'influence de la composante transversale des fluctuations du champ de vitesse sont analysées sur l'exemple d'un champ aléatoire hétérogène de vitesse correspondant à une distribution gaussienne de l'énergie cinétique (une illustration de la répartition des fluctuations est donnée sur la figure C 1).

La distribution spatiale du maximum du pic positif de pression de l'onde en  $N$ , qui se propagent à travers le milieu turbulent, est présentée sur la figure C.5a avec en fond les lignes iso-niveaux des fluctuations de vitesse du milieu. On note qu'à cause de la présence de

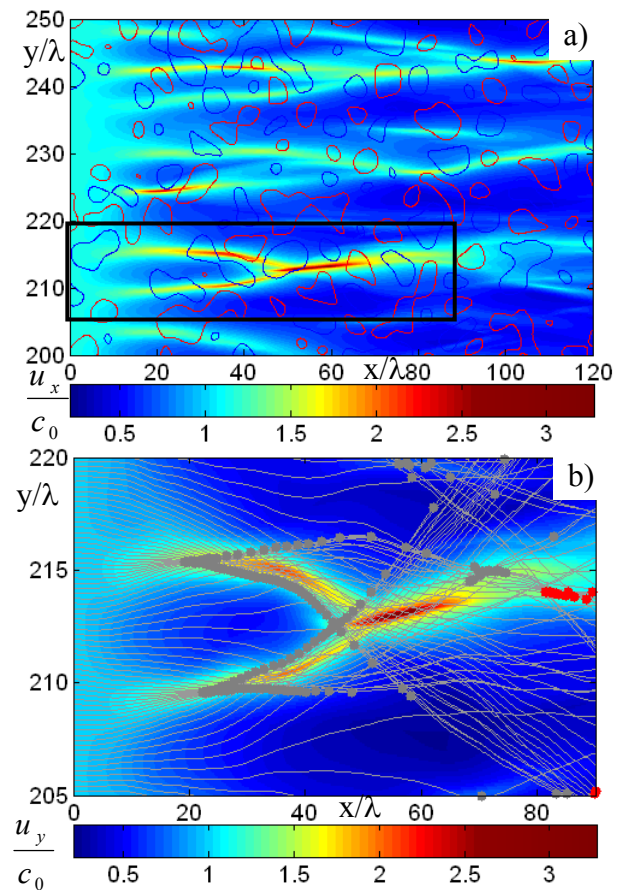


**Fig. C5** a) Distribution du champ acoustique (pression du pic positif) avec les iso-niveaux des fluctuations de la vitesse du milieu  $u_{||} / c_0 = \pm 0.009$  marqués par dessus, b) zoom sur la région focale (le rectangle noir sur fig.5a) avec en plus la distribution des trajectoires des rayons acoustique et les positions des caustiques.

l'inhomogénéité, l'énergie de l'onde acoustique est redistribuée dans l'espace, créant plusieurs régions où la pression est soit augmentée soit diminuée. Et on observe que les régions de pression augmentée se forment juste après le passage par l'onde des secteurs du milieu hétérogène où la vitesse effective du son  $c_0+u_x$  est plus faible que celle du milieu ambiant  $c_0$ . De plus, malgré une forte absorption non linéaire de l'énergie acoustique, la pression du pic positive dans les zones de focalisation peut excéder jusqu'à trois fois l'amplitude de l'impulsion initiale. Les zones de focalisation aléatoires se forment en général à des distances relativement courtes de la source,  $x/\lambda < 60$  ( $x_s/\lambda = 20$ ). Néanmoins, il est quand même toujours possible d'observer des zones de focalisation assez intensive à grandes distances (voir  $x/\lambda = 110$ ).

Sur la figure C 5b un zoom de la région de focalisation est présenté. Cette partie correspond à la région du champ acoustique entourée par un rectangle noir sur la figure C5a. Par-dessus la cartographie de la pression du pic positif, nous avons tracé les trajectoires des rayons (les lignes grises) et les positions des caustiques (les points gris), obtenus en résolvant les équations de l'acoustique géométrique (voir annexe A). Les trajectoires des rayons mettent en évidence très distinctement la formation des caustiques, et leurs positions se trouvent qualitativement en accord avec les prédictions des régions de focalisation obtenue à partir de l'équation d'évolution non linéaire (5). Néanmoins, les positions des caustiques, calculées dans l'approche haute fréquence de l'acoustique géométrique, ne coïncident pas exactement avec les positions des niveaux maxima de la pression du champ acoustique. De plus, comme on néglige les effets de diffraction dans l'approximation haute fréquence, certaines caustiques, (données par l'acoustique géométrique), se forment dans des régions, où l'amplitude de la pression acoustique (calculée avec l'équation parabolique) est en réalité assez faible. Ceci met clairement en évidence que les effets de diffraction jouent un rôle très important dans la formation du champ

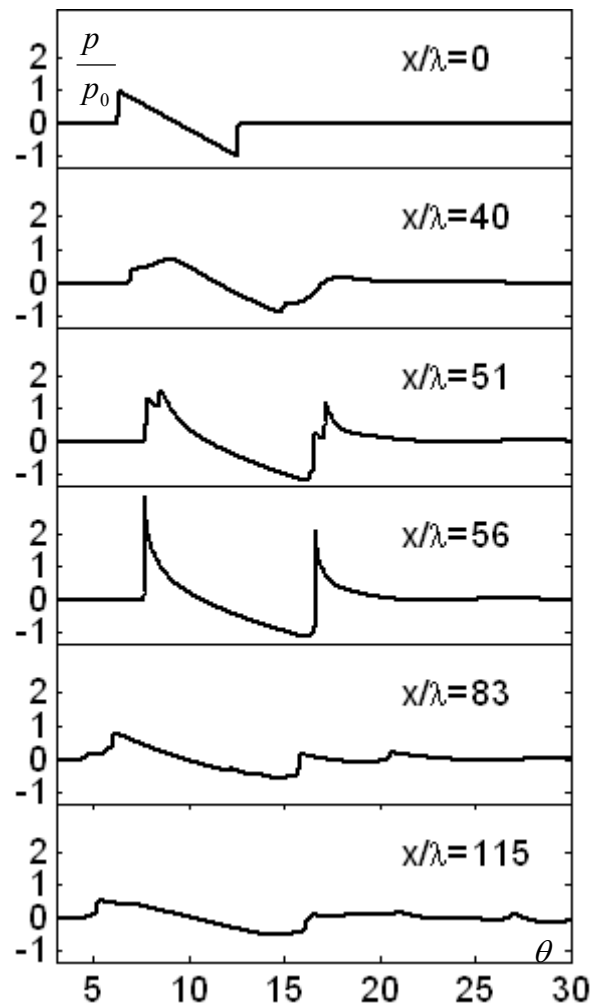


**Fig. C6** Formes temporelles d'ondes mesurées à diverses distances de la source le long de la ligne  $y/\lambda = 212$  passant par une caustique

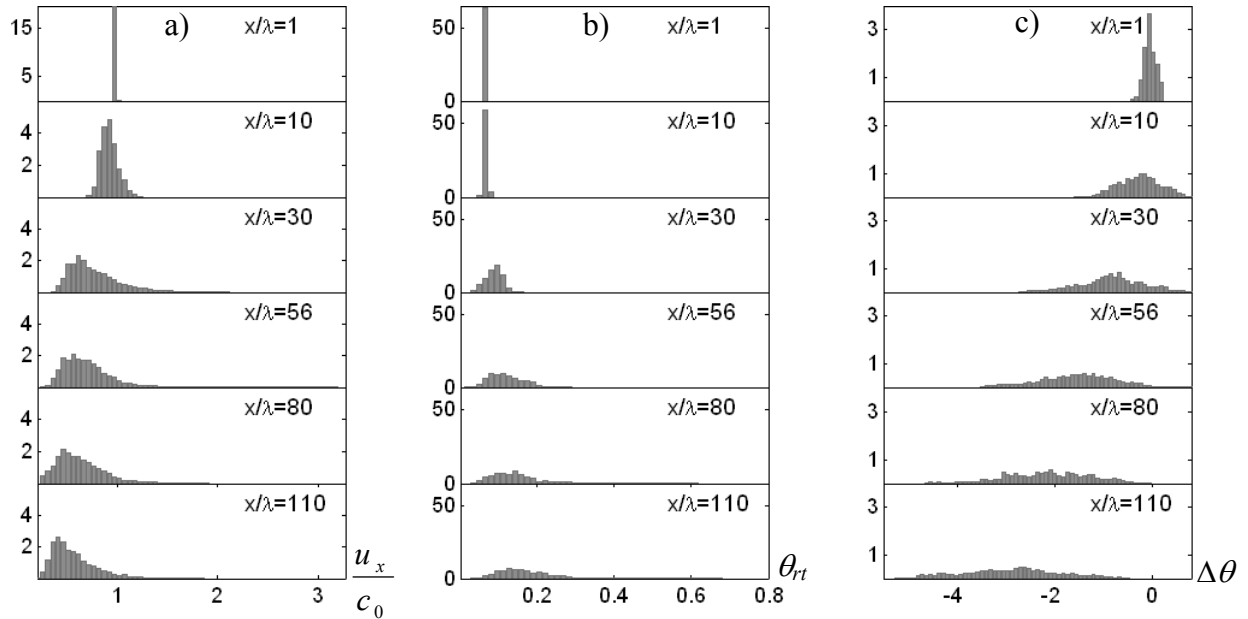


**Fig. C7** Evolutions avec la distance de propagation des distributions de la densité de probabilité de la pression du pic positif (a), du temps de montée du front de choc (b) et du temps d'arrivée relative de l'impulsion

acoustique, et il est nécessaire de les prendre en considération dans les modèles théoriques de prédiction si l'on veut obtenir des résultats réalistes.

Sur la figure C6 nous avons tracé la forme temporelle du signal de pression acoustiques au passage de l'onde en  $N$  à travers une caustique (ou région focale). Au centre de la zone de focalisation, une onde classique en  $U$  avec une grande amplitude de la pression et un front très étroit est formé ( $x/\lambda = 56$ ). Les focalisation et défocalisation aléatoires se traduisent par la formation de formes temporelles plus complexes des ondes propagées. On observe ainsi : des ondes avec une demi - arche positive arrondie ou « rounded wave » pour  $x/\lambda = 40$ , des ondes avec plusieurs fronts de choc pour  $x/\lambda = 83$  et des ondes avec de très longues « queues » pour  $x/\lambda = 115$ ). Près des zones focales, pour  $x/\lambda = 51$ , une forme d'onde avec plusieurs pics est également observée. Ceci est en accord avec le fait que les fronts d'onde se raidissent dans les régions focales où le niveau de la pression acoustique augmente, et, où par conséquent les effets non linéaires sont intensifiés. La distorsion non linéaire de l'onde se manifeste également dans les régions où la pression acoustique baisse due au scattering des harmoniques supérieurs au passage des caustiques. Finalement il faut aussi noter que l'allongement de la durée de l'impulsion avec la distance de propagation dans la turbulence, du aux grandes différences de marches des trajets acoustique qui convergent en un point, rend peu probable l'augmentation de l'amplitude de l'onde aux grandes distances de la source.

Sur la figure C7 on présente les distributions des densités de probabilité de la pression du pic positif, du temps de montée du choc et du temps d'arrivée relatif de l'onde à différentes

distances de la source. On voit, que les distributions initialement étroites, s'élargissent en augmentant la distance de la source. Ainsi, avec une distance à la source croissante, on augmente la probabilité d'observer des amplitudes plus faibles de la pression et des fronts de choc moins raides. Néanmoins pour les grandes distances de propagation, et en accord avec les observations faites dans les expériences (de laboratoire ou in situ), il existe toujours une certaine probabilité d'obtenir des niveaux de la pression du pic positif importants (3 fois plus que la valeur initiale), et des fronts très étroits (le temps de montée du front  $(\theta_{0.1-0.9})_{min} = 0.022$  est 3 fois moins court que le temps initial). La distribution de la densité de probabilité du temps d'arrivée quant à elle devient vite large, montrant l'arrivée « prématurée » de l'impulsion jusqu'à  $\theta = -5.25 = -1.67\pi$ , ce qui fait un écart de plus de 75% de la durée d'impulsion.

Des résultats analogues ont été obtenus pour la propagation de l'onde en  $N$  acoustique dans un milieu aléatoire hétérogène en mouvement avec le spectre d'énergie cinétique de von Kàrmàn modifié, qui décrit plus précisément la structure multi-échelles de la couche limite atmosphérique turbulente.

**Le paragraphe §5.3** est consacré à la comparaison des résultats expérimentaux avec les résultats des calculs effectués avec les paramètres correspondants aux conditions de l'expérience en soufflerie anéchoïde. Cette comparaison montre, que malgré la différence de géométrie (l'expérience est conduite en 3D et la modélisation numérique est réalisée en 2D), la correspondance entre la mesure et le calcul de l'amplitude d'onde est satisfaisante.

En plus d'observer une ressemblance qualitative dans la forme des distributions des densités de probabilité, nous noterons également un accord quantitatif pour les valeurs maximales du pic de pression. Ainsi, dans l'expérience comme dans les simulations numériques, la pression maximale acoustique mesurée dans le milieu turbulent est jusqu'à 4 fois plus grande que la pression mesurée dans le milieu homogène ; la diminution de pression moyenne en fonction de la vitesse du jet est égal 27% dans l'expérience pour 22% dans les simulations ; et la variation de pression du pic dans l'expérience correspond à celle obtenue dans les simulations (la différence n'excédant pas 7%). Nous avons montré de plus, que la probabilité d'observer un niveau de pression acoustique maximal dans le milieu turbulent deux fois plus grand que la pression maximale du pic mesurée dans le milieu homogène est égale à 2%, ce qui n'est pas négligeable pour les problèmes de nuisances sonores.

**Dans paragraphe §5.4**, les résultats principaux et les conclusions du chapitre cinq du travail de thèse sont présentés.

**L'Appendice A** est consacrée à la mise en forme des formules principales de l'acoustique géométrique, qui ont été utilisées pour les calculs de trajectoires des rayons et des positions des

caustiques.

L'Appendice B est consacrée à l'étude numérique des schémas mis au point pour résoudre l'équation parabolique non linéaire développée pour prendre en compte les effets de convection longitudinaux et transversaux.

## CONCLUSION

A la fin de ce travail de thèse nous pouvons résumer les principaux résultats de la façon suivante :

1. Un nouveau dispositif expérimental a été créé pour étudier dans des conditions de laboratoire la propagation des ondes en  $N$  de courte durée et de forte amplitude (la durée  $30 \mu s$ , l'amplitude  $\sim 1000$  Pa) à travers un jet d'air turbulent dont la vitesse moyenne peut varier de 0 m/s jusqu'à 20 m/s. Les mesures effectuées avec une technique d'anémométrie à fils chaud, nous a permis de caractériser la turbulence (taux de fluctuations, échelles de corrélations spatiales, spectres d'énergie). Nous avons montré également que le spectre d'énergie cinétique de la turbulence formée dans le jet plan bidimensionnel pouvait être parfaitement décrit à partir d'un modèle de von Kármán modifié.

2. Une équation parabolique non linéaire modifiée de type de Khokhlov - Zabolotskaya - Kuznetsov a été développée pour décrire la propagation de signaux acoustiques puissants dans un milieu hétérogène en mouvement. Cette équation contient un nouveau terme additionnel prenant en considération l'influence des composantes de la vitesse du milieu dans la direction transversale à la direction de propagation de l'onde acoustique. De plus, un nouvel algorithme numérique de résolution de cette équation d'évolution a été mis au point pour traiter la propagation des signaux périodiques ou celle des impulsions avec les fronts de choc étroits. En utilisant ce nouvel algorithme nous avons fait une étude assez complète des propriétés des signaux acoustiques, périodiques ou impulsions de type onde en  $N$ , se propageant dans des milieux aléatoires hétérogènes en mouvement

3. Nous avons montré, que la structure spatiale et les caractéristiques du pic de pression du champ acoustique dans le milieu aléatoire hétérogène en mouvement sont fortement influencées par les effets non linéaires et les effets de diffraction. Les limites de l'acoustique géométrique par rapport à l'approche non linéaire ont également été mises en évidence dès que

les effets de diffraction deviennent prépondérants. Pour les milieux turbulents, il est établi que les effets non linéaires amènent un changement considérable de la concentration du champ acoustique dans les régions de focalisation aléatoire et que, malgré une forte absorption de l'énergie de l'onde sur le front de choc, ils peuvent conduire à une augmentation significative de l'amplitude de la pression et à un raidissement des fronts d'onde dans les régions focaux et ceci même à des distances de propagation nettement plus grandes que la distance de formation des chocs.

4. Nous avons montré, que la structure du champ acoustique après traversée du jet turbulent est gouvernée principalement par la composante de l'inhomogénéité aléatoire vectorielle, qui est parallèle à la direction de propagation de l'onde. De plus, pour la première fois, l'influence de la composante transversale du champ aléatoire de la vitesse du milieu sur la déformation de la structure du champ acoustique a été également étudiée dans le cadre de l'approche non linéaire. Nos résultats montrent, que les fluctuations transversales amènent un changement de la structure du champ acoustique dans toutes les directions, longitudinale et transversale, et que leur influence se renforce avec l'augmentation des échelles spatiales caractéristiques du milieu turbulent.

5 Sur la base des investigations numériques et expérimentales, il est montré, que la présence du milieu turbulent amène à la réduction importante de la moyenne pression du pic positif (jusqu'à 30% à une distance 2 m de la source), à l'augmentation du temps de montée du front de choc (à 3-4 fois) et à l'arrivée plus rapide d'onde en  $N$  (en moyenne plus que 15  $\mu s$ ) en comparaison avec des mêmes paramètres de l'onde se propageant dans le milieu sans turbulence. Néanmoins, il est également établi, que dans les régions de focalisations, il est possible d'observer des impulsions acoustiques dont l'amplitude augmente de plus d'un facteur quatre et d'avoir des temps de montée du choc réduit d'un facteur trois. Pour la première fois à notre connaissance, l'influence combinée des effets non linéaires et des effets de diffractions sur la statistique du champ acoustique large bande propagé dans un milieu aléatoire et hétérogène en mouvement a été analysée. On notera que les effets non linéaires semblent diminuer les variations relatives des caractéristiques moyennes de l'onde qui se propage à travers la turbulence par rapport au cas de la propagation en milieu homogène.

6. Une nouvelle méthode expérimentale de calibrage du microphone a été proposée, argumentée et réalisée. Cette méthode est basée sur l'analyse de l'allongement non linéaire de

l'onde en  $N$  dans l'air au cours de sa propagation, qui est complétée par une simulation numérique effectuée à partir d'une équation modifiée de Burgers. Il est proposé que la durée de l'impulsion soit définie à partir de la position des minima de pression dans son spectre fréquentiel. Nous obtenons ainsi dans les conditions de l'expérience, les paramètres caractéristiques de l'onde en  $N$ ; la réduction de son amplitude dépend alors des effets non linéaires, des processus de relaxation et des effets de l'absorption thermo visqueuse, tandis que l'allongement en temps du profil de l'onde en  $N$  est relié seulement aux effets non linéaires.

A la suite de ce travail de thèse plusieurs prolongements sont possibles. D'abord, il est nécessaire de développer un code numérique tridimensionnel, qui prends en compte les effets de diffraction, de non linéarité, d'absorption thermo-visqueuse, de relaxation et qui essentiellement intègre les effets relatifs aux vents turbulents transversales. En effet, nous avons montré que la composante transversale de vitesse a déjà un rôle important pour plusieurs configurations bidimensionnelles, et cette contribution augmentera dans le cas tridimensionnel ainsi que nous l'avons observé dans les expériences. Les simulations numériques tridimensionnelles peuvent conduire à un meilleur accord entre les résultats expérimentaux et les résultats de simulation. Toutefois, pour réaliser ces simulations qui auront un coup de calcul élevé il est nécessaire d'examiner comment introduire une condition limite absorbante de type PML (Perfect Matched Layer) dans l'algorithme numérique afin de traiter de façon plus efficace le problème des réflexions parasites introduites par les frontières du domaine de calcul.

Une autre suite naturelle de ce travail de thèse est d'intégrer dans l'algorithme numérique des effets des hétérogénéités de type scalaire, notamment : les variations de densité et de température, ainsi que la stratification de l'atmosphère. Ce modèle numérique peut être alors utiliser pour l'analyse de la propagation des ondes acoustiques à longues distances. L'influence des vents transversaux et des effets de diffraction sur le champ acoustique dans des zones d'ombres acoustique peuvent être alors envisagée. Toutefois, afin de pouvoir examiner des situations réalistes de propagation il conviendra d'introduire une condition limite au sol pour prendre en compte les effets d'impédance.

Finalement il est également très intéressant de poursuivre le développement des outils numériques de traitement de signal en vue de l'amélioration de la méthode de calibration des microphones acoustique dans les milieux dissipatifs en prenant en compte les phénomènes de relaxation. D'un point de vue expérimental, il convient de réaliser une source à étincelle plus stable. Ce travail offre des perspectives intéressantes pour la mise au point d'un microphone à plus large bande (fonctionnant jusqu'à 200kHz) dans l'air.



## LIST OF FIGURES

<b>Fig. 1.1</b> Fourier modes orientation in space.....	38
<b>Fig. 1.2</b> Comparison of random velocity field distributions with Gaussian (a-c) and von Karman (e-g) energy spectra. a) and e) – longitudinal components of medium velocity fluctuations, b) and f) transverse components, c) and g) – absolute value of velocity fluctuations, d) – longitudinal and transverse correlation functions, h) – comparison of Gaussian and von Karman spectra with the Kolmogorov’s law. ....	40
<b>Fig. 2.1</b> Geometry of the experimental setup.....	44
<b>Fig. 2.2</b> Experimental setup to generate turbulent fields. 1- jet, 2- wooden baffles, 3- positioning system.....	44
<b>Fig. 2.3.</b> Photo and sketch view of the cross wire thermo anemometer.....	45
<b>Fig. 2.4</b> a) View of a Pitot tube (2) and anemometer (1) positioning in the potential cone during the calibration; b) calibration curve. Experimental data are well described by the 4 <sup>th</sup> order polynomial law. ....	46
<b>Fig. 2.5</b> 2D distribution of mean flow velocity a) in vertical XZ plane and b) in horizontal XY plane. ....	46
<b>Fig. 2.6</b> The level of turbulent interfusion in the flow a) in OZ axis and b) in OX axis. ....	47
<b>Fig. 2.7.</b> Comparison of the measured energy spectrum of turbulent fluctuations (low and high frequency parts) with the theoretical formulation of von Karman spectrum and with the «-5/3» Kolmogorov’s law for the inertial interval. Measurements were done at the distance $X = 3780$ mm from the jet at the axis of the turbulent flow.....	48
<b>Fig. 2.8</b> Distributions of mean flow velocity $U_{mean} / U_{jet}$ a); root mean square values of turbulent fluctuations $u_{rms} / U_{mean}$ b); and $v_{rms} / U_{mean}$ c) in the plane of acoustic measurements at $X = 3780$ mm from the jet at $U_{jet} = 40$ M/c. Contour lines show the areas of fully developed turbulence (levels of interfusion are $u_{rms} / U_{mean} < 0.28$ and $v_{rms} / U_{mean} < 0.24$ ). ....	49
<b>Fig. 2.9.</b> Dependence of the root mean square and mean medium velocities on flow velocity at the exit of the jet.....	50

<b>Fig. 2.10</b> Spatial spectra of $u$ (left) and $v$ (right) components of medium velocity fluctuations in different points of the acoustic measurement plane.....	51
<b>Fig. 2.11</b> View of the experimental setup for measuring the correlation function. 1 and 2 are the positioning systems, 3 are the mounted cross-wire probes.....	52
<b>Fig. 2.12</b> Correlation functions of the turbulent velocity field.....	52
<b>Fig. 2.13</b> Sketch of the experimental setup. Top view. All distances are given in millimeters....	53
<b>Fig. 2.14</b> Signals, measured by microphones and by antenna in homogeneous air (a) and when the air turbine was switched on (b). .....	55
<b>Fig. 2.15</b> Typical waveform a) and its spectrum b) measured at the distance 210 mm from the spark source in homogeneous air; the derivative of the time profile c); waveforms, measured with different microphones for the same spark at the distance 690 mm from the source d).....	56
<b>Fig. 2.16</b> Typical waveforms measured at different distances from the source in homogeneous air. ....	57
<b>Fig. 2.17</b> Typical waveforms measured at the distance 2.19 m from the source after passing the turbulent layer. $U_{jet} = 30$ m/s.....	58
<b>Fig. 2.18.</b> Waveforms measured by 4 microphones in the vicinity of the focusing zone at the distance 2.19 m from the source. $U_{jet} = 20$ m/s.....	59
<b>Fig. 2.19</b> Mean distributions (red lines) of peak positive pressure a), rise time of the wave front b), and wave front arrival time c) depending on the flow velocity at the exit of the jet $U_{jet}$ (turbulence intensity) at the distance of 2.19 m from the source. Black points – data of individual measurements. Vertical red segments are the standard deviations of each parameter. ....	60
<b>Fig. 2.20</b> Probability density distributions of shock wave peak positive pressure $p_+$ at the distance 2.19 m from the source for various flow velocities $U_{jet}$ at the exit of the jet. <b>std</b> – standard deviation abbreviation. Width of the class is 2 Pa.....	62
<b>Fig. 2.21</b> Probability density distributions of shock wave rise time $t_{0.1-0.9}$ at the distance 2.19 m from the source for various flow velocities $U_{jet}$ at the exit of the jet. <b>std</b> – standard deviation abbreviation. Width of the class is 0.5 $\mu$ s.....	62
<b>Fig. 2.22</b> Distributions of peak positive pressure (a), rise time (b) and arrival time (c) of the shock wave, measured at distance 2.19 m from the spark source during its cold start. $N$ is the spark consecutive number. ....	65
<b>Fig. 2.23</b> Dependence of mean peak positive pressure (a) and mean rise time of the wave shock front (b) on the distance of acoustic wave propagation in inhomogeneous turbulent medium of different intensity. ....	66
<b>Fig. 2.24</b> Dependence of standard deviation of peak positive pressure (a) and rise time of the wave shock front (b) on the distance of the acoustic wave propagation in inhomogeneous turbulent medium of different intensity. ....	66

- Fig. 3.1** Dependence of mean acoustic wave parameters (tension pulse parameters) on the distance between the source and the microphone. (a) – mean peak positive pressure, (b) – mean half duration, (c) – mean shock front rise time, (d) – mean relative arrival time. Points – measured parameters of individual pulses. .... 73
- Fig. 3.2.** Initial  $N$ -pulse waveform (a) and its spectrum (b). Dependence of the sound speed (c) and absorption (d) on frequency due to relaxation in atmosphere. Characteristic relaxation frequencies of oxygen  $O_2$  and nitrogen  $N_2$  are shown with vertical dotted lines. .... 75
- Fig. 3.3** Comparison of the numerical solution to the Eqs. (3.3) (blue line) with the analytical Polyakova solution for monorelaxing medium in the form of stationary wave (red line). Black line is the initial waveform (hyperbolic tangent)..... 78
- Fig. 3.4.**  $N$ -pulse waveforms calculated at the distance  $r = 6$  m from the source with alternate account for different physical effects: ideal linear medium (no effects, grey line), nonlinearity only (red line), relaxation only (blue line), thermoviscous absorption only (green line), and all the effects (black line). The waveforms are multiplied by the ratio  $r/r_0$  to exclude spherical divergence of the wave. .... 79
- Fig. 3.5.** Dependence of the peak positive pressure (a) and half duration (b) of the  $N$ -pulse on the propagation distance. Peak positive pressure  $p_+$  is multiplied by the ratio  $r/r_0$  to exclude spherical divergence of the wave. .... 80
- Fig. 3.6** Linear fit for the squared half duration of the pulse. Correlation coefficient is equal to  $R=0.975$ . .... 81
- Fig. 3.7.** Measured (a) and calculated (b)  $N$ -waves at different distances from the source 0.15, 0.3, 0.5, 1, 1.5, and 2 m. Monotonic decrease of the pulse amplitude corresponds to the increase of the propagation distance. .... 82
- Fig. 3.8.** Averaged amplitude frequency response (a) and random sample of phase response (b) calculated for the total measuring system (blue line) and response of the microphone, provided by the manufacturer (red line)..... 83
- Fig. 3.9.** Experimental (red line) and theoretical (blue line)  $N$ -pulse waveforms and corresponding spectra at the initial distance  $r_0 = 0.15$  m (a, b) and at the distance  $r = 1.5$  m from the source (c, d). Filtered theoretical waveforms and spectra are shown with the black lines..... 84
- Fig. 3.10.** Dependence of peak positive pressure (a), half duration (b) and rise time (c) of the wave on propagation distance. Blue line – calculated results, red crosses – measured results, black circles – calculated results with filter applied. .... 85
- Fig. 4.1** Comparison of nonlinear waveforms, calculated at the distance  $\sigma = 157$  using different numerical algorithms and varying the number of grid points per shock front of the wave. a) – implicit numerical algorithm built on the basis of the exact solution to the simple wave equation, b) – explicit finite difference conservative algorithm, c) Godunov type explicit conservative algorithm. .... 103
- Fig. 4.2.** (a) Sound speed map for a medium with a single scalar focusing Gaussian inhomogeneity with  $\Delta c_{max}/c_0 \sim 3\%$  and (b) corresponding distribution of peak acoustic pressure resulting from linear continuous wave (CW) propagation through the

inhomogeneity. c) distributions of the pressure amplitude, obtained along the symmetry axis by solving KZK type Eq. (4.6) and wide angle parabolic equation (WAPE). ..... 106

- Fig. 4.3.** Comparison of peak pressure distributions in the solution to wave Eq. (4.6) with the distributions of acoustic rays obtained using geometrical acoustics equations for propagation of plane acoustic wave through the single scalar Gaussian inhomogeneities (a) of different sizes:  $R = 1.5\lambda$  (a,b),  $R = 3\lambda$  (c),  $R = 5\lambda$  (d) and same disturbance amplitude  $U_0 = 0.06$ . ..... 108
- Fig. 5.1.** (a) Longitudinal and (b) transverse components of the random velocity field with Gaussian energy spectrum. Characteristic length of inhomogeneities  $L = 3\lambda$ , and root mean square velocity  $u_{rms} = 2.5$  m/s. .... 112
- Fig. 5.2.** Spatial patterns of the peak positive pressure corresponding to (a) linear ( $N = 0$ ) and (b) nonlinear ( $N = 0.05$ ) propagation of an initially plane harmonic wave through the randomly inhomogeneous moving medium. (c) The result for nonlinear propagation ( $N = 0.05$ ) in the presence of an additional transverse constant flow  $U_{\perp}^0 = 0.1$ . Vertical solid line shows the location for the transverse field presented in Fig. 5.6, dashed vertical line - for the transverse distributions shown in Fig. 5.3, and dashed horizontal line - for the longitudinal distributions in Fig. 5.4. .... 112
- Fig. 5.3.** (a) Transverse distributions of the peak positive pressure at a distance  $x/\lambda = 24$  along the dashed segments shown in Fig. 5.2 for linear ( $N = 0$ , dotted line) and nonlinear ( $N = 0.05$ , solid line) propagation. (b) Linear and nonlinear waveforms at locations of maximum positive pressure  $x/\lambda = 24$ ,  $y/\lambda = 21.3$  (indicated as max in (a)). (c) Waveforms at the pressure minimum,  $x/\lambda = 24$ ,  $y/\lambda = 23.15$  (indicated as min in (a)). 113
- Fig. 5.4.** (a) Longitudinal distributions of the peak positive pressure for linear ( $N = 0$ , dotted line) and nonlinear ( $N = 0.05$ , solid line) propagation along the dashed line  $y/\lambda = 16.85$  shown in Fig. 5.2. (b) Linear and nonlinear waveforms at locations of maximum positive pressure,  $x/\lambda = 24$ ,  $y/\lambda = 16.85$  (indicated as max in (a)). (c) Waveforms at the pressure minimum,  $x/\lambda = 54$ ,  $y/\lambda = 16.85$  (indicated as min in (a)). .... 113
- Fig. 5.5.** Dependence on distance of propagation for the wave intensity averaged over the transverse coordinate for: linear propagation in a dissipative medium, nonlinear propagation governed by weak shock theory (WST), nonlinear plane wave propagation in a dissipative medium (Burgers equation), and nonlinear propagation in moving inhomogeneous dissipative media governed by the nonlinear parabolic equation (NPE). Parameters of simulations are  $N = 0.05$ ,  $A = 0.002$ ,  $N_{max} = 150$ . .... 114
- Fig. 5.6** Distributions of peak positive pressure along the transverse segments (solid lines) shown in Fig. 5.2b and Fig. 5.2c at the distance  $x/\lambda = 42$ . Black curve – propagation through random velocity field (Fig. 5.2b), red curve – analytic transformation of the numerical solution to account for additional constant flow, blue circles – full numerical solution in the case of the flow presence (Fig. 5.2c). .... 116
- Fig. 5.7** a) – longitudinal component of a random inhomogeneous velocity field with Gaussian energy spectrum and  $u_{rms} = 2.5$  m/s,  $L = 3\lambda$ . b) – corresponding spatial distribution of peak positive pressure in the case of linear wave propagation and ray paths – grey lines – solutions of the eikonal equation. .... 117

- Fig. 5.8:** a) – longitudinal component of a random velocity field ( $u_{rms} = 7.4$  m/s,  $L = 5\lambda$ ) and b) – corresponding spatial distribution of the peak positive pressure ( $N = 0.1$ ,  $A = 0.0052$ ,  $N_{max}=100$  harmonics). Both longitudinal and transverse components of the velocity field are taken into account. .... 118
- Fig. 5.9** Peak positive pressure distributions in longitudinal direction along the line  $y/\lambda = 39.5$  (a) and in transverse direction along the line  $x/\lambda = 17.5$  (b) in both linear ( $N=0.0$ ) and nonlinear ( $N=0.1$ ) regimes. Calculations are done with account for both longitudinal and transverse components of inhomogeneous field (dotted curves) or only with account for the longitudinal one (solid curves). .... 118
- Fig. 5.10.** a) Spatial distribution of peak positive pressure and longitudinal component of medium velocity fluctuations (grey contour lines). Dashed contours correspond to  $u_x/c_0 = -0.04$  level, and solid contours to  $u_x/c_0 = 0.04$  level. b) peak positive pressure distributions along dashed line in Fig. 5.10a calculated for different value of turbulent fluctuations intensities:  $u_{rms} = 7.4$  m/s and  $u_{rms} = 2.5$  m/s..... 119
- Fig. 5.11** Longitudinal a) and transverse b) components of the random velocity field with Gaussian energy spectrum. Characteristic fluctuation scale is equal to  $L=4\lambda$ , and mean square velocity is equal to  $u_{rms} = 3$  m/s ..... 121
- Fig. 5.12** a) - acoustic rays distribution in inhomogeneous moving medium with Gaussian energy spectrum (Fig. 5.11), b) corresponding acoustic field pattern (peak positive pressure) with marked turbulence levels  $u_x/c_0 = \pm 0.009$  (red – positive, blue - negative), c) expanded view of the peak positive pattern with overlaid rays distribution and caustic locations (grey points – first caustics, red points – second caustics) comparison. Area of expansion is marked with black rectangle in Fig. 5.12b ..... 122
- Fig. 5.13** Waveforms, measured at various locations along  $y/\lambda = 212$  axis while passing through the caustic ..... 123
- Fig. 5.14** Peak positive pressure spatial distributions corresponding to (a) linear ( $N = 0$ ) and (b) nonlinear ( $N = 0.05$ ) propagation of an initially plane acoustic  $N$ -wave through the randomly inhomogeneous moving medium (Fig. 5.11). Peak pressure distributions along dashed lines are shown in Fig. 5.15..... 124
- Fig. 5.15.** Peak positive pressure distribution along horizontal a) and vertical b) dashed lines shown in Fig. 5.14a. c) – Maximum over  $y$  axis peak positive pressure distribution along  $x$  axis..... 125
- Fig. 5.16** Typical linear ( $N=0.0$ ) and nonlinear ( $N=0.05$ ) waveforms measured in different points of the acoustic pressure pattern including (a) focal zones and (b)-(d) shadow areas. Initial  $N$ -wave is shown with the blue curve..... 127
- Fig. 5.17.** Mean peak positive pressure (a), mean rise time (b), and mean arrival time shift (c) of an  $N$ -wave propagating in turbulent medium in linear ( $N=0.0$  dashed lines) and nonlinear ( $N=0.05$  solid lines) regimes. Red lines – standard deviations of considered wave parameters in turbulent medium. Green line – 2<sup>nd</sup> order approximation of geometrical acoustics for mean arrival time ..... 128

- Fig. 5.18.** (a) Peak positive pressure probability density distributions at different distances from the source. Vertical red line is the mean value. Class width equals to 0.04. (b), (c), (d) – mean and standard deviation, skewness and excess parameters distributions over the propagation distance. Vertical dotted line is the prediction of the 1<sup>st</sup> caustics formation distance in the geometrical acoustics approximation. .... 131
- Fig. 5.19.** Shock front rise time (a) and arrival time (b) probability density distributions at different distances from the source. Class width equals to (a) – 0.16, (b) – 0.09. Vertical red line is the mean value of the considered parameter. .... 133
- Fig. 5.20** Peak positive pressure distributions calculated with or without account for the transverse component of the random velocity field. a) maximal over  $y$  axis distribution plotted along  $x$  axis, b) maximal over  $x$  axis distribution plotted along  $y$  axis ..... 134
- Fig. 5.21** Peak positive acoustic pressure distribution formed in inhomogeneous field with von Karman energy spectrum (Fig. 1.2e-g). Levels of turbulence intensity are marked with red – positive and grey –negative contours ( $u_x / c_0 = \pm 0.009$ ). .... 135
- Fig. 5.22** Mean acoustic wave rise time distributions in random medium with Gaussian (solid lines) or Karman (dashed lines) energy spectra. Red curves – corresponding standard deviations. Black line – rise time in motionless medium. .... 135
- Fig. 5.23.** Peak positive pressure distributions calculated with or without account for the transverse component of random velocity field. (a) maximal over  $y$  axis distribution plotted along  $x$  axis, (b) maximal over  $x$  axis distribution plotted along  $y$  axis..... 135
- Fig. 5.24** Comparison of characteristic scales in 2D modified von Karman energy spectrum of turbulent medium ( $L_0 = 19.3$  cm,  $l_0 = 2$  cm, blue) with the spectrum of the modelled initial  $N$ -wave ( $\lambda = 0.85$  cm, red curve, red  $y$ -axis)..... 137
- Fig. 5.25.** Experimental (a) and modelled (b) relative peak positive pressure  $p_+ / \langle p_+^0 \rangle$  probability distributions obtained at distance of 2.19 m from the source. Flow velocity at the exit of the jet  $U_{jet}$  varies from 0 m/s to 40 m/s.  $\langle p_+^0 \rangle$  is the mean value of the peak positive pressure, measured at the same distance in motionless medium. Red dashed lines correspond to the mean value of the pressure amplitude in turbulent medium. With designation *std* the standard deviation is shown. Class width equals to 0.07. .... 138
- Fig. 5.26** Dependence of the peak positive pressure of the acoustic wave and its standard deviation, measured at the distance 2.19 m from the source, on the flow velocity at the exit of the jet  $U_{jet}$  (turbulence intensity). Red curve – experimentally measured values, blue curve – results of simulation, black curve – result of simulations, to which the measuring system frequency response was applied. .... 139
- Fig. 5.27** Dependence of the peak positive pressure of the acoustic wave and its standard deviation on the distance from the source ( $U_{jet} = 20$  m/s). Red curve – experimentally measured values, which are multiplied by the  $r/r_0$  value to exclude the spherical divergence effects, where  $r_0 = 150$  mm. Blue curve – results of the simulation. .... 139
- Fig. 5.28.** Experimental (a) and modelled (b) arrival time probability density distributions measured at distance of 2.19 m from the source varying the flow velocity at the exit of the jet  $U_{jet}$  (turbulence intensity). Red dashed lines correspond to the mean value of the arrival

- time in turbulent medium. With designation *std* the standard deviation is shown.  
Class width equals to 0.095..... 142
- Fig. 5.29** Dependence of the mean arrival time of the acoustic wave and its standard deviation, measured at the distance 2.19 m from the source, on the flow velocity at the exit of the jet  $U_{jet}$  (turbulence intensity). Red curve – experimentally measured values, blue curve – results of simulation using parabolic equation (PE), green curve – values given by geometrical acoustics approach (GA). ..... 143
- Fig. 5.30** Dependence of the mean rise time of the acoustic wave and its standard deviation, measured at the distance 2.19 m from the source, on the flow velocity at the exit of the jet  $U_{jet}$  (turbulence intensity). Red curve – experimentally measured values, blue curve – results of simulation using parabolic equation, black curve – result of simulations, to which the measuring system frequency response was applied. .... 143
- Fig. 5.31** Cumulative probability  $P_c$  of normalized peak positive pressure calculated using the laboratory scale experiment data (a) and data from numerical modelling (b). Results are presented for different turbulence intensities. .... 144
- Fig. 5.32** Cumulative probability  $P_c$  of peak positive pressure measurement, which two times exceeds the acoustic wave amplitude measured in motionless medium at the same propagation distance. Results are presented for different turbulence intensities. .... 145
- Fig. A1.** a) an example of scalar Gaussian inhomogeneity with radius  $R=5\lambda$  and amplitude  $M = \delta c / c_0 \sim 0.06$ . b) acoustic ray paths and caustics corresponding to the plane acoustic wave propagation through presented inhomogeneity..... 155
- Fig. B1** Comparison of waveforms (b), longitudinal (c) and transverse (d) distributions of the peak positive pressure field (a), measured along dashed lines and calculated taking 256 (dotted line) or 512 (solid line) time grid points per duration of the wave. .... 161
- Fig. C1** Exemple d'une réalisation du champ aléatoire de la vitesse du milieu turbulent avec un spectre énergétique Gaussien. a) - composante longitudinale des fluctuations de la vitesse, b) - composante transversale des fluctuations de la vitesse, et c) – valeur absolue des fluctuations de la vitesse..... 168
- Fig. C2** Représentation schématique de la géométrie du dispositif expérimental ..... 169
- Fig. C3** Comparaison de la densité spectrale des fluctuations longitudinales de vitesse mesurée avec les valeurs théoriques obtenues pour un spectre de von Kármán modifié et la loi de décroissance en puissance «-5/3» de Kolmogorov dans la zone inertielle de turbulence. Les mesures ont été faites sur l'axe de la buse et à la distance  $x = 3780$  mm.. 170
- Fig. C4** Evolution du pic positif de la pression  $p_+$ , à une distance de 2,19m de la source, avec la vitesse axiale du jet  $U_{jet}$  : (a) valeurs moyennes et (b) distributions de la densité de probabilité ..... 172
- Fig. C5** a) Distribution du champ acoustique (pression du pic positif) avec les iso-niveaux des fluctuations de la vitesse du milieu  $u_{||} / c_0 = \pm 0.009$  marqués par dessus, b) zoom sur la région focale (le rectangle noir sur fig.5a) avec en plus la distribution des trajectoires des rayons acoustique et les positions des caustiques. .... 179

- 
- Fig. C6** Formes temporelles d'ondes mesurées à diverses distances de la source le long de la ligne  $y / \lambda = 212$  passant par une caustique..... 180
- Fig. C7** Evolutions avec la distance de propagation des distributions de la densité de probabilité de la pression du pic positif (a), du temps de montée du front de choc (b) et du temps d'arrivée relative de l'impulsion..... 181

## LIST OF REFERENCES

- 
- 1 Hill C. R., Bamber J. C., ter Haar G. R., *Physical Principles of Medical Ultrasonics*, 2<sup>nd</sup> Edition, WILEY, 2004
  - 2 Tatarskii V.I., *The effects of turbulent atmosphere on wave propagation*, (in Russian), Moscow, Nauka (1967); English translation: IPST Keter Press, Jerusalem (1971)
  - 3 Blohintsev D.I., *Acoustics of moving inhomogeneous media*, (in Russian), Moscow : Science, 1981
  - 4 Ostashev V.E. *Acoustic in moving inhomogeneous media*, Ed. E&Fn Spon, London, 1997
  - 5 Plotkin K. J., *State of the art of sonic boom modeling*, J. Acoust. Soc. Am. 2002, 111(1), 530–536
  - 6 Krasilnikov V. A., *Linear and nonlinear sound propagation in turbulent and inhomogeneous media*, Acoust. J. 1998, **44**, 559–569
  - 7 Lipkens B., *Experimental and theoretical study of the propagation of N-waves through a turbulent medium*, Ph. D. Thesis, Mechanical Engineering Department, The University of Texas at Austin, 1993
  - 8 Chunchuzov I.P., Bush G.A., and Kulichkov S.N., *On acoustical impulse propagation in a moving inhomogeneous atmospheric layer*, J. Acoust. Soc. Am. 1990, 88(1), 455-461
  - 9 Brehovskih L.M., *Ocean Acoustics*, Moscow, Science, 1974
  - 10 Bass H.E., Raszpet R., Chambers J.P., Kelly M., *Modification of sonic boom wave forms during propagation from the source to the ground*, J. Acoust. Soc. Am. 2002, 111(1), 481-486
  - 11 Averiyarov M.V., Khokhlova V.A., Cleveland R.O., Sapozhnikov O.A., Blanc-Benon Ph., *Nonlinear parabolic equation for acoustic wave propagation in inhomogeneous moving media*, Acoust. Phys. 2006, 52(6), 623-632
  - 12 Godin O.A. *An effective quiescent medium for sound propagating through an inhomogeneous moving fluid*, J. Acous. Soc. Am. 2002, 112 (4), 1269-1275.
  - 13 Babich V.M., Buldirev V.S., *Asymptotical methods in short waves diffraction problems*, (in Russian), Moscow, Science, 1972.
  - 14 Kravtsov Yu. A., Orlov Yu. I., *Geometrical Optics of Inhomogeneous Media*, Springer Verlag, Berlin, 1990

- 15 Kravtsov Yu. A., Orlov Yu. I., *Caustics, catastrophes, and wave fields*, Uspekhi Phys. Nauk. 1983, 26 (12), 1038-1058
- 16 Rudenko O. V., Sukhorukova A. K., *Nonlinear sawtooth-like wave in the inhomogeneous media*, Acoust. Phys. 1991, 37, 753–757
- 17 Rudenko O. V., Sukhorukova A. K., *Nonlinear sawtooth wave in an underwater sound channel*, Acoust. Phys. 1991, 37, 512-514
- 18 Blanc-Benon Ph., Juvé D., Comte-Bellot G., *Occurrence of caustics for high frequency acoustic waves propagating through turbulent fields*. Theoretical and Computational Fluid Dynamics 1991, 2, 271-278
- 19 Karweit M., Blanc-Benon Ph., Juve D. and Comte-Bellot G., *Simulation of propagation of an acoustic wave through a turbulent velocity field: A study of phase variance*, J. Acoust. Soc. Am. 1991, 89(1), 52-62
- 20 Rudenko O.V., Sukhorukova A.K., Sukhorukov A.P., *Equations of high-frequency nonlinear acoustics for inhomogeneous media*, Acoust. Phys. 1994, 40(2), 290-294
- 21 Rudenko O.V., Sukhorukova A.K., Sukhorukov A.P., *Full solutions of geometrical acoustics equations in stratified moving media*, Acoust. Phys. 1997, 43(3), 396-401
- 22 Rudenko O.V., Sukhorukova A.K., Sukhorukov A.P., *Two-Dimensional Nonlinear Waves with Discontinuities in Stratified Media*, Acoust. Physics 1995,41(2), 251-255
- 23 Ostashev V.E., Juve D., Blanc-Benon Ph. *Derivation of a wide-angle parabolic equation for sound waves in inhomogeneous moving media*, Acta Acustica united with Acustica, 1997, 83(3), 455-460
- 24 Dallois L., Blanc-Benon Ph., Juvé D. *A wide angle parabolic equation for acoustic waves in inhomogeneous moving media: applications to atmospheric sound propagation*, J.Comp. Acoustic. 2001, 9 (2), 477-494
- 25 Dallois L., Blanc-Benon Ph., *Wide angle parabolic equation in moving media: Sound diffraction by a core vortex*. AIAA,1-9, 2001
- 26 Godin O.A., *Wide-angle parabolic equation for sound in a 3D inhomogeneous moving medium*, Doklady Physics 2002, 47(9), 643-646
- 27 Godin O.A., *Parabolic approximation in the acoustics of moving media*, Acoust. Phys. 1991, 37, 335–339
- 28 Godin O.A., *Wave equation for sound in a medium with slow currents*, (in Russian), Dokl. Akad. Nauk 1987, 293(1), 63-67
- 29 Ostashev V.E. *Wide angle parabolic equation for sound waves in a refractive, turbulent atmosphere*. 10<sup>th</sup> LRSP simposium, Grenoble, 2002
- 30 Pelinovsky E.N., Freedman V.E., Engelbrekht U.K., *Nonlinear evolution equations*, (in Russian), Tallin, Valgus, 1984
- 31 Blanc-Benon Ph., Lipkens B., Dallois L., Hamilton M. F., Blackstock D. T., *Propagation of finite amplitude sound through turbulence: Modeling with geometrical acoustics and the parabolic approximation*, J. Acoust. Soc. Am., 2002, 111 (1), 487- 498
- 32 Ollivier S., Blanc-Benon Ph., *Numerical simulation of «low level» sonic boom propagation through random inhomogeneous sound speed fields*, Proc. of 19<sup>th</sup> ICA congress, Madrid, 2-7 September, 2007. (e-version)

- 
- 33 McDonald B.E., Kuperman W.A. *Time domain formulation for pulse propagation including nonlinear behaviour at a caustic*, J. Acoust. Soc. Am. 1987, 81(5), 1406-1417.
  - 34 Averiyarov M.V., Khokhlova V.A., Cleveland R.O., Blanc-Benon Ph., *Nonlinear and diffraction effects in propagation of shock N-wave in randomly inhomogeneous moving media*, Proc. XIX session RAO, Nizhniy-Novgorod, 24-28 September 2007,1, 147-151
  - 35 Averiyarov M.V., Khokhlova V.A. *Propagation of nonlinear acoustic waves in inhomogeneous moving medium*. Proc. of scientific school "Waves - 2004", Moscow region, Zvenigorod, Russia, section 1, p. 23-24 (in Russian)
  - 36 Blanc-Benon P., Khokhlova V.A., Averiyarov M.V., Dallois L., Cleveland R.O., *Propagation of nonlinear acoustic signals through inhomogeneous moving Media*, Proc. of the Joint Congress CFA/DAGA'04, March, 22-25, 2004, Strasbourg, France, V.2, 1059-1060. In Book of Abstracts: p.368
  - 37 Averiyarov M.V., Blanc-Benon P., Khokhlova V.A. and Cleveland R.O., *Diffraction of Nonlinear Acoustic Waves in Inhomogeneous Moving Media*, Proceedings of the Forum Acusticum, Budapest, Hungary,2005, 1403-1408
  - 38 Blanc-Benon Ph., Khokhlova V., Averiyarov M., and Cleveland R., *Propagation of nonlinear acoustic signals through inhomogeneous moving media*, In.: Proc. of 2nd International Conference "Frontiers of Nonlinear Physics" (July 5-12, 2004, Nizhny Novgorod - St. Petersburg, Russia) Ed. A Litvak.,674-678. In book of abstracts: p.75
  - 39 Khokhlova V.A., Blanc-Benon Ph., Averiyarov M.V., Cleveland R.O. *Diffraction of nonlinear waves in randomly inhomogeneous moving media*, In: Proc. of Joint Workshop RAS/SFA High intensity acoustic waves in modern technological and medical applications (14-18 November, Moscow, Russia), GEOS, 2005, 41-47
  - 40 Lipkens B., Blackstock D.T., *Model experiment to study sonic boom propagation through turbulence. Part I: Model experiment and general results*, J. Acoust. Soc. Am. 1998, 103(1), 148-158
  - 41 Lipkens B., Blackstock D.T., *Model experiment to study sonic boom propagation through turbulence. Part II: Effects of turbulent intensity and propagation distance through turbulence*, J. Acoust. Soc. Am. 1998, 104(3), 1301-1309
  - 42 Lipkens B., Blackstock D.T., *Model experiment to study sonic boom propagation through turbulence. Part III: Validation of sonic boom propagation models*, J. Acoust. Soc. Am. 2002. V. 111(1). P. 509-519
  - 43 Wright W.M, *Propagation in air of N-waves produced by sparks*, J. Acoust. Soc. Am, 1983, 73(6), 1948-1955
  - 44 Ollivier S., Blanc-Benon Ph., *Model experiment to study acoustic N-wave propagation through turbulence*, AIAA-2004-2921, 10th AIAA/CEAS Aeroacoustics Conference, Manchester, United Kingdom, May 10-12, 2004
  - 45 Ayrault C., Bequin Ph., Legros M., *Experimental study of a spark discharge as an acoustic source*. Proc. of 19<sup>th</sup> ICA congress, Madrid, 2-7 September, 2007. (e-version)
  - 46 Qin Q. and Attenborough K., *Characteristics and application of laser-generated acoustic shock waves in air*, Applied Acoustics 2004, 65, 325-340
  - 47 Vinogradova M.B., Rudenko O.V., Sukhorukov A.P., *Theory of Waves*, Moscow, Nauka, 1990, 2nd Edition, 432 pp

- 
- 48 Rudenko O.V., Soluyan S.I., *Theoretical foundations of nonlinear acoustics*, New York, Plenum, 1977
  - 49 Khokhlova V.A., Blanc-Benon P., Averianov M.V., and Cleveland R.O., *Propagation of nonlinear acoustic signals through inhomogeneous moving media*, Proceeding of the 2004 IEEE UFFC, August 23-27, 2004, Montreal, Canada, 533-536. In: Book of Abstracts, p. 494
  - 50 Blumrich R., Coulouvrat F., Heimann D, *Meteorologically induced variability of sonic-boom characteristics of supersonic aircraft in cruising flight*, J. Acoust. Soc. Am. 2005, 118, 707-722
  - 51 Piacsek, A. A, *Atmospheric turbulence conditions leading to focused and folded sonic boom wave fronts*, J. Acoust. Soc. Am. 2002, 111(1) Pt.2, 520-529
  - 52 Elmer K.R., Joshi M.C., *Variability of measured sonic boom signatures*, volume 1 – technical report, 1994, contract NAS1-19060 (e-version)
  - 53 Haering E. A., Ehernberger, L. J., and Whitmore S. A., *Preliminary Airborne Measurements for the SR-71 Sonic Boom Propagation Experiment*, NASA TM-104307, 1995 (e-version)
  - 54 Lee R.A., Downing, J.M., *Sonic Booms Produced by United States Air Force and United States Navy Aircraft: Measured Data*, USAF AL-TR-1991-0099, Jan 1991 (e-version)
  - 55 Hilton D. A., Hubbard H. H., Huckel V., Maglieri D. J., *Ground measurements of sonic-boom pressures for the altitude range of 10,000 to 75,000 feet*, NASA-TR-R-198, 1964 (e-version)
  - 56 Fidell S., Silvati L., Pearson K., *Relative rates of growth of annoyance of impulsive and non-impulsive noises*, J. Acoust. Soc. Am. 2002, 111(1) Pt 2, 481-486
  - 57 Leatherwood D., Sullivan B. M., Shepherd K. P., McCurdy D. A., *Summary of recent NASA studies of human response of sonic booms*, J. Acoust. Soc. Am. 2002, 111(1) Pt 2, 586 – 598
  - 58 Niedzwiecki A., Ribner H. S., *Subjective loudness of N-wave sonic booms*, J. Acoust. Soc. Am. 1978, 64, 1622–1626
  - 59 Maglieri D.J., Carlson H.W., *The shock wave noise problem of supersonic aircraft in steady flight*, NASA-MEMO-3-4-59L, 1959
  - 60 Haglund G.T., *HSCAT designs for reduced sonic boom*, AIAA-1991-3103, 1991
  - 61 Morgenstern J.M., Arslan A., Lyman V. and Vadyak J., *F-5 shaped sonic boom demonstrator's persistence of boom shaping reduction through turbulence*, AIAA-2005-0012, 2005
  - 62 Pierce A.D., *Acoustics: An Introduction to Its Physical Principles and Applications*, Acoust. Soc. Am. New York, 1989
  - 63 Pierce A. D. and Kang J., *Molecular relaxation effects on sonic boom waveforms*, in *Frontiers of nonlinear acoustics: Proceedings of the 12<sup>th</sup> ISNA*, edited by M. F. Hamilton and D. T. Blackstock Elsevier Applied Science, London, 1990, 165–170
  - 64 Blanc-Benon Ph., Ollivier S., *Model experiments to study acoustic N-wave propagation through turbulence*, 11th Long Range Sound Propagation Symposium, Lake Morey Resort, VT, 1-3 June 2004

- 
- 65 Pierce A.D., *Statistical theory of atmospheric turbulence effects on sonic boom rise times*, J. Acoust. Soc. Am. 1971, 49, 906-924
- 66 Thomas J.-L., Colouvrat F., Marchiano R., Baudoin M., Ganjehi L., *Experimental simulation of the sonic boom at the laboratory scale*, Proc. 19<sup>th</sup> ICA, Madrid, 2-7 September 2007 (e-version)
- 67 Kulichkov S. N., *Evidence for Nonlinear Atmospheric Effects in Infrasound Propagation from Explosions of Different Types and Yields*. In Proc. of 18th international symposium on nonlinear acoustics, Stockholm, Sweden, 7-10 July 2008, pp.401-404
- 68 Kulichkov S. N., Chunchuzov I. P., Bush G. A., and Perepelkin V. G., *Physical Modeling of long-range infrasound propagation in the atmosphere*. Izv. Atm. and Oc. Physics 2008, V.44(2), pp.175-186.
- 69 Chunchuzov I. P., Kulichkov S. N., Otrezov A., and Perepelkin V.G., *Acoustic pulse propagation through a fluctuating stably stratified atmospheric boundary layer*. J. Acoust. Soc. Am. 2005, 117(4), 1, 186-198
- 70 Kulichkov S. N., *Long-range propagation and scattering of low-frequency sound pulses in the middle atmosphere*. Meteorol. Atmos. Phys. 2004, 85, 47–60
- 71 Kulichkov S.N., Chunchuzov I.P., Bush G.A., Perepelkin V.G. *Physical Modeling of Long-Range Infrasonic Propagation*. Atmos. Izv., Atmos. and Oc. Phys. 2008, 44(2), 175–186.
- 72 Ostashev V.E., Lando Liu, Wilson D.K., Moran M.L., Aldridge D.F., Marlin D., *Starting equations for direct numerical simulation of sound propagation in the atmosphere*. J. Acoust. Soc. Am. 2003, 113(4), 2312-2313
- 73 Monin A. S., Yaglom A. M., *Statistical Fluid Mechanics: Mechanics of Turbulence*, Cambridge, Mass., MIT Press 1975, Vol. 2
- 74 Kraichnan, R.H. *Scattering of Sound in a Turbulent Medium*. J. Acoust. Soc. Am. 1953, 25, 1096-1104.
- 75 Lighthill, M. J. *On the energy scattered from the interaction of turbulence with. sound on shock waves*. Proc. Camb. Phil. SOC. 1953, 49, 531-551
- 76 Batchelor, G.K. *Wave scattering due to turbulence*. In Proc. 1st International Symposium on Naval Hydrodynamics, Washington, D.C., Washington 1956, 409–423
- 77 Neubert J.A., Lumley J.L. *Derivation of the stochastic Helmholtz equation for sound propagation in a turbulent fluid*, J. Acoust. Soc. Am. 1970, 48, 1212-1218
- 78 Wochner M.A., Atchley A.A., Sparrow V.W., *Numerical simulation of finite amplitude wave propagation in air using a realistic atmospheric absorption model*, J. Acoust. Soc. Am. 2005, 118(5), 2891-2898
- 79 Pierce A.D., *Propagation of acoustic pulses and sonic booms through small-scale atmospheric turbulence*, 16<sup>th</sup> AIAA/CEAS conference, Munich, Germany 1995, paper number AIAA-95-105
- 80 Gurbatov S.N. *Nonlinear interaction and scattering of random waves in non dispersive media*, Doctoral thesis 1985, Nizhniy Novgorod, Russia (in Russian)
- 81 Rudenko O.V. *Nonlinear sawtooth-shaped waves*, Physics – Uspekhi 1995, 38(9), 965-989
- 82 Coulouvrat F., *Focusing of weak acoustic shock waves at a caustic cusp*, Wave Motion 2000, 32, 233–245

- 
- 83 Coulouvrat F., *Sonic boom in the shadow zone: A geometrical theory of diffraction*, J. Acoust. Soc. Am. 2002, 111, 499–508
- 84 Marchiano R., Coulouvrat F. and Grenon R., *Numerical simulation of shock wave focusing at fold caustics, with application to sonic boom*, J. Acoust. Soc. Am. 2003, 114, 1758–1771
- 85 Marchiano R., Coulouvrat F., *Nonlinear focusing of acoustic shock waves at a caustic cusp*, J. Acoust. Soc. Am. 2004, 117, 566–578
- 86 Coulouvrat F., *Parabolic approximation in ray coordinates for high-frequency nonlinear waves in a inhomogeneous and high speed moving fluid*, Wave Motion 2008, doi:10.1016/j.wavemoti.2008.02.002
- 87 Dubrovskiy A.N., Khokhlova V.A., Rudenko O.V., *Fluctuation characteristics of sonic booms traversing a random inhomogeneous layer*, Acoust. Phys. 1996, 42(5), 623-628
- 88 Gusev V.A., Rudenko O.V., *Statistical characteristics of an intense wave behind a two-dimensional phase screen*, Acoust. Phys. 2006, 52(1) , 24–35
- 89 Yuldashev P.V., Khokhlova V.A., Averiyarov M.V., Blanc-Benon Ph., *Diffraction of nonlinear N-wave behind a random phase screen*, Proc. of ICA congress, Madrid, 2-7 September, 2007. (e-version)
- 90 Yuldashev P.V., Averiyarov M.V., Briseva N.A., Blanc-Benon Ph., Khokhlova V.A., *Statistical properties of an N-wave behind a random phase screen with account to diffraction effects and multiple caustics formation*, Proc. XIX session RAO, 24-28 September, 2007, 1, 147-151
- 91 Rudenko O.V., Enflo B.O., *Nonlinear N-wave propagation trough a one-dimensional phase screen*, Acta Acustica 2000, 86, 229-238
- 92 Shlenov S.A., Kandidov V.P., *Filament beam formation during femtoseconde laser pulse propagation in turbulent atmosphere. Part1. Method*, Optics of atmosphere and ocean 2004, 17(8), 630-636
- 93 Kraichnan R.H., *Diffusion by a random velocity fields*, Phys. Fluids 1970, 13, 22-31
- 94 Juve D., Blanc-Benon Ph., Wert K., *Numerical simulation of sound propagation through time-dependent random media*, Theoretical & Computational Acoustics 1997, World Scientific Publishing Co, pp. 653-665.
- 95 Wert K., Blanc-Benon Ph., Juve D., *Effect of turbulence scale resolution on numerical simulation of atmospheric sound propagation*, AIAA/CEAS 1998, Paper N° 98-2245, 4th AIAA/CEAS Aeroacoustics Conference, Toulouse.
- 96 Wilson D.K. *A turbulent spectral model for sound propagation in the atmosphere that incorporates shear and buoyancy forcing*, J. Acoust. Soc. Am. 2000, 108(5), pp. 2021-2038
- 97 Comte-Bellot G., Bailly C., *Turbulence*. CNRS, 2003
- 98 Gutmark E., Wygnanski I., *The planar turbulent jet*, J. Fluid Mech. 1976, 73 (3), 465-495
- 99 Comte-Bellot G., *Ecoulement Turbulent Entre deaux Parois Paralleles*, Publications Scientifiques et Techniques du Ministere de l'Air No. 419, 1965
- 100 Davy B.A., Blackstock D.T., *Measurements of the refraction and diffraction of a short N-wave by a gas-filled soap bubble*, J. Acoust. Soc. Am. 1971, 49, 732-737
- 101 Yuldashev P.V., Averiyarov M.V., Khokhlova V.A., Ollivier S., Blanc-Benon Ph., *Theoretical and experimental investigation of nonlinear spherically diverging wave*

- 
- propagation in relaxing media*, Proc. XVIII session RAO, Taganrog, 11 – 15 September 2006, 144-148 (In Russian)
- 102 Barrera-Figueroa S., Rasmussen K., *On experimental determination of the random-index response of microphones*, J. Acous. Soc. Am. 2007, 121 (5), 2628-2637
- 103 Averiyarov M.V., Yuldashev P.V., Khokhlova V.A., Ollivier S. and Blanc-Benon Ph., *Nonlinear Propagation of Spark-generated N-waves in Relaxing Atmosphere: Laboratory-Scaled Experiments and Theoretical Study*, 13th AIAA/CEAS Aeroacoustics Conference (28th AIAA Aeroacoustics Conference), paper AIAA 2007-3676
- 104 Yuldashev P.V., Averiyarov M.V., Khokhlova V.A., Ollivier S., Blanc-Benon Ph., *Experimental and theoretical study of nonlinear spherically divergent shock waves propagating in relaxing medium*, Acoust. Phys. 2008, 54(1), 40-50
- 105 Ollivier S., Averiyarov M., Yuldashev P., Khokhlova V., Blanc-Benon Ph. *Experimental and numerical study of the propagation of short duration acoustic N-waves in air*, 8<sup>ème</sup> Congrès Français d'Acoustique, 24-27 avril 2006, Tours, pp. 925-928
- 106 Ollivier S., Averiyarov M., Yuldashev P., Khokhlova V., Blanc-Benon Ph., *Spark-generated N-waves for laboratory-scale propagation experiments in air: measurements and modelling*, Proc. of ICA congress, Madrid, 2-7 September, 2007. (e-version)
- 107 Khokhlova V.A., Averiyarov M.V., Yuldashev P.V., Ollivier S., Blanc-Benon Ph., *Modelling and measurements of nonlinear spherically divergent N-waves in air*, J. Acoust. Soc. Am. 2006, 120(5) Pt.2, 3121-3122. (4th Joint Meeting of Acoustical Society of America and Acoustical Society of Japan, 2006, November 28 – December 2, 2006, Honolulu, USA)
- 108 Andreev V.G., Rudenko O.V., Sapozhnikov O.A., *Nonlinear effects in the 10 MPa acoustic pulses propagating in water*, Proc. of 12<sup>th</sup> ISNA 1990, Elsevier Science Publishers Ltd., London
- 109 Andreev V.G., Karabutov A.A., Rudenko O.V., *Method of wide band microphones calibration in ultrasound beams of finite amplitude*, Vestnik of Moscow State University, ser. 3, physics, 1984, 25(4), 74-77
- 110 Romanenko E.V., *Sound receivers and methods of their calibration*, In book: *Physics and techniques of intense ultrasound*, edited by Rozenberg L.D., Moscow Science, 1967, 327-377.
- 111 Cleveland R.O., Hamilton M.F., Blackstock D.T., *Time-domain modeling of finite-amplitude sound in relaxing fluids*, J. Acous. Soc. Am. 1996, 99, 3312-3318
- 112 Kurganov A.R., Tandmor E., *New high-resolution central schemes for nonlinear conservation laws and convection-diffusion equations*, J. Comp. Phys. 2000, 160, 241-282
- 113 Polyakova A.L., Soluyan S.I., Khokhlov R.V., *Propagation of finite disturbances in a relaxing medium*, Acoust. Zh. 1962, 8 (1), 107-113. (In Russian)
- 114 Picaut J., Simon L., *A scale model experiment for the study of sound propagation in urban areas*, Appl. Acoust. 2001, 62, 327-340
- 115 Cleveland R. O., Chambers J. P., Raspet R., Bass H. E., Hamilton M. F. and Blackstock D. T., *Comparison of computer codes for the propagation of sonic boom waveforms through isothermal atmospheres*, J. Acoust. Soc. Am. 1996, 100, 3017-3027
- 116 Lee Y.-S., and Hamilton M.F., *Time domain modelling of pulsed finite-amplitude sound beams*, J. Acoust. Soc. Am. 1994, 97, 906-917

- 
- 117 Khokhlova V.A., Souchon R., Tavakkoli J., Sapozhnikov O.A., Cathignol D., *Numerical modelling of finite-amplitude sound beams: Shock formation in the near field of a cw plane piston source*, J. Acoust. Soc. Amer. 2001, 110 (1), 95-108
- 118 Filonenko E.A., Khokhlova V.A., *Effect of acoustic nonlinearity on heating of biological tissue by high-intensity focused ultrasound*, Acoust. Phys. 2001, 47(4), 468-475
- 119 Kasheeva S. S., Khokhlova V. A., Sapozhnikov O. A., Averkiou M. A., and Crum L. A., *Nonlinear distortion and attenuation of intense acoustic waves in lossy media obeying a frequency power law*, Acoust. Phys. 2000, 46, 211-219
- 120 Averianov M.V., Basova M.S., and Khokhlova V.A., *Stationary and quasi-stationary solutions of the Burgers-type equations*, XIIth Scientific School "Nonlinear waves - 2004" abstracts (29 February – 7 March 2004, Nizhniy Novgorod, Russia), p.11. (In Russian)
- 121 Averianov M.V., Basova M.S., and Khokhlova V.A., *Stationary and quasi-stationary solutions of the Burgers-type equations*, Proc. of the Joint Congress CFA/DAGA'04, March, 22-25, 2004, Strasbourg, France, 1, 547-548. In Book of Abstracts: p.154
- 122 Averianov M.V., Basova M.S., and Khokhlova V.A., *Stationary and quasi-stationary solutions of the Burgers-type equations*, Acoust. Phys. 2005, 51(5), 495-501
- 123 Basova M.S., Averianov M.V., Khokhlova V.A., *The effect of frequency dependent absorption on propagation of nonlinear acoustic waves with shocks*, International conference «Lomonosov-2004», book of abstracts, section «physic», p.25. In Russian
- 124 Press W.H., Teukolsky S.A., Vetterling W.T., Flannery B.P., *Numerical Recipes in FORTRAN*, Cambridge U.P., New York, 1992
- 125 Lee Y.S., *Numerical solution of the KZK equation for pulsed finite amplitude sound beams in thermoviscous fluids*, PhD thesis (The University of Texas at Austin, 1993); as cited by Dissertation Abstracts International, 54-12 (B), 6246 (1993)
- 126 Jing Y. and Cleveland R.O., *Modeling the propagation of nonlinear three-dimensional acoustic beams in inhomogeneous media*, J. Acoust. Soc. Am. 2007, 122 (3), 1352-1364
- 127 Naze Tjøtta J., Tjøtta S., and Vefring E. H. *Effects of focusing on the nonlinear interaction of two collimated finite amplitude sound beams*, J. Acoust. Soc. Am. 1991, 89(3), 1017 - 1027
- 128 Cleveland R.O., Dallois L., Blanc-Benon Ph., *Effects of nonlinearity on the propagation of acoustic pulses in random media*, 144th ASA meeting, Cancun, J. Acoust. Soc. Am. 2002, Vol. 112, No 5 Pt 2, p. 2214
- 129 Khokhlova V.A., Averianov M.V., Cleveland R.O., Blanc-Benon Ph., *Parabolic approximation versus geometrical acoustics for describing nonlinear acoustic waves in inhomogeneous media*. J. Acoust. Soc. Am. 2005, 117(4) Pt.2, p. 2595 (149<sup>th</sup> Meeting: Acoustical Society of America joint with the Canadian Association, Vancouver 16-20 May)
- 130 Le Floch C., Fink M., *Ultrasonic mapping of the temperature in Hyperthermia: the thermal lens effect*, IEEE Ultrasonic Symposium, 1997, 1301-1305
- 131 Hallaj I.M., Cleveland R., Hynynen K., *Simulation of the thermo-acoustic lens effect during focused ultrasound surgery*, JASA, 2001, 109(5), 2245 - 2253
- 132 Blanc-Benon Ph., Juvé D., Ostashev V. E., Wandelt R., *On the appearance of caustics for plane sound-wave propagation in moving random media*, Waves in Random Media 1995, 5(2), 183-199

- 
- 133 Iooss B., Blanc-Benon Ph. and Lhuillier C., *Statistical moments of travel times at second order in isotropic and anisotropic random media*, *Waves in Random Media* 2000, 10, 381-394
  - 134 Averiyarov M., Khokhlova V., Ollivier S., Blanc-Benon Ph., *Nonlinear propagation of sonic booms in turbulent atmosphere: laboratory scale experiment and theoretical analysis*. In the programme to 18th ISNA, 7-10 July 2008, Stockholm, Sweden, p.32.
  - 135 Whitham G. B. *Linear and Nonlinear Waves*, 1974, New York Wiley
  - 136 Candel S. M., *Numerical solution of conservation equations arising in linear wave theory: Application to aeroacoustics*, *J. Fluid Mech.* 1977, 83, 465–493



## AUTORISATION DE SOUTENANCE

Vu les dispositions de l'arrêté du 7 août 2006,

Vu la demande du Directeur de Thèse

Monsieur Ph. BLANC-BENON

et les rapports de

Monsieur R. CLEVELAND

Professeur - Department of Aerospace and Mechanical Engineering - Boston University  
110 Cummington Street - Boston, MA 02215 - USA

et de

Monsieur V. PREOBRAJENSKI

Professeur - Institut d'Electronique de Micro-électronique et de Nanotechnologie - IEMN-DOAE  
UMR CNRS 8520 - Ecole Centrale de Lille - BP 48 - 59655 VILLENEUVE-D'ASCQ cedex

**Monsieur AVERIYANOV Mikhail**

est autorisé à soutenir une thèse pour l'obtention du grade de **DOCTEUR**

**Ecole doctorale MECANIQUE, ENERGETIQUE, GENIE CIVIL ET ACOUSTIQUE (MEGA)**

Fait à Ecully, le 26 septembre 2008

P/Le Directeur de l'E.C.L.  
La Directrice des Etudes

